INCREASING THE BLAST RESISTANCE OF CONCRETE MASONRY WALLS USING FABRIC REINFORCED CEMENTITIOUS MATRIX (FRCM) COMPOSITES

By

Ramon Perez Garcia

Thesis submitted to the University of Ottawa
in partial fulfillment of the requirements for the degree of
Master of Applied Sciences
in Civil Engineering

uOttawa

Department of Civil Engineering
Faculty of Engineering
University of Ottawa

ABSTRACT

Unreinforced masonry (URM) walls are often used as load-bearing or infill walls in buildings in many countries. Such walls are also commonly found in existing and heritage buildings in Canada. URM walls are strong structural elements when subjected to axial loading, but are very vulnerable under out-of-plane loads. This type of loading may come from different sources , including seismic or blast events. When subjected to blast, wall elements experience large pressures on one of their faces due to the high pressure produced in the air when an explosion takes place. This wave of compressed air travels in a very short time and hits the wall causing immense stresses, which result in large shear and bending demands that may lead to wall failure, and the projection of debris at high velocities that can injure building occupants. This failure process is highly brittle due to the very low out-of-plane strength that characterize such walls.

In the past years, many investigations have been carried out to enhance the structural behaviour of unreinforced masonry walls under out-of-plane loading. Different strengthening methods have been studied, which include the use of polyurea coatings, the application of advanced fiber-reinforced polymer (FRP) composites or the use of concrete overlays in combination with high performance reinforcement. Fabric-reinforced cementitious matrix (FRCM) is a new composite material that overcomes some of the drawbacks of FRP. This composite material consists of applying coatings which consist of one or more layers of cement-based mortar reinforced with a corresponding open mesh of dry fibers (fabric). This material has been studied as a strengthening technique to improve in-plane and out-of-plane capacity of existing URM walls as well as other structural elements, mostly under seismic actions. This thesis presents an experimental and analytical study which investigates the effectiveness of using FRCM composites to improve the out-of-plane resistance of URM walls when subjected to blast loading.

As part of the experimental program, three large-scale URM masonry walls were constructed and strengthened with 1,2 and 3 layers of FRCM using unidirectional carbon fabrics. In all cases the specimens were built as load-bearing concrete masonry (CMU) walls. To increase shear resistance, two of the walls were also grouted with a flowable self-compacting concrete (SCC) mortar. Blast tests were conducted using the University of Ottawa Shock Tube and the results are compared with control walls tested in previous research at the University of Ottawa. The experimental results show that the FRCM retrofit significantly improved the blast performance of the URM load-bearing walls, allowing for increased blast capacity and improved control of displacements. The performance of the retrofit was found to be dependent on the number of retrofit layers.

As part of the analytical research, Single Degree of Freedom (SDOF) analysis was carried out to predict the blast behaviour of the strengthened walls. This was done by computing wall flexural strength using plane sectional analysis and developing idealized resistance curves for use in the SDOF analysis. In general, the analysis procedure is found to produce reasonably accurate results for both the resistance functions and wall mid-height displacements under blast loading.

ACKNOWLEDGEMENTS

I want to thank God for always being in my life and for all the amazing things that he did for me during this process. Specially for my life and better health. I also thank my supervisors Dr. Hassan Aoude and Dr. Murat Saatcioglu for all their support throughout this project.

I would like to thank my family and specially my brother Roberto. “Never give up brother, never give up”. I would like to acknowledge Mr. Benoît Pelletier from Simpson Strong-Tie, the supplier of FRCM materials for my project, Mr. Ben McGregor at Aries Contracting Inc. for the help in FRCM application and Mr. Dan Rheaume from Sika Canada for sponsoring the glue (HIT-RE 500 V3) and providing the gun dispenser.

Lastly, I would like to show my gratitude to all the people who made this project possible, specially to my friends Hyunchul Jung and Yang Li.
Thank you all for all your help and support.

NOTATIONS

Symbol	Definition
A_e	Effective cross-sectional area
A_f	Area of fabrics by unit width of FRCM
A_n	Net area of masonry
A_{fm}	Area of FRCM composite
A_n	Net area of a masonry wall
C’	Compressive force due to the axial load
E_f	Tensile modulus of elasticity of the cracked FRCM
E_m	Modulus of elasticity of a masonry wall
F(t)	Applied load as a function of time
H	Height of a wall
I_{cr}	Cracked moment of inertia
I_o	Uncracked moment of inertia
I_r	Reflected Impulse
K_{LM}	Load mass factor
L	Length of a wall
L_d	Driver length
M_{cr}	Cracking flexural strength
M_f	Moment contribution of FRCM
M_m	Moment contributed by reinforced masonry
M_n	Nominal flexural strength
M_u	Ultimate flexural strength
P_0	Nominal concentric axial capacity
P_d	Axial load applied to the wall
R	Standoff distance
R(t)	Restoring force as a function of time
$P_{ri}(t)$	Idealized triangular pressure as a function of time
S	sectional modulus of the uncracked wall
W	Charge weight
Z	Scaled distance
d_{max}	Maximum displacement
d_{res}	Residual displacement
c	Depth of the neutral axis measured from the extreme compression fiber
f_{cs}	Axial compressive stress due to an axial load
f_{fe}	Effective tensile stress of FRCM
f_{fu}	Ultimate tensile stress of FRCM
f'_{fm}	Compressive strength of FRCM mortar
f'_m	Compressive strength of masonry prisms
$f'_{m.factored}$	Factored compressive strength of masonry prisms
f_r	Modulus of rupture
f_{rfm}	Modulus of rupture of FRCM mortar
f_{rm}	Modulus of rupture of masonry prisms
f_{fu}	Ultimate tensile strength of FRCM
k_1	Uncracked stiffness of masonry

k_2	Post cracking stiffness of masonry
p_d	Driver pressure
p_r	Reflected pressure
p_{cr}	Uniformly distributed pressure at just before cracking
p_u	Ultimate uniformly distributed pressure
t_f	Thickness of FRCM
t_d	Time of duration
t_m	Thickness of the masonry wall
$u(t)$	Displacement of masonry as a function of time
$\dot{u}(t)$	Velocity of masonry at mid-height as a function of time
$\ddot{u}(t)$	Acceleration of masonry at mid-height as a function of time
w	Uniformly distributed load
w_{cr}	Uniformly distributed load at just before cracking
w_u	Ultimate uniformly distributed load
δ_{anls}	Analytical displacement at mid-height
δ_{exp}	Experimental displacement at mid-height
Δ_{cr}	Deflection at just before cracking
Δ_u	Ultimate deflection
ε_f	Tensile strain of FRCM
ε_{fd}	Design tensile strain of FRCM
ε_{fe}	Effective tensile strain of FRCM
ε_{fu}	Ultimate compressive strain of FRCM
ε_{mu}	Ultimate compressive strain of masonry prisms
ρ	Ratio between area of FRCM reinforcement and net area of URM wall
Φ_m	Strength reduction factor for flexure
$\Phi_{v,f}$	Strength reduction factor for shear
ω_f	Calibrated reinforcement ratio

ACRONYMS

Acronym	Definition
ACI	American Concrete Institute
ASTM	American Society for Testing and Materials
CFCM	Carbon Fiber Cement Matrix
CFRP	Carbon Fibre Reinforced Polymer
CMG	Cementitious Matrix-Grid system
CMU	Concrete Masonry Unit
DAS	Data Acquisition System
DIF	Dynamic Increase Factor
ECC	Engineered Cementitious Composite
FE	Finite Element
FRCM	Fabric-Reinforced Cementitious Matrix
FRP	Fibre Reinforced Polymer
GFRP	Glass Fibre Reinforced Polymer
IMG	Inorganic Matrix Grid system
LVDT	Linear Variable Displacement Transducers
MBC	Mineral Based Composite
NSM	Near Surface Mounted
RC	Reinforced Concrete
RM	Reinforced Masonry
SRG	Steel Reinforced Grout
SDOF	Single Degree of Freedom
TNT	Trinitrotoluene
TRC	Textile Reinforced Concrete
TRM	Textile Reinforced Mortar
UDL	Uniformly Distributed Load
URM	Unreinforced Masonry Wall

Table of Contents

Lists of Figures

Lists of Tables

CHAPTER 1. INTRODUCTION

1.1. GENERAL

Blast loads are considered extreme loads, and can be caused by accidental explosions or deliberate bombing attacks. Although these events don't happen every day, they are still a potential threat. Some very unfortunate past events such as the “Toronto Sunrise plant explosion” in Canada (August 10, 2008), the “Lac-Mégantic rail disaster” in Canada (July 6, 2013), and the “Oklahoma City bombing” in the US (April 19, 1995) highlight the urgent and growing need to protect communities and buildings against these threats to ensure that people can live and work in safe environments where buildings and any type of structure can withstand a scenario of this nature with the smallest possible damage and the least number of people affected. That is why a large number of highly relevant structures, whether due to their cost or importance, must be designed under this type of load. Going from high-rise buildings to bridges, shopping centers, airports, government buildings, etc.

One solution to safeguard existing buildings from blast effects involves the introduction of innovative materials such as high-performance composite materials, that can be employed in the development of new construction techniques. One recent system to strengthen/retrofit structures is the Fabric Reinforced Cementitious Matrix (FRCM) composite system which consists basically in a fabric mesh working as reinforcement, bonded to the substrate (masonry/concrete) with a cement-based mortar. This system employs high-strength materials for the fabrics such as carbon, glass and PBO fibers, which present high tensile capacities and make them very attractive for reinforcement of concrete and masonry elements under flexure and shear.

In Canada as well as in many countries in the world, buildings have a large percentage of masonry ranging from structural to non-structural elements and are part of various structures (e.g. houses, hospitals, office buildings, churches, schools, heritage structures, etc.), many times as load-bearing or filling walls, and other times as structural columns, arches or simply as architectural elements. However, many masonry structural elements and in particular walls in older buildings, lack internal reinforcement, in addition to being built with very old design methods which underestimate or do not consider lateral loads and their effects. These deficiencies make them vulnerable to the effects of out-of-plane loads, such as seismic and blast loads, among others. This problem occurs mainly in existing heritage buildings since seismic as well as blast engineering (applied on buildings) are emergent sciences with few decades of existence.

Unreinforced masonry (URM) walls are susceptible to sudden brittle collapse under the effects of out-of-plane bending since they lack internal reinforcement and are built with brittle materials that have low tensile capacities which crack and fail a very low tensile stress. Two examples of out-of-plane bending failures of URM walls during past earthquakes can be seen in **Figure 1-1**.

Figure 1-1. Out-of-plane failures of load-bearing URM walls during the Umbria Earthquake, Italy, 1997 (Babaeidarabad, 2013)

URM walls are also susceptible to collapse under the effects of blast load, since this load is a lateral load that demands high out-of-plane resistance. Recently, URM walls as well as other masonry elements, have been strengthened/retrofitted with different new composite systems, such as FRCM, to enhance their out-of-plane resistance, especially under the effects of seismic loads. This thesis investigates the effectiveness of using FRCM composites to enhance the out-of-plane capacity of URM walls under the effects of blast loads.

1.2. OBJECTIVES AND SCOPE

The primary objective of this research project is to examine the effectiveness of using FRCM-composite systems with carbon fiber meshes as reinforcement, to enhance the out-of-plane blast resistance of unreinforced masonry (URM) walls. To accomplish this objective, this thesis covers the following scope:

1. An experimental program which includes three Load-bearing URM walls built with concrete masonry units (CMU), and retrofitted with one, two and three layers of FRCM-composites, and subjected to blast loading, using the University of Ottawa Shock Tube. The effectiveness of the retrofits will be assessed by comparing the results in terms of ultimate blast resistance, displacement control and failure mode to a control (un-retrofitted) wall tested by Ciornei (2012).

2. An analytical investigation which intends to predict the flexural capacity of the FRCM-retrofitted URM walls and their blast response in terms of maximum mid-height displacement using a single-degree-of-freedom analysis approach.

1.3. THESIS BREAKDOWN

Chapter 1 - Introduction:

- Brief introduction and scope of this research project.

Chapter 2 - Literature review:

- More detailed introduction of FRCM systems, as well as applicable design guidelines;
- Review of previous research carried out on the use of FRCM to strengthen/retrofit masonry and concrete structures subjected to static, dynamic and impact loads.

Chapter 3 - Experimental program:

- Description and explanation of the experimental program including details of the design, construction, testing, and standards or guidelines followed in this research project. It also included the results of the material test program, and the set-up details of the walls and all specimens tested.

Chapter 4 – Experimental Results:

- Details of the experimental results of the three walls tested under blast loading, which includes; driver length and driver pressure used for each shot, reflected pressure and reflected impulse, time duration of the positive phase of the reflected pressure, pressure-time history, displacement-time history, damage progression and important observations during the tests.

Chapter 5 – Discussion:

- Broader discussion and details of the experimental results;
- Comparison of the performance of the three retrofitted walls against the performance of other walls tested by authors, including a control load-bearing URM wall, a stone load-bearing wall and an infill CMU wall. A discussion on the effect of the retrofit ratio is also included.

Chapter 6 – Analysis

- Analysis and comparison of the shear and moment capacities of the three walls;
- Flexural analysis and construction of idealized resistance curves for the three load-bearing CMU walls retrofitted with FRCM composites;
- Single degree of freedom analysis and results of the three walls using the idealized resistance curves obtained from the flexural analysis;
- Comparison of the analytical and experimental displacement results obtained from the Single degree of freedom Analysis.

Chapter 7 – Conclusion

- Conclusions and comments of the overall results obtained in this research project.

CHAPTER 2. LITERATURE REVIEW

2.1. CHAPTER OVERVIEW

This chapter presents a literature review introducing background information and previous research associated with Fabric-Reinforced Cementitious Matrix (FRCM) and its applications as a retrofit material to enhance the structural performance of unreinforced masonry (URM) elements. Especially, the following sections are presented in this chapter:

- Section 2.2: Introduces FRCM and its constituents;
- Section 2.3: Reviews previous research on use of FRCM to strengthen URM walls;
- Section 2.4: Reviews previous research on use of FRCM to strengthen structures tested under extreme dynamic loading.
- Section 2.5: Introduces existing FRCM design guidelines;

2.2. INTRODUCTION TO FRCM

2.2.1.FRCM definition

Fabric-Reinforced Cementitious Matrix (FRCM) can be defined as: "*a composite material consisting of a sequence of one or more layers of cement-based matrix reinforced with dry fibers in the form of open single or multiple meshes that, when adhered to concrete or masonry structural members, forms a FRCM system*" (ACI 549, 2013). Other names are also adopted in the literature to label FRCM systems (Jos, 2016), including: TRC (Textile Reinforced Concrete), TRM (Textile Reinforced Mortar), CMG (Cementitious Matrix-Grid system), MBC (Mineral Based Composites), CFCM (Carbon Fiber Cement Matrix), etc. (Jos, 2016).

FRCM composite systems are used on concrete and masonry structures as a strengthening technique on a variety of elements such as columns, walls, beams and slabs, as shown in Figure 2-1. In the case of masonry walls, different FRCM reinforcement configurations are proposed in the literature with the purpose of increasing out-of-plane flexural strength and/or in-plane shear/seismic resistance as observed in Figure 2-1 (b).

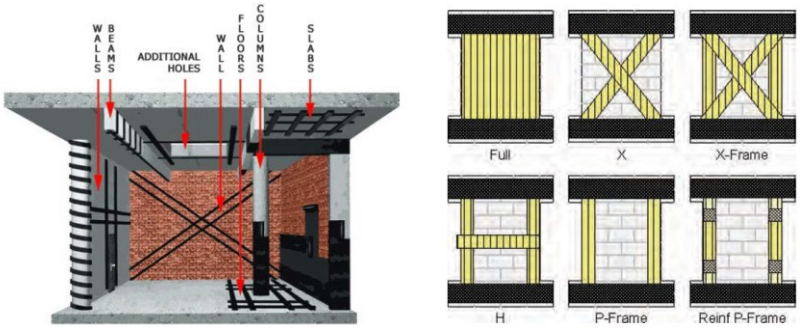

(a) (b)

Figure 2-1. (a) Typical structural elements of a building showing repairs (in black) (Arboleda, 2014), (b) Reinforcement configuration for wall (ACI 549.4R-13, 2013)

2.2.2. Constituents of the FRCM composite

The two main components of FRCM-composite system include the fabrics (fiber grids and cement-based matrix (mortar). The mortar is commonly sprayed adopting the same procedures used to apply wet shotcrete repair mortars; nonetheless, it can be applied by hand using troweling. The fiber grids (carbon, glass, PBO, etc.) can be unidirectional or bidirectional grids, where the FRCM-composite system can be applied in various grid layers (1 to 4 layers) to attain the targeted strengthening level. The thickness of each grid layer is generally half (½") to one (1") inch thick (12.7 to 25.4 mm).

Fabrics

The fabrics in the FRCM system are textile grids that work as structural reinforcement meshes made of dry fibers, yarns, or a combination of both, where a yarn is a bundle of hundreds or thousands of natural or artificial fibers. Codispoti et al. (2015) presents various types of natural fabrics made of jute, sisal, flax and hemp as illustrated in Figure 2-2.

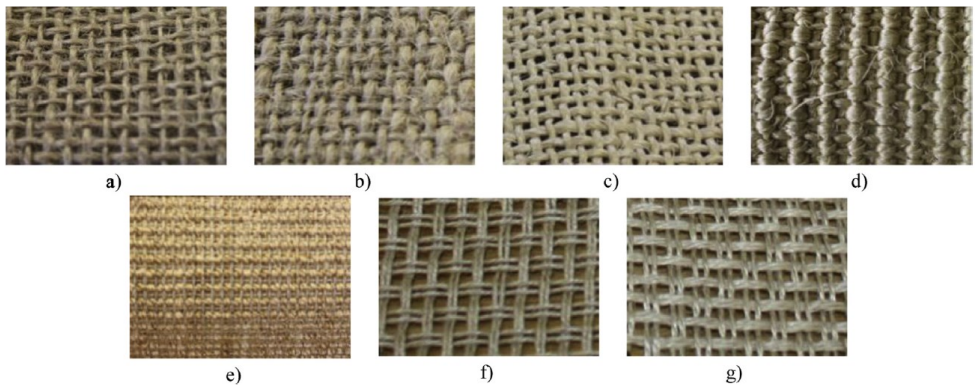

Figure 2-2. Different types of natural fabrics: (a-c) jute, (d, e) sisal, (f) hemp, (g) flax (Codispoti et al., 2015)

On the other hand, artificial fibers were developed to obtain higher strength capacities when compared to natural fibers. Some of them include: aramid, carbon, alkali-resistant (AR) glass, basalt or polymers like polypropylene (PP), polyethylene (PE) and polypara-phenylene benzobisoxazole (PBO) as illustrated in Figure 2-3.

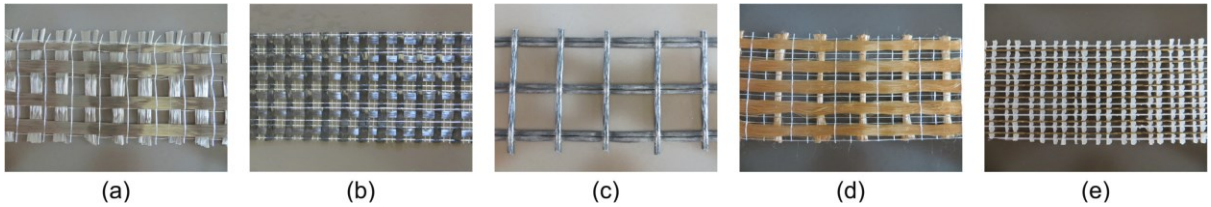

Figure 2-3. Different types of artificial fabrics: (a) basalt, (b) carbon, (c) glass, (d) PBO and (e) steel. (Escrig et al., 2017)

Both unidirectional or bidirectional fabrics are used depending on the loading conditions as presented in Figure 2-4.

Figure 2-4. FRCM carbon grid: Bidirectional (left) and unidirectional (right) (taken from manufacturer's data sheet)

Cementitious matrix

The cementitious matrix or cement-based mortar is the second main component in FRCM composite systems and is used to hold the structural reinforcing fabrics. Even though, cement-based mortars are frequently used for repairing and strengthening concrete structures, non-hydraulic mortars, such as lime-based mortars, are generally used for masonry structural elements, especially in heritage buildings.

Donnini et al. (2017) conducted direct tensile tests on FRCM coupons using either lime-based or cement-based mortar. It was concluded that the mechanical effectiveness for tensile resistance and stiffness modulus of the coupons with cement-based mortar were lightly superior than those with lime-based mortar for the same fabrics.

According to ACI 549.4R-13 (2013), cement based mortars may contain a small dosage (up to 5% by weight of cement) of polymeric additives and/or discontinuous fibers with the objective of enhancing its mechanical properties (strength, deformability) and durability. As noted before, the mortar can be applied by spraying, in the same manner as shotcrete, or by hand troweling, depending on the instructions provided by the manufacturer.

2.2.3. Mechanical properties of FRCM

FRCM systems are typically characterized by their tensile stress-strain response. This response typically shows three stages as shown in Figure 2-5 (ACI 549, 2020). In the first stage (I), the mortar is uncracked, and therefore the capacity and stiffness is governed by the mortar properties. The first crack occurs at the start of second stage (II), and during this stage the crack pattern is gradually developed. This stage is dependant on the matrix and matrix-to-fabric bond properties and is not always easily discernable. The third stage is typically associated with a nearly linear response. No further cracks develop in stage, with widening of the existing cracks. This crack widening results in local sliding and debonding at the fiber-matrix interface. The response (stiffness and load-bearing capacity) in stage III is dependant on the test configuration, and is similar to that of the bare fabrics in the case of clamped systems, and more dependant on the fabric-matrix bond in the case of clevis-grip configurations (ACI 549, 2020).

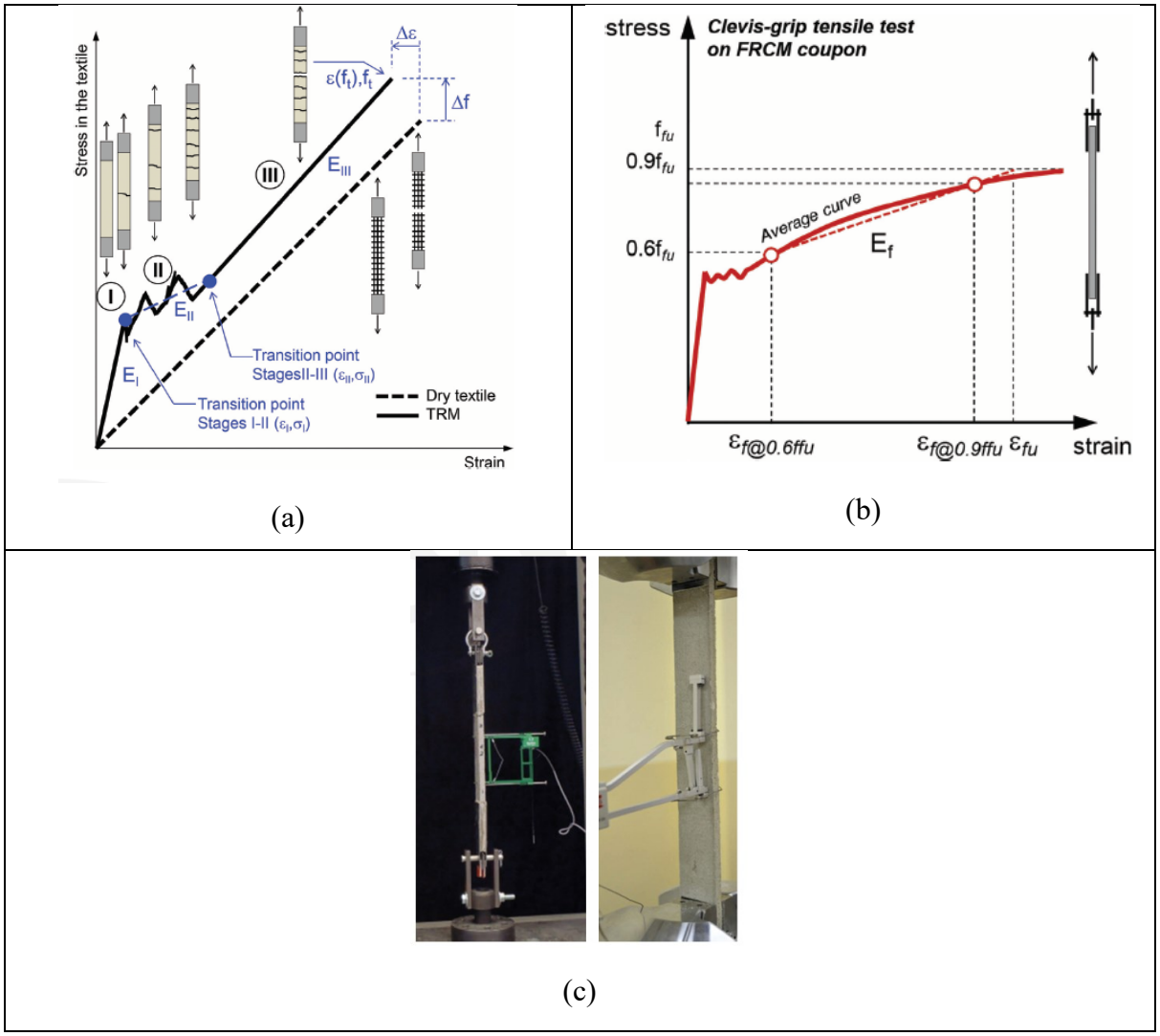

Figure 2-5. FRCM tensile response: (a) stages in response for clamped systems, (b) stages in response for clevis-grip systems, (c) clevis and clamped test setups (Reproduced from ACI 549.6R-20)

2.3.PREVIOUS RESEARCH: FLEXURAL STRENGTHENING OF MASONRY WALLS WITH FRCM.

This section reviews previous studies on masonry walls strengthened with FRCM to measure different parameters like, flexural, shear and displacement capacity under either "in-plane" and 'out-of-plane" loading. Temperature was introduced to some studies as well as other variables like the type of mesh or mortar, the reinforcement ratio, axial loading, etc. Some of the tests made on full-scale walls; whereas, some tests were done on smaller-scale beam or shear elements. An overview of previous studies is presented in Table 2-1.

2.3.1. FRCM strengthened Masonry beams.

C. G. Papanicolaou, T. C. Triantafillou, M. Papathanasiou, K. Karlos (2008)

Papanicolaou et al. (2008) investigated the effect of textile reinforced mortar (TRM) on unreinforced masonry walls under cyclic out-of-plane loading. Twelve medium-scale wall elements were tested. The specimens were divided into two groups according to their dimensions, 1300 x 400 mm and 400 x1300 mm for Series A and Series B, respectively. The test parameters included the number of layers, the orientation of the moment vector with respect to the bed joints, the matrix materials (resin-based versus mortar-based) and the use of FRP systems, TRM jackets and NSM strips. Series A included the control specimen with no strengthening, two specimens strengthened with one or two layers of textile bonded with a polymer-modified cement mortar, and two specimens with the textiles bonded with a two-part epoxy adhesive. Series B included the same test matrix as Series A but also a specimen with two NSM CFRP strips per side and another specimen with three NSM CFRP strips per side. For the test setup the specimens were subjected to cyclic out-of-plane loading and loaded in three-point bending over a span of 1.20 m for Series A and 1.15 m for Series B (Figure 2-6).

The results show that a significant increment in deformability and strength was provided by the TRM jacketing which was noted to be more efficient in comparison with (FRP) that uses an epoxy-resin. Walls retrofitted with TRM had higher strength and displacement capacity at failure than walls with FRP when the failure modes were due to the masonry (Figure 2-6). Whereas, when it was due to the textile (Figure 2-6), TRM was lightly less effective. On the other hand, the NSM strips provided more deformability but less strength due to controlled debonding. Finally, it was observed that as the strengthening layers increased, the higher the flexural strength obtained in the walls.

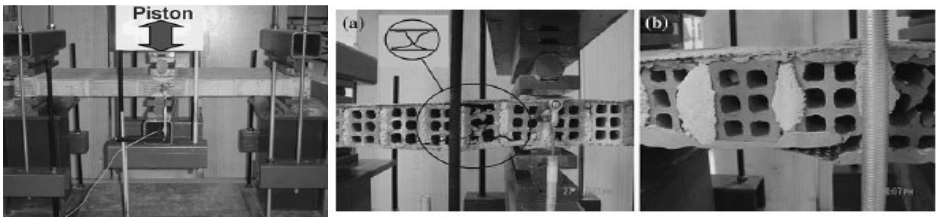

Figure 2-6. Test setup and results (Papanicolaou et al., 2008)

M. Harajli, H. ElKhatib, J. T. San-Jose (2010)

Harajli et al. (2010) investigated the response of unreinforced masonry walls (URM) strengthened with textile-reinforced mortar (TRM) system. Twenty-five masonry walls were tested under four-point bending loading, using bricks, sandstones, or concrete hollow blocks, with dimensions of 200 x 100 x 55, 300 x 100 x 200 and 400 x 100 x 200 mm, respectively. The parameters investigated were the textile material (uncoated basalt, coated basalt, steel wire mesh and bitumen coated E-Glass), the textile reinforcement ratio, the wall dimensions, the mortar for the coating of the textile reinforcement (either a natural lime or a cement-based mortar) and the application of the fabrics on one or both wall faces (on one face for static loading and on both faces for cyclic loading). The static test setup consisted of a load applied by an actuator monotonically at a displacement rate of 5 mm/min until failure. On the other hand, the load was applied in a displacement controlled mode for the cycling loading until failure, with a displacement rate from 0.1 mm/s to 1 mm/s.

The results showed that, regardless of the masonry unit type, the out-of-plane displacement and flexural capacity were increased appreciably in all the walls, in comparable values, under static loading. The performance also improved under cyclic loading, and the out-of-plane displacement and flexural capacity increased. The largest increase in strength was observed in the walls reinforced with steel wire mesh, but brittle failure was observed. The use of coated basalt textile in combination with a lime mortar (either normal or high strength) resulted in the greatest energy dissipation as well as the least strength and stiffness degradation, during the cycling loading tests.

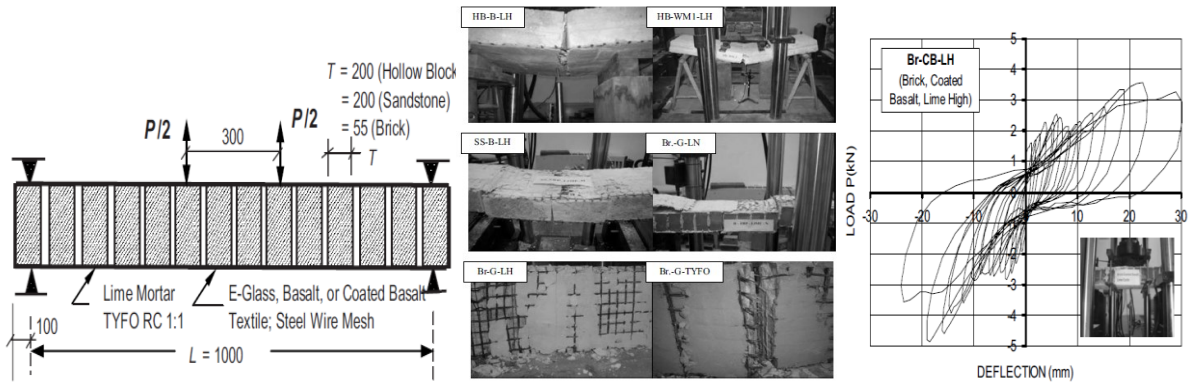

Figure 2-7. Test setup, typical failures modes and Cyclic load-displacement response of TRM strengthened with coated basalt and high strength lime (Harajli et al., 2010)

E. Bernat-Maso, C. Escrig, C. Aranha, L. Gil (2014)

Bernat-Maso et al. (2014) investigated the performance and failure modes of strengthening URM wallettes with Textile Reinforced Mortar (TRM) to enhance flexural behavior. Nineteen wallettes made of clay bricks and with approximate dimensions of 280 mm x 157 mm x 630 mm were tested. The main variables were the reinforcement ratio (1 and 2 grids per layer), the type of fabric (Glass, Carbon, Steel and Basalt), the application method of the TRM (by hand or sprayed) and the shear span length. For the test setup, three-points bending tests were applied to the specimens after 28 days of curing in the mortar of the TRM.

The results showed that the failure mode may depend on the mortar type producing debonding failure on the span length, where the shear may become more influential. No significant differences were observed between specimens built using spraying or hand-applied TRM when compared under the same conditions (number of fiber grids, type and mortar type). It was noted that the flexural strength is generally superior if the grid spacing lets the mortar to pass and properly bond the grid and the masonry. Moreover, introducing a bigger amount of fibers in the TRM strengthening results in higher load-bearing capacities, mainly because of the influence of the additional mortar layers which result in higher cross-sectional area, and higher axial stiffness. Finally, applying TRM on both sides of the specimens (compression and tension sides), does not enhance the performance compared with specimens with TRM only on the tensile side.

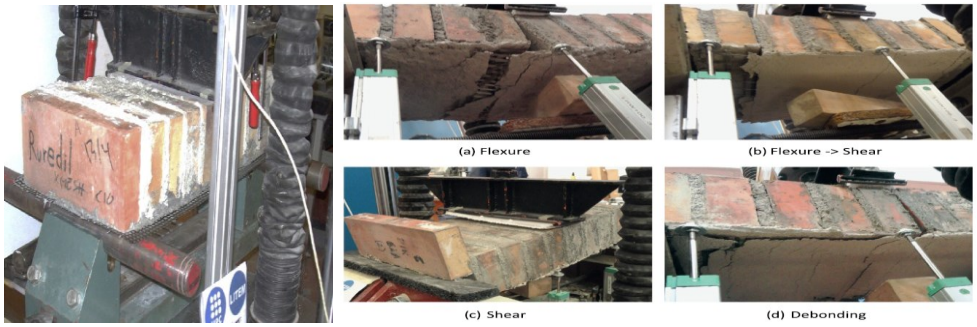

Figure 2-8. Test setup and resulting failure modes; (a) Flexure (left-up), (b) Flexure and shear (right-up), (c) Shear (left-down), (d) Debonding of the fiber layer (right-down) (Bernat-Maso et al., 2014)

M. R. Valluzzi, F. da Porto, E. Garbin, M. Panizza (2014)

Valluzzi et al. (2014) investigated the performance and failure modes of strengthening URM walls using Textile Reinforced Mortars (TRM), Steel Reinforced Grouts (SRG) and Fiber Reinforced Polymers (FRP) to enhance out-of-plane behavior. Twenty-seven wallettes made of clay bricks with nominal dimension of 390 x 780 x 120 mm for compression tests and 250 x 515 x 120 mm for bending tests, were made and tested. The main variables were the type of fabric (Carbon, Basalt, Hemp, Flax, Steel and Glass) and the matrix type (Epoxy resin, Cement putty and Magnesia mortar). For the test setup (Figure 2-9), four-point monotonic bending tests were performed by means of a double-effect hydraulic jack connected to a press. Additionally, the load was measured by a 10-ton load cell, while the displacement was measured by six LVDT transducers. The load was applied along the two central transverse joints, and were 265 mm apart, and the span between supports was 1,100 mm.

The results showed that the reinforcement systems were effective in enhancing the out-of-plane behavior, reaching 3 to 10 times the maximum bending load resistance of plain masonry. It was also noted that the best-performing materials were CFRP and HD SRP and they had the highest load capacities. Moreover, the lowest values in terms of peak load was obtained from natural fibers combined with epoxy, due to tensile fiber failure; even though, the ultimate displacement capacity was very large in comparison with the other composites. Finally, it was concluded that improving the performance of masonry walls does not need big levels of reinforcement, as the use of high-performance materials (SRP or CFRP) can lead to shear failure in the masonry. Hence, it is desirable to use systems in which the application of inorganic mortars (low-density steel textiles or various types of meshes, even quite weak ones like plaster nets) can ensure good performance for both load and displacement (Figure 2-9).

Figure 2-9. Test setup and failure modes, Tensile rupture of a) Flax FRP and b) Plaster net; c) splitting of fibres; d) shear failure in Basalt TRM; debonding in e) Basalt FRP and f) HD SRP (Valluzzi et al., 2014)

F.A. Kariou, S.P. Triantafyllou, D.A. Bournas, L.N Koutas (2018)

Kariou et al. (2018) investigated the response of masonry walls strengthened with textile-reinforced mortar (TRM) system. Eighteen masonry brick walls in total were tested with dimensions of 1340 x 440 x 103 mm. The parameters investigated were the textile material, the textile reinforcement ratio, the wall thickness and the coating of the textile reinforcement with epoxy resin. For the experiment, three-point bending tests were carried out on 18 specimens comprising a set of 9 single-wythe and 9 double-wythe brick masonry walls with an effective span of 1125 mm and supports spaced at 108 mm from the end. The test setup consisted of a stiff steel reaction frame fastened with a vertically positioned servo-hydraulic actuator of 100 kN capacity, used for the load application at a displacement rate equal to 0.017 mm/s.

The results showed that the TRM significantly enhanced the load bearing capacity of masonry walls. On the other hand, the amount of reinforcement used affected both the strength and deformation properties of the specimens, while it seems to modify the failure mode. Additionally, using resin coating on the textile was found to be beneficial for the performance of the TRM overlays. Finally, it was observed that single-wythe walls with TRM system were more efficient than those with double-wythe.

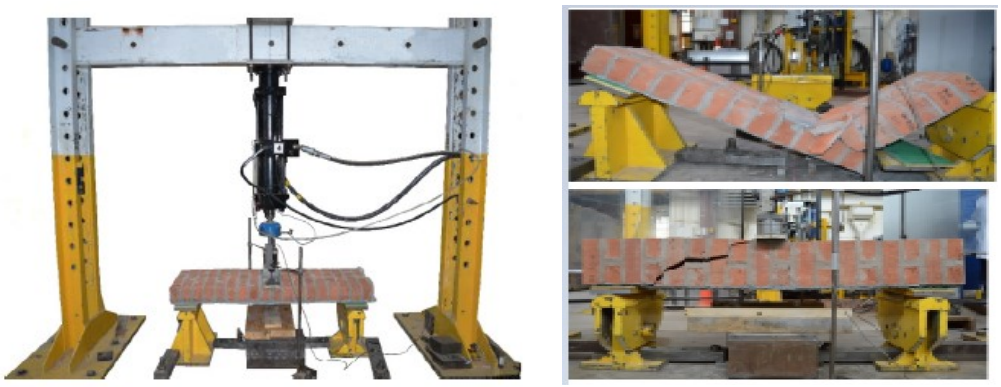

Figure 2-10. Test setup and results. Single-wythe (right-up), Double-wythe (right-down) with one layer of carbon textile (Kariou et al., 2018)

Z.A. Al-Jaberi, J.J. Myers, M.A ElGawady (2018)

Al-Jaberi et al. (2018) investigated the failure mechanism and the flexural behavior of reinforced masonry walls with externally bonded strengthening system subjected to out-of-plane cyclic loading. Twelve reinforced masonry walls were tested with dimensions of 1220 mm height by 610 mm length and steel reinforcement of 2-No.4 bars. In addition, the walls were fully grouted. The main variables were the strengthening system (FRCM and FRP), the reinforcement ratio, the fabric material (carbon vs. glass in EB FRP and PBO vs. carbon in FRCM) and lastly the type of masonry wall bond pattern: stack vs. running. For the test setup the specimens were tested under four-point bending and simply supported conditions. A vertical load was applied by using an MTS double-acting hydraulic jack and transferred to the masonry walls through continuous steel plates and bars along the full width of the specimens producing two equal line loads (see Figure 2-11). The load was applied as a displacement control in cycles of loading and unloading, at a rate of 1.27 mm/min.

The results showed that EB FRP and FRCM systems enhanced the stiffness and flexural capacity of the reinforced masonry walls. The load carrying capacity was enhanced by 100% for the specimens strengthened with two layers of GFRP compared to the increased of 85 % for specimens strengthened with 2 strips of CFRP laminate owing to the high debonding strain of epoxy used with GFRP. The specimens strengthened with 2 layers of PBO or carbon fiber presented slightly higher moment capacity than the ones with FRCM owing to the better bond performance for PBO compared to bond of the carbon in the FRCM system. Finally, it was also concluded that the pre-yielding stiffness was affected by the fiber axial stiffness and the fabric bond agent, concluding that the increase in stiffness of a strengthened specimen, for the same bonding agent, is a function of the fiber axial stiffness.

Figure 2-11. Test setup and results (Al-Jaberi et al., 2018)

2.3.2. FRCM strengthened Wall elements under Out-of-plane loading.

Kolsch (1998)

Kolsch et al. (1998) investigated the failure mechanism and flexural behavior of unreinforced masonry infill walls strengthened with externally bonded CFRCM strengthening system under out-of-plane cyclic loading. One retrofitted masonry wall was tested with dimensions of 3000 x 3000 x 240 mm and built with sand lime-bricks in a cross-bond pattern. The only variable was the comparison between the strengthening system composed of an overlay of 3 layers of unidirectional carbon fabric and a polymer modified mortar and the control wall. For the test setup (Figure 2-12), the specimen were tested under out-of-plane loading, by using a pressure bag with dimensions of 2 x 2 m, placed at the center of the wall. Then quasi-static cyclic loading was applied with increasing load steps.

The results showed that the strengthening system used (CFRCM) enhanced the out-of-plane capacity of the wall. Additionally, it prevented either partial or complete collapse of the masonry walls in the critical out-of-plane direction (Figure 2-12). Finally, it was stated that the wall withstood an equivalent static force of 3g (three times the acceleration of gravity), that exceeds any seismic loads expected for such walls.

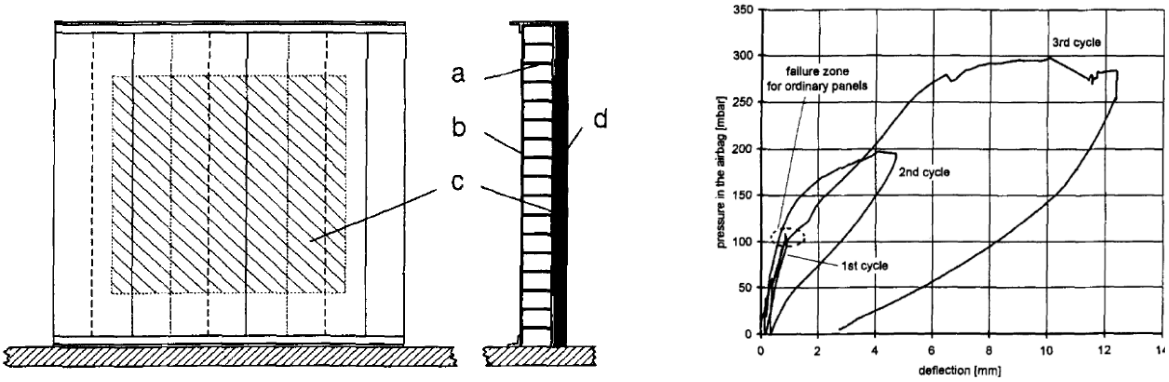

Figure 2-12. Test setup (left); a) Masonry wall, b) Overlay, c) Pressurized airbag, d) Reaction wall; and Load-Deformation Curve for Middle of Masonry Panel (right) (Kolsch, 1998)

S. Babaeidarabad, F. De Caso, A. Nanni (2014)

Babaeidarabad et al. (2014a) investigated the performance of strengthening URM walls using carbon fabric-reinforced cementitious matrix (FRCM) to enhance pseudo-ductility and flexural capacity. Eighteen masonry walls made of clay bricks and concrete blocks with nominal dimension of 1422 by 1220 by 102 mm, were tested. The main variable was the reinforcement ratio of FRCM (1-ply and 4-ply fabrics). For the test setup (Figure 2-13), a uniformly distributed lateral pressure was applied to the walls by using an air bag. The air bag was located between the specimens and a reaction wall. One load cycle was used for control specimens; on the other hand, three cycles of loading and un-loading were used for strengthened walls. Additionally, a close-loop system was created with the anchoring arrangement that consisted on four Dywidag rods and steel channel/tube sections at the top and bottom of the specimens.

The results show an increase in the ultimate out-of-plane moment capacity related to the amount of FRCM. The increment of flexural capacity increase was of 2.7 and 7.8 for concrete block masonry walls and 2.8 and 7.5 for clay brick walls, for 1-ply and 4-ply carbon FRCM, respectively. Additionally, two basic mode of failure were observed (Figure 2-13): shear failure in the substrate at the supports and cracking of the masonry at the mid-height with FRCM slippage. It was noted that FRCM enhanced flexural strength, stiffness, and pseudo-ductility; nonetheless, pseudo-ductility is higher for lower FRCM amounts given that flexure controls the failure mode. Finally, the authors concluded that FRCM and FRP strengthening methods are comparable and provide similar increments in flexural capacity, for the same level of the calibrated reinforcement ratio, ωf. But when ωf is larger than 0.6 for the clay brick and 0.8 for the concrete brick walls, shear controls the failure mode. Therefore, increments of FRCM beyond this value may be ineffecient.

Figure 2-13. Test setup and failure mode of wall specimens: CMU-Control (a); CMU-1ply (b); CMU-4ply (c); CL-Control (d); CL-1ply (e); and CL-4ply (f) (Babaeidarabad et al., 2014)

N. Ismail, J. M. Ingham (2016)

Ismail et al. (2016) investigated the performance of unreinforced masonry walls strengthened with polymer textile reinforced mortar under in-plane and out-of-plane loading. Five specimens were tested. The main variables were the type of the TRM system, the type pf loading (in-plane or out-of-plane), the strengthening fabric and the type of mortar. The testing was presented in two series, series 1 involved in-plane testing of two pier-spandrel assemblages (Figure 2-14) that represented part of a perforated URM wall, while series 2 involved out-of-plane testing of three slender walls with no perforations (Figure 2-15). Vintage solid clay bricks and a low strength hydraulic cement mortar were used to replicate the physical characteristics of historic masonry materials. For the test setup a gradually increasing displacement controlled reversed cyclic loading history was applied at the topmost section of the Series 1 test assemblages using a rigid steel loading beam. Series 2 specimens were subjected to reversed cyclic out-of-plane testing. Additionally, a pair of air bags were positioned on each side of the wall, between the wall and a backing frame, to apply a uniformly distributed pseudo-static load.

The results show an increase in strength in the URM test walls, from 128% to 136% for in-plane loading, and from 575% to 786% for out-of-plane loading, due to TRM strengthening. Additionally, a remarkable increase in ductility and deformation capacity was observed. However, the ductile behavior was seen on the strengthened walls until the polymer textile failed in a brittle manner. Based on the results, the authors concluded that TRM systems can increase the strength, ductility and energy dissipation properties of URM walls.

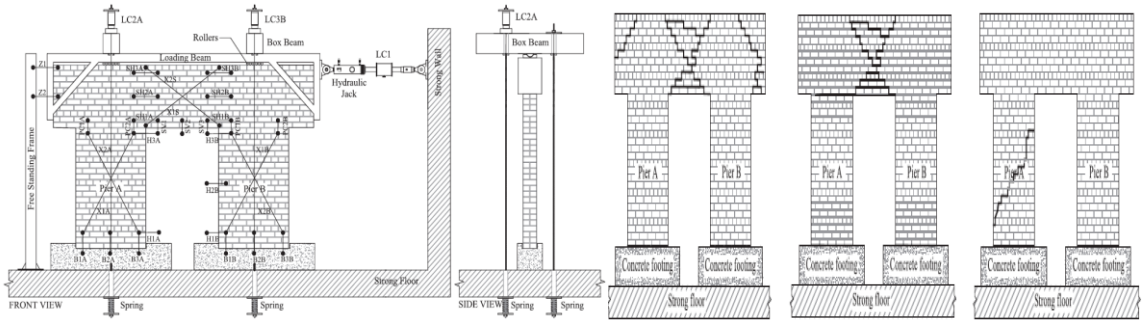

Figure 2-14. Test setup for in-plane reversed cyclic loading, and test results showing damage patterns of the two pier-spandrel assemblage (Ismail et al., 2016)

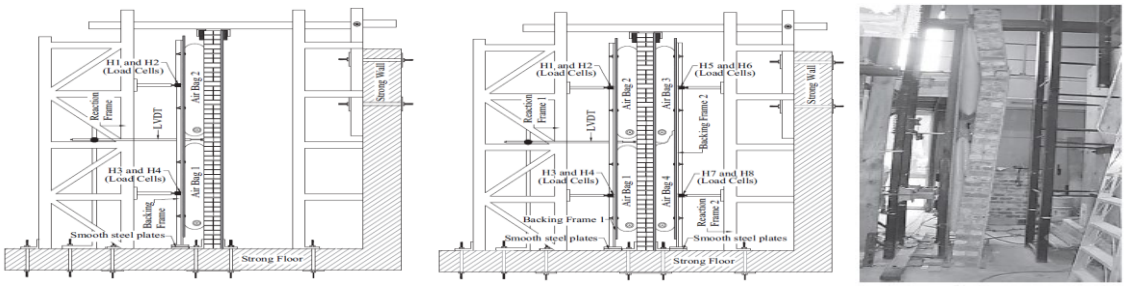

Figure 2-15. Test setup for out-of-plane one directional cyclic loading (left), reversed cyclic loading (middle) and test results showing failure of wall (Ismail et al., 2016)

Santis, S. D., Casadei, P., Canio, G. D., Felice, G. D., Malena, M., Mongelli, M., Roselli, I. (2016)

Santis et al. (2016) investigated the seismic out-of-plane performance of unreinforced masonry walls retrofitted with steel reinforced grout (SRG) under lateral loads. Full-scale U-shaped masonry walls made of tuff units and hydraulic lime mortar were tested. They consisted of a façade and two transverse walls with nominal dimension of 3300 mm long, 3440 mm high and 250 mm thick, for the façade and the same dimensions for the transverse walls except that the length was 2300 mm. Additionally, a reinforced concrete foundation was built and the first layer of masonry was laid in it. Moreover, the walls were not connected or interlocked at the corners except by a mortar joint to simulate conditions found in historic buildings; nonetheless steel connectors were used in the connections when the retrofit was applied. The main variables were the type of fabric used as a retrofit in the SRG (galvanized ultra-high tensile strength Steel, UHTSS, and slate-stainless steel) and the comparison between unreinforced masonry and retrofitted masonry walls. For the test setup (Figure 2-16), seismic lateral forces were applied by means of a shaking table based on six natural records chosen among some of the most severe earthquakes in Italy during the last 50 years.

The results (Figure 2-16) showed that the reinforcement with SRG system was very effective, improving the out-of-plane seismic capacity of the masonry walls and its bending capacity. For example, for the unreinforced wall the maximum peak ground acceleration was 0.29 g, failing by overturning, for the wall reinforced with steel tie bars it was 0.82 g with severe damage without collapse, and for the wall retrofitted with SRG it was 1.49 g with severe damage without collapse. Additionally, the connection between the transverse walls and the façade was very efficient due to the use of the SRG connectors, preventing the façade from out-of-plane overturning. Finally, it was concluded that SRG reinforcement lead to a narrow alteration of the initial dynamic properties of the masonry walls and restrains damage during earthquake loading.

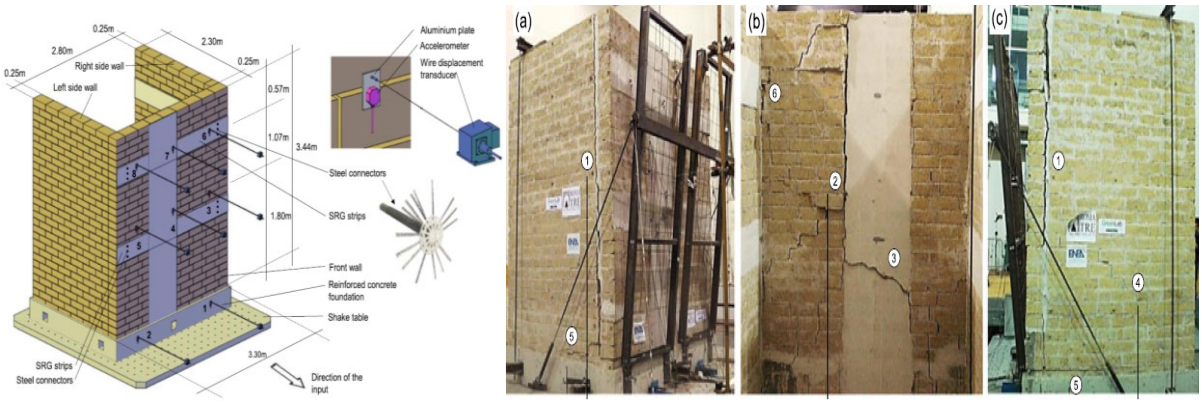

Figure 2-16. Test set up and test results (Santis et al., 2016)

A. Bellini, A. Incerti, M. Bovo, C. Mazzotti (2017)

Bellini et al. (2017) investigated the performance and failure modes of URM walls strengthened using fabric-reinforced cementitious matrix (FRCM) under out-of-plane loads. Several full-scale masonry walls made of clay bricks and with dimensions of 2,700 × 1,200 × 250 mm, were tested. The main variables were the reinforcement ratio of FRCM (1-ply and 2-ply fabrics), and the type of fabric (Glass Fiber Grid variations). For the test setup (Figure 2-17), distributed horizontal forces were applied along the wall out-of-plane direction while a constant axial load was applied in the longitudinal direction independently. The wall was placed in its vertical position, was double hinged at its supports, and was kept in position by a horizontal restraining system which integrated two steel trusses connected to a reaction wall. Four horizontal forces were applied along the height of the wall by two hydraulic jacks, while the vertical axial stress was applied using two hydraulic jacks were placed at the top. Finally, the horizontal forces were applied monotonically well beyond the appearance of nonlinear degradation, then an unloading and reloading cycle was executed until the final failure.

The results showed that the reinforcement system was effective, restraining the formation of the predicted hinge at mid-height of the wall and redistributing forces over a broader portion of it. In all cases, the determined failure mode was associated with the tensile failure of the fibers, which happened before the debonding of the reinforcement from the substrate (Figure 2-17). The cracking pattern was heavily guided by the discontinuities defined by the wall mortar joints, that also caused cracks inside the FRCM matrix. Finally, the structural tests revealed that, when local debonding appeared, the system was able of redistributing forces to sections of the wall with a smaller bending moment. Therefore, allowing for an additional increase of displacement, prior to the final failure.

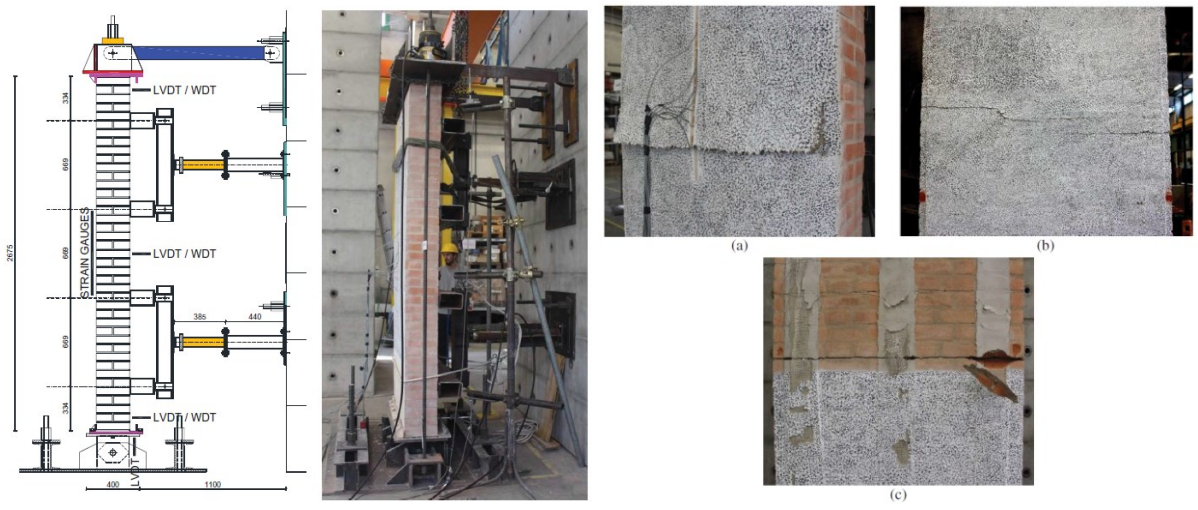

Figure 2-17. Test setup and test results (Bellini et al., 2017)

C. D'Ambra, G.Lignola, A. Prota, E. Sacco, F. Fabbrocino (2018)

D'Ambra et al. (2018) investigated the performance and failure modes of URM walls strengthened using fabric-reinforced cementitious matrix (FRCM) to enhance out-of-plane behavior, by retrofitting un-damaged and pre-damaged walls using an innovative composite basalt grid system. Two full-scale masonry walls made of clay bricks with nominal dimensions of 1515×1755×120 mm, were tested under bidirectional loading. The main variable was comparing the behaviour of the retrofitted un-damaged and pre-damaged walls with those of the unreinforced wall (control wall). For the test setup (Figure 2-18), an incremental point load was applied to the top corner through a steel square plate to spread the load and to produce double bending and hence a bidirectional stress state. To achieve this, a support was provided to the bottom edge and one of the two consecutive edges of the walls using an UPN (European Normal Channels) profile in each case which was fixed in three points to a rigid steel frame.

The results showed a progressive stiffness reduction for unreinforced masonry walls which was associated with progressive damage of the joints, with cracks mostly in the mortar and no other elements which remained elastic (Figure 2-18). The behavior of the repaired and reinforced walls, was characterized by a force-displacement curve which showed trilinear behavior. Finally, strengthening with FRCM increased the out-of-plane capacity of the walls to almost two times their original capacity; in spite of the complex stresses induced by the loading setup.

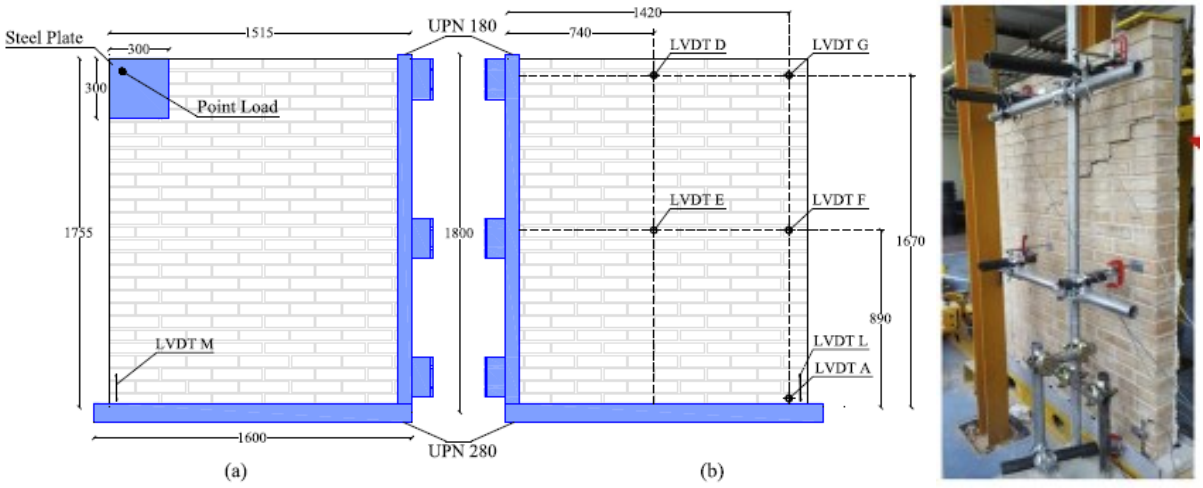

Figure 2-18. Test setup, Rear view (left), Front view (middle) and test results (D'Ambra et al., 2018)

T. D'Antino, F.G. Carozzi, P. Colombi, C. Poggi (2018)

D'Antino et al. (2018) developed a new analytical procedure to estimate the out-of-plane maximum bending moment resistance of FRCM strengthened masonry walls, using a database of 63 FRCM strengthened walls obtained from the literature. In addition, a comparison with the only available guideline, the ACI 549.4R-13 and with another procedure by Ascione et al. (2015), was made. Moreover, cross-section equilibrium and plane sections were assumed in the analysis, so sections were assumed to remain plane during loading.

The results showed that the new suggested procedure produced accurate results (CoVref=30.46%) and tended to lightly overestimate the experimental maximum resisting bending moment (r =0.96), whereas the ACI 549.4R-13 method and the approach proposed by Ascione et al. (2015) usually tended to underestimate the experimental maximum resisting bending moment, presenting low accuracy (CoVref=98.62% & r =1.95 and CoVref=59.49% & r =1.31, respectively). Finally, for each specimen and each method, the ratio between the i-th experimental and i-th analytical maximum resisting bending moment, ri, was computed, $ri=M_{exp,i}/M^{ii}_{R,I}$ (Figure 2-19).

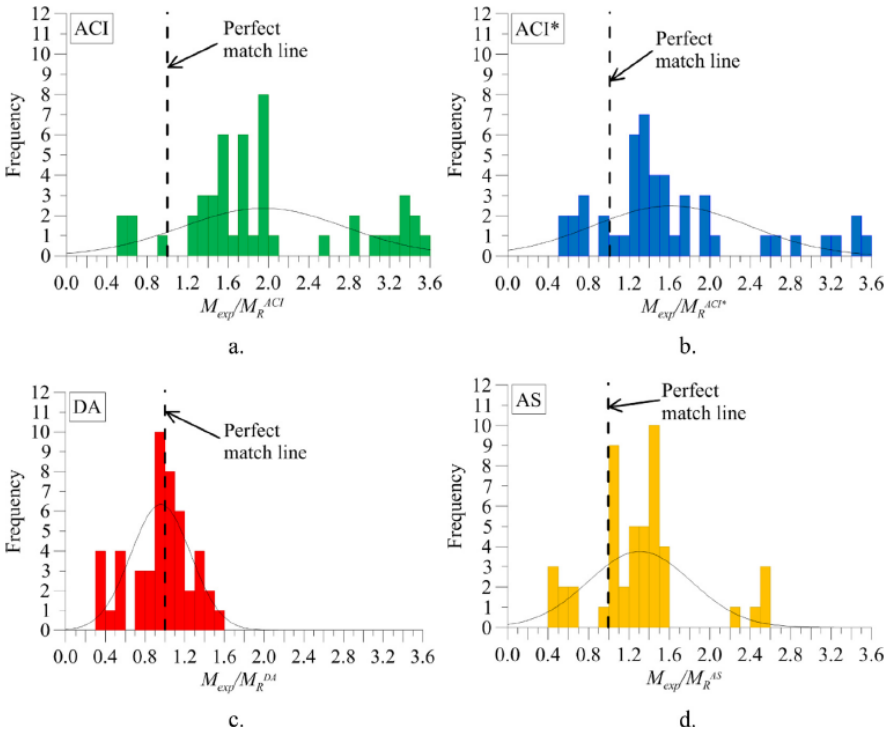

Figure 2-19. Distribution of ratios $ri=M_{exp,i}/M^{ii}_{R,i}$, obtained with a) ACI, b) ACI*, c) DA, and d) AS procedure. (D'Antino et al., 2018)

2.3.3. FRCM strengthened Wall elements under In-plane loading.

E. Bernat, L. Gil, P. Roca, C. Escrig (2013)

Bernat et al. (2013) investigated full-scale Textile Reinforced Mortar (TRM) strengthened brickwork walls under eccentric compressive loads. Twenty-nine full-scale walls built using solid clay bricks were tested, with the following dimensions, 1650 mm height 900 mm width and 132 mm thick. The main variables were the type and number of fibre grids installed, the type of mortar and the possible use of connectors to enhance bonding with the masonry. From the 29 walls, 20 were unreinforced brickwork walls (URMW) and 9 were TRM strengthened brickwork walls (TRMW). In the test setup (Figure 2-20), a specific device was constructed to test the specimens under in-plane compressive eccentric loads uniformly distributed on the width of the walls which were hinged with the same eccentricity at both edges.

The results showed that under the applied eccentric axial load, the use of TRM produced an increment of over 100% of the initial load bearing capacity. Additionally, amore homogeneous and stiffer behavior was noticed for both the in- and the out-of-plane directions, when the TRM system was used. Finally, it was shown that TRM strengthening restrains masonry walls from failing due to pure mechanism formation, reduces second order effects and magnifies their load-bearing capacity under eccentric axial loads (Figure 2-20).

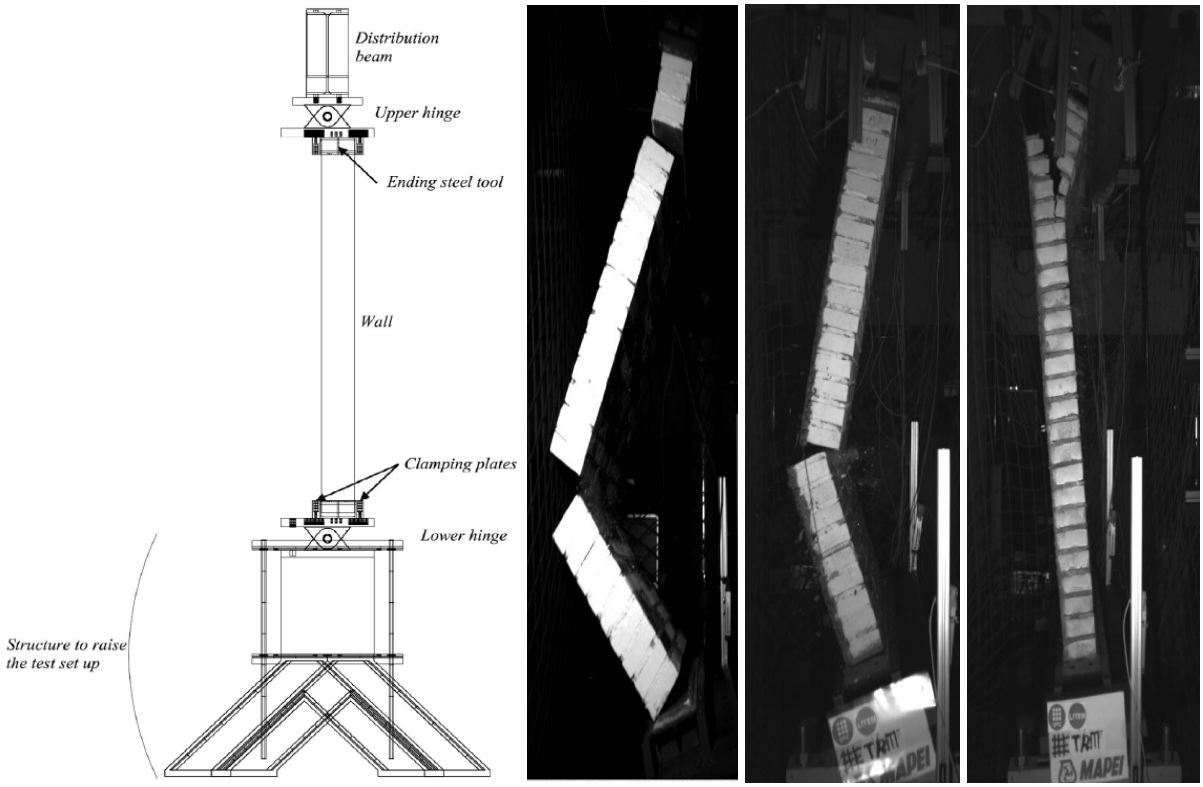

Figure 2-20. Test setup and failure mode of wall specimens (Bernat et al., 2013)

S. Babaeidarabad, A. Nanni (2013)

Babaeidarabad et al. (2013a) investigated the performance of concrete block and clay brick masonry walls, strengthened with FRCM systems under in-plane shear forces. Eighteen masonry walls made of clay bricks and concrete blocks with nominal dimension of 1220 x 1220 x 92 mm, were tested. The main variable was the reinforcement ratio of FRCM (1-ply and 4-ply fabrics). For the test setup (Figure 2-21), diagonal compression was applied through two double acting hollow plunger cylinders seated on a top corner. Additionally, two steel shoes were mounted diagonally on opposite corners of the wall, and two steel Dywidag rods went through the shoes and tied them together so the load could be transmitted and so that a close-loop system was created. Subsequently, the load was applied in three stepped cycles of loading and unloading; besides, the last cycle continued until failure.

The results showed different failure modes (Figure 2-21) and an increase in the shear capacity of masonry walls strengthened with FRCM. The increment in terms of ultimate in-plane load was of 2.4 and 4.7 times that of clay brick control wall, and 2.0 and 2.4 times of concrete control wall using 1-ply and 4-ply carbon FRCM, respectively. Additionally, the shear capacity of the strengthened walls corresponded well to the calibrated reinforcement ratio derived as the ratio of axial stiffness of FRCM and masonry A_fE_f/A_nE_m. For the equivalent level of calibrated reinforcement ratio, FRCM and FRP provide identical increments in shear capacity.

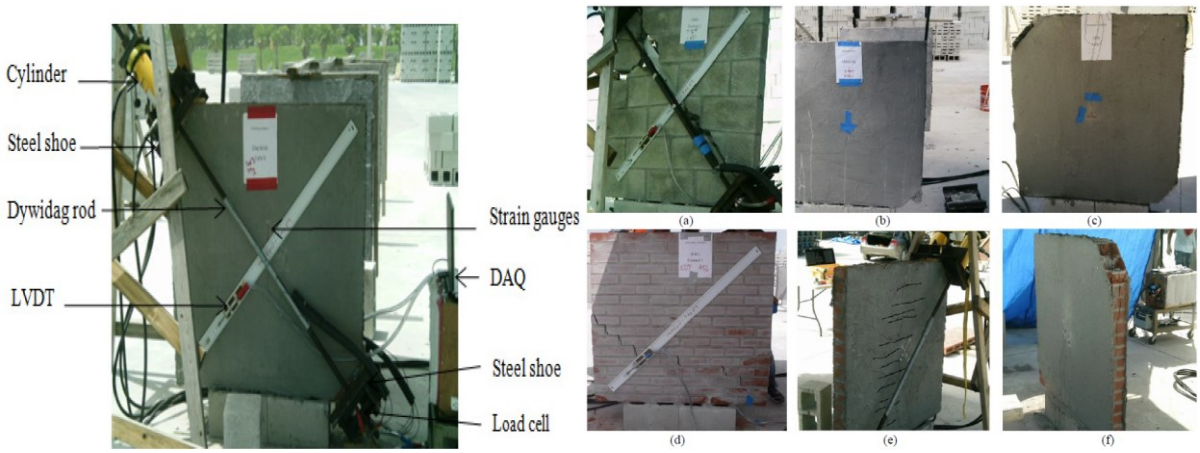

Figure 2-21. Test setup and Failure mode of wall specimens: CMU-Control (a); CMU-1ply (b); CMU-4ply (c); CL-Control (d); CL-1ply (e); and CL-4ply (f) (Babaeidarabad et al., 2013)

C. B. de Carvalho Bello, A. Cecchi, E. Meroi, D.V. Oliveira (2017)

De Carvalho Bello et al. (2017) investigated the performance of strengthened URM walls using fabric-reinforced cementitious matrix (FRCM) made with sisal fibers (RM-SISAL) to enhance their in-plane shear capacity. Also, wall behaviour was also studied using a numerical finite element model (FEM) (Figure 2-22). In the experiments, masonry walls made of clay bricks with nominal dimension of 1160 × 1160 × 250 mm, were tested. The main variable was the influence of different fibers for reinforcement, (i.e. glass, carbon, steel, sisal) using different mortars and substrates. For the test setup (Figure 2-22), diagonal compression was applied through two double acting hollow plunger cylinders seated on a top corner. Additionally, two steel shoes were mounted on diagonally opposite corners of the wall and two steel Dywidag rods went through the shoes and tied them together to allow the load to be transmitted. Subsequently, the load was applied in cycles with steps of 25–50 kN of loading and unloading until the peak load was reached (when diagonal cracking occurred). Then the tests continued until diagonal displacement values reach almost 10 mm.

The results showed brittle behaviour response and diagonal cracks on the bed and head of the mortar joints along the loading direction, for URM walls. It was concluded that, in comparison to URM walls, RM-GLASS strengthened walls had a better post-peak response, with a softening behaviour until the ultimate failure stress. Hence, the FRCM strengthening System enhanced shear capacity and ductility.

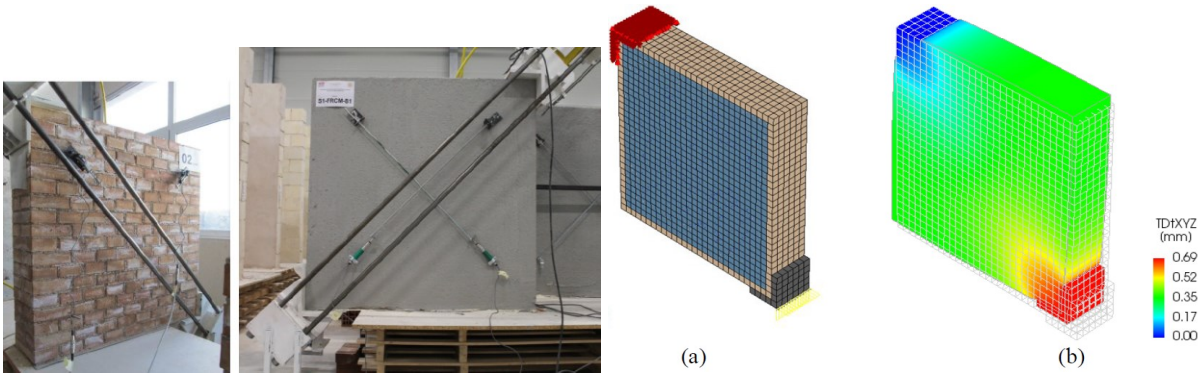

Figure 2-22. Test setup for unreinforced (left) and reinforced masonry specimens, and FEM model: (a) 3d geometry; (b) displacements contours over deformed configuration at peak load (URM) (De Carvalho Bello et al., 2017)

Table 2-1. Summary of previous research on flexural strengthening of masonry walls with FRCM.

Author(s)	Testing Elements			Loading		FRCM (TRM) systems			
	Type	Detail	Dimensions (h x w x l)	Type	Properties	Applied Surface	Fabrics (no. of layers)	Matrix	Thickness
Papanicolaou et al. (2008)	Beam - like (URM)	6-hole Clay Brick	1.3 x 0.085 x 0.4 m 0.4 x 0.085 x 1.3 m	3 point	Cyclic loading (0.1 mm/s)	Double face	Carbon (1, 2) * Carbon (1, 2) for FRP	Polymer-modified cement mortar * Epoxy for FRP	Variable (one layer of mortar: 2 mm)
Harajli et al. (2010)	Beam - like (URM)	Concrete Block, Brick, Sandstone	1.0 x 0.1 x 0.4 m 1.0 x 0.1 x 0.3 m 1.0 x 0.1 x 0.2 m	4 point	Monotonic load (5 mm/min) Cyclic loading (0.1-0.5 mm/s)	Single face (for static) Double face (for cyclic)	Basalt / E-Glass (1), Steel mesh (1, 2)	lime mortar cement based mortar	Variable (one layer of mortar: 2-3 mm, for base mortar: 5 mm)
Bernat-Maso et al. (2014)	Beam - like (URM)	Clay Brick	0.28 x 0.157 x 0. 63 m	3 point	Monotonic load (5 mm/min)	Single face and Double face.	Basalt (1,2), Carbon (1), Glass (1,2), Steel (1)	Cement based, lime based, pozzolana based and plastering mortar (dry mix of cement, lime and chemical additives).	Variable (one layer of mortar: 4 mm, for base mortar: 6 mm)
Valluzzi et al. (2014)	Beam - like (URM)	Clay Brick	0.39 x 0.78 x 0.12 m 0.25 x 0.515 x 0.12 m	4 point	Monotonic load	Single face	Basalt (1), Carbon (1), Glass (1), Steel (1), Flax (1). Hemp (1),	Epoxy resin, Cement putty, Magnesia mortar.	Variable (4~5mm)
Kariou et al. (2018)	Beam - like (URM)	Solid clay brick	1.34 x 0.1 x 0.44 m (Single-wythe) 1.34 x 0.2 x 0.44 m (Double-wythe)	3 point	Monotonic load (1 mm/min)	Single face	Carbon (1), Basalt / Glass (3, 7),	Cement based mortar with polymers	Variable (3~13mm)
Al-Jaberi et al. (2018)	Beam - like (RM)	Concrete Block	1.22 x 0.15 x 0.61 m	4 point	Cyclic loading (1.25 mm/min)	Single face	Carbon / PBO (1, 2) * Carbon (1), Glass (1, 2) for NSM	cement based mortar	Variable (one layer of mortar: 5 mm)
Kolsch (1998)	Infill walls (URM)	Sand Lime Brick	3 x 0.24 x 3 m	UDL (Air bag)	Cyclic loading (Out-of-plane)	Double face	Carbon (3)	Polymer modified cementitious mortar	Approx. 4.5 mm
Babaeidarabad et al. (2014)	Infill walls (URM)	Concrete Block, Clay Brick,	1.4 x 0.1 x 1.2 m	UDL (Air bag)	Cyclic loading (max 0.14 MPa) (Out-of-plane)	Single face (tension) (out-of-plane)	Carbon (1, 4)	cement based mortar	Variable (one layer of mortar: 5 mm)

Author(s)	Testing Elements			Loading		FRCM (TRM) systems			
	Type	Detail	Dimensions (h x w x l)	Type	Properties	Applied Surface	Fabrics (no. of layers)	Matrix	Thickness
Ismail et al. (2016)	Infill walls (URM)	Solid Clay Brick	3.76 x 0.22 x 1.2 m	UDL (Air bag)	Reversed Cyclic (up to 4% drift), One Direction Cyclic (up to collapse)	Single face (tension) (out-of-plane)	Aramid FRP / Steel mesh (1)	Commercial adhesive mortar	5-7 mm
Ismail et al. (2016)	Pier-spandrel assembl ages	Solid Clay Brick	0.94 x 0.22 x 4.42 (Spandrel) 1.71 x 0.22 x 1.19 (2 Piers)	Lateral loading (Hydraul ic ram)	Reversed cyclic pseudo-static	Single face on the spandrel (in-plane)	Aramid FRP / Steel mesh (1)	Commercial adhesive mortar	5-7 mm
Santis et al. (2016)	Infill walls (URM)	Tuff Brick	3.44 x 0.25 x 3.3 m (Façade) 3.44 x 0.25 x 2.3 m (Side walls)	Shake table	Seismic inputs from six natural recordings in Italy	Single face partially (external for façade, internal for side walls) (out-of-plane)	ultra high tensile strength steel (1) aramid-stainless steel (1)	natural hydraulic lime mortar	7-8 mm
Bellini et al. (2017)	Load-bearing walls (URM)	Solid clay brick	2.7 × 1.2 × 2.5 m	Lateral loading (Hydraul ic jacks)	Monotonic load and one Reversed cycle (up to failure) (Out-of-plane)	Single face (tension) (out-of-plane)	Glass (1)	Lime-based mortar	3-5 mm
D'Ambra et al. (2018)	Infill walls (URM)	Solid clay brick	1.515 × 1.755 × 1.2 m	Lateral loading (Hydraul ic jacks)	Monotonic load (up to failure) (Out-of-plane) (double bending)	Single face (tension) (out-of-plane)	Basalt (1),	pozzolanic based + lime based +sand, + special additives + polymers + short glass fibers	3-5 mm
D'Antino et al. (2018)	Infill walls (URM)	Clay brick, CMU, rubble stone, cobblestone	1.515 × 1.755 × 1.2 m	Lateral loading	Analytical model to estimate out-of-plane maximum resisting bending moment	Single face (tension) (out-of-plane)	Carbon, glass, basalt, steel, PBO, mixed PBO and glass	Lime-based, cementitious, pozzolanic, mixed cement and lime, magnesia	unknown
Bernat et al. (2013)	Load-bearing walls (URM)	Solid clay brick	0.165 x 0.9 x 0.132 m	Compres sive eccentric loads	Cyclic loading (In-plane)	Single face	Carbon (1), Glass (1, 2),	Portland based, lime based, pozzolana based	unknown

Author(s)	Testing Elements			Loading		FRCM (TRM) systems			
	Type	Detail	Dimensions (h x w x l)	Type	Properties	Applied Surface	Fabrics (no. of layers)	Matrix	Thickness
Babaeidarabad et al. (2013)	Infill walls (URM)	Solid clay brick	1.145 × 1.22 × 0.092 m	Lateral loading (Plunger cylinder)	Cyclic loading Diagonal compression (In-plane)	Single and double face	Carbon (1,4),	Cement based	unknown
Bello et al. (2017)	Infill walls (URM)	Solid clay brick	1.160 × 1.160 × 0.250 m	Lateral loading (Plunger cylinder)	Cyclic loading Diagonal compression (In-plane)	Double face	Glass (1), Sisal (1)	Lime-based,	unknown

2.4.PREVIOUS RESEARCH ON USE OF FRCM TO STRENGTHEN STRUCTURES TESTED UNDER EXTREME DYNAMIC LOADING

This section reviews previous research conducted on the impact and blast performance of FRCM strengthened masonry and concrete structures. It should be noted that FRCM is to some extent an emerging retrofitting method, with little research on this specific topic, specifically in the case of blast research. Table 2-2 presents a summary of some of the previous research conducted under extreme dynamic loading.

Abbas, H., Almusallam, T., Al-salloum, Y., Siddiqui, N., & Abadel, A. (2016)

For this research project, ten (10) specimens consisting on reinforced concrete (RC) slabs (600 mm square, 90 mm thick) were strengthened by either FRP or TRM systems and were tested under impact loading. The impact tests were performed using an hemispherical nose steel projectile with a diameter of 40 mm, producing different impact velocities from 108 to 158 m/s, Figure 2-23 (a) shows more details. The specimens consisted of three (3) slabs strengthened on the rear side using a single layer of carbon FRP with epoxy resin, three (3) slabs strengthened on the rear side using 2 layers of carbon fiber textiles with a polymer modified cement mix and four (4) RC slabs with no strengthening that were tested as controls. Additionally, one single layer of FRP sheet as well as 2 layers of textile were chosen for comparison purposes since they had equal quantity of carbon fibers. Later, during the testing a gas gun was employed to strike the projectile perpendicularly to the specimens. Within the parameters investigated are the penetration depth and the crater size on the front and rear faces of the specimens, for different projectile velocities. Part of the test results performed with CFRP and TRM strengthening systems are presented in Figure 2-23 (b) and (c), respectively. It was concluded that the two strengthening systems were effective in reducing local damage and secondary debris in RC slabs subjected to projectile impacts. The ballistic limit velocity of TRM and CFRP systems was enhanced by 21% and 15 % respectively when compared with the control specimens. In summary, TRM reinforcement performance was similar or better than that of CFRP.

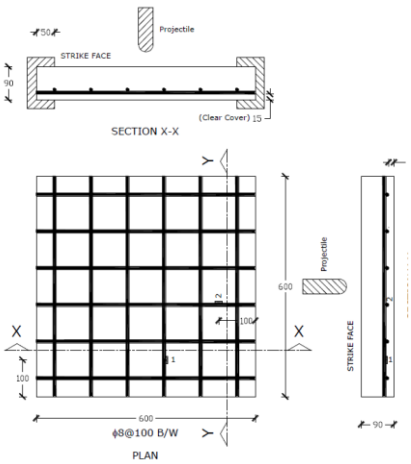

(a)

(b) Front and rear side of CFRP strengthened RC slab (129 m/s)

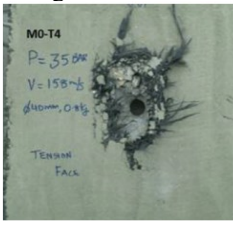

(c) Front and rear side of TRM strengthened RC slab (158 m/s)

Figure 2-23. Preparation of test specimens (a), and test results (b, c) (Abbas et al., 2016)

S. Liu, D. Zhu, Y. Ou, Y. Yao, C. Shi (2018a)

Liu et al. (2018a) investigated the performance and failure modes of basalt textile-reinforced concrete (BTRC) under impact loading. Thirty square specimens, with nominal dimension of 60 x 60 x 15 mm, were tested. The main variables were the impact velocity (0.77 m/s, 2.31 m/s and 4.62 m/s), boundary conditions (free and fixed), number of basalt textile layers (4 and 6), and applied temperature during testing (-25, 0, 25, 50 and 100 °C). As shown in Figure 2-24, a drop weight set-up was used, with a capacity of 22 kN. The impact load was measured using a piezoelectric load sensor and the impact velocity was achieved by adjusting the drop height. Lastly, the effect of temperature was introduced at each impact velocity tested.

The results showed that at a constant temperature, the maximum impact force and the energy absorption increased when increasing impact velocity. On the contrary, the absorbed energy and the maximum impact force decreased with temperature (for the same impact velocity) but, they improved when the number of basalt textile layers increased from four to six. Additionally, all specimens were capable of absorbing the kinetic energy under impact velocity of 4.62 m/s. On the other hand, for the same impact velocity, the fixed boundary conditions enhanced the peak impact force, but diminished energy absorption (in comparison with free boundary condition). Finally, it was concluded that failure patterns are unquestionably affected by the varying impact velocities, but not by the boundary conditions and temperature (Figure 2-24).

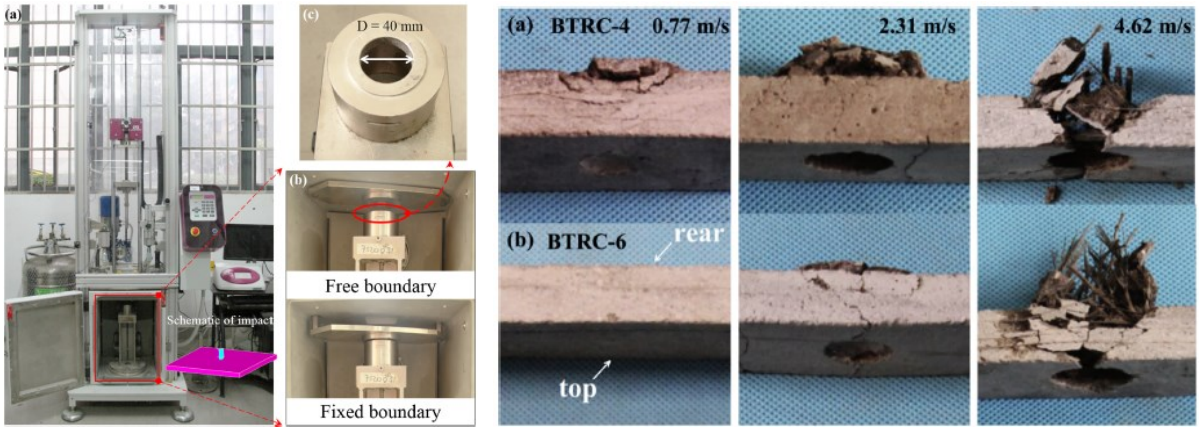

Figure 2-24. Test setup and test results (Liu et al., 2018a)

S. Liu, D. Zhu, Y. Yao, C. Shi (2018b)

Liu et al. (2018b) investigated the flexural performance of textile-reinforced concrete (TRC) under three-point bending loading with quasi-static and low-velocity impact loadings (1.0 - 4.5 m/s). Several slender rectangular plates, with nominal dimension of 250 x 250 x 15 mm, were cast and cured under standard conditions, then cut into test samples of 40 x 250 x 15 mm and tested. The main variables were the fiber type in the composites; glass textile-reinforced concrete and basalt textile reinforced concrete (GTRC and BTRC respectively), the loading velocity, (for quasi-static the strain rate was 3.33 × 10−5 s−1 and for flexural impact 4, 8, 12, 16, and 18 s−1 corresponding to 1.0, 2.0, 3.0, 4.0 and 4.5 m/s) and temperature (−50, 0, 25, 50, and 100°C). An MTS universal testing machine, with a capacity of 30 kN and 1 kHz, was used for the Quasi-static three-point bending tests and for the Dynamic flexural tests, it was used a drop weight Impact with an anti-rebound system (Figure 2-25).

The results showed that as the initial strain rate increased from 3.33 × 10−5 s^{-1} to 18 s^{-1}, the flexural strength increased linearly for both BTRC and GTRC; on the other hand, the flexural ultimate strain and toughness first declined and then incremented, and the flexural modulus first incremented and then declined. Moreover, when increasing temperature, the flexural strength, flexural ultimate strain, flexural modulus, and toughness decreased for both BTRC and GTRC. Finally, it was concluded that the failure modes were associated with the loading conditions, the number of textile layers and temperature (Figure 2-25).

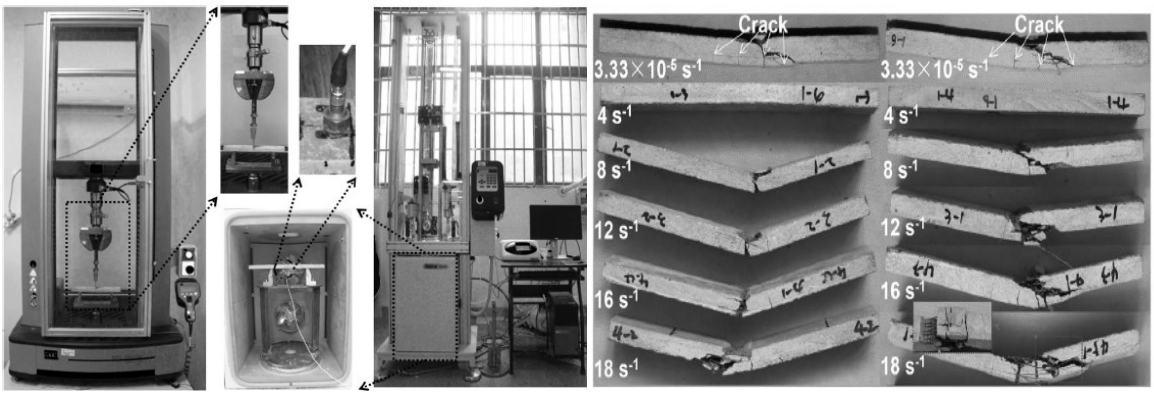

Figure 2-25. Test setup and test results (Liu et al., 2018b)

D. Zhu, M. Gencoglu, B. Mobasher (2009)

Zhu et al. (2009) investigated the flexural impact performance and failure modes of Alkali Resistant (AR) glass fabric composites under low-velocity impact loading. Several specimens, with nominal dimension of 50 x 150 mm with thicknesses of 7–9 mm and 11–13 mm (for six and eight fabric layers respectively), were tested under three-point bending impact loading. The main variables were: the impact velocity (1.0, 1.4, 2.0 and 2.2 m/s), the reinforcement ratio (6 and 8 fabric layers) and the testing position (vertical and horizontal positions, simulating a beam and a plate, respectively). The test setup (Figure 2-26) used a drop weight set-up with an anti-rebound system, where the impact load was measured through a piezoelectric load sensor and a set of accelerometers mounted on the specimen and hammer. The Impact velocity was achieved by adjusting the drop height. Lastly, the effect of temperature was introduced at each impact velocity tested.

The results showed a reduced deflection and a higher load carrying capacity for the beam type specimens, in comparison with the plate specimens, due to the fabric direction and to the coupled effect of the orientation of the cross-section (Figure 2-26). Additionally, as the number of fabric layers was increased, the absorbed energy and the maximum flexural stress of beam specimens was enhanced; on the contrary, they decreased for the plate specimens due to inter-laminar shear failure. Finally, it was concluded by the authors that complete fracture does not take place as cracks form and close, for the beam specimens; whereas, inter-laminar shear is the dominant failure mode for the plate specimens.

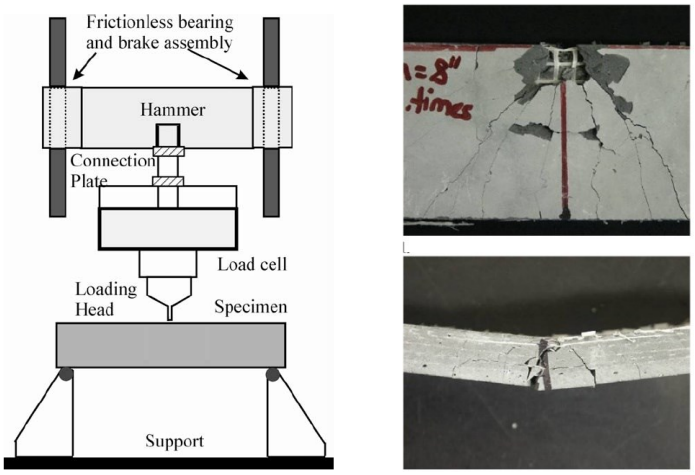

Figure 2-26. Test setup (left) and test results, beam specimen (right-up) and plate specimen (right-down) (Zhu et al., 2009).

Silva, F. de A., Butler, M., Mechtcherine, V., Zhu, D., & Mobasher, B. (2011)

Little research has been conducted to study the high-strain rate response of TRC and FRCM systems. Silva et al. (2011) studied the effect of strain rates on textile-reinforced concrete (TRC) plates of 300 x 50 x 10 mm. Eleven (11) specimens were built and tested, consisting of five (5) plates tested under low-speed tensile strain rates of 10^{-4} to 10^{-1} employing an Instron Universal servo-hydraulic machine (Figure 2-27 (a)), and six (6) specimens tested under higher strain rates of 5, 20, and 50 s^{-1} adopting a servo-hydraulic MTS machine (Figure 2-27 (b)). Three layers of alkali-resistant (AR) glass textiles were employed as reinforcement and a finely grained matrix was employed with or without short AR-glass fibers (diameter of 14 µm, length of 6 mm) at a content of 0.5 % by volume as secondary reinforcement. Moreover, one of the parameters investigated was the effect of gauge length which varied from 50 to 150 mm, at a loading rate of 20 s^{-1}.

The results showed that the strain capacity, tensile strength, work-to-fracture and first crack strength were enhanced for all the specimens when subjected to low-rate tensile loadings. The work-to-fracture and tensile strength were increased up to strain-rate of 50 s^{-1}; nonetheless, the strain capacity was reduced due to the increased stiffness of the composites in the post-crack region. It was also concluded that the short fibers added in the cement-based matrix resulted in bigger values for first-cracking and tensile strengths. Also, when the gauge length was increased, a decreased strain capacity and tensile strength was observed.

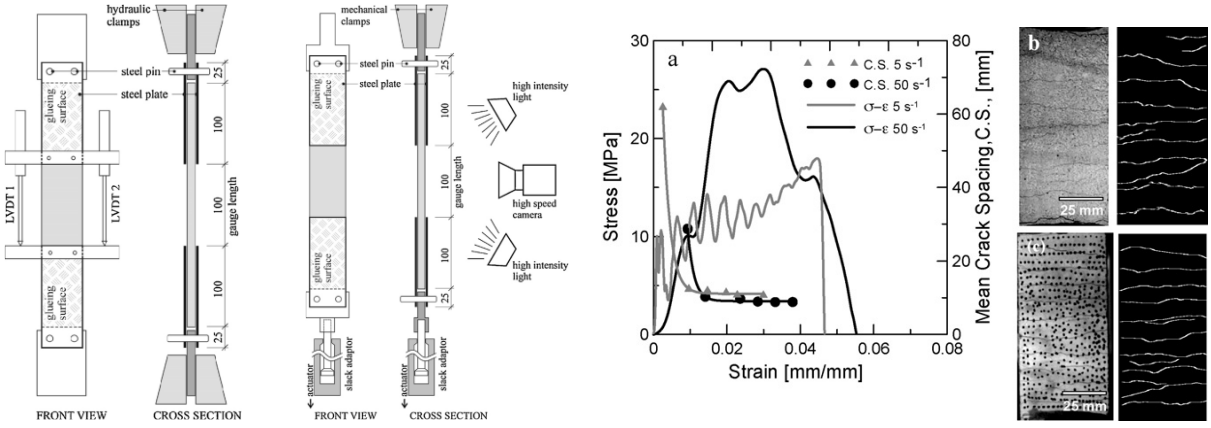

(a) (b) (c)

Figure 2-27. Test setup for low strain rate (a) and high strain rate (b), and results (c) (Silva et al., 2011)

M. Gencoglu (2008)

Gencoglu (2008) investigated the damage propagation, the static and impact flexural strength, and the ultimate deflections in FRCC specimens under impact and static monotonic loads. Eighteen specimens, with nominal dimension of 50 x 150 x 12 mm, were tested under three-point bending caused by static and impact loading. The main variables were, the impact velocity, the fabric type (polyvinyl alcohol (PVA) and polyethylene (PE)) and the testing position (vertical and horizontal positions, simulating a beam and a plate, respectively). The test were conducted using a drop weight set-up with an anti-rebound system. The impact load was measured through a load cell with range of 90 kN, while the displacement was measured by means of a linear variable displacement transducer (LVDT). Lastly, the Impact velocity was achieved by adjusting the drop height.

The results showed that, the impact strengths in flexure for both, PVA and PE when loaded vertically (like beams), are almost equal to their flexural strengths under static loading but when loaded horizontally (like plates), are almost 42 and 35% higher (for PVA and PE, respectively) than their flexural strengths under static loading. Additionally, under impact flexural loading, the vertical specimens with PE fabric could absorb higher energy than the ones with PVA fabric, even when the first ones (specimens with PE fabric) had much less flexural strength and initial stiffness than the ones with PVA fabric. Finally, it was noted that vertical FRCCs with PE fabric showed larger ultimate deflection capacity and exhibited stronger ductile behavior than the ones with PVA fabrics.

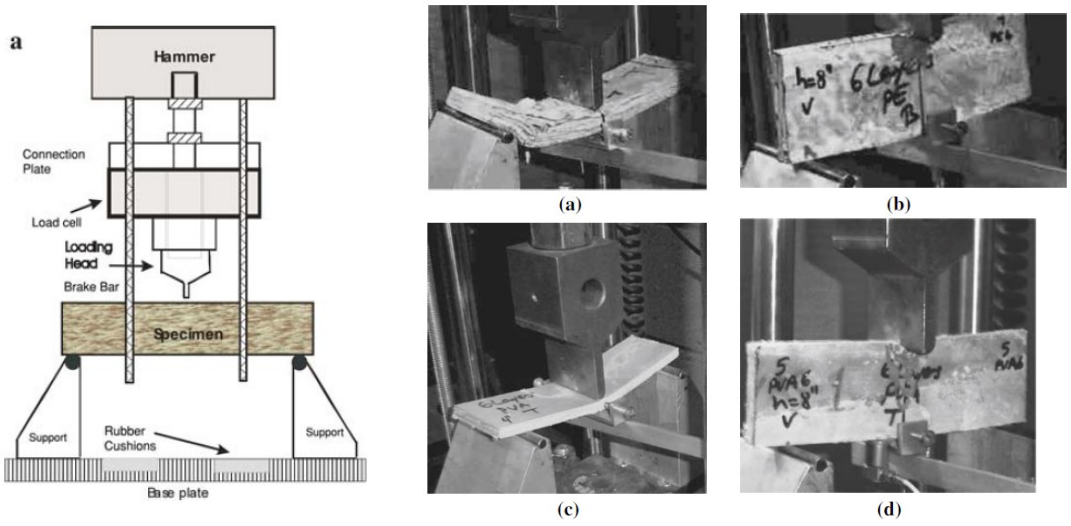

Figure 2-28. Test setup and test results (Gencoglu et al., 2008)

H. Jung (2020)

Jung (2020) investigated the performance and failure modes of URM walls strengthened using fabric-reinforced cementitious matrix (FRCM) under out-of-plane loads. The walls were subjected to Blast Loading, using an air blast simulator (University of Ottawa Shock tube Facilities). Two full-scale masonry walls were constructed and tested after being strengthened with three layers of FRCM retrofit: a concrete masonry (CMU) infill wall and a stone load-bearing wall. Their plain dimensions were of 2,000 × 2,000 × 90 mm. The main variables were the masonry type (CMU and stone), and the axial load applied (Infill and load-bearing). For the test setup (Figure 2-29), air blast pressure was applied along the wall out-of-plane direction while a constant axial load of 171 kN was applied on the top, independently. The wall was placed in its vertical position, at the end of the shock tube frame and was provided with simply supported boundary conditions, by a horizontal restraining system which integrated two steel HSS of 6 in by 6 in and two steel plates, connected to the shock tube frame. Moreover, the vertical axial force was applied using two hydraulic jacks with 85.5 kN each, placed at the top. Finally, the blast loading was applied several times, starting with shots with low pressures (Pr or Ir) and increasing these pressures for each subsequent shot until reaching failure.

The results showed that FRCM strengthening system was an effective mean of increasing the strength and energy-absorption capacity of unreinforced masonry walls subjected to blast loading. It also enhanced the control of displacements (maximum and residual) at the mid-height of the walls. The reinforcement system was effective in restraining/delaying the formation of the predicted hinge at mid-height of the wall. Finally, the failure modes occurred by crushing of the substrate (CMUs) on the compression side, for the CMU wall, and by rupture of the carbon fibers, on the tension side, with debonding of the reinforcement from the substrate (Figure 2-29), for the stone wall. The cracking pattern was heavily guided by the discontinuities defined by the wall mortar joints, that also caused cracks inside the FRCM matrix.

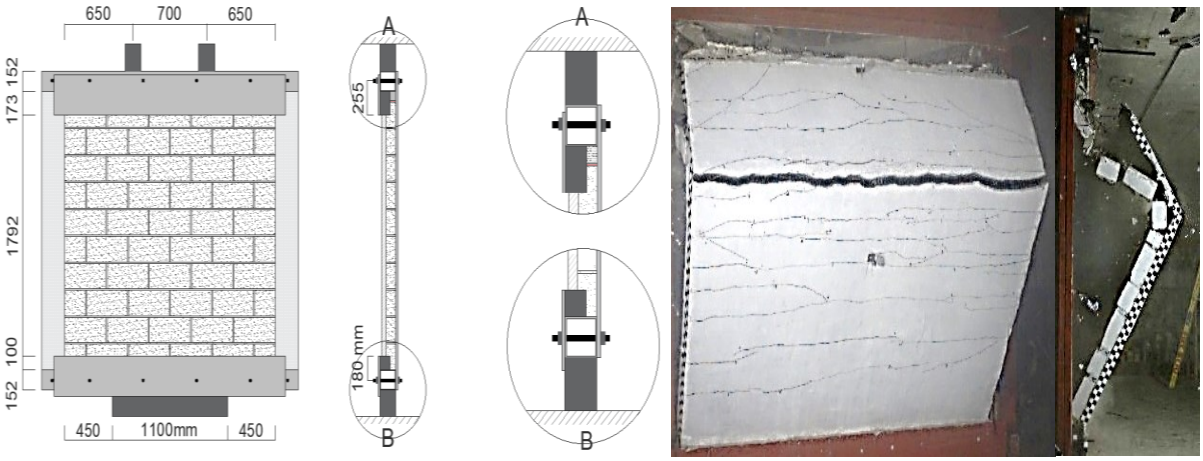

Figure 2-29. Test setup and test results (Jung, 2020)

Table 2-2. Summary of impact and blast research on use of FRCM to strength structural elements

Author(s)	Testing Elements			Loading		FRCM systems			
	Type	Detail	Dimensions (h x w x l)	Type	Properties	Applied Surface	Fabrics (no. of layers)	Matrix	Thickness
Abbas et al. (2016)	RC slab	Reinforced with Ø8 x 100 mm	600 x 600 x 90 mm	Strike of hemispherical nosed steel projectile (40mm)	Striking velocity of 108-152 m/s	Rear face	Carbon (2) * 1 layers for FRP	Cement based mortar * Epoxy for FRP	unknown
Liu et al. (2018)	Concrete panel	Reinforced with basalt textiles	60 x 60 x 15 mm	Drop weight	Impact velocity of 0.77, 2.31, and 4.62 m/s * under different temperature; -25, 0, 25, 100℃	Embedded within the concrete panel	Basalt (4, 6)	Concrete (TRC)	15 mm
Zhu et al. (2009)	Concrete panel	Reinforced with AR glass textiles	25 x 150 x 7-9 (with 6 layers), 25 x 150 x 11-13 (with 8 layers) mm	Free fall drop hammer on 3 point bending	Drop height of 50, 100, 200, and 250 mm	Embedded within the concrete panel	AR glass (6, 8)	Concrete (TRC)	7-13 mm
Silva et al (2011)	Concrete panel	Reinforced with AR glass textiles	300 x 50 x 10 mm	High tensile strain rate	Low-rate; 10^{-4} to 10^{-1} High-rate; 5, 20, and 50 s^{-1}	Embedded within the concrete panel	AR-glass (3)	Concrete * with or without short AR-glass fibers	- (TRC)
Gencoglu et al (2008)	Concrete panel	Reinforced with PVA and PE textiles	50 x 150 x 12 mm	Three point bending static and impact loading (Drop weight)	Impact velocity of 1.00, 1.41, and 2.00 m/s	Embedded within the concrete panel	PVA (6) PE (6)	Concrete (FRCC)	- (FRCC)
Jung (2020)	Load-bearing & Infill walls (URM)	CMU & Stone bricks	2000 x 2000 x 90 mm	Air Blast (Shock tube)	Several Shots with Increasing Pressure (up to failure) (Out-of-plane)	Single face (tension) (out-of-plane)	Carbon (3, 3)	Cement-based mortar	43-46 mm

2.5.EXISTING GUIDELINE FOR USING FRCM

2.5.1. AC434 Acceptance Criteria

The AC434 (2013) "Masonry and Concrete Strengthening Using Fabric-reinforced Cementitious Matrix (FRCM) and Steel Reinforced Grout (SRG) Composite Systems", published by ICC-ES, dictates guidelines for material, structural and durability tests as well as the minimum acceptable design criteria for the use of FRCM in the strengthening of concrete and masonry structures. AC434 (2013) acceptance criteria prescribes parameters and procedures to address strength, serviceability, combustibility, durability and fire safety (Eknel et al. 2018). Figure 2-30 illustrates the direct tensile test specified in Annex A of AC434 (2013). For this test, at least five FRCM coupons have to be cut from a bigger FRCM panel. To hold the FRCM coupons, thin metal tabs have to be glued at both ends, with the specimens connected using a clevis grip device. A Clip-on extensometer is attached to measure the tensile strains.

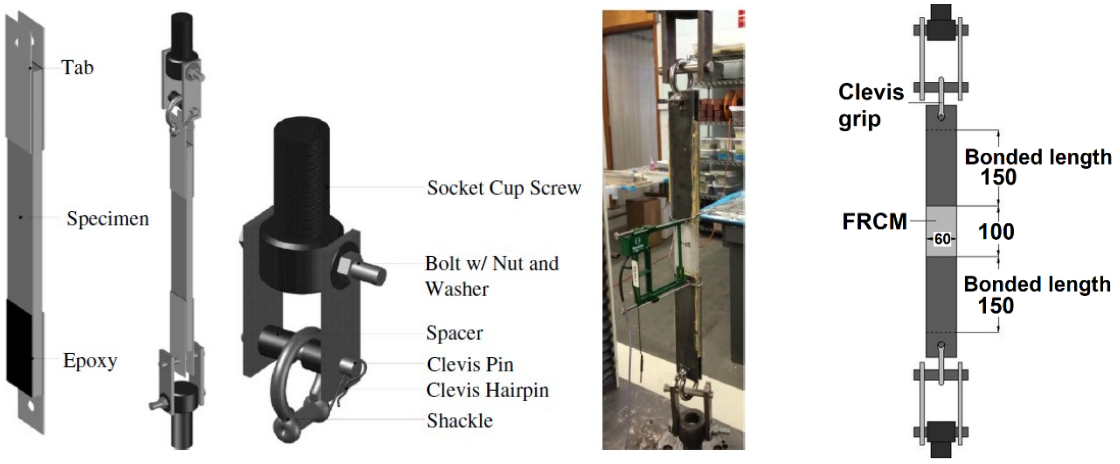

(a) (b)

Figure 2-30. FRCM direct tension test setup (a) and coupon dimensions (Pino et al., 2017) (b) according to AC434 Annex A (Donnini et al., 2017)

2.5.2. ACI 549.4R Guide to Design and Construction of FRCM

One more document that presents guidelines for the strengthening of concrete and masonry structures using FRCM systems is ACI 549.4R-13 (2013) "Guide to Design and Construction of Externally Bonded Fabric-Reinforced Cementitious Matrix (FRCM) Systems for Repair and Strengthening Concrete and Masonry Structures", which is published by ACI Committee 549. This document works as a guide for the construction and/or design of FRCM composite systems and details the capability of FRCM to increase the flexural and shear capacities of masonry and concrete structures. Furthermore, it presents background information and design guidelines for the strengthening of masonry and concrete structures. Appendix B of ACI 549.4R-13 (Table 2-3) presents a summary of design limitations associated with different strengthening applications.

Table 2-3. Design limitations for FRCM for different applications (ACI 549.4R-13)

Parameter	Concrete			Masonry	
	Flexure	Shear	Axial	Out-of-plane	In-plane
ε_{fe} or ε_{fd}	Less than 0.012	Less than 0.004	Less than 0.012 and ε_{ccu} less than 0.01	Less than 0.012	Less than 0.004
ϕ	0.9 to 0.65 based on ε_t	0.75	0.9 to 0.65 based on ε_t	0.6 for flexure 0.8 for shear	0.75
f_{fe}/f_{fd}	0.2 to 0.55 based on fiber	NA	NA	NA	NA
Allowable maximum enhancement*	50 percent	50 percent	20 percent	URM: 6000 lbf./ft (87.6 kN/m); Reinforced masonry: 50 percent	50 percent

*Allowable maximum enhancement is above existing capacity. ACI 562-13 supersedes when limits are lower than as listed in this table.

In accordance with ACI 549.4R-13 (2013), the FRCM composite can be bonded to the surface of masonry walls to enhance the out-of-plane flexural capacity, and it works as reinforcement on the tension side of the section. For the case when flexural strengthening in the out-of-plane direction is needed, which is the case in this research project, the main direction of the reinforcement in the fabrics, must be placed parallel to the bending span and located on the tension side.

For computing the nominal flexural out-of-plane capacity of structural elements, it can be applied sectional analysis (in accordance with ACI 549.4R-13, 2013) and based on the following assumptions:

- Plane sections remain plane;
- There is strain compatibility among the masonry, the FRCM composite and FRCM material;
- Maximum compressive strain in the masonry is obtained from MSJC-11or experimental tests;
- FRCM is assumed to have a bi-linear stress-strain performance and the FRCM contribution prior cracking is ignored;

In addition, ACI 549.4R-13, 2013 also describes the distinctive failure modes that are likely to happen when using FRCM for strengthening the out-of-plane flexural capacity of masonry walls:

- Fiber slippage within the FRCM mortar;
- Fiber rupture;
- FRCM debonding from the substrate;
- Crushing of the masonry in compression;
- Tensile yielding of the steel (in the case of reinforced masonry walls).

The effective tensile strain (ε_{f_e}) of the FRCM composite system at failure is confined to the following design limit:

$$\boldsymbol{\varepsilon_{f_e} = \varepsilon_{f_d} \leq 0.012} \qquad [2\text{-}1]$$

The effective tensile stress of the FRCM composite at failure (f_{f_e}) is computed as:

$$\mathbf{f_{f_e} = E_f \varepsilon_{f_e} \ \ where\ \varepsilon_{f_e} \leq \varepsilon_{f_d}} \quad [2\text{-}2]$$

where E_f is the tensile modulus elasticity of the cracked FRCM composite.

Later, the design flexural strength is obtained as:

$$\Phi_m M_n = \Phi_m (M_m + M_f) \quad [2\text{-}3]$$

where M_n is the nominal flexural capacity and where M_m and M_f are the contributions of reinforced masonry (RM) and FRCM composite material, respectively. For the case when unreinforced masonry (URM) walls have no axial load, M_m is taken as zero. The strength reduction factor for flexure (Φ_m) for URM and RM walls is 0.6, and 0.8 for shear ($\Phi_{v,f}$). In cases where the FRCM system is attached to both sides of the wall, the one attached on the compressive side will not be considered. Besides, it is presumed that the FRCM does not contribute to improving the out-of-plane shear capacity of the masonry walls; hence, the shear capacity can be computed using standard procedures in masonry design codes such as MSJC-11 (2011) or CSA S304.1-04 (2004).

CHAPTER 3. EXPERIMENTAL PROGRAM

3.1.1. CHAPTER OVERVIEW

This chapter provides an overview of the experimental research program. Details of the test specimens, the materials used and their properties are discussed. The construction procedure, test setup, instrumentation and shock tube testing parameters are also described.

3.2. DETAILS OF TEST SPECIMENS

3.2.1. Specimen Overview

A total of three walls were built and tested in the experimental program. All walls were built as load-bearing masonry walls made from concrete masonry units (CMU), and were strengthened by applying FRCM retrofits. The three walls were built by the same professional mason. Thereafter, self-consolidating (SCC) concrete was poured inside the voids in two of the walls (for walls with 2 and 3 FRCM layers) to increase their shear capacity. After curing, the FRCM system was installed on the walls by professional applicators who were trained by the manufacturer. It is noted that the retrofit was applied by hand and the FRCM mortar was applied by troweling. Further details on the wall designs are provided in the following sub-sections.

3.2.1.1. CMU wall design

The three walls in the research program were load-bearing walls and were built with concrete masonry units (CMU), with nominal dimensions of 100 x 200 x 400 mm (actual dimensions are 90 x 190 x 390 mm, with Face Shell and Web thickness of 26 mm) as shown in Figure 3-1(a). The walls had planar dimensions of 2.0 m x 2.0 m (Figure 3-1(b)). All the walls were built in a running bond pattern with Type S mortar, and with 10 mm thick joints (Figure 3-1(b)). In order to transport the walls, and to facilitate their setup in the shock-tube, they were built on top of steel HSS beams (152 x 152 x 6.4 mm, with a length of 2440 mm). To ensure that the FRCM retrofit surface would be even (flush) with the HSS, the front face of the walls was placed 1.0, 1.5 and 2.0 inches back from the front edge of each HSS beam for the application of 1, 2 and 3 FRCM-layers, respectively. Half the height of the walls was built during the first day by the mason, and the remaining portion was built two days after to allow for some curing. Later, the walls were cured for 28 days and restrained from falling with a wood frame until the application of the retrofit (Figure 3-2). After wall construction SCC concrete was used to infill the CMU voids in two of the walls. This mix was poured after the walls were fully built and the concrete was poured from the top of the walls (see Figure 3-3). The construction process of the walls is shown in Figure 3-2. During setup in the shock-tube, there was a small gap between the top of the wall and the top steel frame; consequently, fast-setting high strength mortar was applied to fill the gap to allow for the axial load application and to promote arching action. It should be noted that the SCC cast inside the voids of two of the walls (MS-S6 SCC) is a high performance, pre-blended, pre-packaged, self-consolidating, concrete repair material. It is a flowable concrete material containing Portland cement, silica fume, 6 mm (1/4 in) stone and other carefully selected admixtures. Lastly, the slump flow test result for

the SCC was 620mm and its compressive strength after 28 days (ASTM C 39) was an average of 55 MPa.

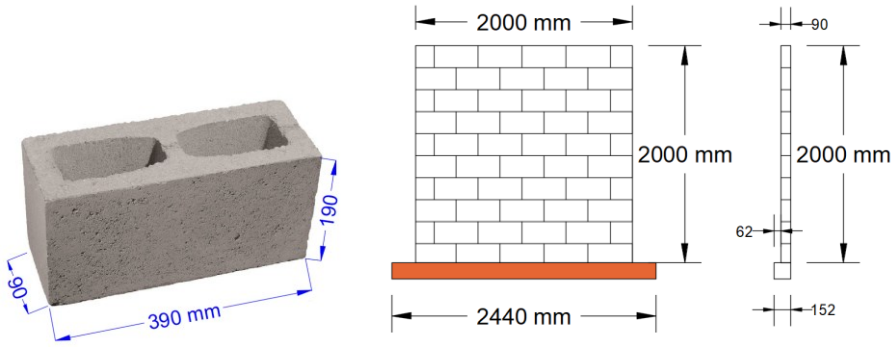

(a) (b)

Figure 3-1. (a) CMU block dimensions, (b) Walls dimensions (front and side view)

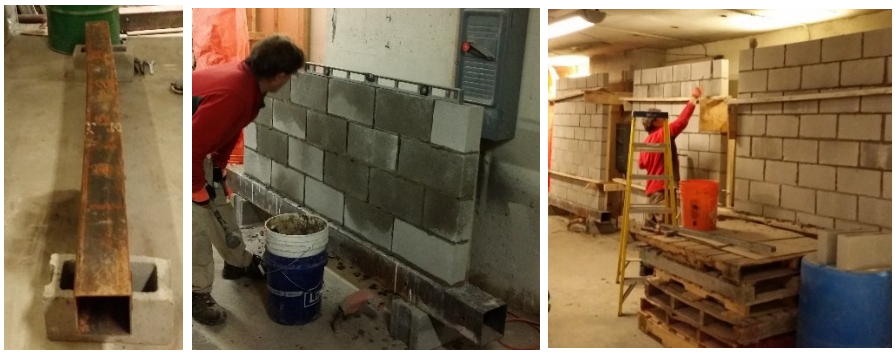

(a) (b) (c)

Figure 3-2. Construction of CMU wall; (a) Bed HSS, (b) Leveling of wall (c) Completion of the three walls and wood frame protection.

(a) (b) (c) (d)

Figure 3-3. Pouring SCC in voids of two CMU walls; (a) SCC bag, (b) SCC mixture (c) slump flow test, (d) SCC casting

3.2.1.2. FRCM strengthening system.

The strengthening system used to retrofit the walls in this research was Fabric-Reinforced Cementitious Matrix (FRCM) composite. It consisted of two main components, the carbon-fiber grid and the high-performance cementitious matrix (mortar). The first component consisted of a unidirectional carbon grid that correlates to the one-way bending demand during tests. For the second component, the cementitious matrix, a cement-based mortar reinforced with polypropylene fibers, was used. The polypropylene fibers had a length of 6 mm (1/4in) as shown in Figure 3-4(c). Figure 3-4(b) shows the carbon strands (vertical black strands), that were placed in the longitudinal direction of the walls for the one-way bending demand. It is noted that the horizontal strands are just for keeping the main strands in position with their correspondent grid spacing, but with no structural function assigned (they are mainly made out of plastic). The distance between two adjacent strands was of 17 mm (4 inches per 6 strands).

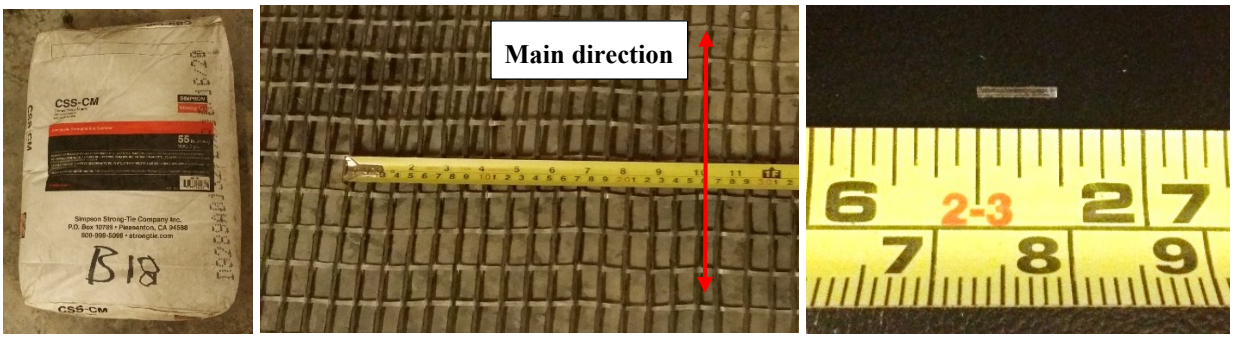

(a) (b) (c)

Figure 3-4. (a) Cement-based mortar bag, (b) Unidirectional carbon fiber fabric, (c) Polypropylene-reinforced-mortar fiber

The FRCM system was installed as follows:

1) Preparation of the surface: Dust and irregularities were removed from the wall surface to enhance the bond between the substrate and the mortar. Additionally, the wall surface or substrate was watered for 24 hrs. before the FRCM application to avoid loss of water in the mortar by absorption in the substrate (Figure 3-5(a)).
2) Mixing of Mortar (matrix): The mortar was mixed with the required amount of water until adequate consistency following the manufacturer's instructions and using an electric mixer tool (Figure 3-5(b)).
3) Installation: A base mortar layer of 0.5 in thick was first applied on the surface of the walls by hand troweling. Later, one layer of carbon grid was placed on the base layer and another mortar layer of 0.5 in thick was applied for every extra layer of carbon grid and/or as a final layer. Therefore, for the first wall (1 layer), we applied the base mortar layer of 0.5 in. thick plus, one layer of carbon grid plus, the final mortar layer of 0.5 in. thick; resulting

in a total thickness of 1.0 in. For the second wall (2 layers), we applied the base mortar layer of 0.5 in. thick plus, the first layer of carbon grid plus, one mortar layer of 0.5 in. thick plus, the second layer of carbon grid plus, the final mortar layer of 0.5 in. thick; resulting in a total thickness of 1.5 in. The same procedure was used for the third wall (3 layers), resulting in a total thickness of 2.0 in. (Figure 3-5(c)-(e)).

4) Curing: After applying the FRCM system, the three walls were cured for 28 days with wet burlaps and plastic tarps that covered them. This curing was applied to achieve the maximum strength resistance of the cement-based mortar / matrix (Figure 3-5(f)).

(a) (b) (c)

(d) (e) (f)

Figure 3-5. FRCM application; (a) Preparation of the surface, (b) Mixing of Mortar, (c) Base mortar layer (0.5 in thick), (d) Carbon grid layer, (e) Final mortar layer (0.5 in thick), (f) Walls curing with burlaps and plastic tarps.

3.2.2. Test Specimens Description

In this research, three masonry walls were built and retrofitted with FRCM. The performance of the FRCM retrofit was studied by comparing the results to a control wall tested by Ciornei (2012) in a previous project at the University of Ottawa. The control CMU wall had the same dimensions and characteristics as those in this research project, but no retrofit was applied. The details of the three specimens in this research and the control are shown in Table 3-1. The table displays the wall type (load-bearing), the masonry type (CMU) and the strengthening method. The specimens tested for this research are identified as "RCL-NC-1" and "RCN-YC-1". The first letter "R" indicates that the wall had retrofit. The second letter stands for the masonry type: "C" for concrete masonry (CMU). The third letter reveals the axial loading conditions: "L" for load bearing and "N" for non-load bearing (infill). In order to identify the walls which included SCC concrete inside the masonry units, the legend "YC" is used, while "NC" stands for the wall without SCC. Finally, the number at the end implies the number of carbon grid layers used in the FRCM retrofit. The wall tested by Ciornei (2012) is used as a reference; it is described using the same nomenclature used by the original author, where URM-3, stands for: unreinforced concrete masonry load-bearing wall. Lastly, since all walls were load-bearing, an axial load with a total magnitude of 122kN was applied on the CMU walls. For this purpose, one hydraulic pump and two hydraulic jacks were used. These jacks were placed on top of the upper HSS, and reacted against the underside of the lab strong-floor, with 61kN applied from each jack. This load was then transmitted as a uniformly distributed axial load to the wall through the 6inx6in top HSS. Figure 3-6 shows more details.

(a) (b) (c)

Figure 3-6. Axial load application on wall; (a) Two hydraulic jacks on the top of the wall, (b) Bottom supports for bottom HSS, (c) Front view of hydraulic jacks and supports.

Table 3-1. Test Specimens Description

Wall	Masonry Type and Axial Load Conditions	Retrofit	SCC infill	Tested by
URM-3	CMU Load Bearing (122 kN)	None (Control)	NO	1
RCL-NC-1	CMU Load Bearing (122 kN)	FRCM (1.0” thick, 1-layer carbon grid)	NO	2
RCL-YC-2		FRCM (1.5” thick, 2-layer carbon grids)	YES	2
RCL-YC-3		FRCM (2.0” thick, 3-layer carbon grids)	YES	2

1. Ciornei (2012), 2. Author

3.2.2.1. URM-3

Specimen URM-3 is the control wall and it was tested by Ciornei (2012). It consisted of an unreinforced CMU load-bearing wall, with dimensions of 2.0 m x 2.0 m, built with standard CMU blocks with dimensions of 100 mm x 200 mm x 400 mm and Type S mortar. The wall had complete contact with the top and bottom of the enclosing steel frame and an axial load was applied using two hydraulic jacks located 508 mm left and right of the vertical center line of the wall. The total axial load applied was 122 kN. Moreover, simply supported boundary conditions were implemented by the use of two HSS (152 mm x 152 mm x 6.4 mm) supports, provided on the top and bottom of the wall. This helped to prevent out-of-plane translation of the walls during the tests. Additionally, the horizontal HSS beams were connected to the shock-tube frame using vertical HSS (76 mm x 76 mm x 6.4 mm) sections, at their ends. The setup resulted in simply supported boundary conditions. A total of seven shock waves were applied on the URM-3 wall specimen until reaching global failure. The driver pressure of the shock tube was increased by approximately 40 kPa (6 psi) increments and the load duration was kept constant by using the same driver length of 1829 mm. More details of the URM-3 setup are shown in Figure 3-7.

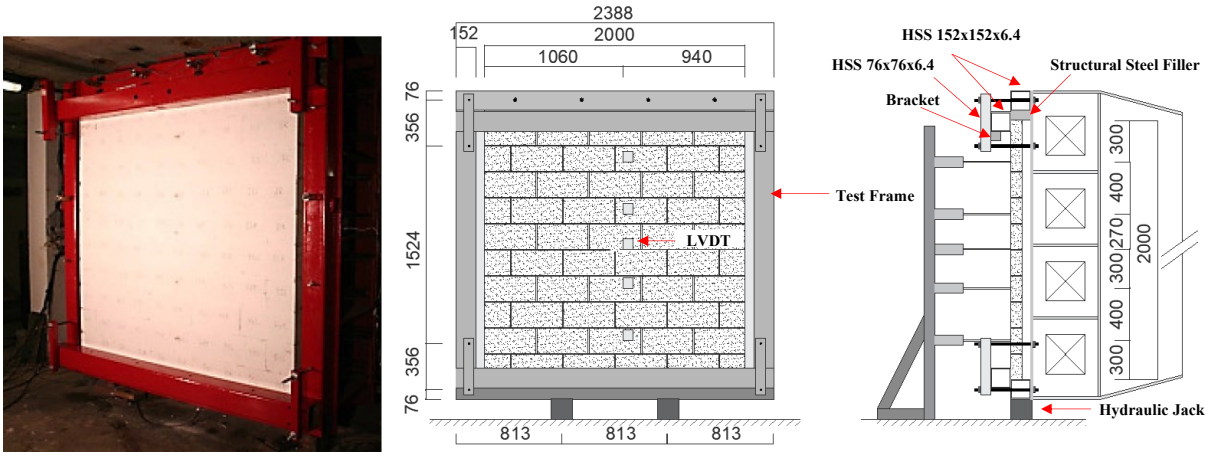

Figure 3-7. Detail of the URM-3 setup (Dimensions in mm) (Ciornei, 2012)

3.2.2.2. RCL-NC-1

RCL-NC-1 is a load-bearing wall, with no concrete cast inside the masonry blocks. The wall was built using the same procedure as URM-3 (same type of CMU blocks and same mortar type); however, RCL-NC-1 was retrofitted with FRCM composites. The FRCM retrofit consisted of one layer of carbon grid and matrix, resulting in a total retrofit thickness of 1.0 in (25 mm). After the installation of the FRCM and a minimum curing of 28 days, the wall was moved to the shock tube and prepared for setup. Later, the gap between the top of the wall and the shock tube frame was filled with high strength mortar to ensure transmission of axial load and promote arching action. The same axial load of 122 kN was applied to the wall prior to blast testing. To prevent out-of-plane translation of the wall, simply supported boundary conditions were provided at top and bottom, but the setup was slightly different when compared to the control. The setup consisting of 13 mm thick steel plates (2200 mm x 310 mm) fixed with 19 mm bolts to the top and bottom of the shock tube frame; these plates were used to prevent delamination/debonding of the FRCM at the wall ends. Thereafter, the simply supported boundary condition was ensured by adding to two lateral HSS (152 mm x 152 mm x 6.4 mm) beam supports. The horizontal HSS beams were connected to the shock-tube frame using vertical HSS (76 mm x 76 mm x 6.4 mm) sections at their ends using a single connection point (one at each end). This setup was chosen to stiffen the supports and promote simply supported boundary conditions, and prevent out of plane translation at the top of the wall (Jung, 2020). Figure 3-8 shows details of the RCL-NC-1 wall specimen setup.

(a) (b) (c) (d)

Figure 3-8. Set-up details for RCL-NC-1 (also for RCL-YC-2 and RCL-YC-3): (a) Left side, (b) Front, (c) Right side, (d) Right side top.

3.2.2.3. RCL-YC-2

RCL-YC-2 is a Load-Bearing wall, with concrete cast inside the bricks, built using the same procedure, same type of CMU blocks and same mortar type as wall URM-3; but unlike wall URM-3, RCL-YC-2 wall was infilled with an SCC concrete and retrofitted with FRCM composites. The FRCM composite consisted of two layers of carbon grid and matrix, resulting in a total retrofit thickness of 1.5 in (38 mm). After the installation of the FRCM and a minimum curing of 28 days, the wall was moved to the shock tube and setup. Later, the gap between the top of the wall and the shock tube frame was filled with high strength mortar to promote arching action. The same axial load and boundary conditions used in RCL-NC-1 were used. The simply supported boundary conditions consisting of 13 mm thick steel plates (2200 mm x 310 mm) fixed with 19 mm bolts to the top and bottom of the shock tube frame. The plates were then stiffened using two HSS (152 mm x 152 mm x 6.4 mm) beams which were connected to the shock-tube frame using vertical HSS (76 mm x 76 mm x 6.4 mm) sections, at their ends. Figure 3-8 shows details of the RCL-YC-2 wall specimen setup.

3.2.2.4. RCL-YC-3

RCL-YC-3 is a Load-Bearing wall, with concrete cast inside the bricks, built using the same procedure, same type of CMU blocks and same mortar type as URM-3; but unlike wall URM-3, RCL-YC-3 wall was infilled with an SCC concrete and retrofitted with FRCM composites. The FRCM composite consisted of three layers of carbon grid and the matrix, resulting in a total thickness of 2.0 in (50 mm). After the installation of the FRCM and a minimum curing of 28 days, the wall was moved to the shock tube and prepared for setup. Later, the gap between the top of the wall and the shock tube frame was filled with high strength mortar to promote arching action. In addition, to prevent out-of-plane translation, simply supported boundary conditions were provided at top and bottom, consisting of the same 13 mm thick steel plates (2200 mm x 310 mm) and supporting HSS (152 mm x 152 mm x 6.4 mm) beams used in the previous two walls. Also, the same axial load of 122 kN was applied to the wall prior to blast testing. Figure 3-8 shows details of the RCL-YC-3 wall specimen setup.

3.3. EXPERIMENTAL SETUP AND DATA ACQUISITION

3.3.1.Experimental Setup

3.3.1.1.The Shock tube

The University of Ottawa Shock Tube is a pressure-driven blast simulator that can simulate the shock waves caused by free-air detonation of high explosives. It is composed of four sections: the driver, double-diaphragm section, expansion section and end-frame. Figure 3-9 (a) shows more details. The driver length can be adjusted in increments of 12 in (305 mm), from 12 in (305 mm) to 204 in (5185 mm) as presented in Figure 3-9 (d), allowing for a flexible range of reflected pressures and impulses as shown in Figure 3-10. Different driver length/pressure combinations can be related to an equivalent TNT mass, standoff and scaled distance (see Figure 3-10). For producing the desired reflected pressure, two sets of aluminum foils (32 in x 32 in) are placed at each side of the diaphragm section, as shown in Figure 3-9 (c). The capacities of the aluminum foils are somewhat above half the targeted driver pressure. In this study the nominal strength of the aluminum foils were 5 psi [34 kPa], 13 psi [90 kPa] or 25 psi [172 kPa] (thickness of 0.005 in, 0.008 in, or 0.014 in respectively). After the diaphragm section has been sealed with the foils, the targeted pressure is attained by filling the driver section with air using an air compressor (Figure 3-9 (e)). The diaphragm is filled with half of the targeted pressure and later it is released at the time when the driver attains the intended pressure. Consequently, the aluminum foils break firstly in the diaphragm, and secondly in the driver section due to the achieved differential pressure between the diaphragm and the expansion section, where the expansion section remains with atmospheric pressure. Next, the compressed air travels through the expansion section in milliseconds and reaches the wall, at the end of the shock tube, where the attached specimen gets hit by the resulting shock wave producing a higher pressure known as “reflected pressure”.

The dimensions of the expansion section are 6096 mm (240 in) long, while the end frame is 2032 mm wide and 2032 mm high (80 in x 80 in section): see (Figure 3-9 (b)). Moreover, it has twelve sliding vents on the top and sides of the opening. These vents function as a mean of pressure relief, being closed before the shock tube releases the overpressure wave and being open by the pressure itself. These vents help to reproduce the negative phase of the pressure-time function of common blasts. Additionally, to cover the gaps left between the wall and the shock tube end-frame, timber frames were installed on the sides of the walls ensuring a seal at the test frame. This was done because the wall (2.0 m x 2.0 m) was slightly smaller than the end-frame opening. Further details on the shock tube can be found in Lloyd et al. (2009).

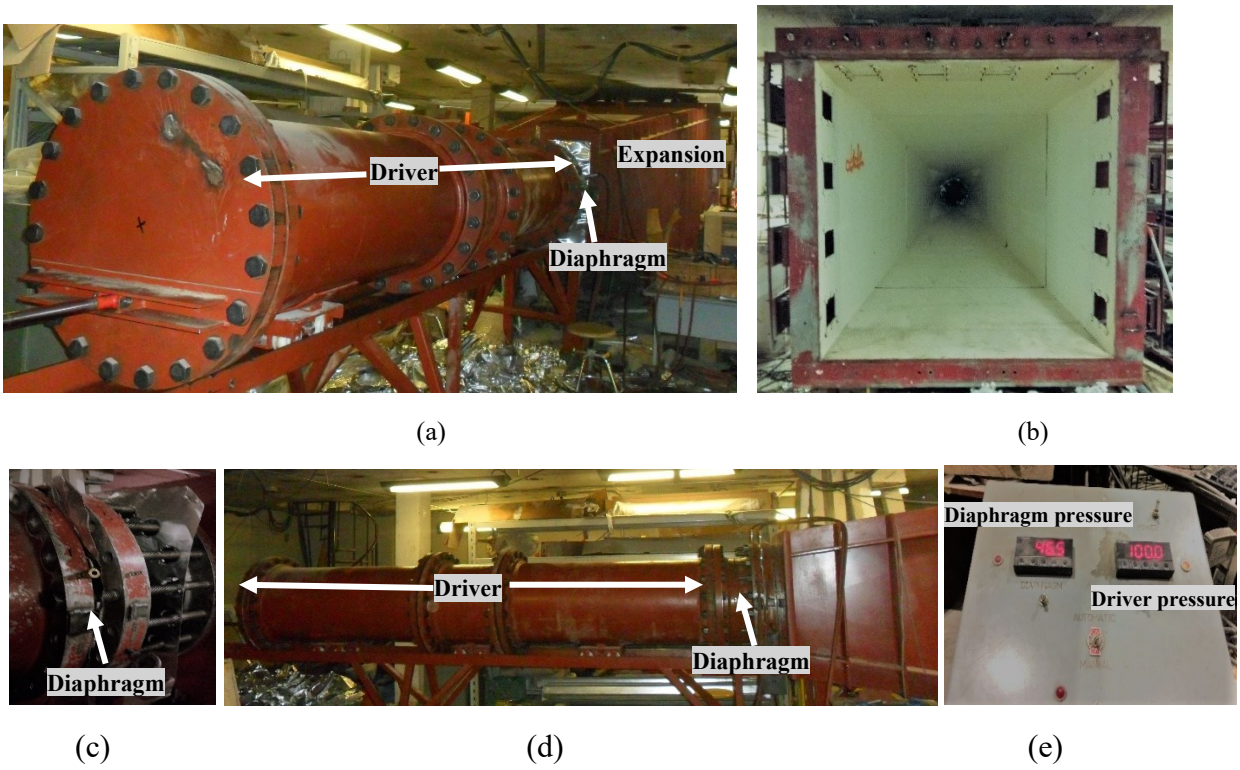

(a) (b)

(c) (d) (e)

Figure 3-9. Details of Shock tube; (a) Shock Tube, (b) Openings/Vents, (c) Opened diaphragm with foils, (d) Driver section (13ft long), (e) Firing control box

			Approximate Equivalent TNT (Hemispherical-Reflected)		
Driver Length	Reflected Pressure	Reflected Impulse	Mass	Standoff	Scaled Distance
(mm)	(kPa)	(kPa-ms)	(kg)	(m)	(m/kg$^{1/3}$)
305	78	217	8	12	6.0
915	92	410	42	18	5.2
1830	100	840	290	33	5.0
3355	103	1760	2500	67	4.9
4880	104	2690	10000	106	4.9

Figure 3-10. Maximum Shock Tube range (Lloyd et al., 2009)

3.3.1.2.Boundary conditions

Boundary conditions:

The three walls in the current study, RCL-NC-1, RCL-YC-2 and RCL-YC-3 had the same boundary conditions. Simply supported conditions were provided to prevent out-of-plane wall translation and to allow for one-way bending behavior. After the walls cured more than 28 days, they were moved to the shock tube for setup. Then the gap between the top of the wall and the

shock tube frame was filled with high strength mortar to promote arching action. In addition, to prevent out-of-plane translation of the wall, simply supported boundary conditions were provided at top and bottom, consisting of 13 mm thick steel plates (2200 mm x 310 mm) fixed with 19 mm bolts to the top and bottom of the shock tube frame. Moreover, the plates were stiffened by adding two HSS (152 mm x 76 mm x 6.4 mm) supports which extended the full width of the shock-tube. The horizontal HSS beams were connected to the shock-tube frame using vertical HSS (76 mm x 76 mm x 6.4 mm) sections, at their ends. Finally, to restrain the vertical movement of the walls during testing, hydraulic jacks and steel fillers were located between the top HSS and the laboratory strong-floor (ceiling), and between the bottom HSS and the laboratory slab on grade (bottom). Figure 3-11 shows more details.

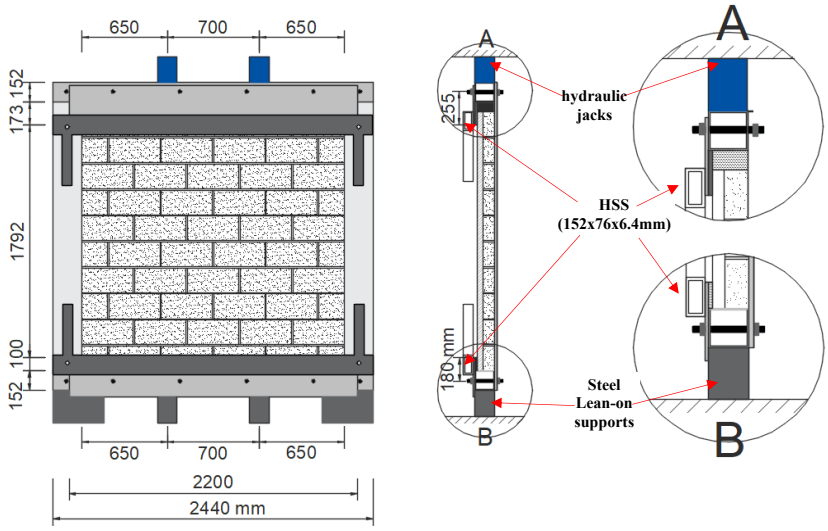

Figure 3-11. Boundary condition for RCL-NC-1, RCL-YC-2 and RCL-YC-3 walls (FRCM is not shown on the front view)

Axial load application:

Axial load was applied to the three specimens, RCL-NC-1, RCL-YC-2 and RCL-YC-3 to test them as load-bearing CMU walls. This was done by means of two hydraulic jacks located on the top HSS, placed at the same distance from the center of the top HSS. An axial load of 122 kN was applied to each wall by using the hydraulic jacks which reacted against the underside of the laboratory strong floor. The load applied matches the one used for the control wall, URM-3. See Figure 3-11 for more details.

Arching action:

For promoting arching action, the gap between the top of the wall and the shock tube frame was filled with high strength mortar. For avoiding the ingress of mortar into the brick-hollowed-wall RCL-NC-1, a piece of plastic was placed on top of the wall, before the high strength mortar was

applied. Additionally, the top HSS had slotted bolt holes, to allow for the application of the axial load (for walls RCL-YC-2 and RCL-YC-3), resulting in a better contact between the top of the wall and the top HSS.

3.3.1.3.Data acquisition

Instrumentation set up:

Instrumentation included a Data Acquisition System (DAS), Linear Variable Displacement Transducers (LVDTs), pressure sensors and two high speed cameras with tracking software. The DAS gets triggered by pressure sensors inside the shock tube (at bottom and side of the end-frame of the shock tube) immediately after the compressed air wave travels the expansion section and reaches the wall; at this point, the DAS receives the signal form the pressure sensors and immediately starts recording the pressure and displacement time histories. Right after the DAS is triggered, two high speed cameras are also triggered, which start recording the wall responses. The data captured by the cameras is saved in a laptop computer, so that the video can be stored and replayed afterwards. Details are displayed in Figure 3-12.

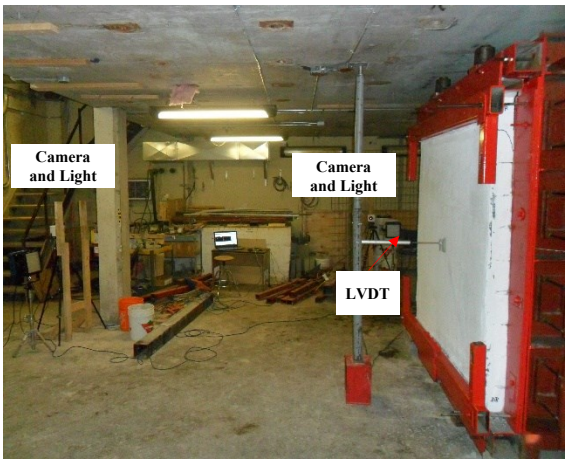

Instrumentation set up

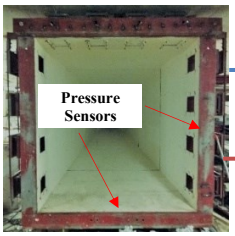

Pressure sensors

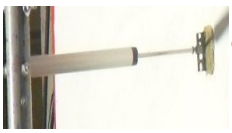

LVDT

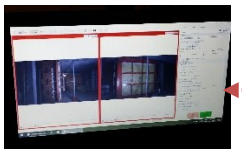

Camera software

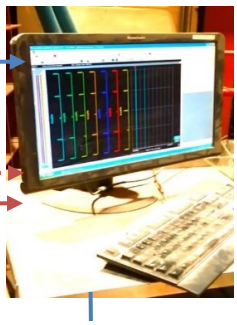

DAS

High speed camera

Trigger

Record

Record

Trigger

Record

Figure 3-12. Instrumentation of blast tests

Data Acquisition System (DAS):

The DAS is able to process different signal inputs, like pressures, strains, displacements etc., by means of pressure sensors, strain gauges, LVDTs, etc., all through 16 different channels. On the other hand, for this project, one LVDT and two reflected pressure sensors were set for each wall test. Where the measured displacements and pressures were recorded at a rate of 1000 kilo-samples per second (kS/s).

Pressure sensors:

The shock tube has two pressure sensors at the side and bottom as seen in Figure 3-12. Once the air wave reaches these sensors the DAS is triggered, recording the reflected pressure produced on the walls by the blast wave. Sometimes these sensors report slightly different values, so for the analysis the higher-pressure value was always used (the Appendix at the end shows the reflected pressure measured by the side and bottom pressure sensors). Additionally, flying aluminum foils apparently caused some high-pressure measures, but these arbitrary peaks were neglected.

Linear Variable Displacement Transducers (LVDTs):

One LVDT was installed at the center of each wall. The LVDT was attached to the wall and to a metal post; this post worked as a rigid member and was able to take the LVDT's reaction and therefore to keep it in position (Figure 3-13). The LVDT measured the displacement time history so a plot could be drawn with the data. When the failure of the wall was expected, for the penultimate and/or last shock-wave shot, the LVDT was removed to avoid any damage, and the wall displacement was tracked by the high speed cameras.

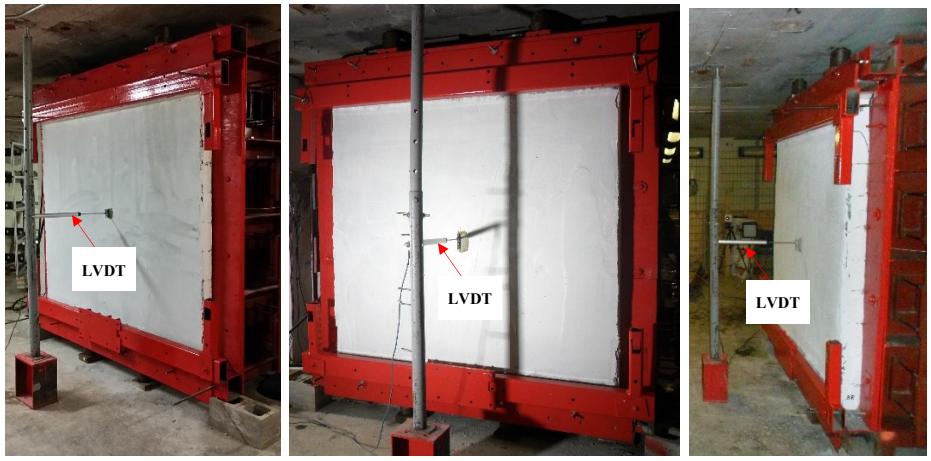

(a) (b) (c)

Figure 3-13. LVDT setup; (a) RCL-NC-1, (b) RCL-YC-2, (c) RCL-YC-3

High speed video cameras:

Two high speed cameras with tracking software were used to record the tests. They were placed at the side and at 45 degrees from the front of the wall to capture the motion of the specimens during the test, from different angles as shown in Figure 3-12. In order to make easier the tracking of the displacements on the walls, a sticker with tracking points was placed at each side of the wall. This sticker had black and white squares, that allowed the tracking of the wall motion by the camera as showed in Figure 3-13. Finally, the frame rate used for the tests was set at 2000 frames per second (fps).

3.3.1.4. Test sequence

The test sequence for the walls specimens is summarized in Table 3-2. The blast IDs are numbered depending on the driver pressure (in psi) used for each blast test in order to be able to compare the results from different walls tested in this study and in previous research. The initial driver length used for all three wall specimens was 6ft (1829 mm). The blast sequence for RCL-NC-1 followed the same order as the control wall URM-3, from Blast ID #2 (18 psi [121.4 kPa]) to Blast ID #6 (42 psi [288.2 kPa]), which was the failure shot for URM-3. After that, the driver pressure was increased to 60 psi [414 kPa], 80 psi [552 kPa] and finally, 100 psi [689 kPa]. This last one (Blast ID #11) caused the failure of RCL-NC-1. All the shots performed used a driver length of 6ft.

RCL-YC-2 followed the same sequence as RCL-NC-1, from Blast ID #2 (18 psi [121.4 kPa]) to Blast ID #11 (100 psi [689 kPa]), however the following blasts were skipped: Blast ID #3 (24 psi [165 kPa]) and Blast ID #4 (30 psi [207 kPa]). After that, the driver length was changed from 6ft to 11 ft, with blasts applied using driver pressures of 80 psi [552 kPa] and finally, 100 psi [689 kPa]. This last shot caused the failure of wall RCL-YC-2. Finally, wall RCL-YC-3 followed exactly the same sequence as RCL-YC-2, from Blast ID #2 (18 psi [121.4 kPa]) to Blast ID #13 (100 psi [689 kPa], with 11-ft-driver length). However, one more shot was performed on RCL-YC-3, with Blast ID #15 (100 psi [689 kPa]) and with 13-ft-driver length. The last shot did not cause the failure of RCL-YC-3, however given the limitations of the shock tube no more shots were performed. Table 3-2 summarize the test sequence followed.

Table 3-2. Summary of test sequence with Blast ID and Driver pressure (the Driver length is indicated in the brackets in feet for other than the 6-foot-long driver)

Blast ID	URM-3 *		RCL-NC-1 **		RCL-YC-2**		RCL-YC-3**	
	psi	kPa	psi	kPa	psi	kPa	psi	kPa
#0	5	34.5						
#1	12	79.3						
#2	18	121.4	16	110	16	110	16	110
#3	24	166.9	24	165				0
#4	31	212.4	30	207				0
#5	36	248.2	36	248	36	248	36	248
#6	42	288.2	42	290	42	290	42	290
#7***								
#8***								
#9			60	414	60	414	60	414
#10			80	552	79	545	80	552
#11			100	689	100	689	100	689
#12					80 (11)	552	80 (11)	552
#13					100 (11)	689	100 (11)	689
#14***								
#15							100 (13)	689
Total	4 shots		8 shots		8 shots		9 shots	

* Tested by Ciornei (2012), ** Tested by Author (2020), ***Test conducted on wall URM-S-L or R-C-N by Jung (2020)

Table 3-3 shows the properties of the shock waves in terms of reflected pressure and impulse for each blast shot. Additionally, the table makes a comparison of the results with the approximate values of equivalent TNT, where blast shots with same Blast ID correspond to same values of equivalent TNT. It is noted that the driver pressure was controlled manually using the firing station (Figure 3-9 (c)) as a result slight differences between the actual and intended pressure occurred. The two sensors installed at bottom and side of the shock tube end, were used to measure the reflected pressure (Figure 3-12), taking always the higher pressure from the two lectures. The reflected impulse, was computed as the area under the reflected pressure-time history function, for the positive phase.

The approximate equivalent values of TNT were computed in Table 3-3 following the CSA S850-12 standard (CSA, 2012) and Lloyd (2010). Where the CSA S850-12 recommends using the following equation [3-1] to estimate blast loading parameters:

$$\mathbf{x = c_0 + c_1 z + c_2 z^2 + c_3 z^3 + c_4 z^4 \ \ where, x = ln(x), z = ln(Z)} \qquad [3\text{-}1]$$

Where "x" is a scaled wave front parameter as specified "normally reflected pressure" with a scaling factor of 1 and kPa units. The term "c" represents the coefficients obtained for the spherical TNT surface burst and they are recommended to be taken as 9.7457, -4.7276, 1.1734, and -0.1337 for c_0, c_1, c_2, and c_3 respectively in the case of "normally reflected pressure $1.95 < Z < 39.67$". If the standoff distance is chosen from Figure 3-10 as recommended by Lloyd (2009), the scaled distance, Z, and the charge weight, W, could be computed with the equation above.

Table 3-3. Blast properties from Shock tube and Equivalent values to TNT

Shock Tube (University of Ottawa)								Approximate Equivalent to TNT (CSA-S850-12, Lloyd (2010))		
Blast ID	Driver Pressure: P_d		Driver Length: L_d		Avg. Reflected Pressure: P_r	Avg. Reflected Impulse: I_r	Avg. Positive Phase Duration: t_d	Scaled Distance: Z	Charge Weight: W	Standoff Distance: R
	(psi)	(kPa)	(mm)	(ft)	(kPa)	(kPa-ms)	(ms)	($m/kg^{1/3}$)	(kg)	(m)
#1	12	83	1829	6	22.0	145	14.5	12.9	16.6	33
#2	18	124	1829	6	29.3	204	14.6	10.5	30.9	33
#3	24	165	1829	6	38.1	285	16.1	8.8	52.9	33
#4	31	214	1829	6	39.5	427	16.0	8.6	56.8	33
#5	36	248	1829	6	53.4	347	16.0	7.1	100.1	33
#6	42	290	1829	6	46.5	574	16.3	7.7	77.5	33
#7	48	331	1829	6	56.4	619	16.7	6.9	110.3	33
#8	54	372	1829	6	57.1	600	18.0	6.8	112.7	33
#9	60	414	1829	6	73.1	514	18.1	5.9	171.7	33
#10	70	483	1829	6	73.4	557	19.0	5.9	172.9	33
#11	100	689	1829	6	112.9	857	22.7	4.7	337.2	33
#12	80	552	3353	11	83.2	1247	31.7	5.5	1772.0	67
#13	100	689	3353	11	103.3	1713	57.8	5.0	2475.0	67
#14	85	586	3962	13	86.5	1838	61.4	5.4	3985.2	86
#15	100	689	3962	13	114.0	2002	58.8	4.7	6056.5	86

3.4. MATERIAL PROPERTIES

3.4.1. Masonry and Mortar Properties

3.4.1.1.CMU units and prisms

Five CMU units, five plane CMU prisms (without SCC) and three prisms with SCC cast inside the masonry cavities, were tested for compressive strength according to the ASTM C140 and CSA S304.1-04 standards. The top and bottom of the specimens were capped with high strength mortar and leveled to ensure a flat load application surface and a better contact area during testing. The thickness of the capping was not more than 10 mm, as stated in the standard. Typical specimens are shown in Figure 3-14. The specimens were built and tested under a displacement control rate of 0.1 mm/min until failure using a Universal Testing Machine at the University of Ottawa. The CMU block specimens' dimensions were 90 mm (W) x 190 mm (H) x 390 mm (L), while the prisms had dimensions of 90 mm (W) x 386 mm (H) x 390 mm (L). The prisms were built using the same type of CMU, same Type S mortar and 10 mm thick joints used in the walls. According to CSA S304.1-04, a factor of 1.0 was used for the prisms (for compressive strength test) because they were built with hollow concrete blocks. For measuring the strain of the CMU units and prisms during the tests, two LVDTs were placed, one at the front and the other at the back, nonetheless the displacement could not be recorded until failure (to avoid damaging the LVDTs) and just a very small portion of the ultimate strain was collected, therefore the strains are not reported herein. Figure 3-15 shows the set up and typical failure modes for the CMU units and CMU prisms. The experimental results are presented in Table 3-4. The mean compressive strength of the CMU units was 14.0 MPa, while it was 12.0 MPa for the plane prisms (without SCC) and 19.7 MPa for the prisms with SCC. Strain data was not collected because the main purpose of this test was getting the ultimate compressive strength (f'm).

Figure 3-14. Leveling and capping of the specimens with high strength mortar

(a) (b)

(c)

Figure 3-15. Experimental set up and typical failure modes for compressive strength of; (a) CMU units, (b) CMU prisms (plane), (c) CMU prisms with SCC cast.

Table 3-4. Compressive strength for CMU blocks and CMU prisms

CMU		1	2	3	4	5	Average	Std Dev	CV
Blocks	f'_m (MPa)	14.9	15.4	12.1	12.8	15.0	14.0	1.5	0.11
Prisms (Plane)	f'_m (MPa)	12.3	10.4	13.8	10.8	12.5	12.0	1.4	0.12
Prisms (SCC)	f'_m (MPa)	20.2	18.0	21.0	----	----	19.7	1.6	0.08

3.4.1.2.Mortar

To determine the compressive strength of the Type-S mortar, used for the joints in the three walls, 9 standard cubes (50 mm) were built, cured for more than 28 days and finally tested according to the ASTM C109 standard. The test setup and the typical failure mode for the mortar are presented in Figure 3-16. Table 3-5 summarizes the results; the average of the compressive strength of the cubes was found to be 20.5 MPa.

Table 3-5. Compressive strength of mortar cubes for Type-S mortar joints

Batch from	RCL-NC-1			RCL-YC-2			RCL-YC-3			
Specimen (Mortar cube)	1	2	3	4	5	6	7	8	9	Average
Compressive Strength (MPa)	22.2	20.4	17.7	22.3	21.2	21.7	17.6	20.7	20.6	20.5

(a) (b)

Figure 3-16. Experimental setup for the compressive strength of mortar cubes (a), and typical failure mode (b)

3.4.2.FRCM properties

3.4.2.1.Cementitious matrix (cement-based mortar)

Eight standard cylinders (100 x 200 mm) were tested to determine the compressive strength of the cement-based mortar which was used as a binder in the FRCM composite. Four of the cylinders were cast from the same mortar batch used during the wall retrofits, while the remaining four were obtained during the construction of the mini-beams. The cylinders were cured for more than 28 days and only the four belonging to the walls, were tested accordingly to ASTM C39, for their compressive strength. The other 4 cylinders were not tested given that the mini-beams were not tested in the final thesis program and were saved for future testing.

As stated before, the mortar had micro fibers to improve its toughness (Figure 3-4 (c)) and their characteristics are presented in Table 3-7. Table 3-8, shows the test results of the FRCM mortar cylinders. It should be noted that it was not possible to measure the strain in the FRCM cylinders until failure due to lack of available equipment at the University. However, a dual LVDT setup was used to collect the strain up to 40% of the expected compressive strength in order to measure the modulus of elasticity. Figure 3-17 shows the partial compressive stress-strain curves and Figure 3-18 shows the test setup and typical failure modes.

The tests resulted in an average compressive strength of 58.6 MPa. The compressive strength of a standard 50mm cube was calculated to be 49.8 MPa by using a conversion factor of 0.85 from the cylinder strength (Viso et al. 1998). This strength value was comparable with the one provided by the manufacturer, as showed in Table 3-6. Figure 3-18, shows that the fracture patterns were either 'well-formed cone on one end, vertical cracks running through caps, no well-defined cone on other end (Type 2)', 'Columnar vertical cracking through both ends or no well-formed cones (Type 3)' as described in ASTM C39. The tested modulus of elasticity of FRCM mortar cylinders is reported in Table 3-9 and it was found to be an average of 32,040 MPa.

Table 3-6. Material properties of FRCM cement-based mortar *

Unit weight	2,240 kg/m^3	Flexural strength	6.9 MPa
Tensile modulus	26.8 GPa	Compressive strength	21 MPa (1 day) 43 MPa (7 day) 52 MPa (28 day)
Direct tensile bond strength	2.7 MPa		

* Provided by the manufacturer

Table 3-7. Physical characteristics of polypropylene fibers in cement-based mortar *

Fiber type	Polypropylene film	Specific gravity	0.91 g/cm^3
Width	250-400 µm	Tensile strength	250-525 N/mm^2
Thickness	35-40 µm	Elongation at break	6-13 %
Length	6 mm	Modulus	10500-20840 N/mm^2

* Provided by the manufacturer

Table 3-8. Compressive strength of FRCM mortar cylinders (tested)

Cylinders (Ø100 x H 200mm)	1	2	3	4	Average
Compressive Strength (MPa)	55.8	58.6	62.6	57.4	58.6

Table 3-9. Compressive modulus of elasticity of FRCM mortar cylinders (tested)

Cylinders (Ø100 x H 200mm)	1	2	3	4	Average
Compressive modulus of elasticity (MPa)	33385	27688	39512	27575	32040

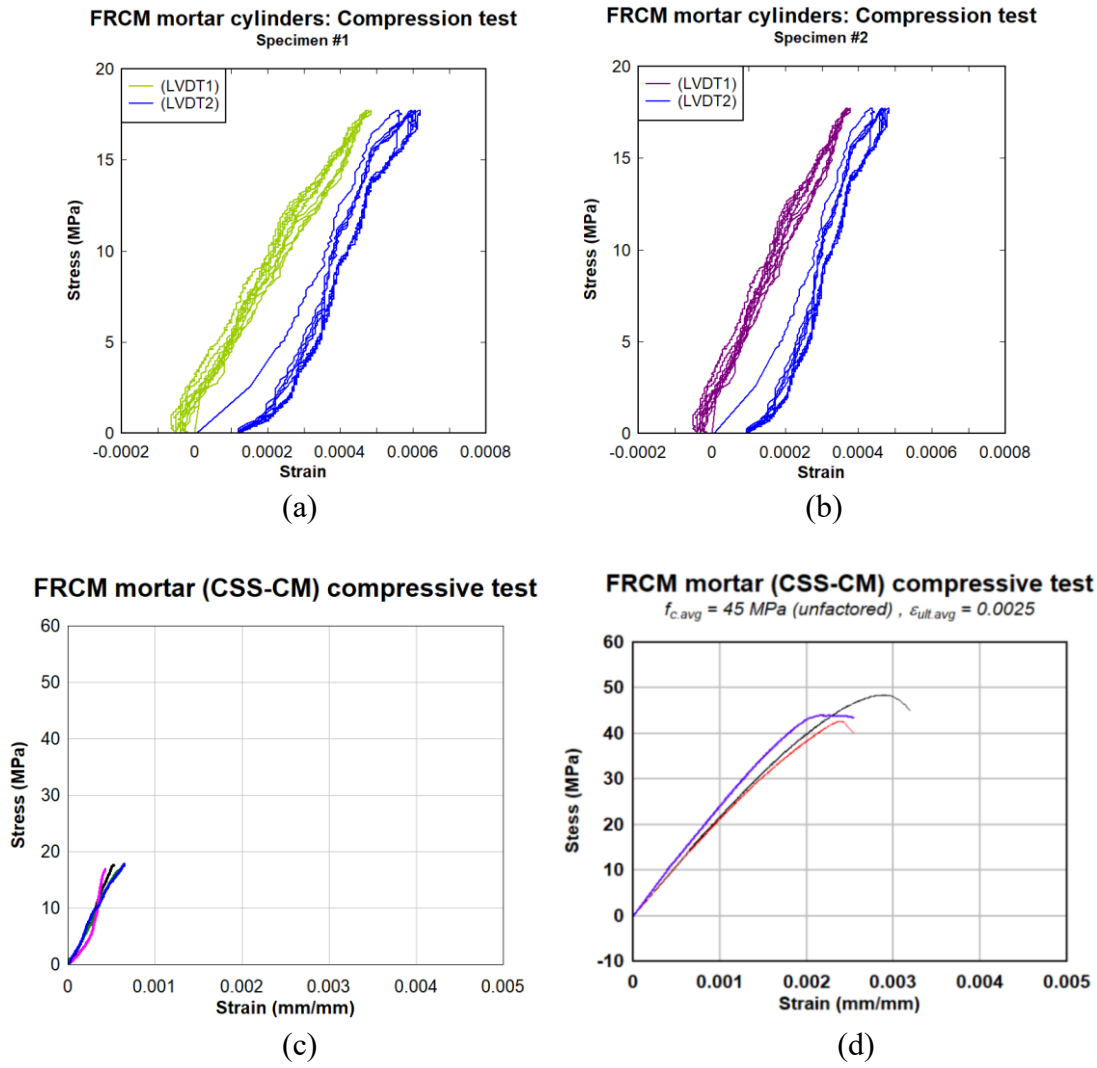

Figure 3-17. (a-b) Initial part of compressive stress-strain curves of FRCM mortar and (c)average for each specimen, (d) compressive stress-strain curves of FRCM mortar as determined by Jung (2020)

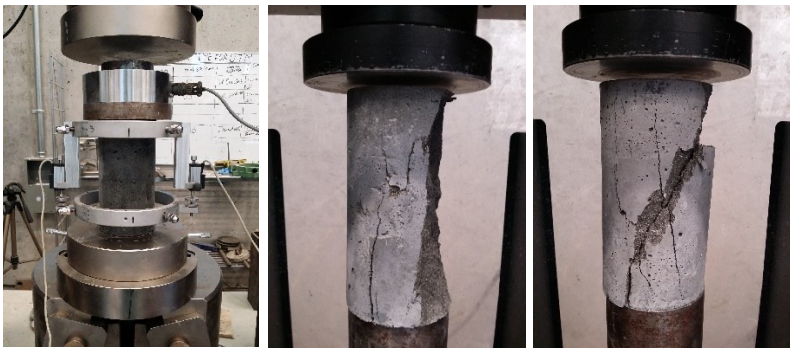

(a) (b) (c)

Figure 3-18. (a) Compressive test setup; (b) failure modes Type 3, (c) Type 4

3.4.2.2. FRCM coupons

Three specimens were made and 27 coupons were cut from them and tested to measure the tensile properties of the FRCM composite according to Annex A of AC434 (2013): Acceptance Criteria for "Masonry and Concrete Strengthening Using Fabric-reinforced Cementitious Matrix (FRCM) and Steel Reinforced Grout (SRG) Composite Systems". In order to meet the standard, the following criteria was applied:

- To build at least five coupons for each representative case;
- Specimens curing for seven days or more, and a minimum of fourteen days before testing.
- Cutting the coupons from a bigger panel specimen;
- A minimum of three strands within the appropriate width;
- Coupons should have rectangular shapes and width four times their thickness or bigger, with a minimum length of two times the width and gauge length (gripping distance included);
- Two-millimeter-thick metallic tabs or thicker, glued at minimum length of 75mm at each end, and connection to the test machine using clevis-type grips;

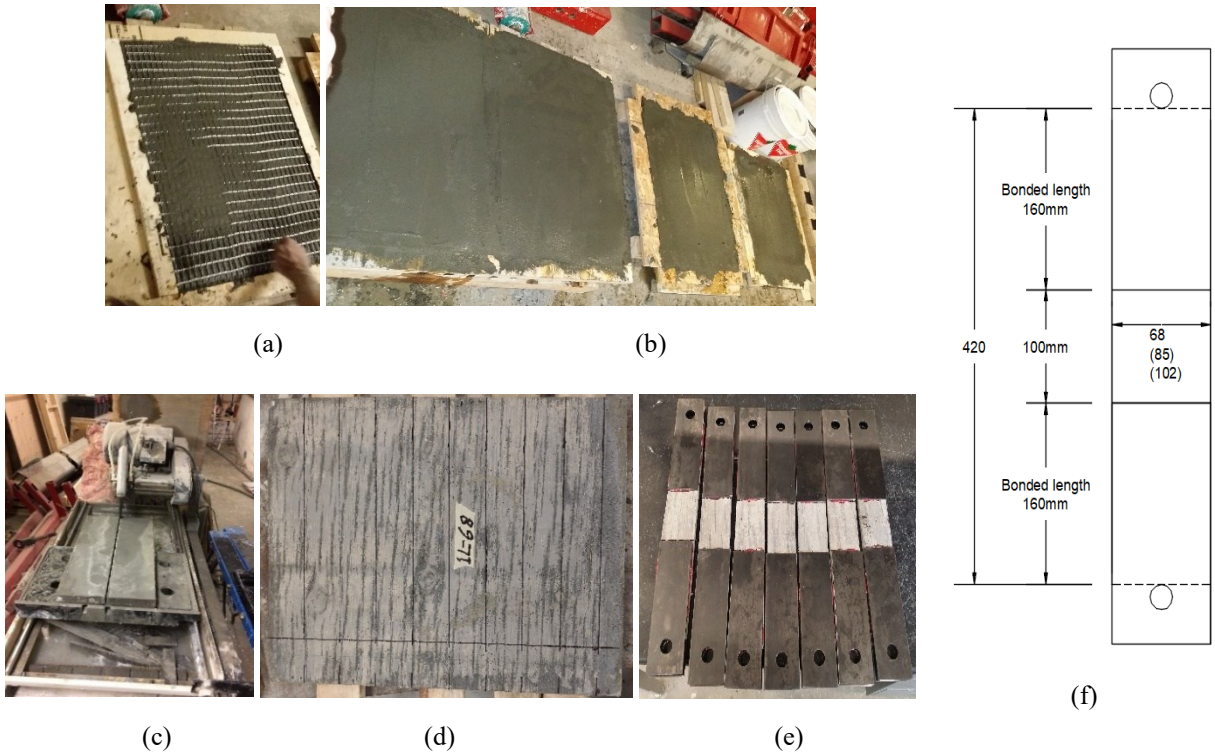

Figure 3-19. FRCM coupons: (a) FRCM application, (b) After application, (c) Concrete wet saw, (d) After cutting, (e) Completion, (f) Intended dimensions (Brackets for 2 and 3 layers)

In total 3 large panel specimens were cast using 3 wooden molds of 500 mm x 700 mm, 550 mm x 900 mm and 600 mm x 1200 mm, with thicknesses of 12 mm, 18 mm and 24 mm, respectively, for the FRCM composite with 1, 2 and 3 carbon-fabric layers, respectively. After curing more than 28 days, nine coupons were cut from each specimen, resulting in 9 coupons for each condition (1, 2 and 3 layers), and adding up a total of 27 coupons. For coupons with FRCM with 1 carbon-fabric layer, their width was 68 mm; for 2 layers: 85 mm; and for 3 layers: 102 mm. These widths were chosen according to the standard of having at least a width of 4 times the coupon thickness and assuring a minimum of 3 strands in each coupon. All coupons had the same total length of 420 mm, a gripping distance of 160 mm for each metal tab and a gauge length of 100 mm. The average dimensions of six measures for the thickness and three for the width of each coupon, are reported in Table 3-10. Additionally, steel tabs with 3mm of thickness were glued onto the coupons with high strength epoxy (HILTI, HIT-RE 500 V3). The steel tabs had the same width as the coupons. It should be noted that, AC434 suggests 75 mm as minimum length for the gripping distance; nonetheless, 160mm was used as recommended by Donnini et al. (2017), to improve the bond between the steel tabs and the coupons. Donnini et al. (2017), concluded that a 150-milimiter contact length was enough to develop a satisfactory bond strength. The panels were moist cured for 28 days and after that were cut into coupons with a concrete wet saw. Figure 3-19 shows details about dimensions and preparation of the FRCM coupons. Moreover, clevis-type grips were used for the test as suggested by Annex A of AC434 (2013). These grips allow for movement in the perpendicular direction, minimizing bending moment forces on the coupons (Figure 3-20 (a-b)). Two LVDTs were placed, one at front and the other one at the back of the specimens, to measure the average axial deformation. These were attached to the steel tabs as shown in Figure 3-20. The load rate used was of 0.2 mm/min as recommended by AC434.

It should be noted that rectangular shaped holders were used as a substitute of the suggested socket cup screws, due to the limitations of the testing machine: Figure 3-20 (b). Finally, monotonically increasing uniaxial tensile loading was applied under displacement control at a rate of 0.2 mm/min with the Universal Testing Machine at the University of Ottawa. A typical failure mode from the coupon tests, it is shown in Figure 3-20 (d).

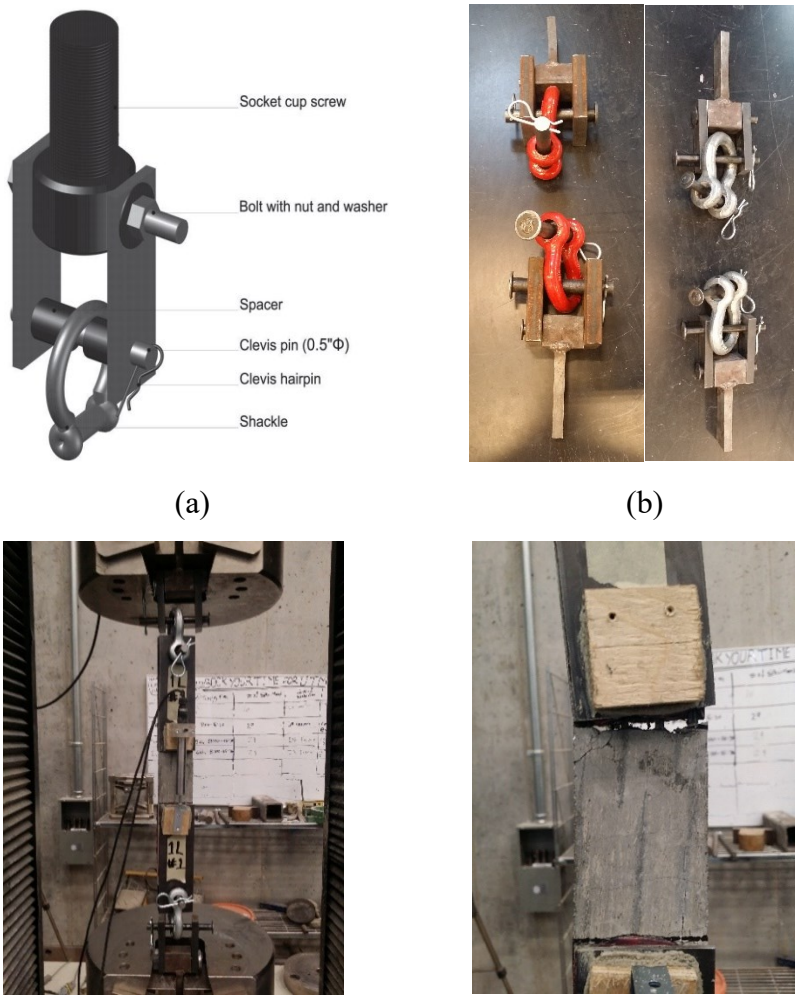

Figure 3-20. Tensile test; (a) Clevis-type gripping mechanism (AC434, 2013), (b) Clevis-type gripping mechanism used instead, (c) Test setup for this study, (d) Example of typical failure mode.

The tensile capacity of a coupon, T (kN), as stated in ACI 549.4R-13 (2013), can be computed as:

$$\mathbf{T = n\ x\ A_f\ x\ E_f\ x\ \varepsilon_{fe}} \qquad [3\text{-}2]$$

where n is the number of FRCM plies, A_f is the area of mesh reinforcement by unit width (mm^2/mm), E_f is the tensile modulus of elasticity of the cracked specimen (MPa), and ε_{fe} is the FRCM effective tensile strain, which is computed as the minimum of the ultimate tensile strain (ε_{fd}) or 0.012. The computed and tested tensile capacities for the FRCM coupons are compared in Table 3-10, the computed values were calculated using the actual carbon fabric area within each tested coupon (instead of using A_f), E_f was taken as 49000 MPa and ε_{fd} as 0.011 mm/mm, as specified in the manufacturer datasheet. It can be said that, the number of strands of carbon fabric

in each coupon, was constant (with few exceptions), with 4 strands for the 1-FRCM-Layer coupons and with 10 strands for the 2-FRCM-Layer coupons. The modified-2-FRCM-Layer coupon had 6 strands of carbon fabric.

It should be noted that this test has many variables and therefore many error sources, like the glue quality and gluing technique used, the contact surface, the cleanliness, the positioning and alignment of the strands, the mortar thickness, etc. The results for the 1-FRCM-Layer coupons were satisfactory, with well-defined stress-strain curves and similar trends. Also, the tested tensile capacity of these coupons is close in value to the computed one. Being around 1 to 45% bigger than the computed capacity, Table 3-10. The failure mode for the 1-FRCM-Layer coupons, was fiber slippage: Figure 3-22 (a). On the other hand, the results from the 2-FRCM-Layer coupons were less reliable due to premature failure. In general the tests show low tensile capacities and fiber debonding failures as shown in Figure 3-22 (b). The tested tensile capacities were 6% to 34% lower than the computed capacity: see Table 3-10. The premature failure could be led by the larger thickness of the coupon and the short bonding length which was limited by the available machine headroom. For this reason, one 2-FRCM-Layer coupon was modified and tested later with the expectation of better results (coupon 2-9). The modification consisted in decreasing the width of the gauge length, from 85mm to 68mm and therefore the number of carbon fabric strands, from 10 to 6 strands. It should be noted that the bonded length as well as all the other dimensions were not modified: see Figure 3-23 (a). As a result, the tensile capacity was modified (reduced) but the bonded length was kept constant and therefore the coupon did not develop premature failure. The failure mode for the 2-FRCM-Layer-modified coupon, was fiber slippage as shown in Figure 3-23 (b). This modified coupon followed the expected response, having a well-defined stress-strain curve and failure process as shown in Figure 3-21 (c), and a tensile capacity which was 47% bigger than the computed capacity, Table 3-10.

Table 3-10. Average dimensions of tested coupons and tensile capacities; tested vs. calculated

Coupons		Avg. Dimension (mm)			Tensile capacity (N)		
		Length	Thickness	Width	Calculated	Tested	% of calc.
1 Layer	1-1	420	13.7	66.4	5754	Not saved	-----
	1-2	420	12.1	64.7	5754	6496	113
	1-3	420	12.1	64.3	5444	6947	128
	1-4	420	12.5	66.0	5754	6767	118
	1-5	420	13.5	66.1	5754	8333	145
	1-6	420	12.0	66.1	5590	7153	128
	1-7	420	12.4	66.9	5754	5793	101
	1-8	420	11.7	65.9	5578	6833	123
	1-9	420	12.9	66.1	5754	7581	132
2 Layers	2-1	420	19.6	82.5	14386	11355	79
	2-2	420	16.8	82.0	14386	12913	90
	2-3	420	20.4	86.9	14386	10281	71
	2-4	420	15.9	82.2	14386	13463	94
	2-5	420	17.9	81.7	14386	12210	85
	2-6	420	18.3	80.5	14386	13403	93
	2-7	420	19.1	79.0	14386	12041	84
	2-8	420	20.7	78.6	14386	9554	66
	2-9*	420	16.1	61.4	8632	12674	147

* Modified 2-FRCM-Layer coupon.

Next several mechanical properties were computed following the AC434 (2013) using the data from the previous tensile tests on the FRCM coupons:

- The tensile modulus of elasticity of the uncracked specimen, E_f^*, equivalent to $\Delta f / \Delta \varepsilon$. Where Δf and $\Delta \varepsilon$ are the differential tensile stress and the differential strain respectively, between two different points on the stress-strain function, before the cracking point delimited on the curve.
- The tensile modulus of elasticity of the cracked specimen, E_f, equal to the slope between two points at stresses of $0.90\,f_{fu}$ and $0.60\,f_{fu}$, and computed using $E_f = (0.90f_{fu} - 0.60f_{fu}) / (\varepsilon_{f@0.90ffu} - \varepsilon_{f@0.60ffu})$.
- The ultimate tensile strain, ε_{fu}, computed as $\varepsilon_{fu} = (f_{fu} - \text{y intercept}) / E_f)$ where "y intercept" is equal to: y intercept = $0.60f_{fu} - E_f - \varepsilon_{f@0.60ffu}$.

The computed test results are reported in Table 3-11. This table contains the uncracked and cracked tensile modulus of elasticity, the ultimate tensile strain and ultimate tensile strength.

Table 3-11. Mechanical properties of FRCM coupons

Property	Symbol	Unit	One layer	Two layers	Two layers
			Average	Average	Modified (2-9)
Tensile modulus of elasticity of the uncracked specimen (divided by A_f) (1).	E_f^*	GPa	1506	942.8	253.2
Tensile modulus of elasticity of the uncracked specimen (divided by gross area of coupons)	E_f^*	GPa	18.6	16.6	4.1
Tensile modulus of elasticity of the cracked specimen (1).	E_f	GPa	29.0	24.0	28.1
Ultimate tensile strength (1).	f_{fu}	MPa	591.4	396.6	790.9
Ultimate tensile strain	ε_{fu}	mm/mm	0.0181	0.0194	0.0296

(1) Fiber area by the number of strands in each tested coupon was used for computing the properties.

Figure 3-21 presents the mechanical behavior of the FRCM coupons with one and two layers of carbon fiber grid, tested under direct tensile loading. In general, the diagrams are comparable to those defined in Section 2.2.5, having the three different branches representing; un-cracked, crack development and the cracked stages. The responses have an initial stiffness until the first crack appears (un-cracked stage), after this there is a drop in strength follow by a degradation of the stiffness and a redistribution of stresses. This happens because the section has cracked completely and all the stresses are distributed from the entire cross-sectional area (gross area) to the area of the carbon fibers within the coupon (crack development stage). Finally, there is an increase in the strength capacity again, but with a decayed stiffness until reaching the ultimate capacity and failure (cracked stage). The stress-strain relationship was computed based on the AC434 (2013) guidelines and is plotted in Figure 3-21.

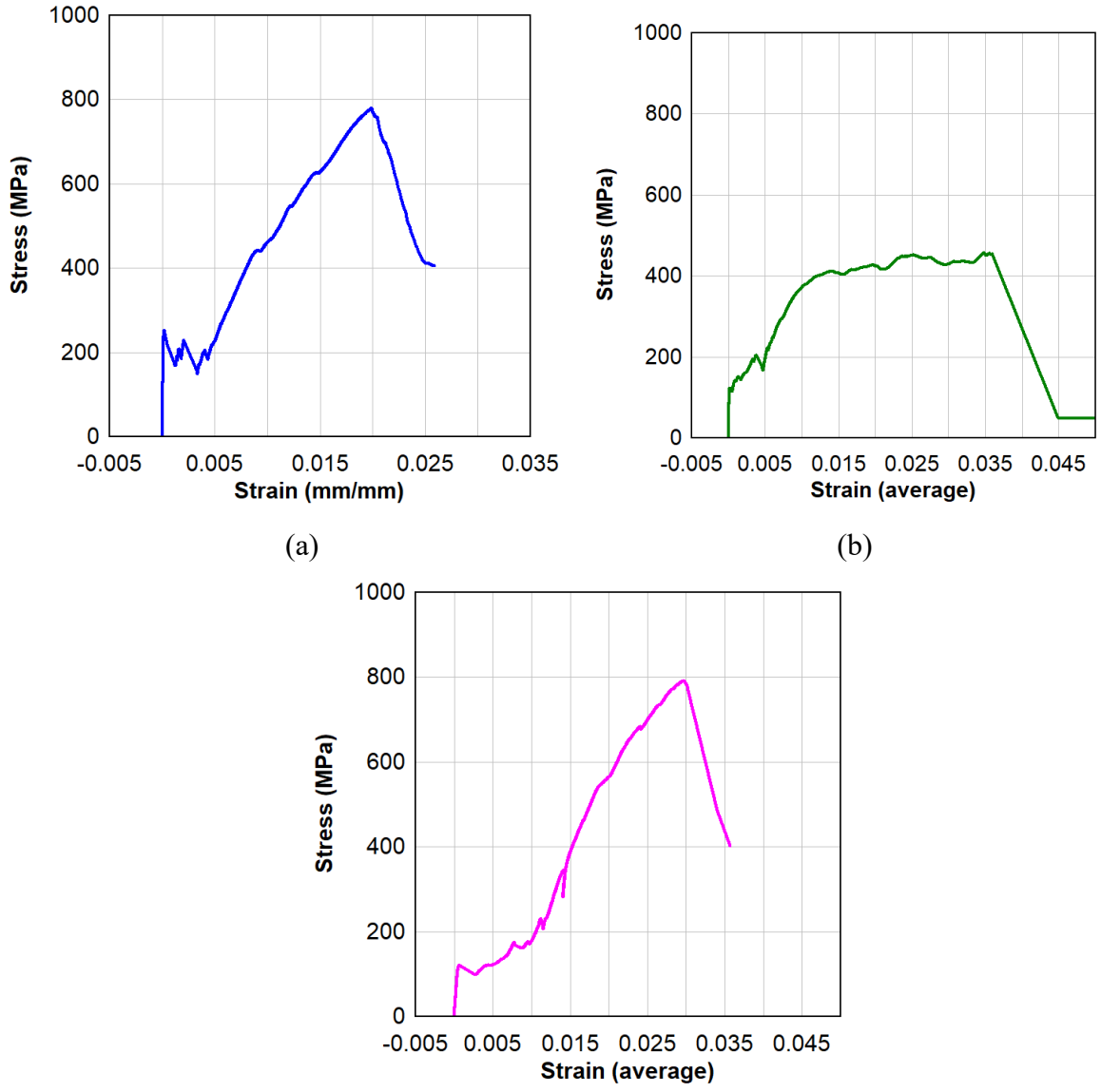

Figure 3-21. Typical Stress-strain curves from FRCM coupon direct tensile tests: (a) 1 layer, (b) 2 layers, (c) 2-layer-modified coupon

Figure 3-22 presents samples failure modes for the tested FRCM coupons. As discussed before, the failure mode for the 1-FRCM-Layer coupons, was fiber slippage and is shown in Figure 3-22 (a). On the other hand, the results from the 2-FRCM-Layer coupons were characterized by premature failure at the ends, with low tensile capacities and fiber debonding as shown in Figure 3-22 (b). In general, the 1-FRCM-Layer coupons presented one wide critical crack, and few minor cracks (2 to 4 cracks): Figure 3-22 (a). On the contrary, the 2-FRCM-Layer coupons did not develop any wide crack, instead only hairline cracks formed: Figure 3-22 (b). This confirms the premature failure where the fiber strands did not fully activate during the tests; thus, the ultimate

tensile strength of the fibers was not reached and the failure mechanism was due to a weak bond between the carbon fibers and the cementitious matrix at the specimen ends. The result may have occurred due to gripping length which could not be increased due to the limitations in the testing machine. It is suggested to reduce the coupon width and increase this bonded length for future tests. It is noted that the 1-FRCM-Layer coupons had mostly 4 carbon-fiber strands, with a few having three and a half strands. On the contrary, the 2-FRCM-Layer coupons had 10 carbon-fiber strands, while the modified 2-FRCM-Layer coupon (2-9) had only 6 carbon-fiber strands. The failure mode of the modified 2-FRCM-Layer coupon (2-9) was discussed above and it is shown in Figure 3-23 (b).

(a) (b)

Figure 3-22. Failure modes of tested coupons with fiber slippage: (a) 1 layer, and fiber debonding: (b) 2 layers

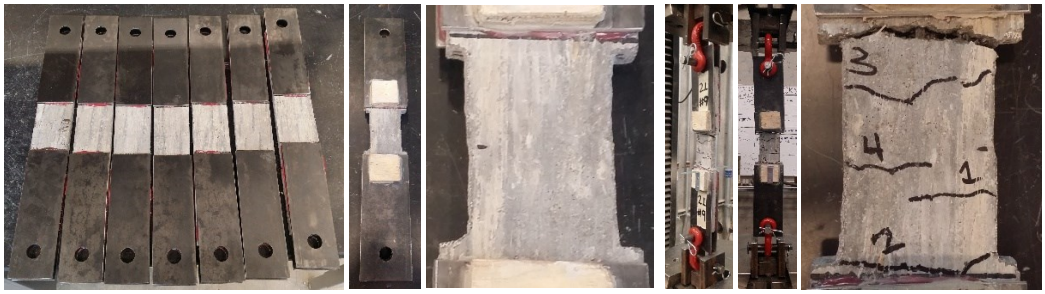

(a) (b)

Figure 3-23. Modification on 2-FRCM-Layer coupon, original and modified respectively (a), failure mode after tested: fiber slippage (b)

An additional 9 FRCM coupons with three layers of carbon grids were prepared for testing, as well. Their average dimensions were 420 mm long, 99 mm wide, and 22.8 mm thick. Unfortunately, they had the three layers of carbon grid placed wrongly in the transverse direction, consequently after cutting the coupons it was impossible to correct this error. This was realized during testing (and visible at failure) since the coupons had very small resistance since the capacity was only

provided by the cementitious matrix. Therefore, testing was discontinued after the first specimen was tested and not useful data was provided from the three-layer-coupons.

3.4.2.3.Mini beams strengthened with FRCM composites

Eight small masonry beams were prepared to be tested under two-point bending load following ASTM C1390. Each specimen was made-up of 4 rows of CMU blocks with dimesions of 90 mm x 390 mm x 790 mm. Three specimens were prepared as controls with no retrofit, and five specimens were retroffited with FRCM on one face, on the tension side with one, two and three layers of carbon fabrics. Two minibeams with concrete cast inside the hollow blocks and retrofitted with two and three layers of FRCM were also prepared for testing. For the joints, Type S mortar was used with a thickness of 10 mm. The FRCM composite was applied using the same technique used for the walls. Unfortunately this specimens could not be tested due to the closure of the university laboratory as a response to the COVID-19 situation. Nonetheless, the primary objective of this test was to establish the impact of the number of retrofit layers and influence of SCC infill on failure mode response.

(a) (b)

Figure 3-24. Specimen preparation: (a) Construction, (b) Installation of FRCM composite

CHAPTER 4. EXPERIMENTAL RESULTS

4.1. RESULTS SUMMARY

This chapter presents the experimental results in detail for walls RCL-NC-1, RCL-YC-2 and RCL-YC-3. The test results including the Shock Tube parameters, shock wave properties and specimen response are summarized in Table 4-1. Walls RCL-NC-1, RCL-YC-2 and RCL-YC-3 were subjected to 8, 8 and 9 shots of blast loading, respectively. All the shots are being numbered in sequence to meet the blast ID used in Table 3-2 of Chapter 3. Some terms reported in the table, will be explained below:

- ***Shock Tube parameters***: P_d represents the driver pressure in KPa; L_d represents the driver length which started at 6 ft (1829 mm), and then was expanded to 11 ft (3353 mm) and 13 ft (3962 mm) to produce stronger impulses when needed, accordingly to the stage reached during testing.
- ***Shock wave parameters:*** P_r represents the maximum reflected pressure in KPa acting on the wall during the test, which was gathered from the pressure sensor at the bottom of the shock tube (the bottom pressure sensor registered bigger peak values than the side pressure sensor, the Appendix at the end shows the reflected pressure measured by the side and bottom pressure sensors); I_r represents the positive impulse in kPa-ms which was calculated as the area under curve of the reflected pressure-time history function up to the end of the positive phase; t_d represents the time duration of positive phase in milliseconds.
- ***Specimen response:*** The maximum and residual displacements of the wall at the mid-height, are labeled as d_{max} and d_{res}, respectively. The accumulation of displacements from previous shots it is reported as the cumulative residual displacement ($\sum d_{res}$). The time at the maximum displacement is reported as t_{dmax}. For all three walls, RCL-NC-1, RCL-YC-2 and RCL-YC-3, the displacements registered at the top and bottom were very closed to zero, therefore is concluded that the supports used on the walls worked adequately as pin supports, allowing only for rotation. Consequently, top and bottom displacements will not be reported, only mid-height displacements.

Table 4-1. Summary of testing

Wall ID	Shot	Blast ID	P_d (kPa)	L_d (mm)	P_r (kPa)	I_r (kPa-ms)	t_d (ms)	d_{max} (mm)	d_{res} (mm)	$\sum d_{res}$ (mm)	t_{dmax} (ms)
RCL-NC-1	1st	#2	110.3	1829	23.9	160.9	15.2	6.1	0.4	0.4	18.2
	2nd	#3	165.5	1829	30.8	243.5	15.2	11.3	1.3	1.7	21.8
	3rd	#4	206.8	1829	45.0	297.0	15.7	17.4	2.6	4.3	21.1
	4th	#5	248.2	1829	48.1	317.6	16.7	19.2	0.7	5.0	20.9
	5th	#6	289.6	1829	53.7	383.8	16.3	24.7	2.9	7.9	20.6
	6th	#9	413.7	1829	66.8	512.6	18.4	32.7	4.6	12.5	24.8
	7th	#10	551.6	1829	95.7	665.4	20.4	48.5	6.6	19.1	36.3
	8th	#11	689.5	1829	107.3	762.1	20.6	251.0	failure	failure	53.0
RCL-YC-2	1st	#2	110.3	1829	24.2	170.1	15.1	1.4	0.0	0.0	15.0
	2nd	#5	248.2	1829	45.9	291.7	16.5	4.5	0.9	0.9	17.1
	3rd	#6	289.6	1829	52.3	384.3	16.5	8.8	1.4	2.3	19.4
	4th	#9	413.7	1829	71.0	529.6	18.0	14.9	1.7	4.0	20.9
	5th	#10	551.6	1829	92.4	660.5	21.7	22.8	3.5	7.5	22.0
	6th	#11	689.5	1829	116.6	828.7	21.6	29.8	3.6	11.1	22.7
	7th	#12	551.6	3353	77.8	1432.4	34.5	40.7	5.7	16.8	29.1
	8th	#13	689.5	3353	89.1	1709.1	37.6	284.3	failure	failure	71.5
RCL-YC-3	1st	#2	110.3	1829	28.4	203.4	15.0	0.9	0.0	0.0	15.0
	2nd	#5	248.2	1829	47.5	360.9	16.1	3.1	0.7	0.7	17.1
	3rd	#6	289.6	1829	51.3	378.7	18.2	5.6	0.9	1.6	19.3
	4th	#9	413.7	1829	68.1	519.7	18.9	10.4	2.5	4.1	18.8
	5th	#10	551.6	1829	85.0	672.1	21.6	13.7	2.1	6.2	18.3
	6th	#11	689.5	1829	103.6	828.3	22.6	21.4	4.5	10.7	20.8
	7th	#12	551.6	3353	78.7	1103.8	35.0	27.9	7.3	18.0	25.9
	8th	#13	689.5	3353	102.3	1816.9	36.1	36.5	5.9	23.9	27.1
	9th	#15	689.5	3962	111.8	2081.4	43.7	79.0	12.0	35.9	74.0

4.2. RCL-NC-1

RCL-NC-1 was tested as a CMU load-bearing wall, strengthened on its tension face with 1 layer of FRCM composites. The average thickness for the 1-FRCM layer applied was, 25.4 mm (1 in) (1 layer of carbon grid plus the cementitious matrix). Additionally, an axial load of 122 KN, corresponding to 4 % of the wall nominal axial capacity, was applied to the wall during the tests. Eight shots of blast loading (simulated with the shock tube) were applied onto the wall. Table 4-2 shows the test results and some brief details for important events for each shot. The displacements were measured with the use of one LVDT placed at the mid-height/center of the wall up to the penultimate shot that corresponds to shot 7, then the high-speed camera was used for tracking the displacements. Displacements at the top and bottom of the wall were measured with the high-speed camera, getting values very close to zero due to the pin supports provided. Therefore, these last values are considered as zero. The displacement profiles of the wall at the time of maximum deformation for each shot are shown in Figure 4-1. In order to get these profiles, the high-speed camera was used by selecting and tracking several points with the use of camera software. Additionally, for each shot, video stills are shown in Figure 4-1 using the same scale as the displacement profile plots, to allow for comparison. Furthermore, the pressure and impulse time histories are shown in Figure 4-5, as well as, the pressure and displacement time histories for each shot. The impulse was computed as the area under the reflected-pressure-curve function, Pr(t), for the first positive phase duration. As the impulse increases, by increasing the driver pressure, the duration of the positive phase of the blast (t_d) increases, meaning a load wave striking the wall longer.

Table 4-2. Summary of testing results with major events (RCL-NC-1)

Wall ID	Shot	Blast ID	P_d (kPa)	L_d (mm)	P_r (kPa)	I_r (kPa-ms)	t_d (ms)	d_{max} (mm)	d_{res} (mm)	$\sum d_{res}$ (mm)	t_{dmax} (ms)
RCL-NC-1	1st	#2	110.3	1829	23.9	181.6	15.2	6.1	0.0	0.0	18.2
			No cracks, just one during set-up (local shear crack in only one brick at top-right-side (3mm), because the wall was not straight in the right corner, force was applied when setting up the top support and small crack appeared): Figure 4-3 (a)								
	2nd	#3	165.5	1829	30.8	233.6	15.2	11.3	0.4	0.4	21.8
			No damage appeared								
	3rd	#4	206.8	1829	45.0	353.9	15.7	17.4	1.8	2.2	21.1
			No damage appeared, just crack since set-up wider (5mm)								
	4th	#5	248.2	1829	48.1	401.6	16.7	19.2	4.5	6.7	20.9
			Flexural cracks appeared at midspan: Figure 4-2 (a) No shear cracks, just crack since set-up wider 6mm								
	5th	#6	289.6	1829	53.7	438.7	16.3	24.7	5.2	11.9	20.6
			More Flexural cracks appeared at midspan: Figure 4-2 (b). No shear cracks, just crack since set-up wider 7mm.								
	6th	#9	413.7	1829	66.8	613.9	18.4	32.7	8.3	20.2	24.8
			More Flexural cracks appeared at midspan. No shear cracks, just local crack since set-up 7mm. One vertical crack appeared at the top: Figure 4-2 (c).								
	7th	#10	551.6	1829	95.7	977.1	20.4	48.5	13.1	33.3	36.3
			More Flexural cracks appeared at midspan: Figure 4-2 (d). No shear cracks, just local crack since set-up wider with 7mm: Figure 4-3 (b). Cover cementitious matrix spalling locally at edge: Figure 4-3 (c)								
	8th	#11	689.5	1829	107.3	1103.6	20.6	251.0	failure	failure	53.0
			Wall broke at midspan into 2 halves: Figure 4-2 (e). Furthest projectile reached 20 ft, with 20x20 cm (half brick): Figure 4-3 (d).								

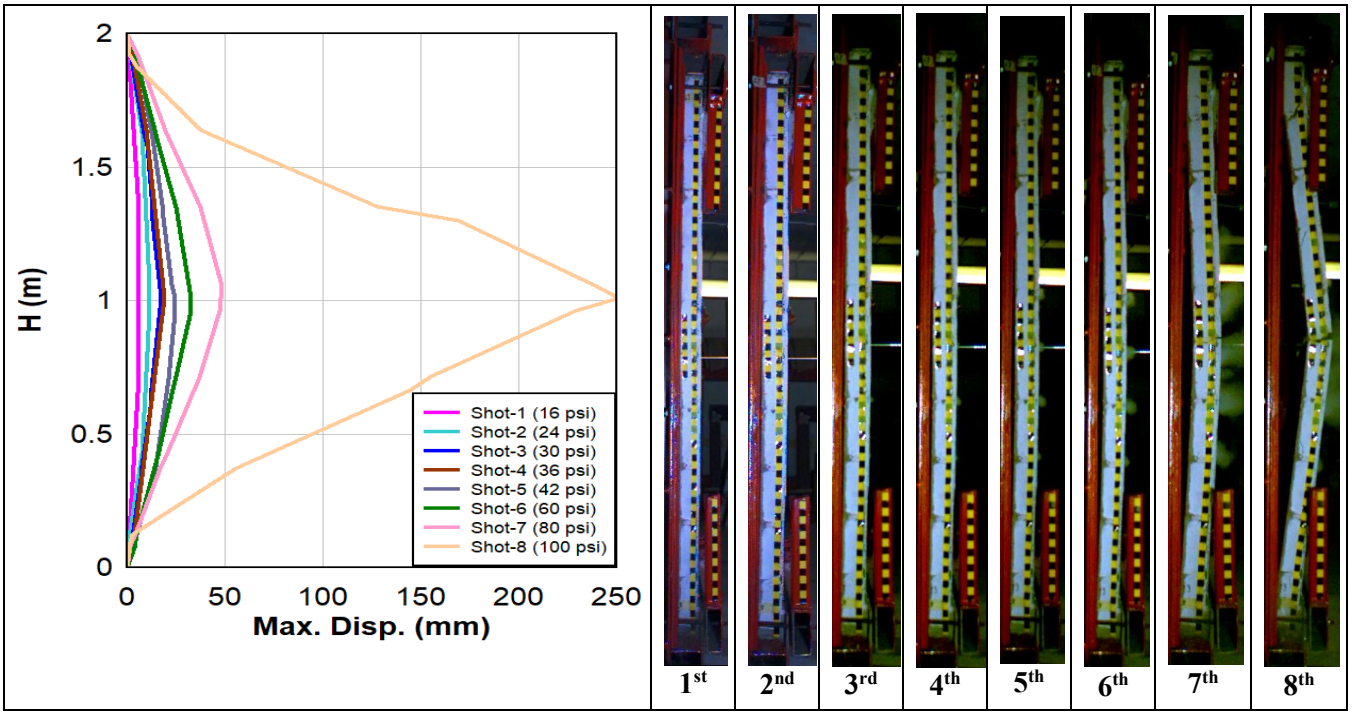

Figure 4-1. Displacement profile with video stills for each shot at maximum displacement (RCL-NC-1)

1st shot (Blast ID #2)

A driver pressure of 110.3 kPa (16 psi) with a length of 1829 mm (6 ft) was used for the first shot on wall RCL-NC-1. The peak reflected pressure and reflected impulse were 23.9 kPa and 181.6 kPa-ms, respectively. The positive phase duration was 15.2 ms. The maximum mid-height displacement was 6.1 mm. The maximum deflection occurred at a time of 18.2 ms. The pressure-impulse time history and the pressure-displacement time history are shown in Figure 4-5 (a).

The first shot resulted in a small displacement at the mid-height of the wall without any residual deformations or damage and therefore the wall remained in the elastic range. Also, no visible cracking or damage was observed.

2nd shot (Blast ID #3)

The second shot used a driver pressure of 165.5 kPa (24 psi), with the same driver length of 1829 mm. The peak reflected pressure and reflected impulse were 30.8 kPa and 233.6 kPa-ms, respectively. The positive phase duration was 15.2 ms. The maximum mid-height displacement was 11.3 mm. Maximum deflection occurred at a time of 21.8 ms and the residual displacement was 0.4 mm at the mid-height of the wall. The pressure -impulse time history and the pressure-displacement time history are shown in Figure 4-5 (b). No visible damage was observed.

3rd shot (Blast ID #4)

The third shot used a driver pressure of 206.8kPa (30 psi), with the same driver length of 1829 mm. The peak reflected pressure and reflected impulse were 45.0 kPa and 353.9 kPa-ms, respectively. The positive phase duration was 15.7 ms. The maximum mid-height displacement was 17.4 mm. Maximum deflection occurred at a time of 21.1 ms and the residual displacement was 1.8 mm at the mid-height of the wall. The pressure -impulse time history and the pressure-displacement time history are shown in Figure 4-5 (c). No visible damage was observed and no flexural cracks appeared on the wall, up to the third shot.

4th shot (Blast ID #5)

The fourth shot used a driver pressure of 248.2 kPa (36 psi), with the same driver length of 1829 mm. The peak reflected pressure and reflected impulse were 48.1 kPa and 401.6 kPa-ms, respectively. The positive phase duration was 16.7 ms. The maximum mid-height displacement was 19.2 mm. Maximum deflection occurred at a time of 20.9 ms and the residual displacement was 4.5 mm at the mid-height of the wall. The pressure -impulse time history and the pressure-displacement time history are shown in Figure 4-5 (d). Not any shear cracks have appeared, contrary to horizontal flexural hairline cracks that were visible on the tension side (front face) of the wall. The space among them was about 18 to 22 cm apart from each other, mainly at the same

locations as the CMU mortar joints. They were located at the mid-height of the wall, within the middle third of the wall. The crack progression on the tension side (the front face) of the wall from the fourth shot (Figure 4-2 (a)) to the last shot (shot eight) is shown in Figure 4-2.

5th shot (Blast ID #6)

The fifth shot used a driver pressure of 289.6 kPa (42 psi), with the same driver length of 1829 mm. The peak reflected pressure and reflected impulse were 53.7 kPa and 438.7 kPa-ms, respectively. The positive phase duration was 16.3 ms. The maximum mid-height displacement was 24.7 mm. Maximum deflection occurred at a time of 20.6ms and the residual displacement was 5.2 mm at the mid-height of the wall. The pressure -impulse time history and the pressure-displacement time history are shown in Figure 4-5 (e). No shear cracks have appeared but horizontal flexural hairline cracks were visible on the tension side (front face) of the wall. The space among them was about 18 to 22 cm apart from each other, mainly at the same locations as the CMU mortar joints. They were located at the mid-height of the wall, within the middle third of the wall. Also, the existing flexural cracks were not widened much, they were about 0.1 mm wide, Figure 4-2 (b).

6th shot (Blast ID #9)

The sixth shot used a driver pressure of 413.7 kPa (60 psi), with the same driver length of 1829 mm. The peak reflected pressure and reflected impulse were 66.8 kPa and 613.9 kPa-ms, respectively. The positive phase duration was 18.4 ms. The maximum mid-height displacement was 32.7 mm. Maximum deflection occurred at a time of 24.8 ms and the residual displacement was 8.3 mm at the mid-height of the wall. The pressure -impulse time history and the pressure-displacement time history are shown in Figure 4-5 (f). No shear cracks have appeared but horizontal flexural hairline cracks were visible on the tension side (front face) of the wall. The space among them was about 18 to 22 cm apart from each other, mainly at the same locations as the CMU mortar joints. Also, one vertical crack appeared at the top center of the wall: Figure 4-2 (c).

7th shot (Blast ID #10)

The seventh shot used a driver pressure of 551.6kPa (80 psi), with the same driver length of 1829 mm. The peak reflected pressure and reflected impulse were 95.7 kPa and 977.1 kPa-ms, respectively. The positive phase duration was 20.4 ms. The maximum mid-height displacement was 48.5 mm. Maximum deflection occurred at a time of 36.3 ms and the residual displacement was 13.1mm at the mid-height of the wall. The pressure -impulse time history and the pressure-displacement time history are shown in Figure 4-5 (g). No shear cracks have appeared but more horizontal flexural cracks appeared on the tension side (front face) of the wall, with a maximum

crack width of around 0.2 mm. The space among them was about 18 to 22 cm apart from each other, mainly at the same locations as the CMU mortar joints: Figure 4-2 (d). Also, the cementitious matrix started spalling locally at edge: Figure 4-3 (c)

8th shot (Blast ID #11)

The eighth shot used a driver pressure of 689.5 kPa (100 psi), with the same driver length of 1829 mm. The peak reflected pressure and reflected impulse were 107.3 kPa and 1103.6 kPa-ms, respectively. The positive phase duration was 20.6 ms. The maximum mid-height displacement at failure was 251.0 mm. Maximum deflection occurred at failure at time of 53.0 ms when the wall broke into two pieces: Figure 4-2 (e). The pressure -impulse time history and the pressure-displacement time history are shown in Figure 4-5 (h). At this shot the wall failed, it broke into two pieces at the mid-height and it fell down, Figure 4-2 (e). Additionally, Figure 4-4 shows video stills of the failure mechanism of wall RCL-NC-1 for the eighth shot. The wall developed a big crack at the mid-height which opened widely during the blast shot, causing the rupture of the carbon-fiber mesh at the main crack. Consequently, the wall broke into 2 pieces (as mentioned above) and fell down. It should be noted that there was no debonding seen between the substrate and the wall.

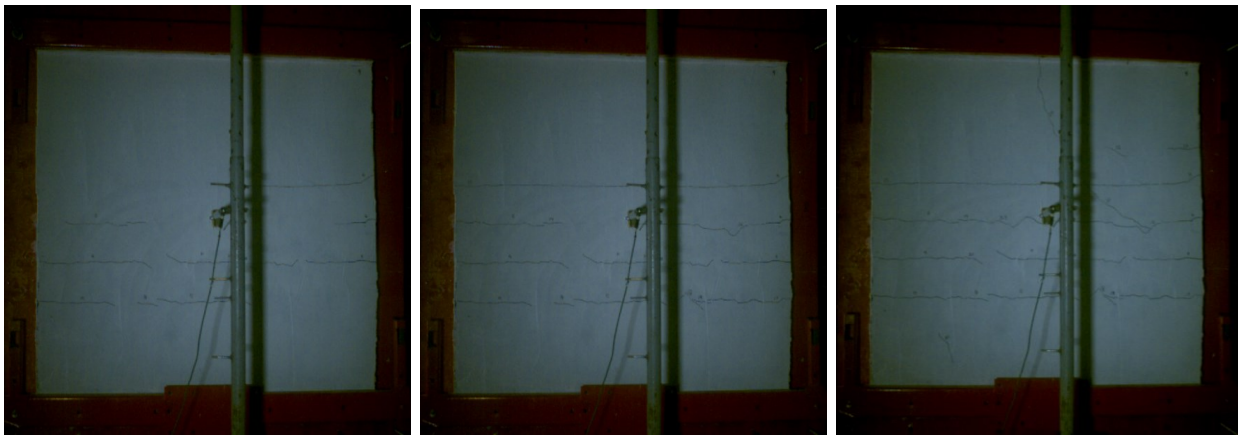

(a) 4th shot (b) 5th shot (c) 6th shot

(d) 7th shot (e) 8th shot

Figure 4-2. Damage Progression (from 4th to 8th shots, no flexural cracks until 4rd shot)

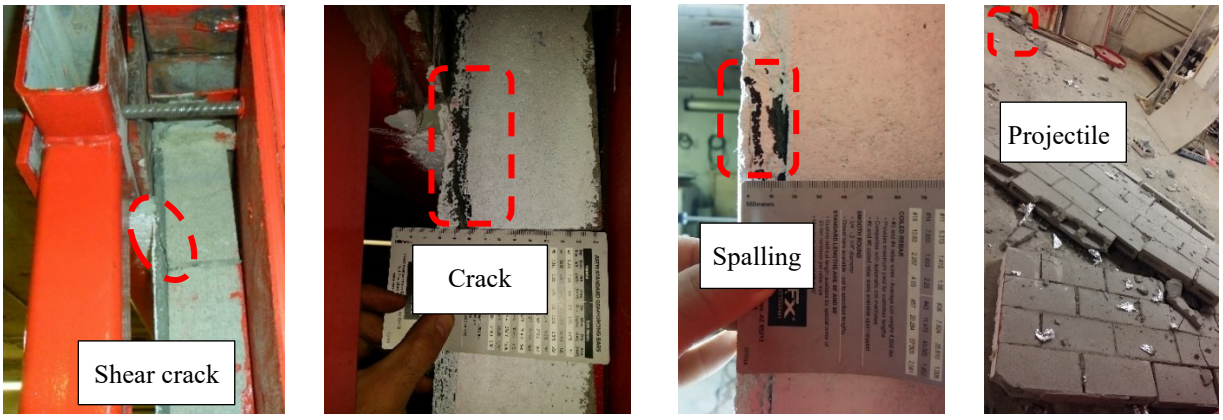

(a) During set-up (b)7th shot "set-up Crack" (c) 7th Matrix spalling (d) Furthest projectile

Figure 4-3. Major shear cracks and other details (RCL-NC-1)

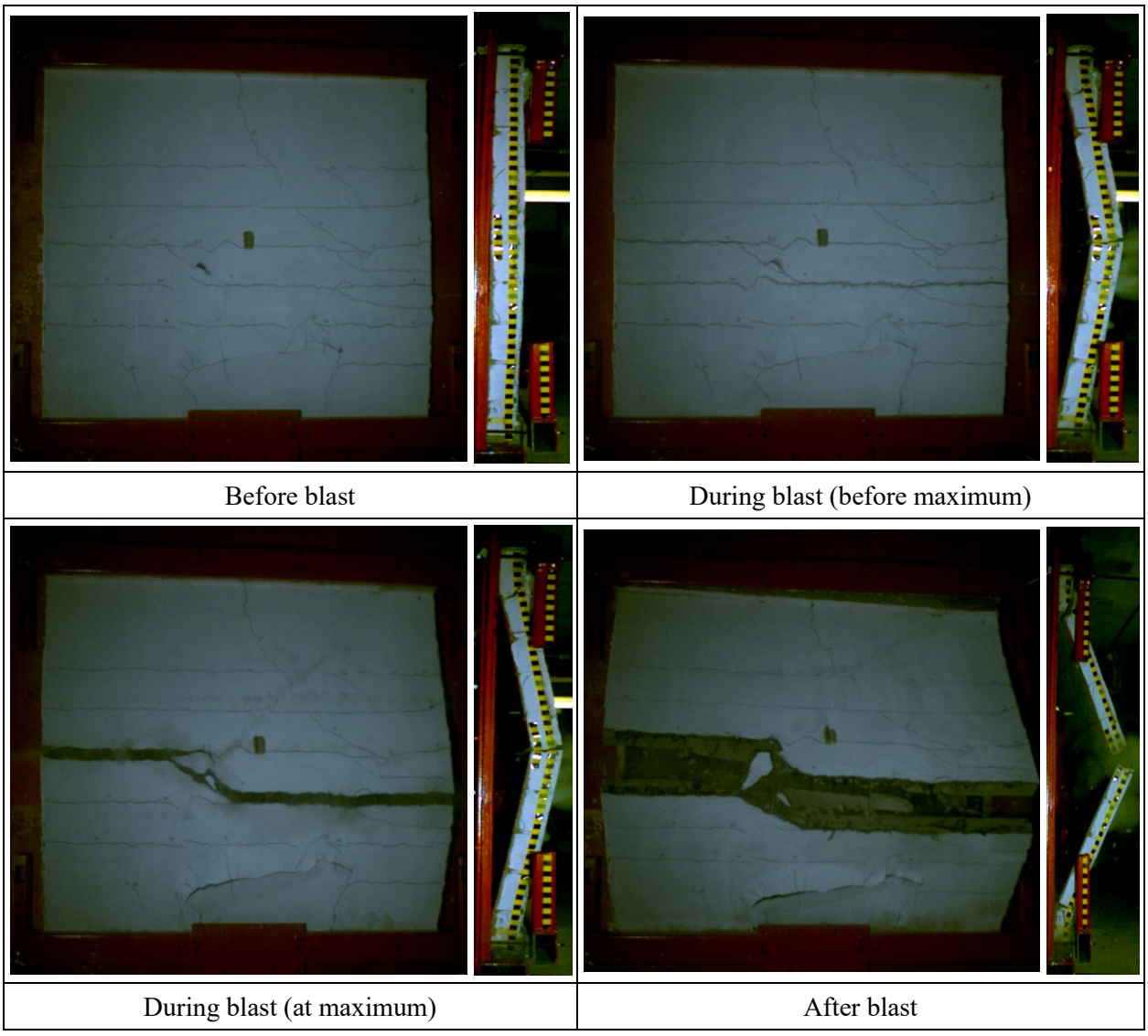

Before blast	During blast (before maximum)
During blast (at maximum)	After blast

Figure 4-4. Video stills of failure mechanisms of RCL-NC-1 at the 8th shot

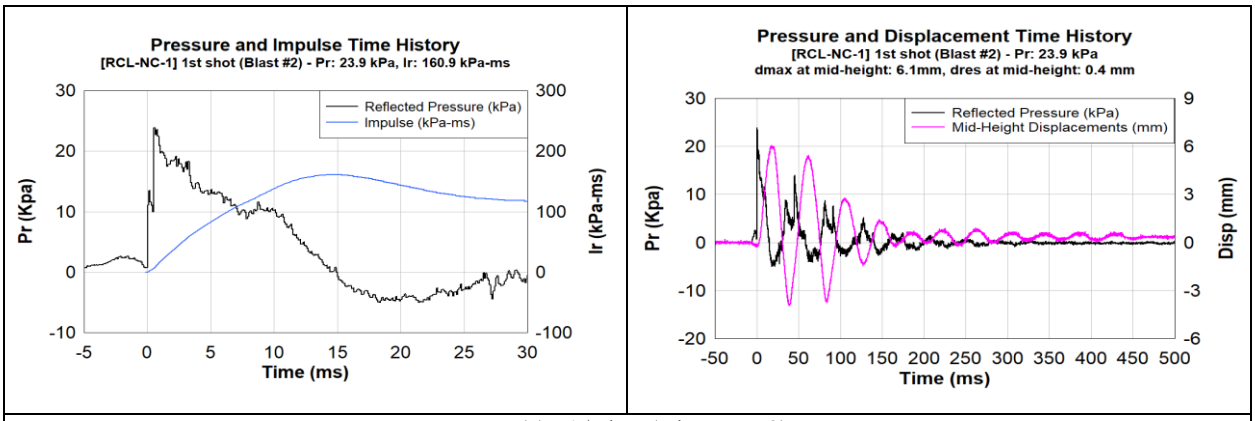

(a) 1st shot (Blast ID #2)

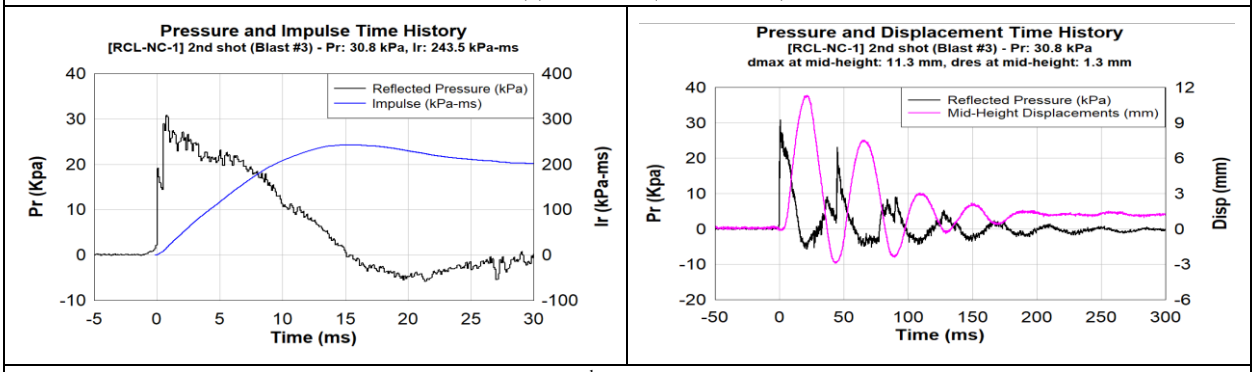

(b) 2nd shot (Blast ID #3)

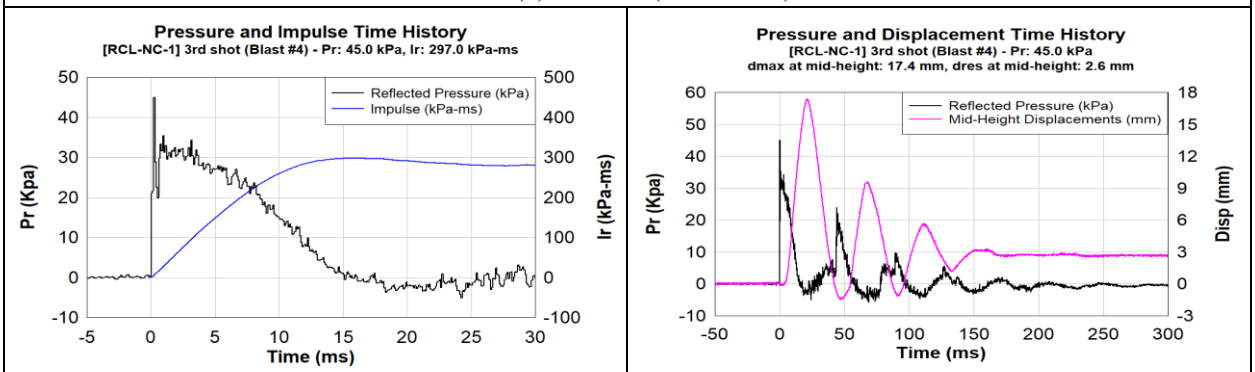

(c) 3rd shot (Blast ID #4)

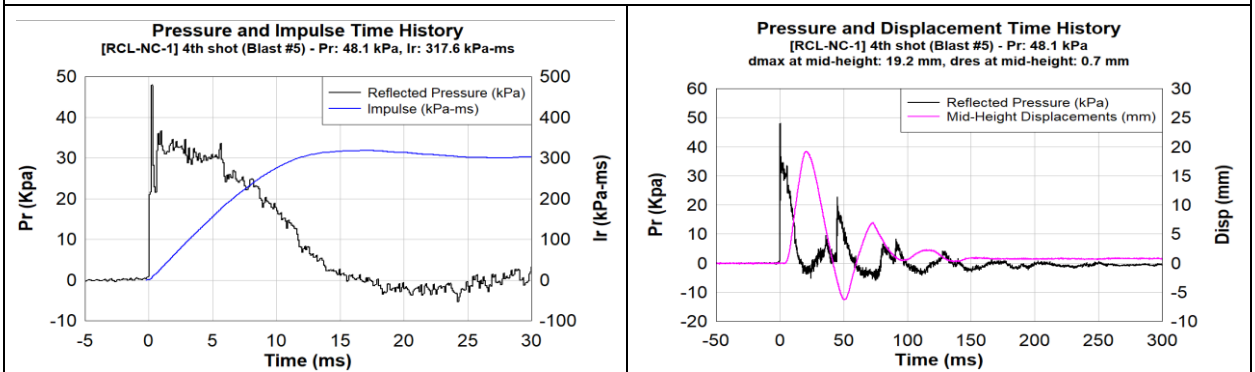

(d) 4th shot (Blast ID #5)

Figure 4-5. Pressure, Impulse, and Displacement Time history of RCL-NC-1

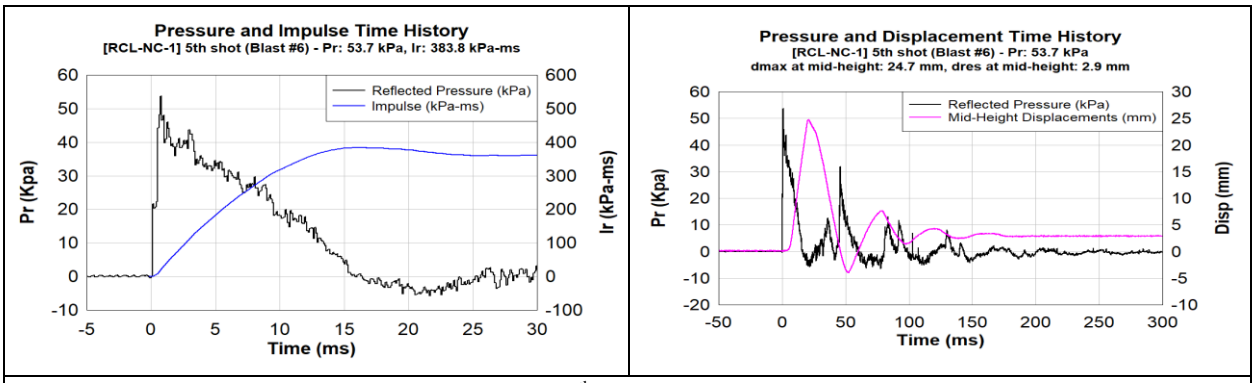

(e) 5th shot (Blast ID #6)

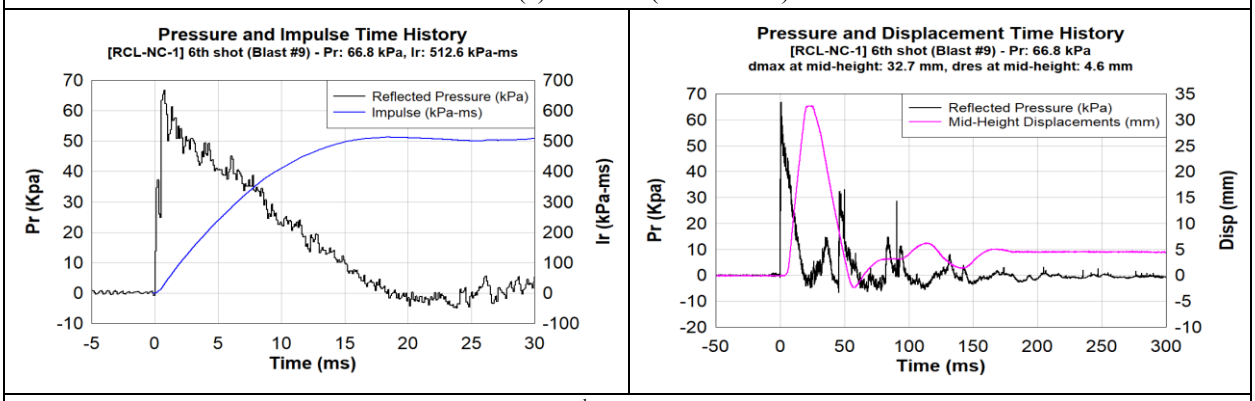

(f) 6th shot (Blast ID #9)

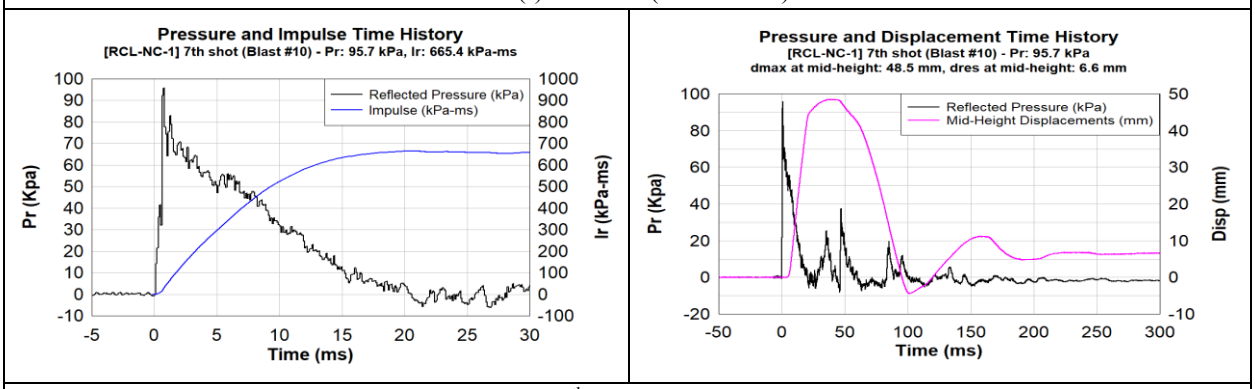

(g) 7th shot (Blast ID #10)

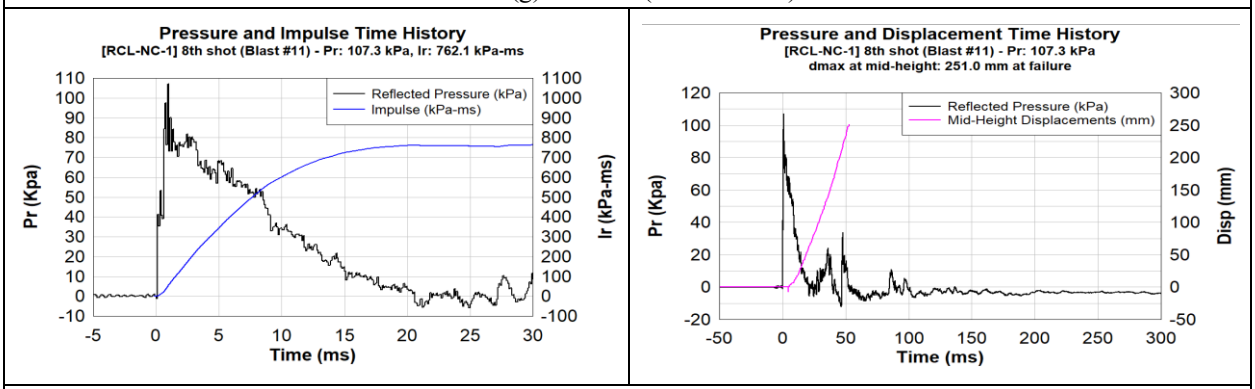

(h) 8th shot (Blast ID #11)

Figure 4-5. Pressure, Impulse, and Displacement Time history of RCL-NC-1, continuation.

4.3.RCL-YC-2

RCL-YC-2 was tested as a CMU load-bearing wall, strengthened on its tension face with 2 layers of FRCM composites. The average thickness for the 2-FRCM layers applied was, 38.1 mm (1.5 in, 2 layers of carbon grid plus the cementitious matrix). Additionally, an axial load of 122 KN, corresponding to 4 % of the wall nominal axial capacity, was applied to the wall during the tests. Eight shots of blast loading (simulated with the shock tube) were applied onto the wall. Table 4-3 shows the test results and some brief details for important events for each shot. The displacements were measured with the use of one LVDT placed at the mid-height/center of the wall up to the shot 6 because for shot 7, the LVDT had one cable disconnected and data collection was not possible. Then the high-speed camera was used for tracking the displacements. Displacements at the top and bottom of the wall were measured with the high-speed camera, getting values very close to zero due to the pin supports provided. Therefore, these last values are considered as zero. The displacement profiles of the wall at the time of maximum deformation for each shot are shown in Figure 4-6. In order to get these profiles, the high-speed camera was used by selecting and tracking several points with the use of camera software. Additionally, for each shot, video stills are shown in Figure 4-6 using the same scale as the displacement profile plots, to allow for comparison. Furthermore, the pressure and impulse time histories are shown in Figure 4-9, as well as, the pressure and displacement time histories for each shot. The impulse was computed as the area under the reflected-pressure-curve function, Pr(t), for the first positive phase duration. As the impulse increases, by increasing the driver pressure, the duration of the positive phase of the blast (t_d) increases, meaning a load wave striking the wall longer.

Table 4-3. Summary of testing results with main events (RCL-YC-2)

Wall ID	Shot	Blast ID	P_d (kPa)	L_d (mm)	P_r (kPa)	I_r (kPa-ms)	t_d (ms)	d_{max} (mm)	d_{res} (mm)	$\sum d_{res}$ (mm)	t_{dmax} (ms)
RCL-YC-2	1st	#2	110.3	1829	24.2	182.7	15.1	1.4	0.0	0.0	15.0
			No damage appeared								
	2nd	#5	248.2	1829	45.9	379.1	16.5	4.5	0.0	0.0	17.1
			One flexural crack at midspan: Figure 4-7 (a)								
	3rd	#6	289.6	1829	52.3	430.7	16.5	8.8	1.0	1.0	19.4
			3 flexural cracks in total at midspan. No shear cracks yet: Figure 4-7 (b)								
	4th	#9	413.7	1829	71.0	639.7	18.0	14.9	2.6	3.6	20.9
			3 flexural cracks in total at midspan. No shear cracks yet								
	5th	#10	551.6	1829	92.4	1001.6	21.7	22.8	4.3	7.9	22.0
			4 flexural cracks in total at midspan. No shear cracks yet. Top grout cracking only locally at the sides, but not shear: Figure 4-7 (c)								
	6th	#11	689.5	1829	116.6	1259.3	21.6	29.8	7.8	15.7	22.7
			Many flexural cracks, deeper to neutral axis. Two vertical cracks at top and bottom of wall at middle (from axial load problably): Figure 4-7 (d). Not cracks at supports, just grout cracking at top-sides of wall (locally)								
	7th	#12	551.6	3353	77.8	1340.1	34.5	40.7	5.7	21.3	29.1
			More flexural cracks at midspan (considerably) and deeper to neutral axis. Not shear cracks at supports. Additionally, 4 vertical cracks in total appeared at middle, 2 at top and 2 at bottom: Figure 4-7 (e)								
	8th	#13	689.5	3353	89.1	1675.1	37.6	284.3	failure	failure	71.5
			Wall broke into 3 pieces. By half at midspan and one of these halves broke perpendicularly at the center, into two halves: Figure 4-7 (f). Furthest projectile at 17ft, size 2x4in.								

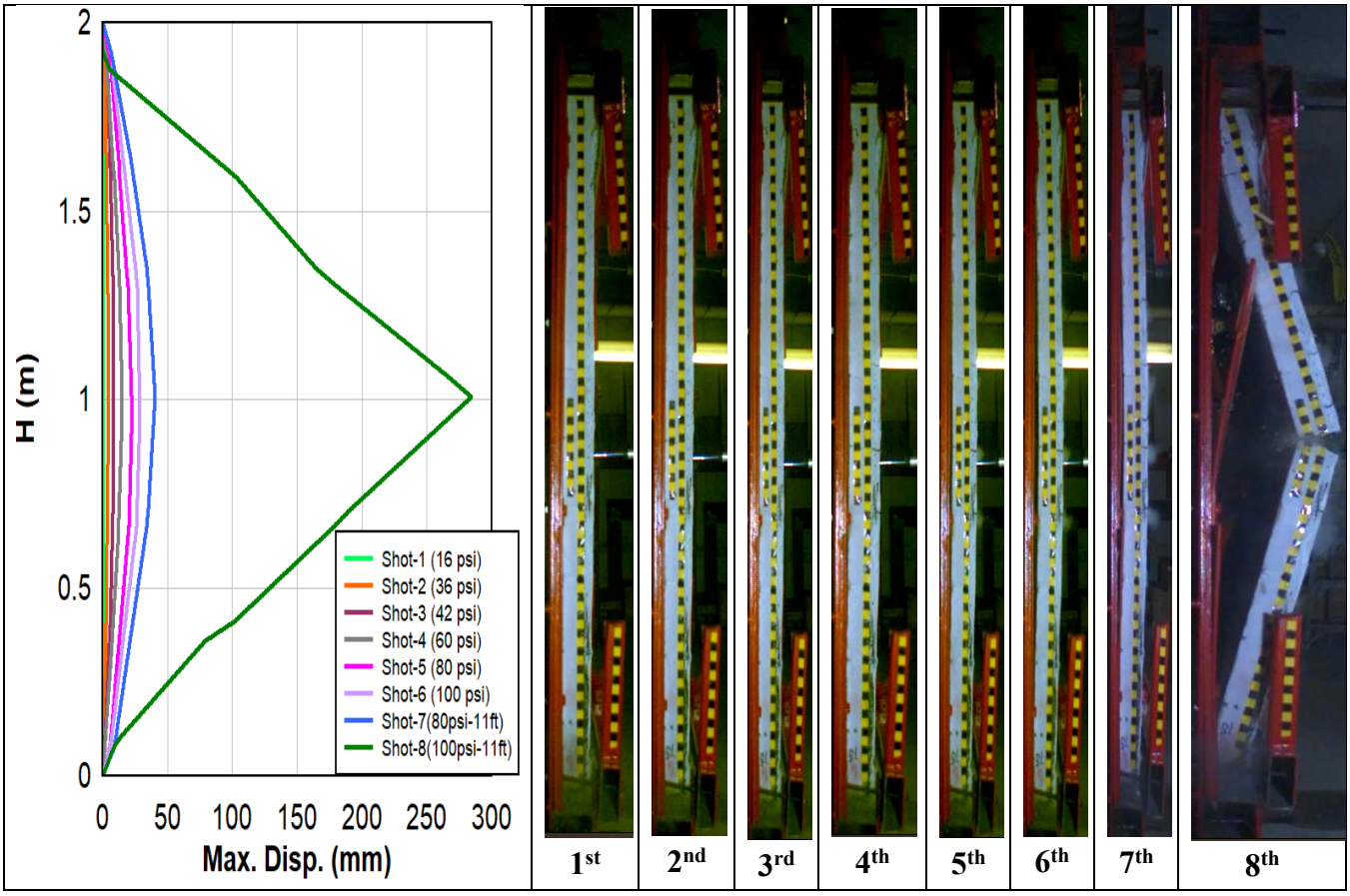

Figure 4-6. Displacement profile with video stills for each shot at maximum displacement (RCL-YC-2)

1st shot (Blast ID #2)

A driver pressure of 110.3 kPa (16 psi) with a length of 1829 mm (6 ft) was used for the first shot on wall RCL-YC-2. The peak reflected pressure and reflected impulse were 24.2 kPa and 182.7 kPa-ms, respectively. The positive phase duration was 15.1 ms. The maximum mid-height displacement was 1.4 mm. The maximum deflection occurred at a time of 15.0 ms. The pressure-impulse time history and the pressure-displacement time history are shown in Figure 4-9 (a).

The first shot resulted in a small displacement at the mid-height of the wall without any residual deformations or damage and therefore the wall remained in the elastic range. Also, no visible cracking or damage was observed.

2nd shot (Blast ID #5)

The second shot used a driver pressure of 248.2 kPa (36 psi), with the same driver length of 1829 mm. The peak reflected pressure and reflected impulse were 45.9 kPa and 379.1 kPa-ms, respectively. The positive phase duration was 16.5 ms. The maximum mid-height displacement

was 4.5 mm. Maximum deflection occurred at a time of 17.1ms. The pressure -impulse time history and the pressure-displacement time history are shown in Figure 4-9 (b).

This shot resulted in a small displacement at the mid-height of the wall without any residual deformations therefore the wall remained in the elastic range. Nonetheless, one flexural crack appeared at midspan: Figure 4-7 (a), but no visible shear cracks were observed.

3rd shot (Blast ID #6)

The third shot used a driver pressure of 289.6 kPa (42 psi), with the same driver length of 1829 mm. The peak reflected pressure and reflected impulse were 52.3 kPa and 430.7 kPa-ms, respectively. The positive phase duration was 16.5 ms. The maximum mid-height displacement was 8.8 mm. Maximum deflection occurred at a time of 19.4 ms and the residual displacement was 1.0 mm at the mid-height of the wall. The pressure -impulse time history and the pressure-displacement time history are shown in Figure 4-9 (c). Finally, 3 flexural cracks in total at midspan appeared but not any shear cracks: Figure 4-7 (b).

4th shot (Blast ID #9)

The fourth shot used a driver pressure of 413.7 kPa (60 psi), with the same driver length of 1829 mm. The peak reflected pressure and reflected impulse were 71.0 kPa and 639.7 kPa-ms, respectively. The positive phase duration was 18.0 ms. The maximum mid-height displacement was 14.9 mm. Maximum deflection occurred at a time of 20.9 ms and the residual displacement was 2.6 mm at the mid-height of the wall. The pressure -impulse time history and the pressure-displacement time history are shown in Figure 4-9 (d).

Lastly, there was not too much extra damage visible just the previous 3 flexural cracks in total at midspan wider, 0.1 wide mm approximately. No cracks appeared on the side of the wall and there is still not shear cracks seen: Figure 4-7 (b).

5th shot (Blast ID #10)

The fifth shot used a driver pressure of 551.6 kPa (80 psi), with the same driver length of 1829 mm. The peak reflected pressure and reflected impulse were 92.4 kPa and 1001.6 kPa-ms, respectively. The positive phase duration was 21.7 ms. The maximum mid-height displacement was 22.8 mm. Maximum deflection occurred at a time of 22.0 ms and the residual displacement was 4.3 mm at the mid-height of the wall. The pressure -impulse time history and the pressure-displacement time history are shown in Figure 4-9 (e).

No shear cracks have appeared but 4 horizontal flexural hairline cracks were visible on the tension side (front face) of the wall. The space among them was about 18 to 22 cm apart from each other, mainly at the same locations as the CMU mortar joints. They were located at the mid-height of the

wall, within the middle third of the wall. Also, the existing flexural cracks were not widened much, they were about 0.1 mm wide, Figure 4-7 (c). Lastly, the top grout was cracking a bit locally at the top corners for the compression and/or vibration of the wall.

6th shot (Blast ID #11)

The sixth shot used a driver pressure of 689.5 kPa (100 psi), with the same driver length of 1829 mm. The peak reflected pressure and reflected impulse were 116.6 kPa and 1259.3 kPa-ms, respectively. The positive phase duration was 21.6 ms. The maximum mid-height displacement was 29.8 mm. Maximum deflection occurred at a time of 22.7 ms and the residual displacement was 7.8 mm at the mid-height of the wall. The pressure -impulse time history and the pressure-displacement time history are shown in Figure 4-9 (f).

Many horizontal flexural hairline cracks were visible on the tension side (front face) of the wall. The space among them was about 18 to 22 cm apart from each other, mainly at the same locations as the CMU mortar joints. Additionally, two vertical cracks appeared at the top and bottom center of the wall (from axial load problably). Finally, no shear cracks were visible: Figure 4-7 (d).

7th shot (Blast ID #12)

The seventh shot used a driver pressure of 551.6 kPa (80 psi), with a longer driver length of 3353 mm. The peak reflected pressure and reflected impulse were 77.8 kPa and 1340.1 kPa-ms, respectively. The positive phase duration was 34.5 ms. The maximum mid-height displacement was 40.7 mm. Maximum deflection occurred at a time of 29.1 ms and the residual displacement was 5.7 mm at the mid-height of the wall. The pressure -impulse time history and the pressure-displacement time history are shown in Figure 4-9 (g). No shear cracks have appeared but more horizontal flexural cracks appeared on the tension side (front face) of the wall, with a maximum crack width of around 0.2 mm and depth to neutral axis of 10mm approximately. The space among them was about 18 to 22 cm apart from each other, mainly at the same locations as the CMU mortar joints. Lastly, 4 vertical cracks in total appeared in the middle, 2 at top and 2 at bottom: Figure 4-7 (e)

8th shot (Blast ID #13)

The eighth shot used a driver pressure of 689.5 kPa (100 psi), with a longer driver length of 3353 mm. The peak reflected pressure and reflected impulse were 89.1 kPa and 1675.1 kPa-ms, respectively. The positive phase duration was 37.6 ms. The maximum mid-height displacement at failure was 284.3 mm. Maximum deflection occurred at failure at time of 71.5 ms when the wall broke into two pieces. It will break later into 3 pieces, by half at midspan and one of these halves broke perpendicularly at the center, into two halves: Figure 4-7 (f). Furthermore, the furthest projectile with dimensions of 2x4in landed at 17ft from the original wall.

The pressure -impulse time history and the pressure-displacement time history are shown in Figure 4-9 (h). Additionally, Figure 4-8 shows video stills of the failure mechanism of wall RCL-YC-2 for the eighth shot. The wall developed a big crack at the mid-height which opened widely during the blast shot, causing the rupture of the carbon-fiber mesh at the main crack. Consequently, the wall broke into 3 pieces (as mentioned above) and fell down. It should be noted that there was no debonding seen between the substrate and the wall.

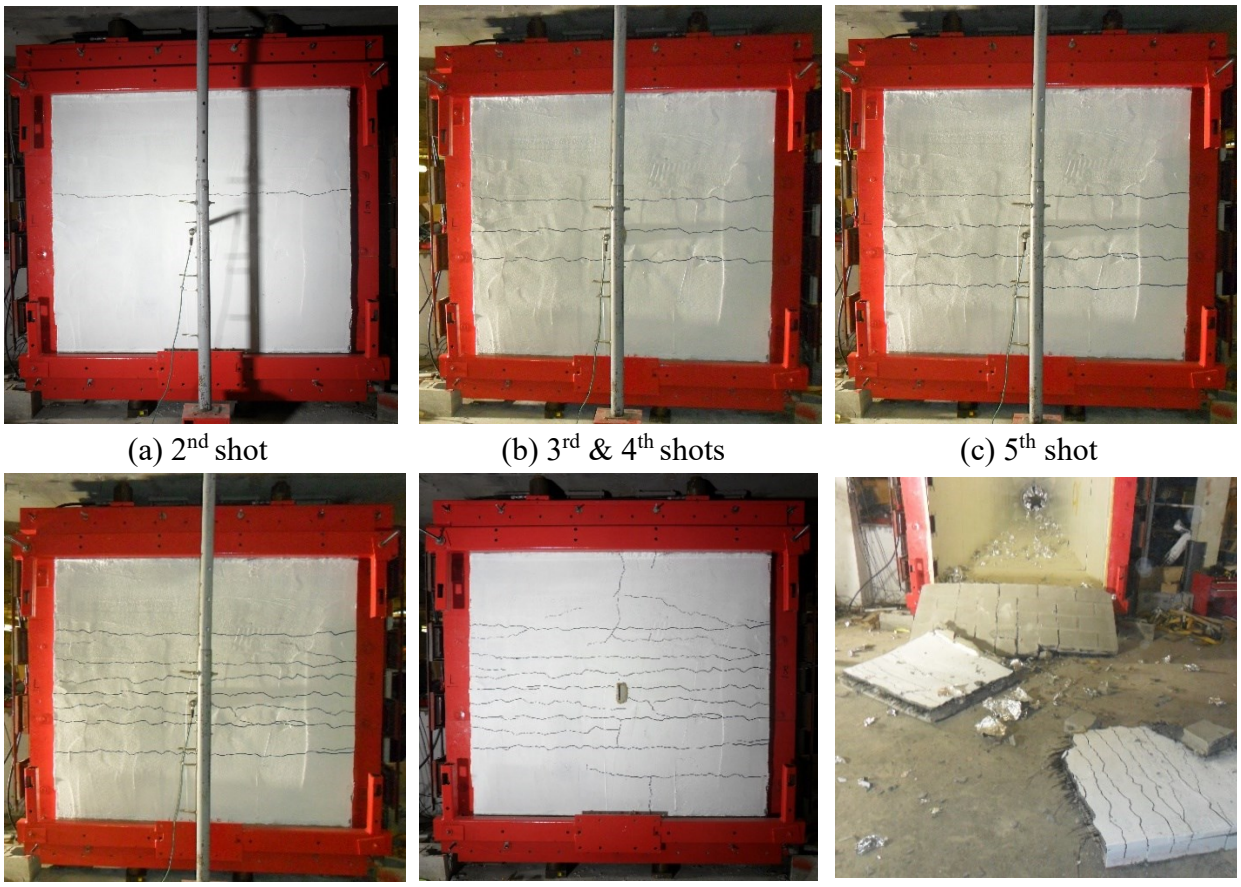

(a) 2nd shot (b) 3rd & 4th shots (c) 5th shot

(d) 6th shot (front) (e) 7th shot (side) (f) 8th shot (Demolished)

Figure 4-7. Damage Progression (from 2nd to 6th shots, no flexural cracks until 2nd shot)

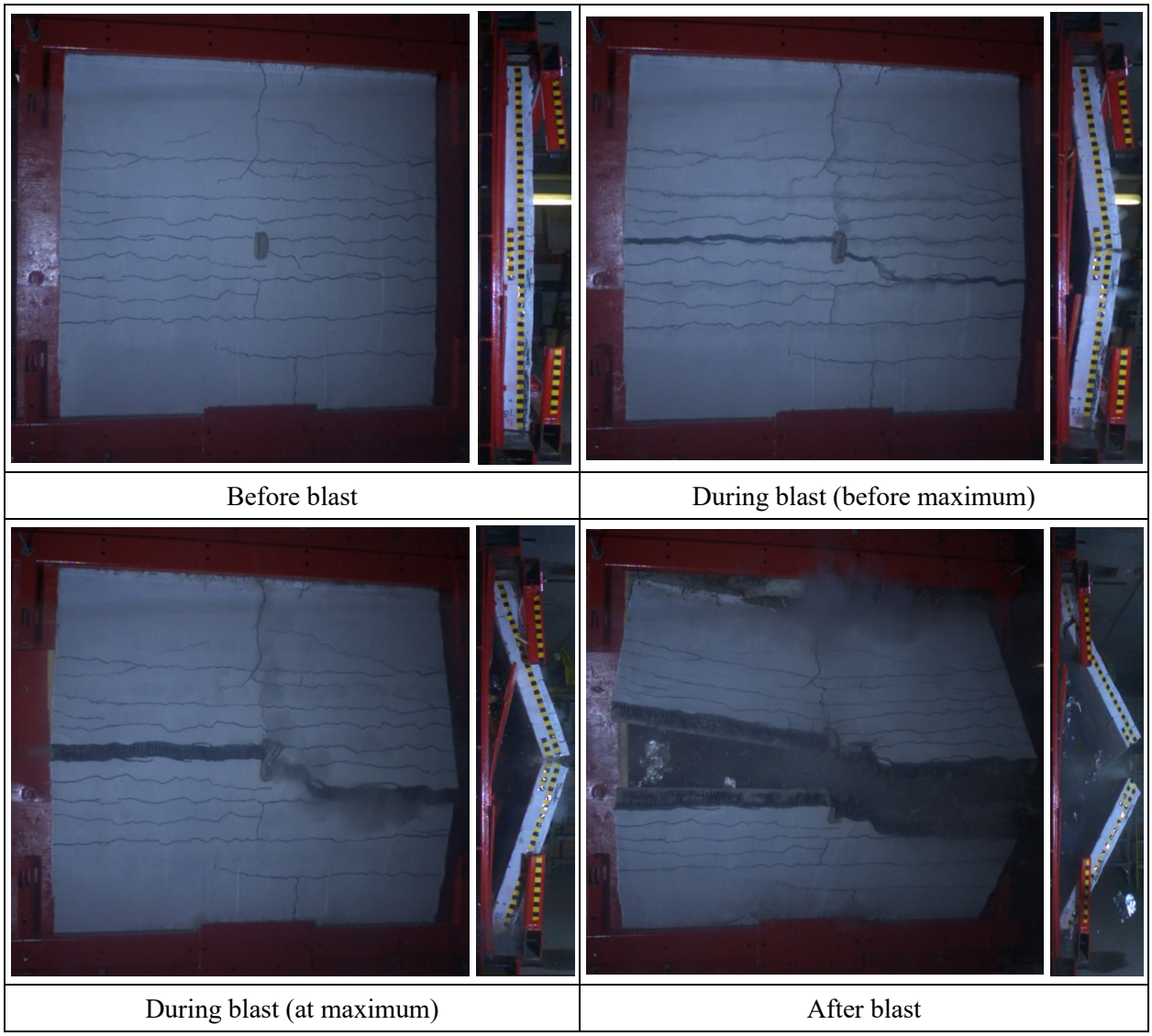

Before blast	During blast (before maximum)
During blast (at maximum)	After blast

Figure 4-8. Video stills of failure mechanisms of RCL-YC-2 at the 8th shot

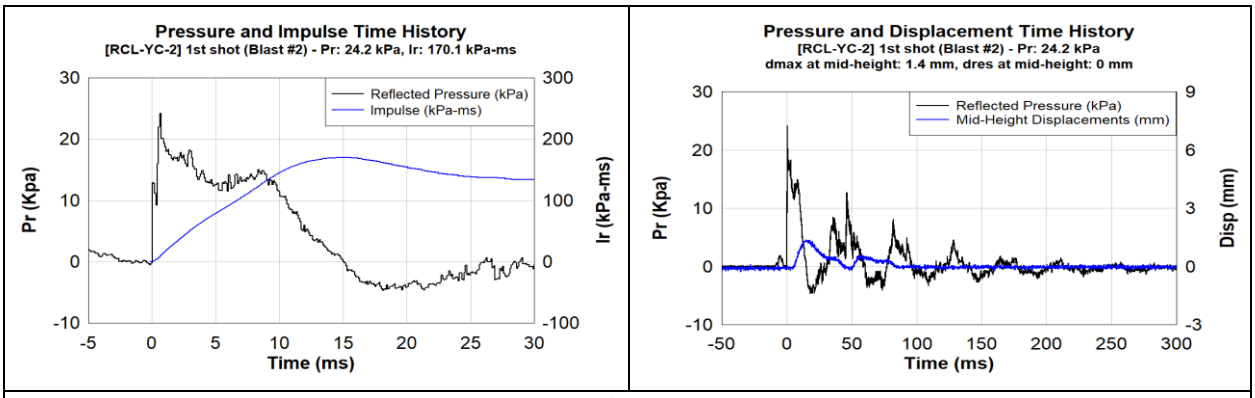

(a) 1st shot (Blast ID #2)

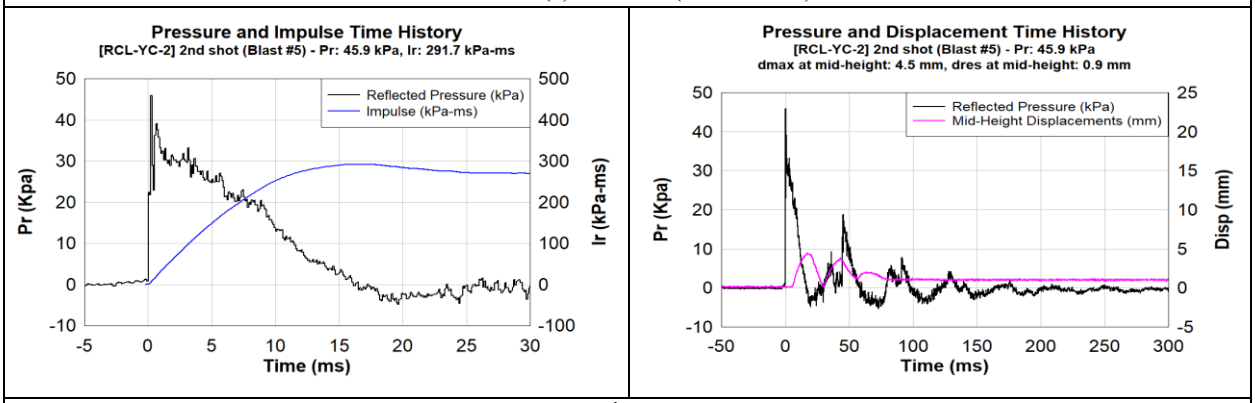

(b) 2nd shot (Blast ID #5)

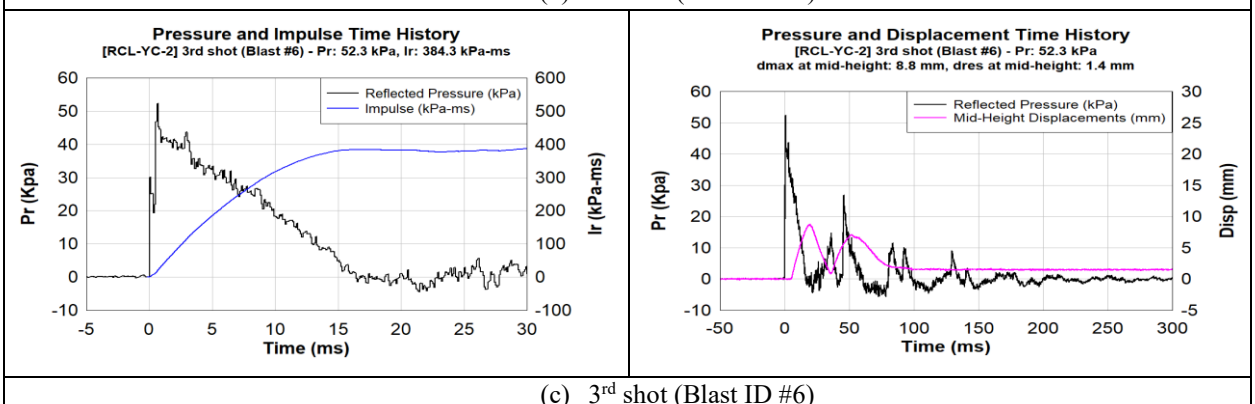

(c) 3rd shot (Blast ID #6)

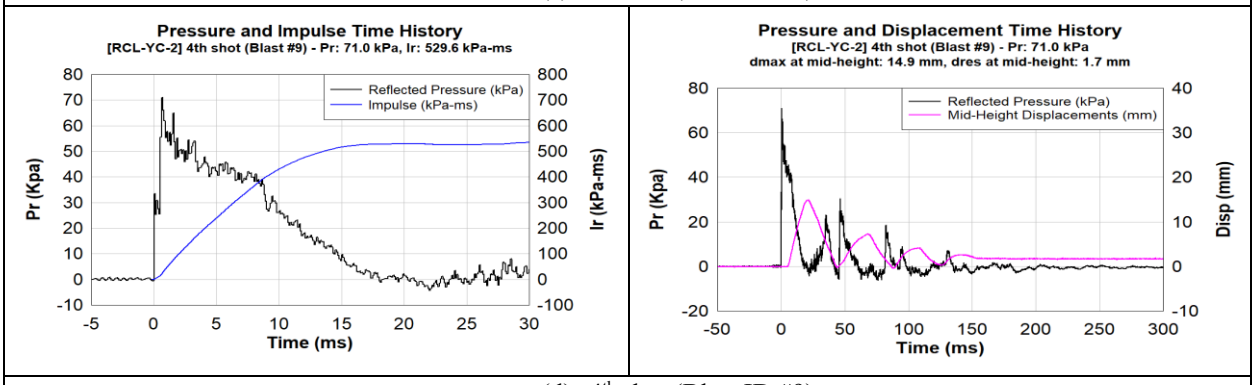

(d) 4th shot (Blast ID #9)

Figure 4-9. Pressure, Impulse, and Displacement Time history of RCL-YC-2

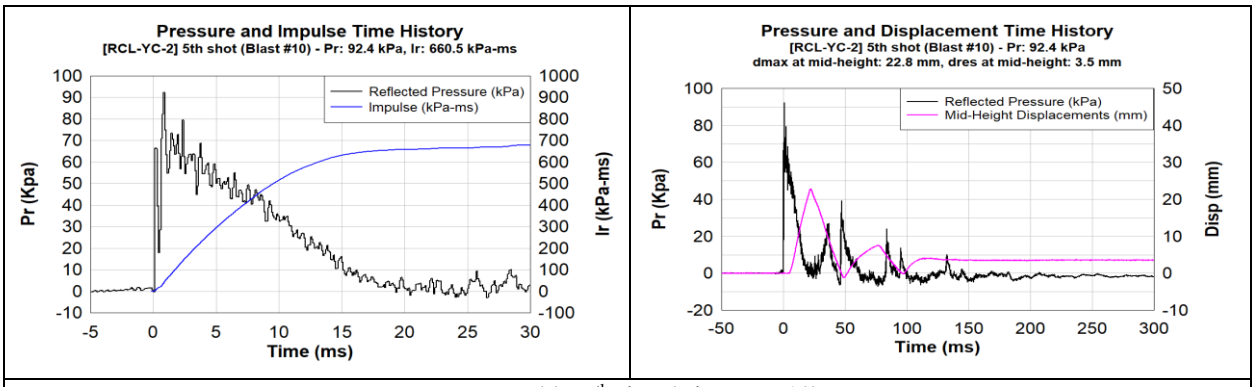

(e) 5th shot (Blast ID #10)

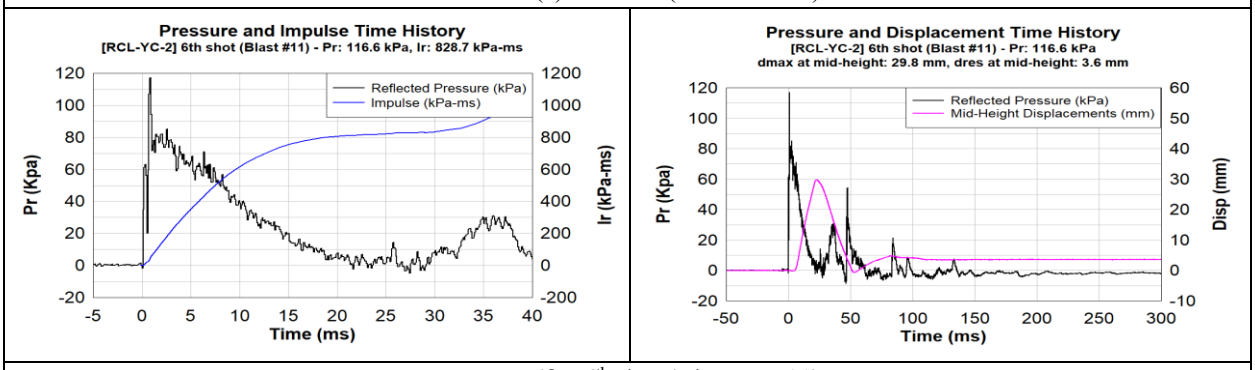

(f) 6th shot (Blast ID #11)

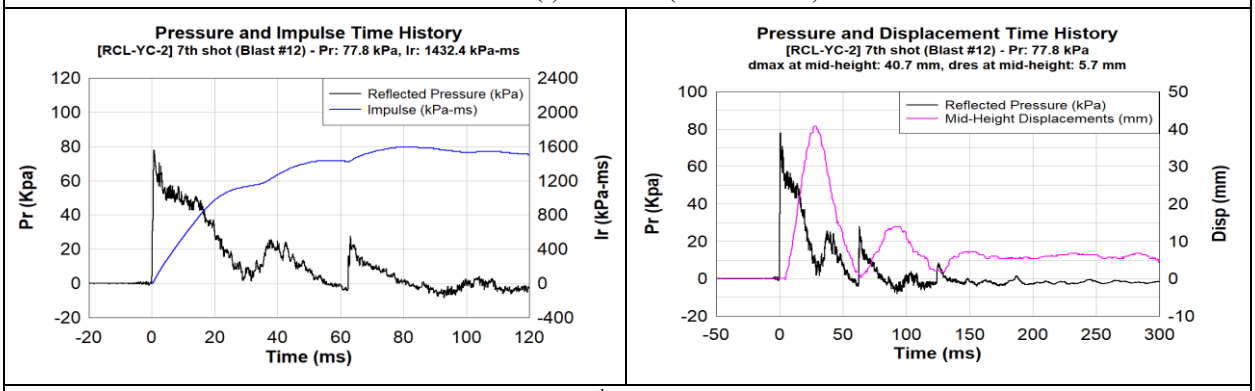

(g) 7th shot (Blast ID #12)

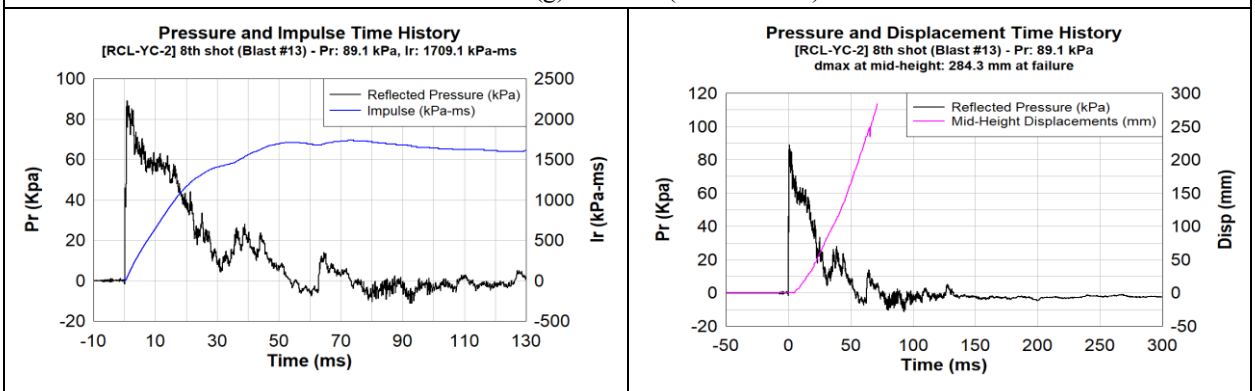

(h) 8th shot (Blast ID #13)

Figure 4-9. Pressure, Impulse, and Displacement Time history of RCL-YC-2, continuation.

4.4.RCL-YC-3

RCL-YC-3 was tested as a CMU load-bearing wall, strengthened on its tension face with 3 layers of FRCM composites. The average thickness for the 3-FRCM layers applied was, 50.8 mm (2 in, 3 layers of carbon grid plus the cementitious matrix). Additionally, an axial load of 122 KN, corresponding to 4 % of the wall nominal axial capacity, was applied to the wall during the tests. Nine shots of blast loading (simulated with the shock tube) were applied onto the wall. Table 4-4 shows the test results and some brief details for important events for each shot. The displacements were measured with the use of one LVDT placed at the mid-height/center of the wall up to the shot 7. Then the high-speed camera was used for tracking the displacements. Displacements at the top and bottom of the wall were measured with the high-speed camera, getting values very close to zero due to the pin supports provided. Therefore, these last values are considered as zero. The displacement profiles of the wall at the time of maximum deformation for each shot are shown in Figure 4-10. In order to get these profiles, the high-speed camera was used by selecting and tracking several points with the use of camera software. Additionally, for each shot, video stills are shown in Figure 4-10 using the same scale as the displacement profile plots, to allow for comparison. Furthermore, the pressure and impulse time histories are shown in Figure 4-13, as well as, the pressure and displacement time histories for each shot. The impulse was computed as the area under the reflected-pressure-curve function, Pr(t), for the first positive phase duration. As the impulse increases, by increasing the driver pressure, the duration of the positive phase of the blast (t_d) increases, meaning a load wave striking the wall longer.

Table 4-4. Summary of testing results with main events (RCL-YC-3)

Wall ID	Shot	Blast ID	P_d (kPa)	L_d (mm)	P_r (kPa)	I_r (kPa-ms)	t_d (ms)	d_{max} (mm)	d_{res} (mm)	$\sum d_{res}$ (mm)	t_{dmax} (ms)
RCL-YC-3	1st	#2	110.3	1829	28.4	213.4	15.0	0.9	0.0	0.0	15.0
			No cracks, just the one at top (local shear crack in only one brick at top-right-side since set up, before testing): Figure 4-11 (a)								
	2nd	#5	248.2	1829	47.5	382.9	16.1	3.1	0.0	0.0	17.1
			No cracks, just the one at top (local shear crack in only one brick at top-right-side since set up, before testing).								
	3rd	#6	289.6	1829	51.3	466.8	18.2	5.6	0.7	0.7	19.3
			Few flexural cracks appeared at midspan. No shear cracks yet: Figure 4-11 (b)								
	4th	#9	413.7	1829	68.1	642.9	18.9	10.4	1.6	2.3	18.8
			Few more flexural cracks at midspan. No shear cracks yet (no cracks at supports): Figure 4-11 (c)								
	5th	#10	551.6	1829	85.0	918.4	21.6	13.7	4.2	6.5	18.3
			Few more flexural cracks at midspan. No shear cracks yet (no cracks at supports): Figure 4-11 (d)								
	6th	#11	689.5	1829	103.6	1169.1	22.6	21.4	6.1	12.6	20.8
			Same as previous. Just crack at support (local) since beginning, it is wider and deeper but it is still local, one brick: Figure 4-11 (d)								
	7th	#12	551.6	3353	78.7	1378.4	35.0	27.9	10.8	23.3	25.9
			More flexural cracks at midspan (considerably) and deeper to neutral axis. Not cracks at supports (just one from beginning, local crack at top). Additionally, vertical cracks appeared at middle-top of wall: Figure 4-11 (e)								
	8th	#13	689.5	3353	102.3	1847.0	36.1	36.5	5.9	29.2	27.1
			Many flexural cracks, deeper to neutral axis. More vertical cracks at top of wall at middle (from axial load problably). Not cracks at supports (just one from beginning, local crack at top): Figure 4-11 (f)								
	9th	#15	689.5	3962	111.8	2443.4	43.7	79.0	12.0	41.3	74.0
			Many flexural cracks, deeper to neutral axis. More vertical cracks at top of wall at middle (from axial load problably). Not cracks at supports (just one from beginning, local crack at top). Midspan crack depth 3mm. Midspan compression crack all over the lenght of the wall: Figure 4-11 (g)								

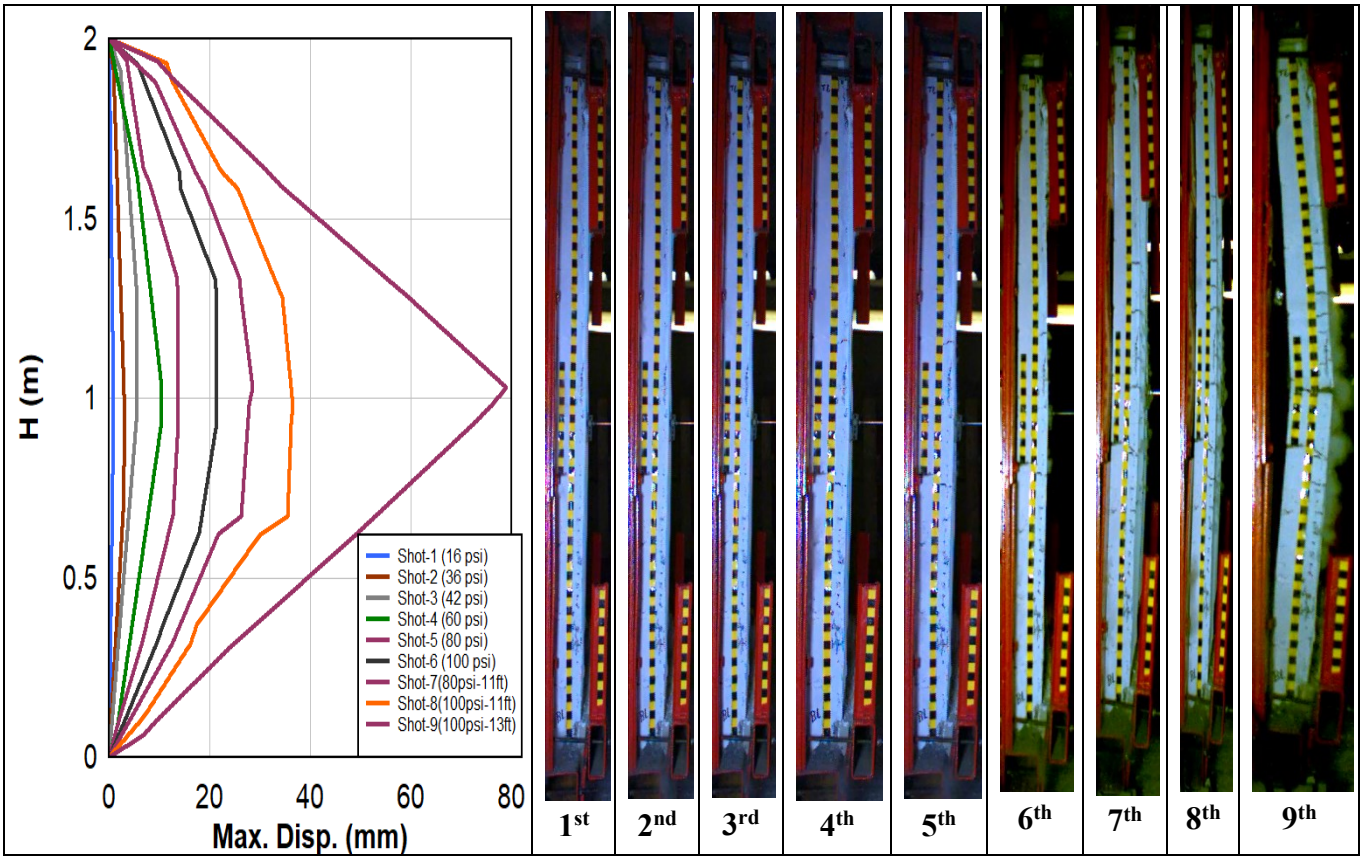

Figure 4-10. Displacement profile with video stills for each shot at maximum displacement (RCL-YC-3)

1st shot (Blast ID #2)

A driver pressure of 110.3 kPa (16 psi) with a length of 1829 mm (6 ft) was used for the first shot on wall RCL-YC-3. The peak reflected pressure and reflected impulse were 28.4 kPa and 213.4 kPa-ms, respectively. The positive phase duration was 15.0 ms. The maximum mid-height displacement was 0.9 mm. The maximum deflection occurred at a time of 15.0 ms. The pressure-impulse time history and the pressure-displacement time history are shown in Figure 4-13 (a).

The first shot resulted in a small displacement at the mid-height of the wall without any residual deformations or damage and therefore the wall remained in the elastic range. Also, no visible cracking or damage was observed.

2nd shot (Blast ID #5)

The second shot used a driver pressure of 248.2 kPa (36 psi), with the same driver length of 1829 mm. The peak reflected pressure and reflected impulse were 47.5 kPa and 382.9 kPa-ms, respectively. The positive phase duration was 16.1 ms. The maximum mid-height displacement

was 3.1 mm. Maximum deflection occurred at a time of 17.1ms. The pressure -impulse time history and the pressure-displacement time history are shown in Figure 4-13 (b).

This shot resulted in a small displacement at the mid-height of the wall without any residual deformations therefore the wall remained in the elastic range. Nonetheless, there is one local shear crack in only one brick at top-right-side (3mm wide) that occurred during the set-up because the wall was not straight in the right corner, when some force was applied when placing the top support a small shear crack appeared: Figure 4-11 (a), but no additional shear crack were observed.

3rd shot (Blast ID #6)

The third shot used a driver pressure of 289.6 kPa (42 psi), with the same driver length of 1829 mm. The peak reflected pressure and reflected impulse were 51.3 kPa and 466.8 kPa-ms, respectively. The positive phase duration was 18.2 ms. The maximum mid-height displacement was 5.6 mm. Maximum deflection occurred at a time of 19.3 ms and the residual displacement was 0.7 mm at the mid-height of the wall. The pressure -impulse time history and the pressure-displacement time history are shown in Figure 4-13 (c). Finally, few flexural cracks appeared at midspan but not any shear crack: Figure 4-11 (b).

4th shot (Blast ID #9)

The fourth shot used a driver pressure of 413.7 kPa (60 psi), with the same driver length of 1829 mm. The peak reflected pressure and reflected impulse were 68.1 kPa and 642.9 kPa-ms, respectively. The positive phase duration was 18.9 ms. The maximum mid-height displacement was 10.4 mm. Maximum deflection occurred at a time of 18.8 ms and the residual displacement was 1.6 mm at the mid-height of the wall. The pressure -impulse time history and the pressure-displacement time history are shown in Figure 4-13 (d).

Lastly, few more flexural cracks appeared at the midspan. No cracks appeared on the side of the wall and there is still not shear cracks seen: Figure 4-11 (c).

5th shot (Blast ID #10)

The fifth shot used a driver pressure of 551.6 kPa (80 psi), with the same driver length of 1829 mm. The peak reflected pressure and reflected impulse were 85.0 kPa and 918.4 kPa-ms, respectively. The positive phase duration was 21.6 ms. The maximum mid-height displacement was 13.7 mm. Maximum deflection occurred at a time of 18.3 ms and the residual displacement was 4.2 mm at the mid-height of the wall. The pressure -impulse time history and the pressure-displacement time history are shown in Figure 4-13 (e).

No shear cracks have appeared, only more horizontal flexural hairline cracks were visible on the tension side (front face) of the wall. The space among them was about 18 to 22 cm apart from each

other, mainly at the same locations as the CMU mortar joints. They were located at the mid-height of the wall, within the middle third of the wall. Also, the existing flexural cracks were not widened much, they were about 0.1 mm wide, Figure 4-11 (d).

6th shot (Blast ID #11)

The sixth shot used a driver pressure of 689.5 kPa (100 psi), with the same driver length of 1829 mm. The peak reflected pressure and reflected impulse were 103.6 kPa and 1169.1 kPa-ms, respectively. The positive phase duration was 22.6 ms. The maximum mid-height displacement was 21.4 mm. Maximum deflection occurred at a time of 20.8 ms and the residual displacement was 6.1 mm at the mid-height of the wall. The pressure -impulse time history and the pressure-displacement time history are shown in Figure 4-13 (f).

No shear cracks have appeared, only more horizontal flexural hairline cracks were visible on the tension side (front face) of the wall. The space among them was about 18 to 22 cm apart from each other, mainly at the same locations as the CMU mortar joints. They were located at the mid-height of the wall, within the middle third of the wall. Also, the existing flexural cracks were not widened much, they were about 0.1 mm wide, Figure 4-11 (d). Finally, the local crack at support since set-up is wider and deeper but it is still local, in only one brick.

7th shot (Blast ID #12)

The seventh shot used a driver pressure of 551.6 kPa (80 psi), with a longer driver length of 3353 mm. The peak reflected pressure and reflected impulse were 78.7 kPa and 1378.4 kPa-ms, respectively. The positive phase duration was 35.0 ms. The maximum mid-height displacement was 27.9 mm. Maximum deflection occurred at a time of 25.9 ms and the residual displacement was 10.8 mm at the mid-height of the wall. The pressure -impulse time history and the pressure-displacement time history are shown in Figure 4-13 (g). No shear cracks have appeared but more horizontal flexural cracks appeared on the tension side (front face) of the wall, with a maximum crack width of around 0.2 mm and deeper to the neutral axis. The space among them was about 9 cm apart from each other, mainly at the same locations as the CMU mortar joints and at the middle of the bricks between. Lastly, few vertical cracks appeared in the middle, at top and bottom: Figure 4-11 (e)

8th shot (Blast ID #13)

The eighth shot used a driver pressure of 689.5 kPa (100 psi), with a longer driver length of 3353 mm. The peak reflected pressure and reflected impulse were 102.3 kPa and 1847.0 kPa-ms, respectively. The positive phase duration was 36.1 ms. The maximum mid-height displacement was 36.5 mm. Maximum deflection occurred at a time of 27.1 ms and the residual displacement

was 5.9 mm at the mid-height of the wall. The pressure -impulse time history and the pressure-displacement time history are shown in Figure 4-13 (h).

No shear cracks have appeared but more horizontal flexural cracks appeared on the tension side (front face) of the wall, with a maximum crack width of around 0.3 mm and deeper to the neutral axis. The space among them was about 9 cm apart from each other, mainly at the same locations as the CMU mortar joints and at the middle of the bricks between. Lastly, few more vertical cracks appeared in the middle, at top and bottom (from axial load problably): Figure 4-11 (f)

9th shot (Blast ID #15)

The eighth shot used a driver pressure of 689.5 kPa (100 psi), with a longer driver length of 3962 mm. The peak reflected pressure and reflected impulse were 111.8 kPa and 2443.4 kPa-ms, respectively. The positive phase duration was 43.7 ms. The maximum mid-height displacement was 79.0 mm. Maximum deflection occurred at a time of 74.0 ms and the residual displacement was 12.0 mm at the mid-height of the wall. The pressure -impulse time history and the pressure-displacement time history are shown in Figure 4-13 (i). No shear cracks appeared but more horizontal flexural cracks appeared on the tension side (front face) of the wall, with a maximum crack width of around 1.0 mm and deeper to the neutral axis. The space among them was about 9 cm apart from each other, mainly at the same locations as the CMU mortar joints and at the middle of the bricks between. Lastly, few more vertical cracks appeared in the middle, at top and bottom (from axial load problably): Figure 4-11 (g). The wall withstood the last shot and had to be demolished. Some crashing of the compression side of the wall at the mid-height was seen: Figure 4-11 (h)

At this shot, the wall was considered failed given that all the mid-height bricks at the compression side of the wall, crashed during the blast shot, (Figure 4-11 (h)). However, the retrofit was still standing, including the carbon-fiber mesh. Nonetheless, even if the wall was able to withstand another blast shot, the shock tube had reached almost the maximum driver pressure allowed and the maximum driver length and going further would have been dangerous. The wall remained standing after this shot and the only visible damage was a wide crack at the midheight at the tension side, the crashing on the compression side and all the less wide flexural cracks at the tension side. Lastly, it should be noted that no shear cracks were seen on the wall. Figure 4-12 shows video stills of the failure mechanism of wall RCL-YC-3 for the nineth shot. After this shot the wall was removed from the shock tube and it was demolished manually.

(a) Before1st shot

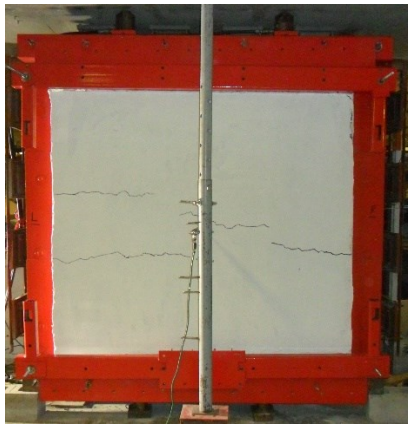

(b) 3rd shot

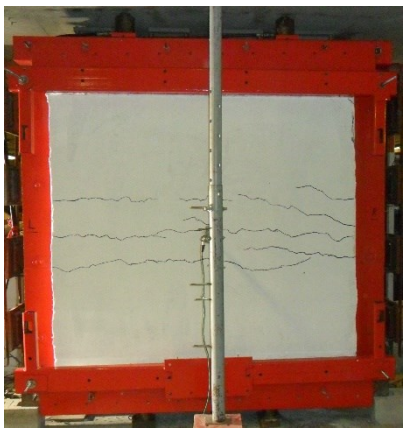

(c) 4th shot

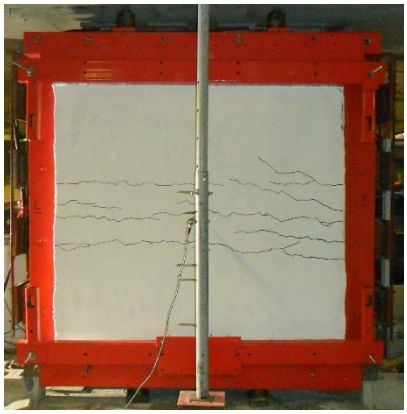

(d) 5th & 6th shots

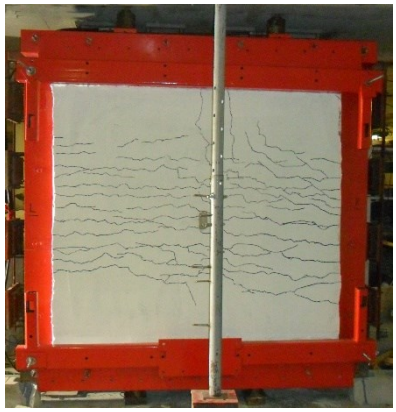

(e) 7th shot

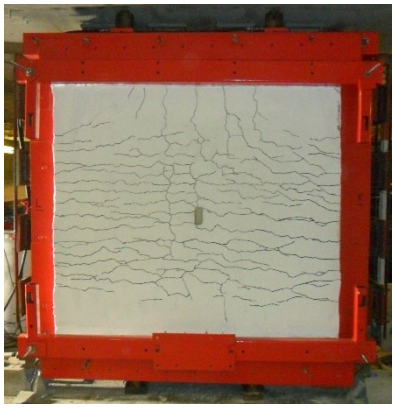

(f) 8th shot

(g) 9th shot

(h) 9th shot (back)

Figure 4-11. Damage Progression (from 3rd to 9th shot, no flexural cracks before the 3rd shot)

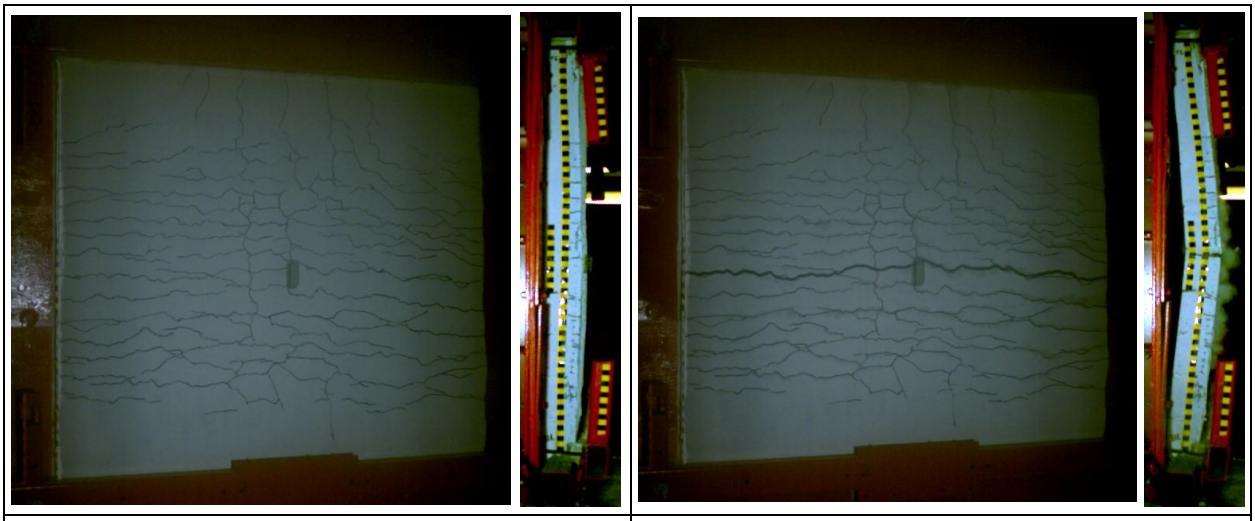

Before blast	During blast (before maximum)
During blast (at maximum)	After blast

Figure 4-12. Video stills of failure mechanisms of RCL-YC-3 at the 9th shot

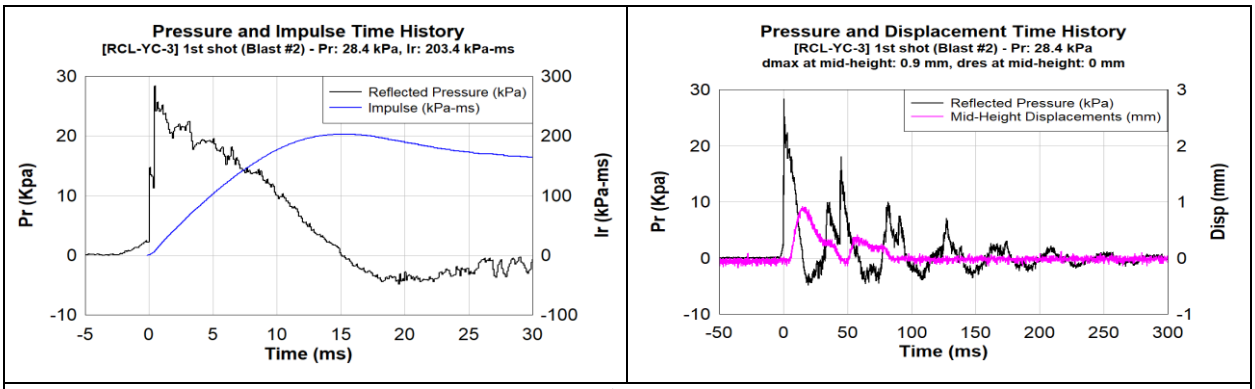

(a) 1st shot (Blast ID #2)

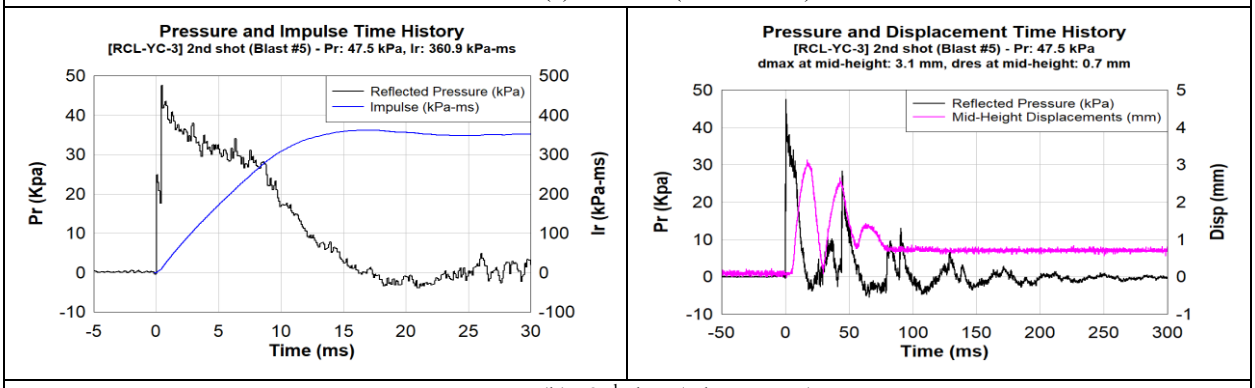

(b) 2nd shot (Blast ID #5)

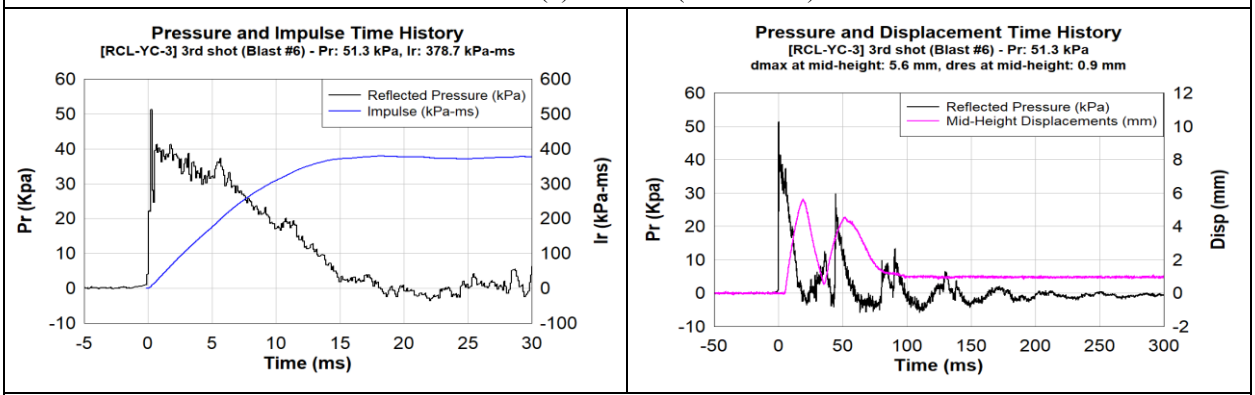

(c) 3rd shot (Blast ID #6)

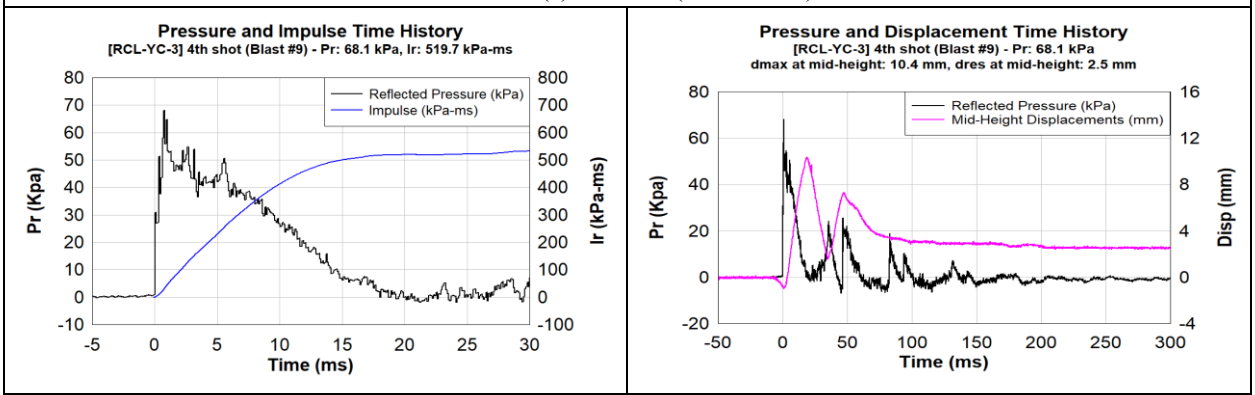

(d) 4th shot (Blast ID #9)

Figure 4-13. Pressure, Impulse, and Displacement Time history of RCL-YC-3

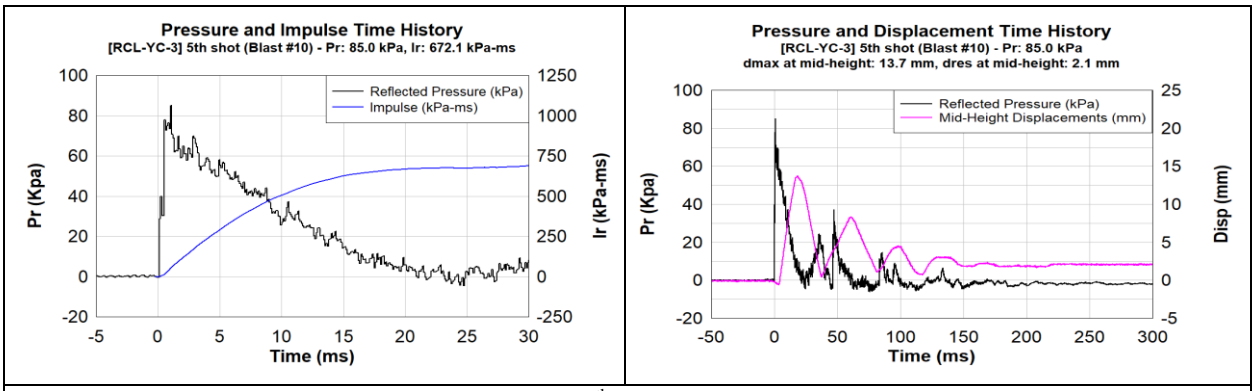

(e) 5th shot (Blast ID #10)

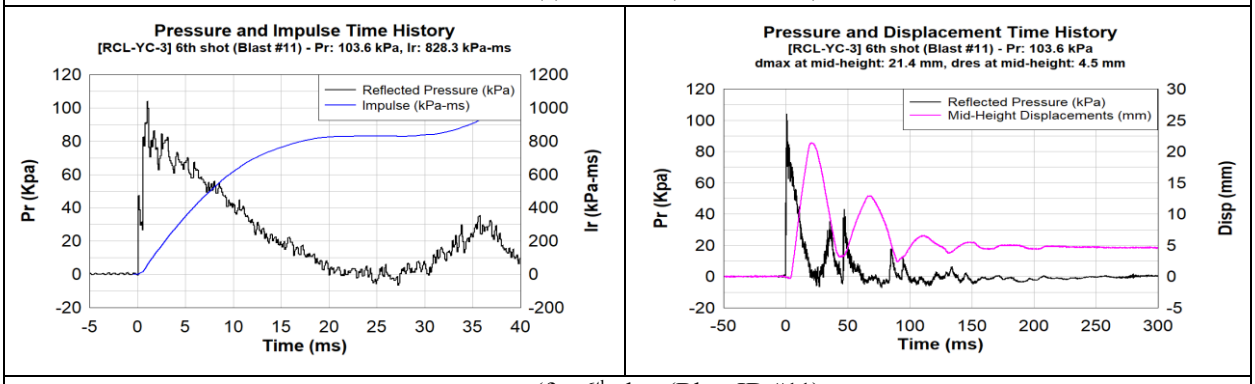

(f) 6th shot (Blast ID #11)

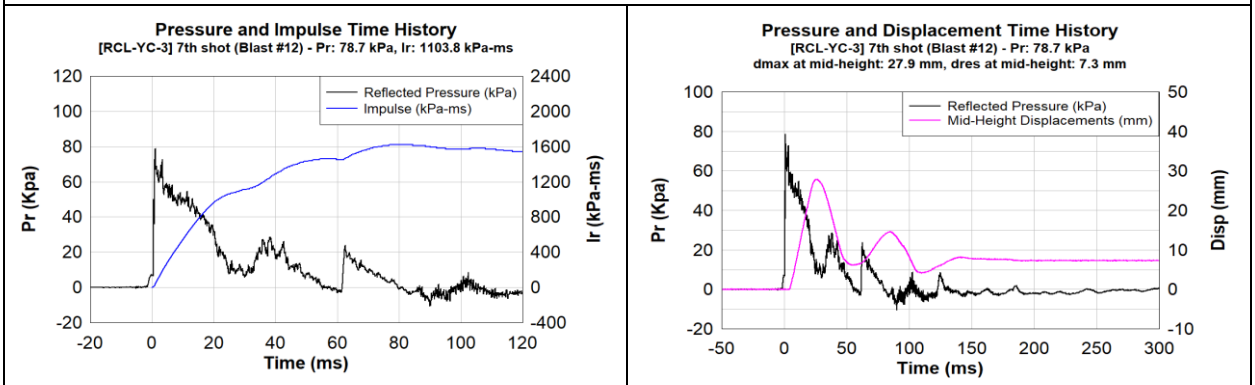

(g) 7th shot (Blast ID #12)

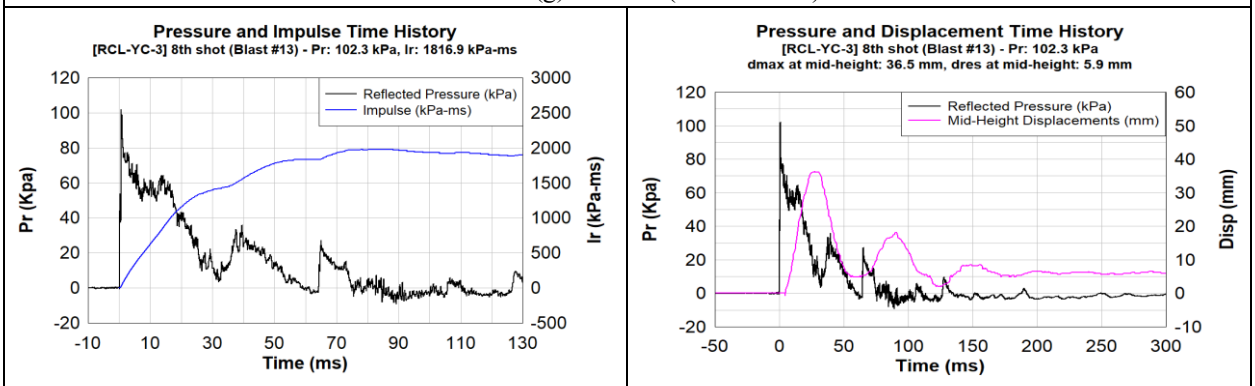

(h) 8th shot (Blast ID #13)

Figure 4-13. Pressure, Impulse and Displacement Time history of RCL-YC-3, continuation.

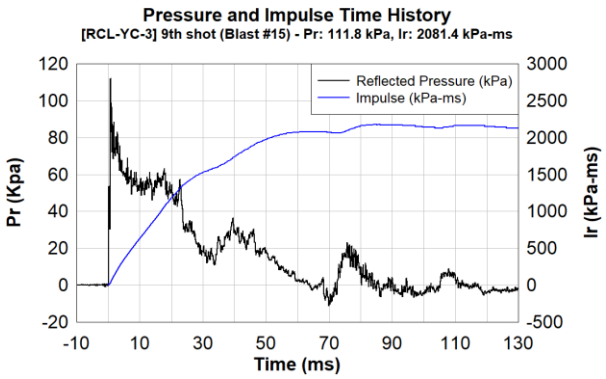

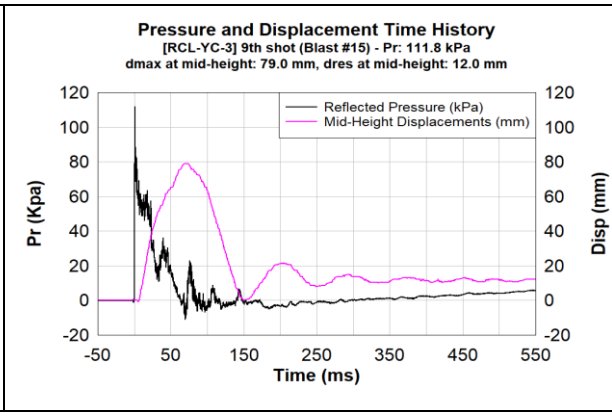

(i) 9th shot (Blast ID #13)

Figure 4-13. Pressure, Impulse and Displacement Time history of RCL-YC-3, continuation.

CHAPTER 5. DISCUSSION

5.1. OVERVIEW

This chapter discusses and compares the performance of walls RCL-NC-1, RCL-YC-2 and RCL-YC-3. The criteria for discussion includes the number of test shots, the maximum displacement at midheight, the residual displacement, the magnitude of the reflected pressure & impulse, and failure mode. The parameters discussed include the effects of FRCM retrofit and number of FRCM layers. These parameters are studied by comparing the responses of the walls with 1-, 2- and 3-FRCM Layers with the response of the control load-bearing CMU wall tested by Ciornei (2012). The influence of masonry type (CMU vs STONE) is examined by comparing wall RCL-YC-3 with the response of a load-bearing Stone wall retrofitted with 3-FRCM Layers tested by Jung (2020). The effect of axial load is studied by comparing the load-bearing RCL-YC-3 wall with the response of a CMU infill wall retrofitted with 3-FRCM Layers, also tested by Jung (2020).

5.2. GENERAL OBSERVATIONS

This section gives a general overview of the test results presented in Chapter 4. **Figure 5-1** shows an example of the typical tensile response of the FRCM-composite system which demonstrates the stages in failure . The diagram is similar to those presented in Section 2.2.5, with three different branches; un-cracked, crack development and the cracked stage. The response shows a high initial stiffness until the first crack appears (un-cracked stage), after this, there is a drop in strength followed by a degradation of the stiffness and a redistribution of stresses. This happens because the section has cracked completely and all the stresses are distributed from the entire cross-sectional area (gross area) to the area of the carbon fibers within the coupon (crack development stage). Finally, there is an increase in strength/capacity, but with a decayed stiffness until reaching the ultimate capacity and failure (cracked stage). It should be noted that after peak load there is an abrupt fall of the tensile capacity, and finally a plateau with a remaining low capacity due to a few carbon-fiber strands that remain unbroken.

The maximum and residual displacements for each wall tested in this study are presented in **Figure 5-2**. As will be demonstrated in the following sections, the retrofit shows improved blast performance according to the increase in composite reinforcement ratio. The greater the retrofit ratio, the smaller the displacements due to the blast loading. Further discussions on the effects of the test parameters is presented in the following sections.

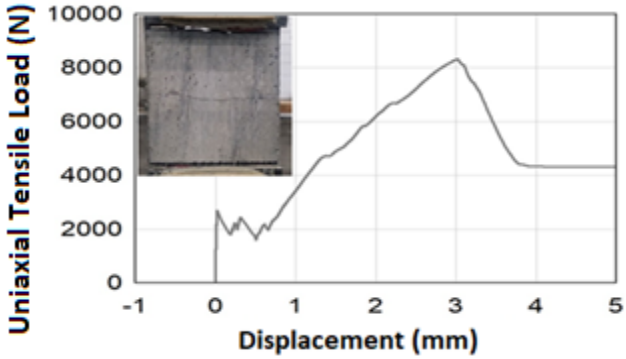

Figure 5-1. Typical tensile load-displacement relationship for FRCM composite

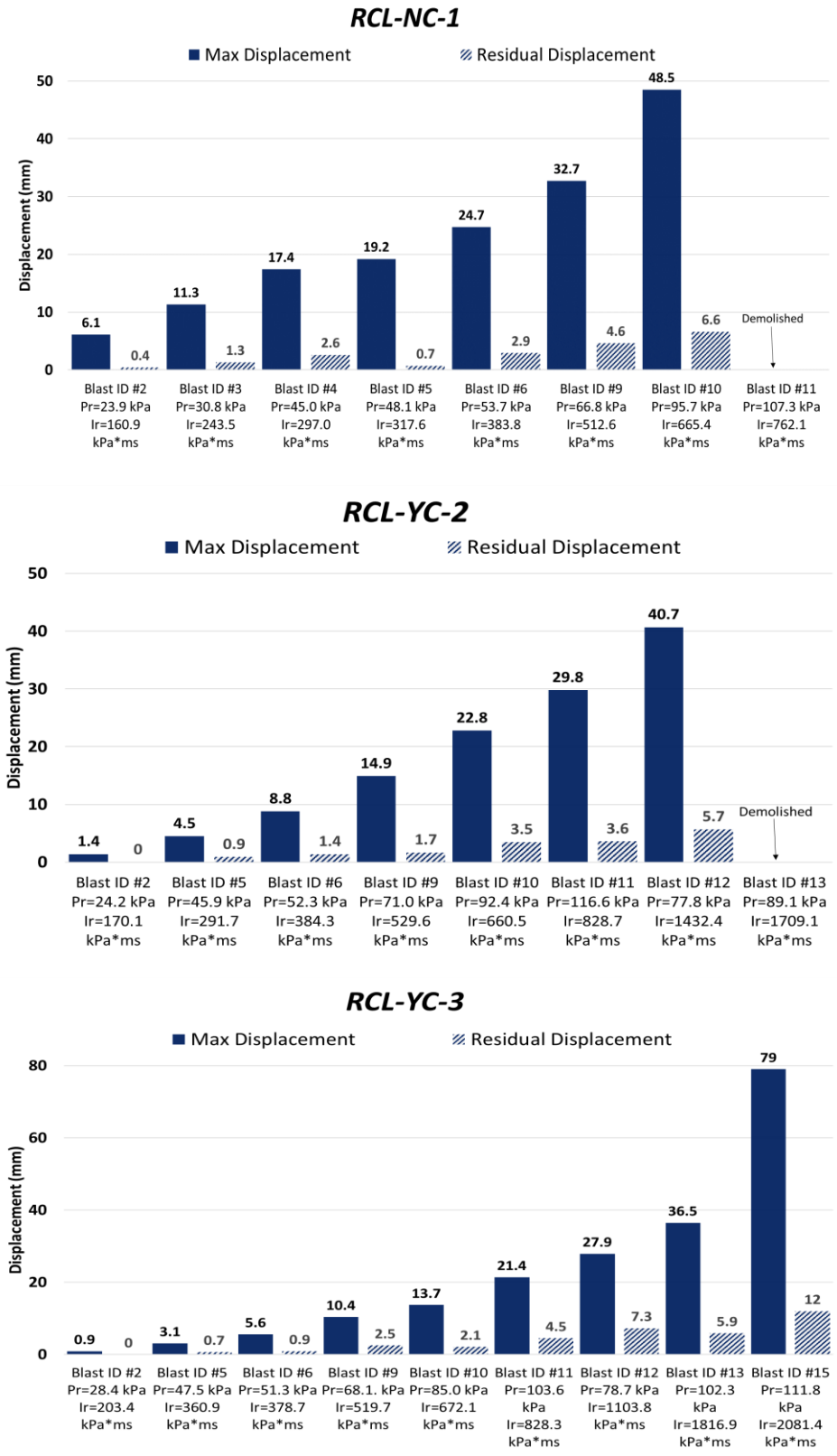

Figure 5-2. Maximum and Residual Displacements for wall: RCL-NC-1, RCL-YC-2 and RCL-YC-3

5.3. EFFECT OF RETROFIT

5.3.1. Retrofit walls vs URM-3

The effect of the FRCM-retrofit is investigated by comparing the response of the retrofit walls tested in this project to that of the control URM-3 tested by Ciornei (2012). Wall URM-3 was built as an control (un-retrofitted) concrete masonry (CMU) load-bearing wall, with an axial load of 122kN. Walls RCL-NC-1, RCL-YC-2 and RCL-YC-3 were loaded with the same axial load magnitude, and were built in the same manner, but were retrofitted with one, two and three layers of FRCM layers, respectively. To increase shear capacity, the voids in the CMU blocks of RCL-YC-2 and RCL-YC-3 were also filled with SCC concrete. **Figure 5-3**, **Figure 5-5** and **Figure 5-7** compares the displacements sustained by the walls over the course of testing and presents selected displacement time history graphs and maximum/residual displacement comparisons. **Figure 5-4, Figure 5-6** and **Figure 5-8** present photos of the walls during testing.

In general, the results show that the retrofit remarkably enhanced blast capacity of the URM wall. The FRCM-composite system enhanced the wall's moment resistance in the out-of-plane direction and thus allowed for delayed failure and increased blast resistance. The control wall (URM-3), failed in a brittle manner, and was fully demolished, after seven shots at Blast #6 (51 kPa, 414.6 kPa-ms). In comparison, retrofit wall RCL-NC-1 was demolished after eight shots at Blast #11 (107.3 kPa, 762.1 kPa-ms), with corresponding increases of 210% and 184% in maximum reflected pressure and impulse when compared to URM-3. Likewise, retrofit wall RCL-YC-2, was demolished after eight shots at Blast #13 (89.1 kPa, 1709.1 kPa-ms). The increases in reflected pressure and impulse against the control, are 175% and 412%, respectively. Lastly, wall RCL-YC-3, failed after nine shots at Blast #15 (111.8 kPa, 2081.4 kPa-ms). The increases in reflected pressure and impulse against the control wall are 219% and 502%, respectively. It should be noted that RCL-YC-3 was not demolished at Blast #15 meaning that its ultimate capacity could be higher than reported. No additional shots were performed due to the need of higher pressure and the limitations of the shock tube.

In addition to the improvement in blast capacity, the FRCM system also enhanced the control of displacements at equivalent blasts due to the increase in wall stiffness and mass. In all cases, the maximum displacements were lower in the retrofits when compared to the control URM-3 wall at Blast #2 (24.7 kPa, 193.3 kPa-ms) and Blast #5 (39.0 kPa, 290.8 kPa-ms). For Blast #2, the retrofits reduced maximum displacements by -63%, -92% and -95% in RCL-NC-1, RCL-YC-2 and RCL-YC-3 walls, respectively, while residual displacements reduced by -88%, -100% and -100%, respectively. As shown in **Figure 5-3**, RCL-NC-1 also showed important reductions in maximum and residual displacements at Blasts #3 and 4. At Blast #5, the retrofits reduced maximum displacements by -54%, -89% and -93% in RCL-NC-1, RCL-YC-2 and RCL-YC-3 walls, with corresponding reductions of -92%, -90% and -92% in residual displacements.

The retrofit system also affected the progression of damage and failure mode. Damage detected on RCL-NC-1, RCL-YC-2 and RCL-YC-3 walls can be correlated to the displacements during the tests. Generally, the retrofit walls presented less visible damage than the non-retrofitted-control wall, URM-3, for each correspondent blast. The damage observed in the retrofit walls consisted of the gradual development of cracks in the FRCM cementitious matrix, with crack widths ranging from hairline to 0.3 mm - 2.0mm. In the case of the walls with 1 and 2 layers, the development of cracks continued to be controlled until the capacity of the composite system was exhausted,

resulting in rupture of the carbon fibers and brittle failure, with the wall breaking into 2 or 3 large pieces.

The control wall (URM-3) failed in a brittle manner, and was completely demolished at failure, with the launching of large fragments and projectiles. Failure of retrofit walls RCL-NC-1 and RCL-YC-2 was also brittle due to the rupture of the carbon mesh, but was greatly delayed and associated with very few projectiles at failure. Indeed, the FRCM-composite system kept the blocks together at failure, causing fewer flying projectiles and causing the wall to break in two or three large pieces. The use of 3 FRCM layers prevented brittle failure and held the wall in place until the end of testing.

Retrofit Performance - RCL-NC-1 vs URM-3

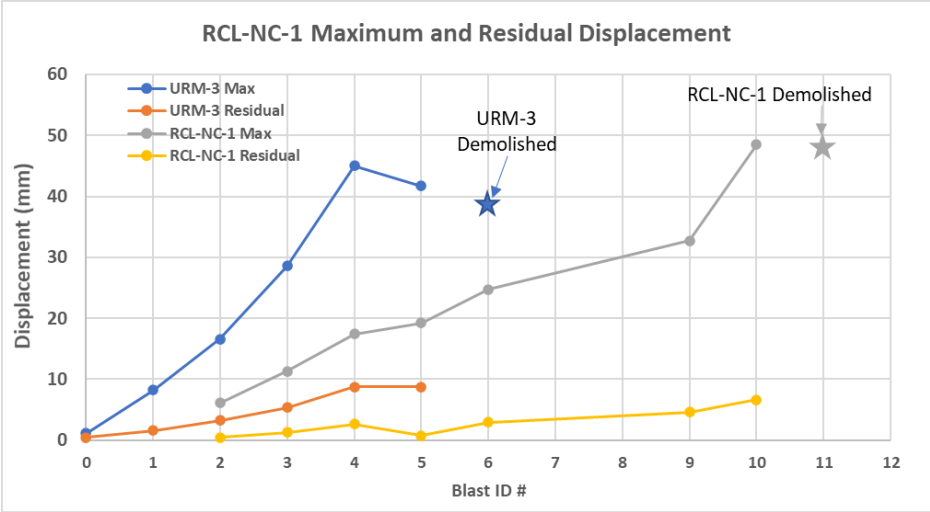

Displacement Time History Comparison - RCL-NC-1 vs URM-3

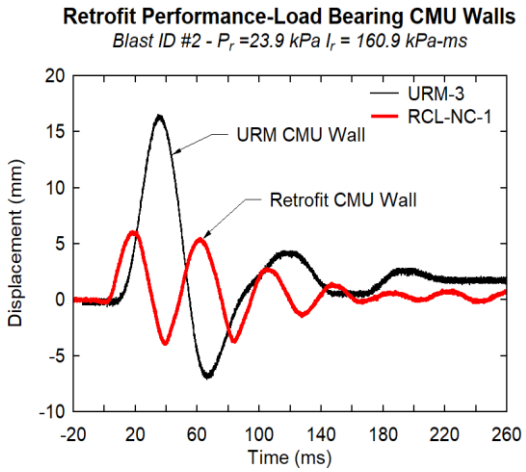

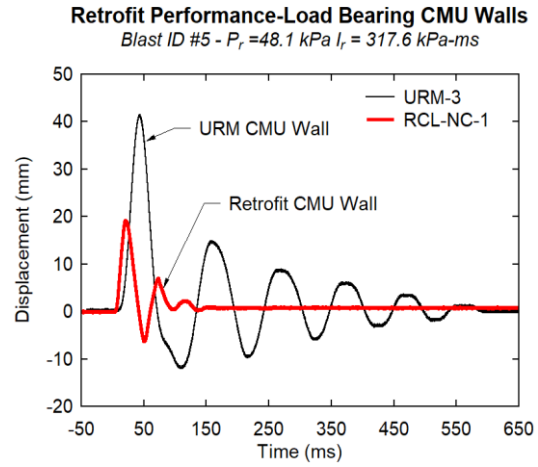

Maximum and Residual Displacements - RCL-NC-1 vs URM-3

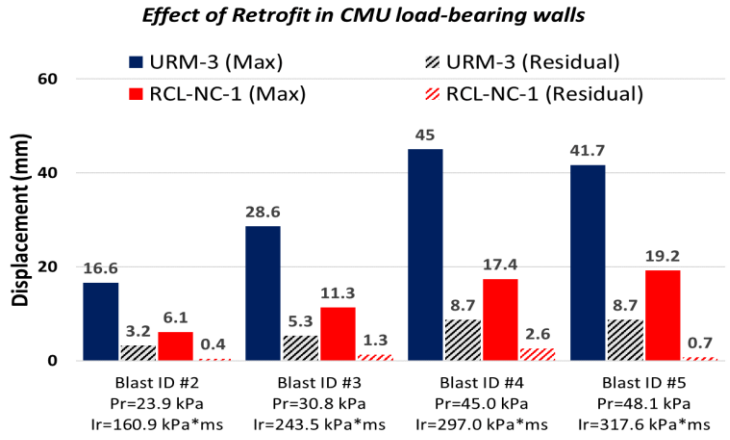

Figure 5-3. Retrofit Performance of Load-Bearing-CMU Walls: RCL-NC-1 vs URM-3 (URM-3 data from Ciornei, 2012)

Blast ID 3 Damage Comparison: RCL-NC-1 vs URM-3 (Left: Ciornei, 2012)

Blast ID 4 Damage Comparison: RCL-NC-1 vs URM-3 (Left: Ciornei, 2012)

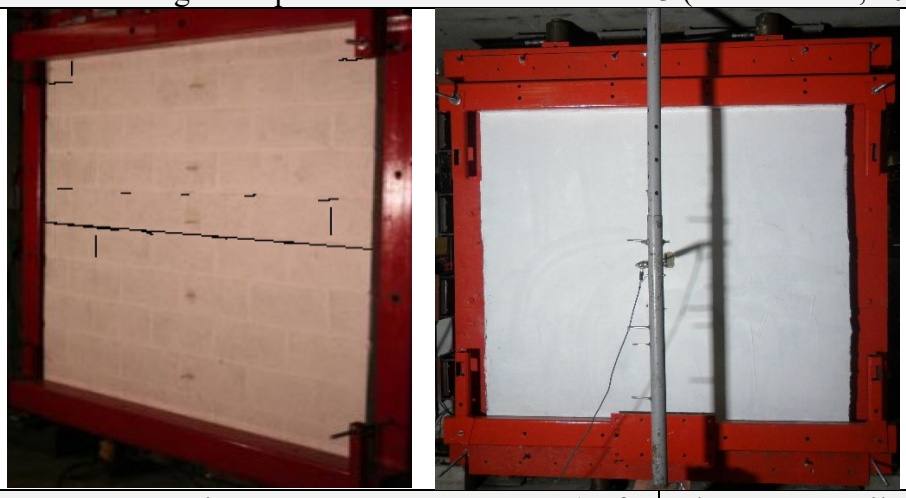

Blast ID 6 Damage Comparison: RCL-NC-1 vs URM-3 (Left: Ciornei, 2012)	Blast ID 11: Failure Mode for RCL-NC-1

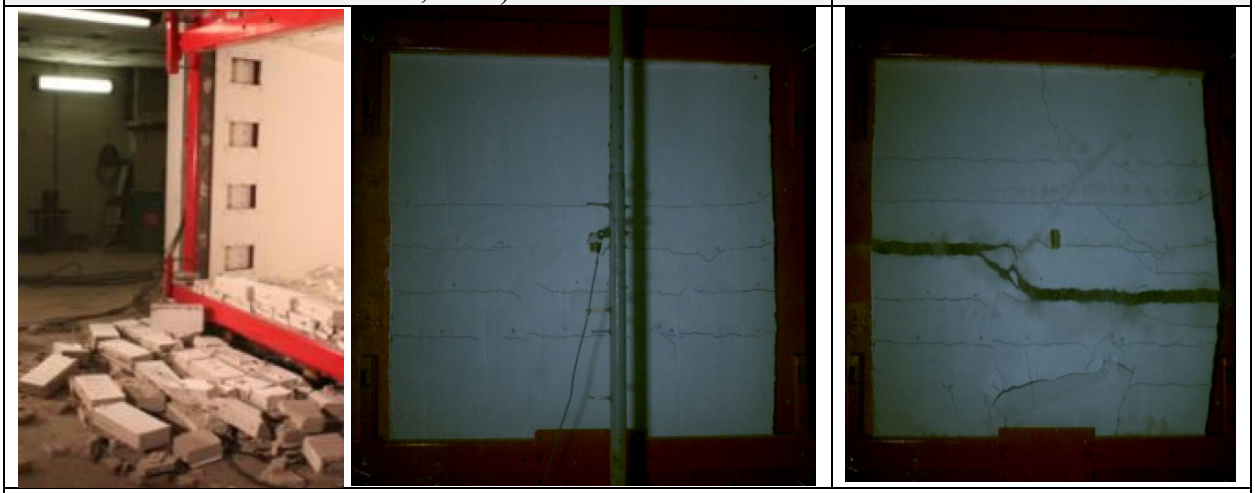

Figure 5-4. Load-Bearing-CMU Walls Retrofit Comparison

Retrofit Performance - RCL-YC-2 vs URM-3

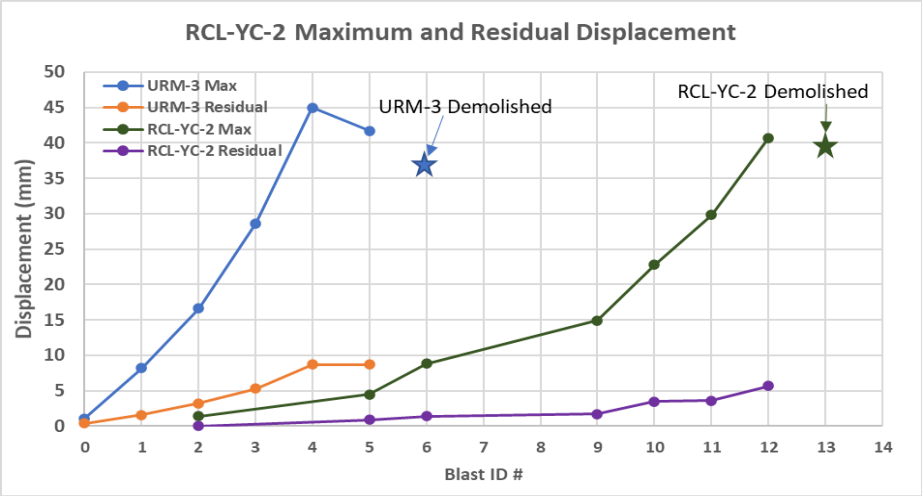

Displacement Time History Comparison

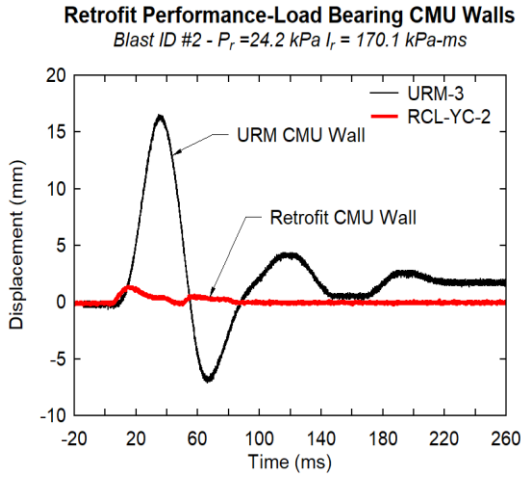

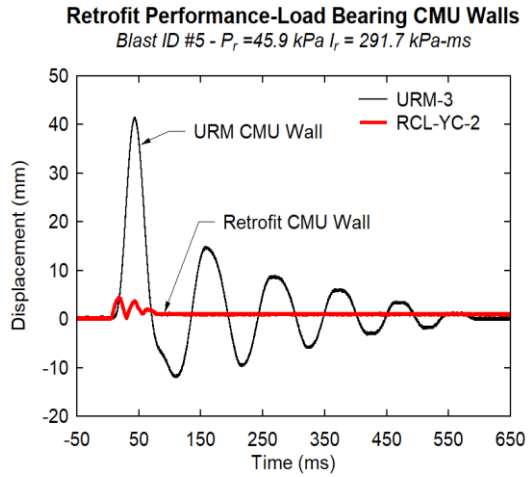

Maximum and Residual Displacements

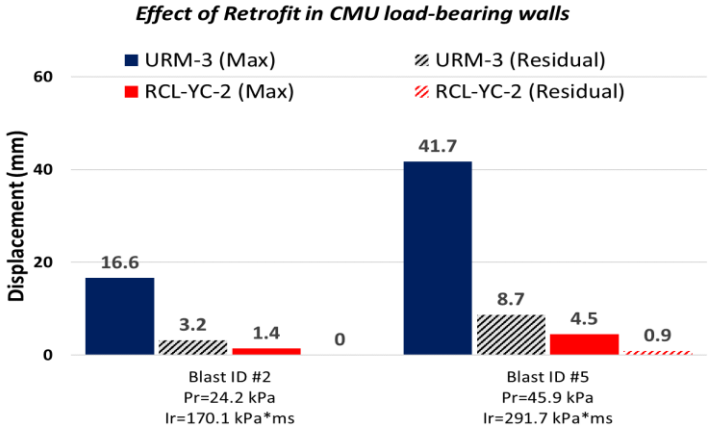

Figure 5-5. Retrofit Performance of Load-Bearing-CMU Walls (URM-3 data from Ciornei, 2012)

Blast ID 3 Damage Comparison: RCL-YC-2 vs URM-3 (Left: Ciornei, 2012)

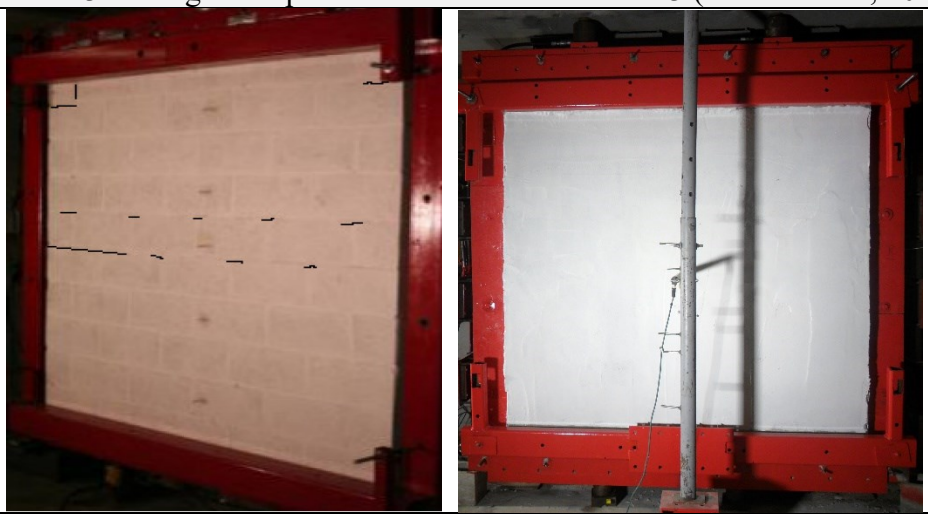

Blast ID 4 Damage Comparison: RCL-YC-2 vs URM-3 (Left: Ciornei, 2012)

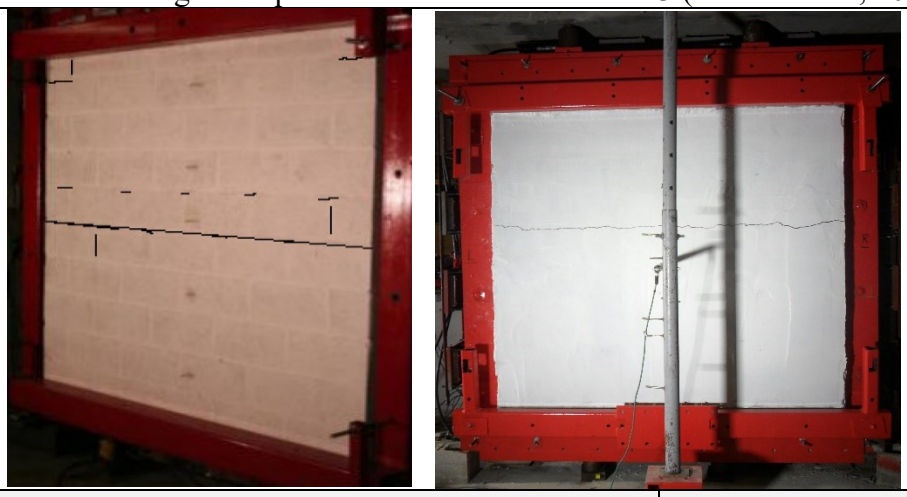

Blast ID 6 Damage Comparison: RCL-YC-2 vs URM-3 (Left: Ciornei, 2012)

Blast ID 13: Failure Mode for RCL-YC-2

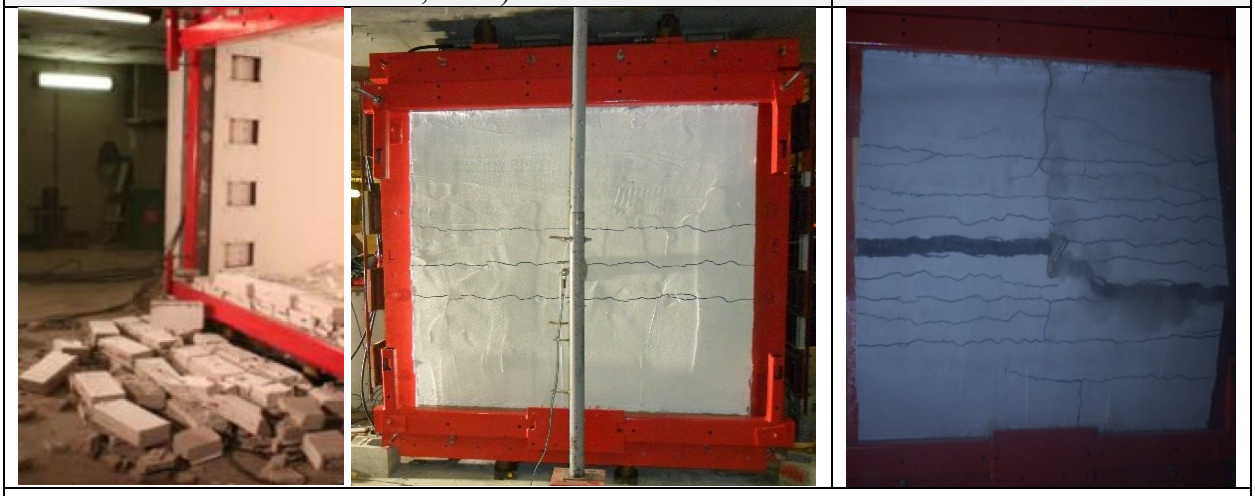

Figure 5-6. Load-Bearing-CMU Walls Retrofit Comparison

Retrofit Performance - RCL-YC-3 vs URM-3

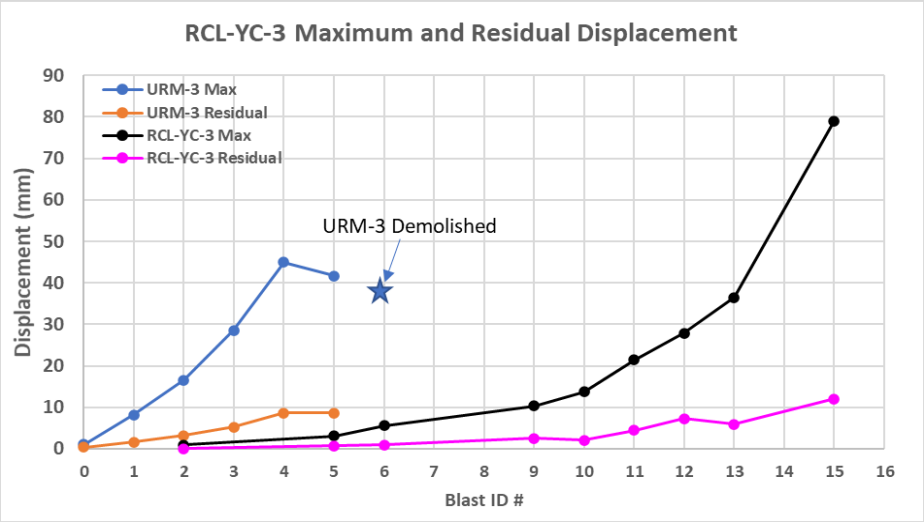

Displacement Time History Comparison

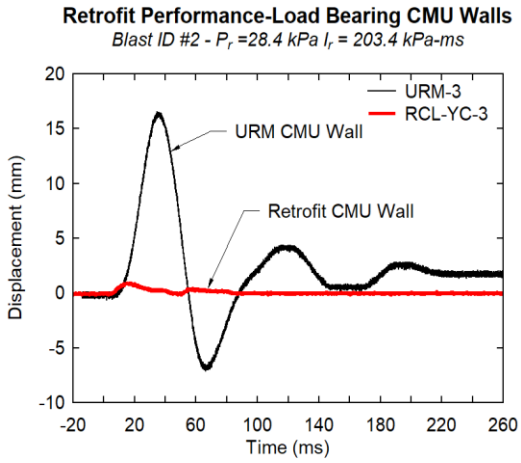

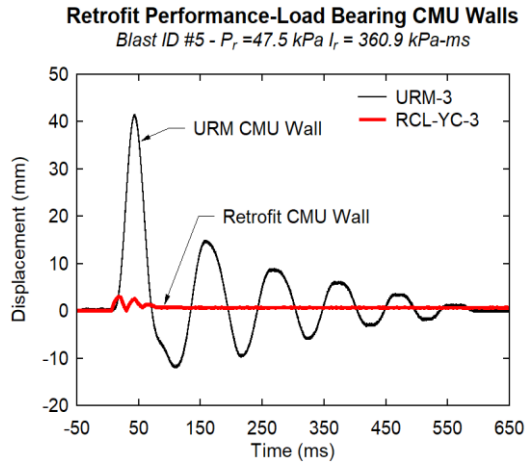

Maximum and Residual Displacements

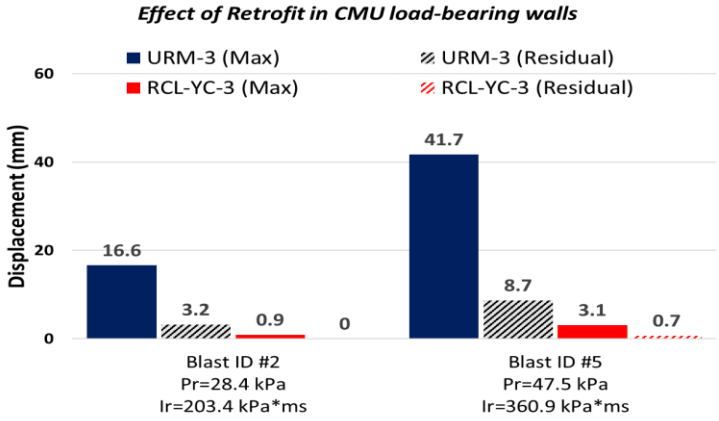

Figure 5-7. Retrofit Performance of Load-Bearing-CMU Walls (URM-3 data from Ciornei, 2012)

Blast ID 3 Damage Comparison: RCL-YC-3 vs URM-3 (Left: Ciornei, 2012)

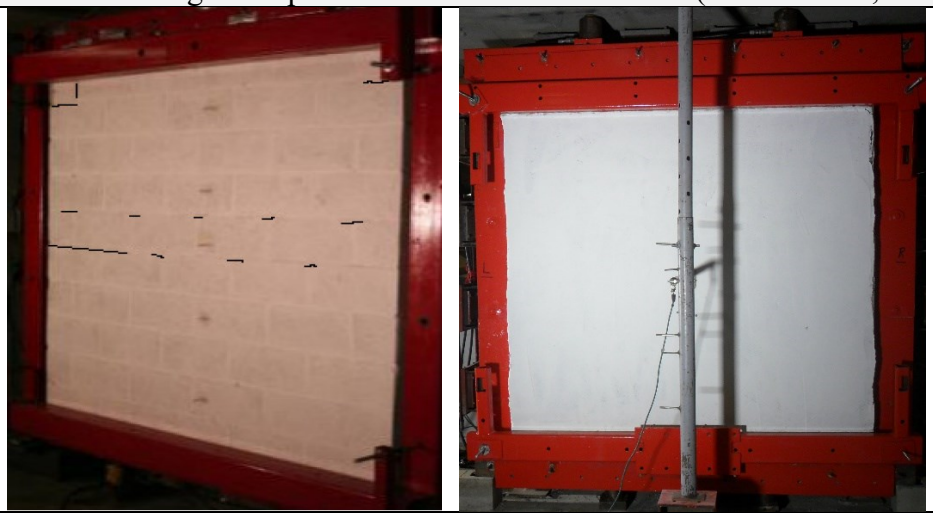

Blast ID 4 Damage Comparison: RCL-YC-3 vs URM-3 (Left: Ciornei, 2012)

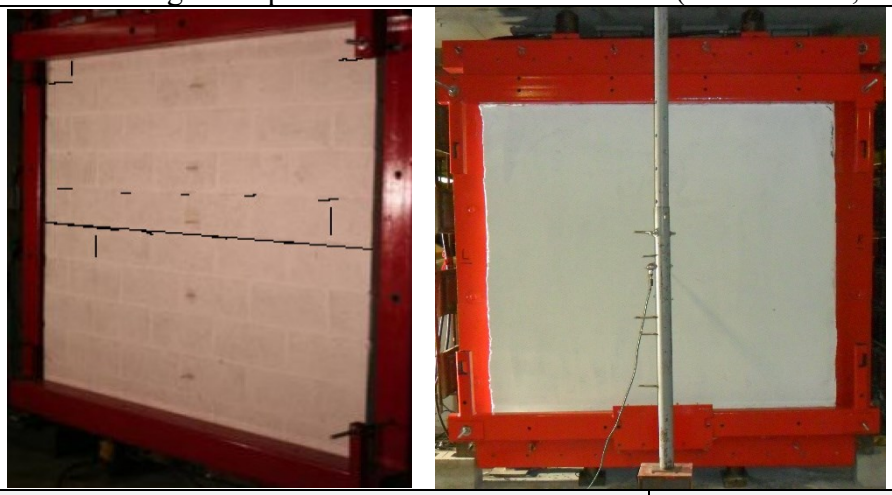

Blast ID 6 Damage Comparison: RCL-YC-3 vs URM-3 (Left: Ciornei, 2012)

Blast ID 15: Failure Mode for RCL-YC-3

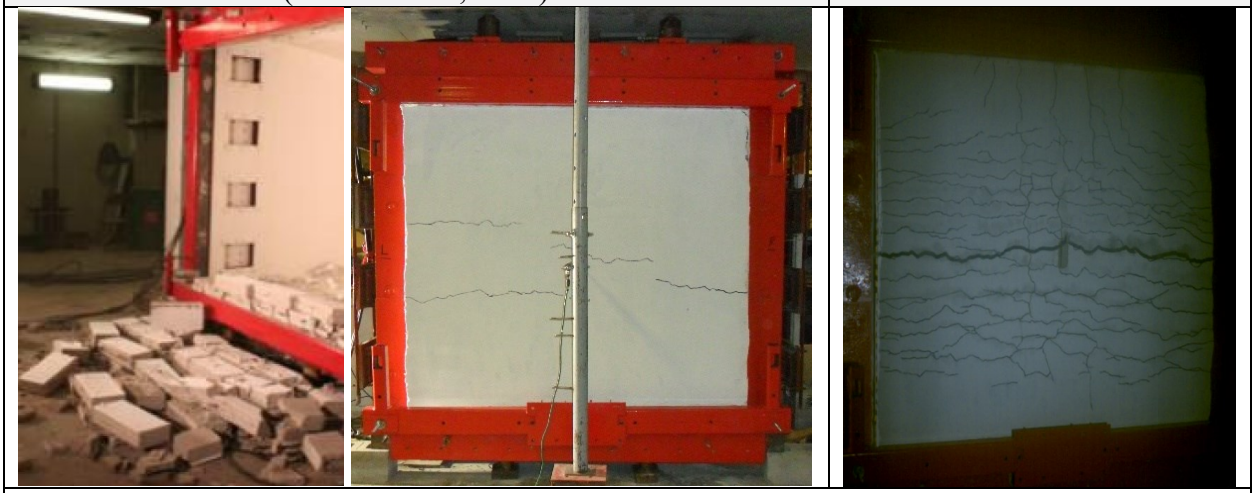

Figure 5-8. Load-Bearing-CMU Walls Retrofit Comparison

5.4. EFFECT OF FRCM LAYERS

5.4.1. Retrofit Ratio Performance: RCL-NC-1, RCL-YC-2 and RCL-YC-3

The effect of the retrofit reinforcement ratio (or FRCM layers) can be studied by comparing the results for walls RCL-NC-1, RCL-YC-2 and RCL-YC-3. All walls were built in the same manner but had the following differences: (1) the retrofit ratio, with 1, 2 and 3 layers of carbon grid in the FRCM-system for RCL-NC-1, RCL-YC-2 and RCL-YC-3, respectively; (2) the other difference is the presence of SCC concrete cast inside the CMU voids for walls RCL-YC-2 and RCL-YC-3. This concrete grouting was applied to avoid shear failure caused by the higher shear demands as the FRCM retrofit ratio is increased. **Figure 5-9** compares the mid-height displacements of the walls during testing and presents selected displacement time history graphs and maximum/residual displacement comparisons. **Figure 5-10** presents photos comparing damage in the walls at the same Blast ID (and therefore similar reflected pressure and impulse), as well as at failure.

The results show that the increase in retrofit ratio resulted in a corresponding enhancement in blast capacity. Increasing the number layers in the FRCM-composite results increased wall moment resistance in the out-of-plane direction. Likewise, the concrete cast inside walls RCL-YC-2 and RCL-YC-3 increased shear capacity, and increased wall mass and stiffness.

RCL-NC-1 (1 layer), was demolished after eight shots at Blast #11 (107.3 kPa, 762.1 kPa-ms). RCL-YC-2 (2 layers), was demolished after eight shots at Blast #13 (89.1 kPa, 1709.1 kPa-ms); thus doubling the number of FRCM layers delayed failure and increased ultimate capacity. The increase in reflected impulse at failure against RCL-NC-1 was 224%. Lastly, RCL-YC-3 (3 layers), failed after nine shots at Blast #15 (111.8 kPa, 2081.4 kPa-ms), allowing for a further increase in blast capacity. The difference in reflected impulse at failure is 273% when compared to against RCL-NC-1, and 122% when compared to RCL-YC-2. It should be noted that wall RCL-YC-3 wall was not demolished at Blast #15 meaning that its ultimate capacity may be higher than reported. No more shots were performed due to the need of higher pressures and the limitations of the shock tube. Nonetheless the wall had many visible damages at the end of testing.

In addition to the increment in blast capacity, increasing the number of carbon grid layers (and the inclusion of SCC concrete) also enhanced control of displacements at equivalent blasts due to the increase in wall stiffness and mass. Indeed, a clear reduction in maximum displacements is observed as the retrofit ratio was increased. When compared to RCL-NC-1, the use of 2 retrofit layers in RCL-YC-2 reduced maximum displacements by -77%, -77%, -64%, -54%, and -53%, at Blasts # 2, 5, 6, 9 and10, with corresponding reductions of -100%, +29%, -52%, -63%, and -47% in residual displacements. Likewise, the use of 3 layers in RCL-YC-3 reduced maximum displacements by of -85%, -84%, -77%, -68%, and -72%, with corresponding reductions of -100%, 0%, -69%, -46%, and -68% in residual displacements, when compared to RCL-NC-1 at these same blasts. Noticeable decreases are also observed when comparing the wall deformations at 3 vs. 2 layers in **Figure 5-9**, although the increment in the displacement reductions are not as significant when compared to 2 vs. 1 layers.

The damage detected on RCL-NC-1, RCL-YC-2 and RCL-YC-3 walls can be correlated to the displacements sustained by the walls during the tests. Generally, the walls with larger FRCM ratios presented less visible damage, for each correspondent blast. The damage observed in the retrofit walls consisted of hairline cracks in the cementitious matrix of the FRCM with crack widths ranging from 0.3mm to 2.0mm, with the gradual development of cracks until reaching the

limitations of the embedded carbon grids. Prior to failure, a more diffused cracking pattern, and reduced crack spacing are observed for wall RCL-YC-3 which had 3 retrofit layers. The walls with 1 and 2 layers failed in a brittle manner, with rupture of the carbon fibers and the subsequent break-up of the walls into 2 or 3 large pieces. While RCL-NC-1 and RCL-YC-2 were completely demolished, wall RCL-YC-3 remained standing at the end of testing. It is also noted that all the retrofitted walls, RCL-NC-1, RCL-YC-2 and RCL-YC-3, failed by flexure as intended, with no shear failure, despite the increase in shear demand which demonstrates the effectiveness of the SCC infill. Although failure was brittle in two of the walls due to rupture of the carbon mesh, limited projectiles were launched at large distances at failure. In all cases, the FRCM-composite system kept the blocks together, without debonding of the FRCM from the CMU substrate.

Retrofit Ratio Performance: RCL-NC-1, RCL-YC-2 and RCL-YC-3

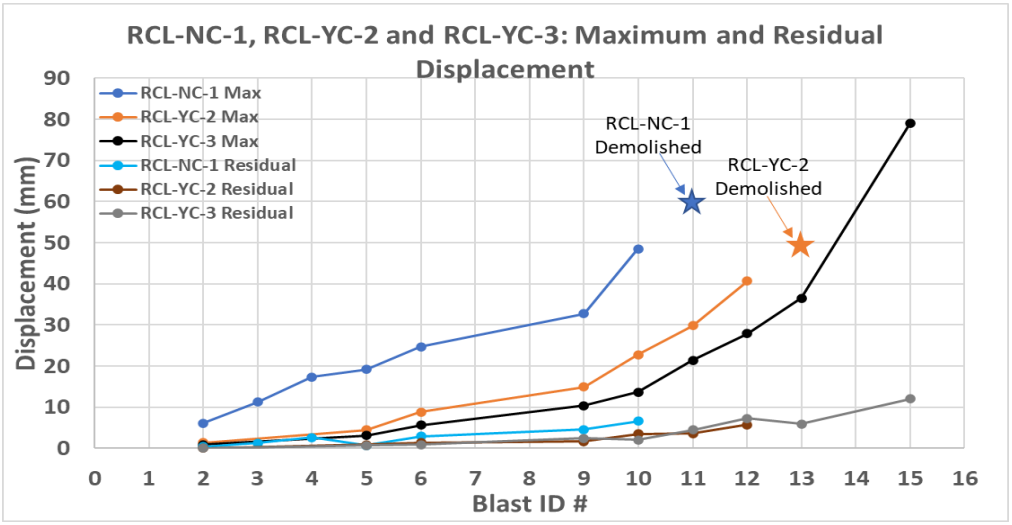

Displacement Time History Comparison

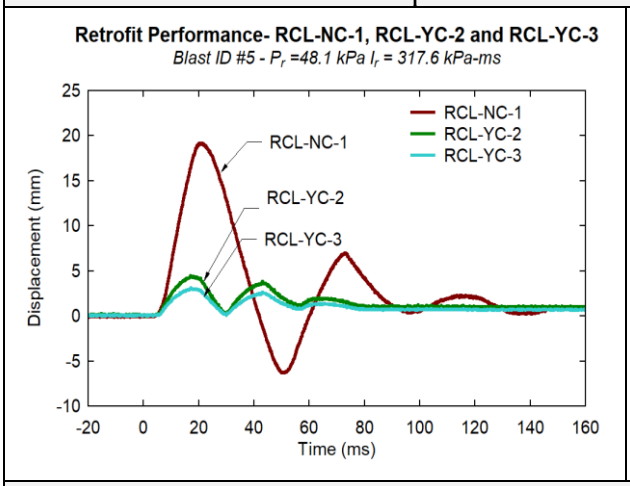

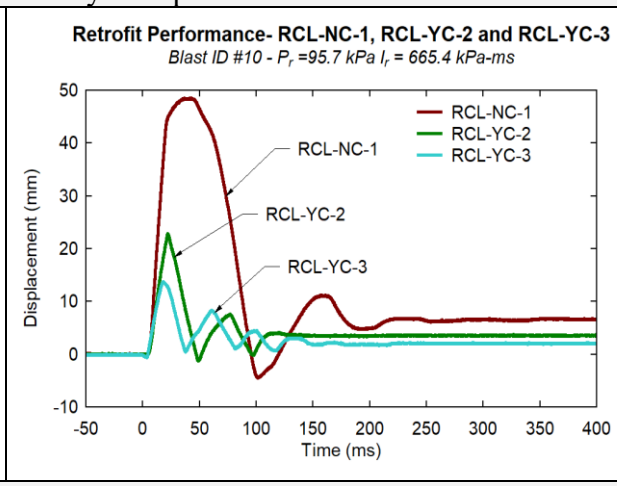

Maximum and Residual Displacements

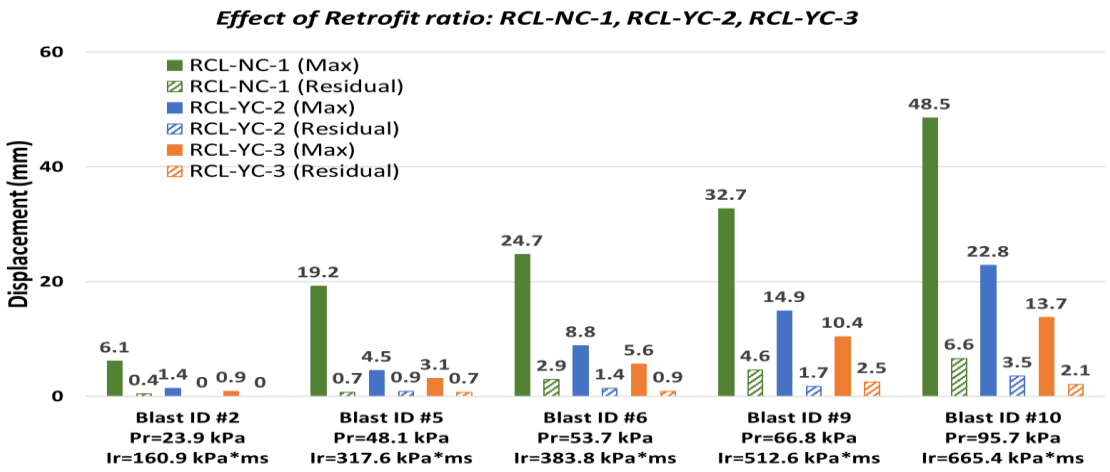

Figure 5-9. Retrofit Ratio Performance: RCL-NC-1, RCL-YC-2, RCL-YC-3

Blast ID 2 Damage Comparison: RCL-NC-1, RCL-YC-2 and RCL-YC-3 (left to right respect.)

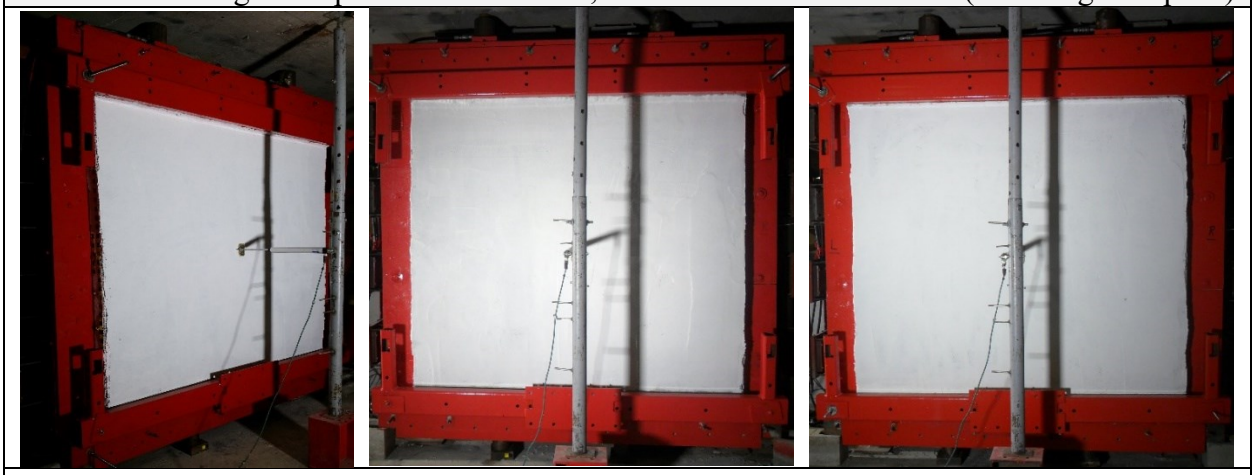

Blast ID 5 Damage Comparison: RCL-NC-1, RCL-YC-2 and RCL-YC-3 (left to right respect.)

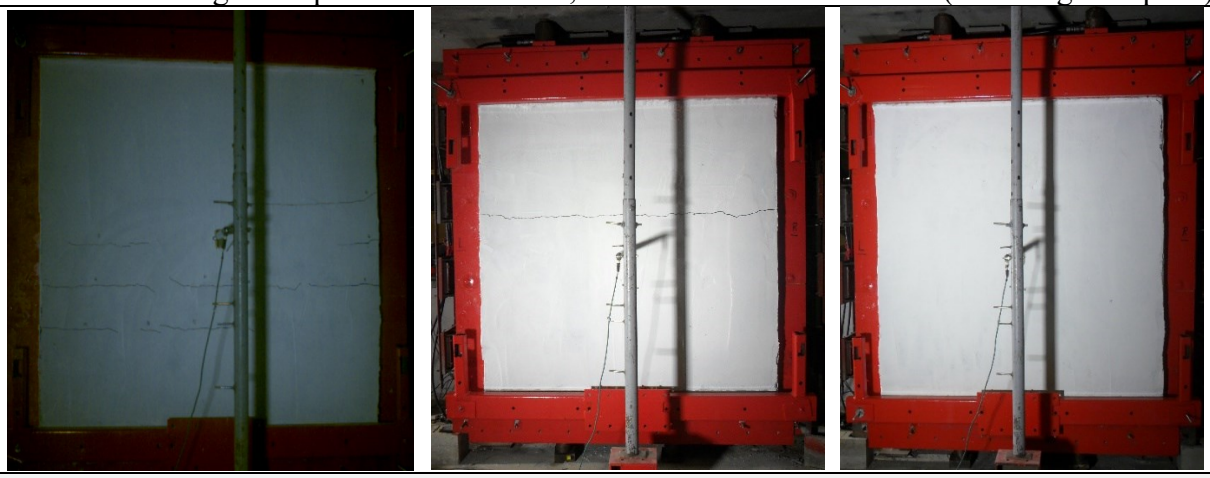

Blast ID 6 Damage Comparison: RCL-NC-1, RCL-YC-2 and RCL-YC-3 (left to right respect.)

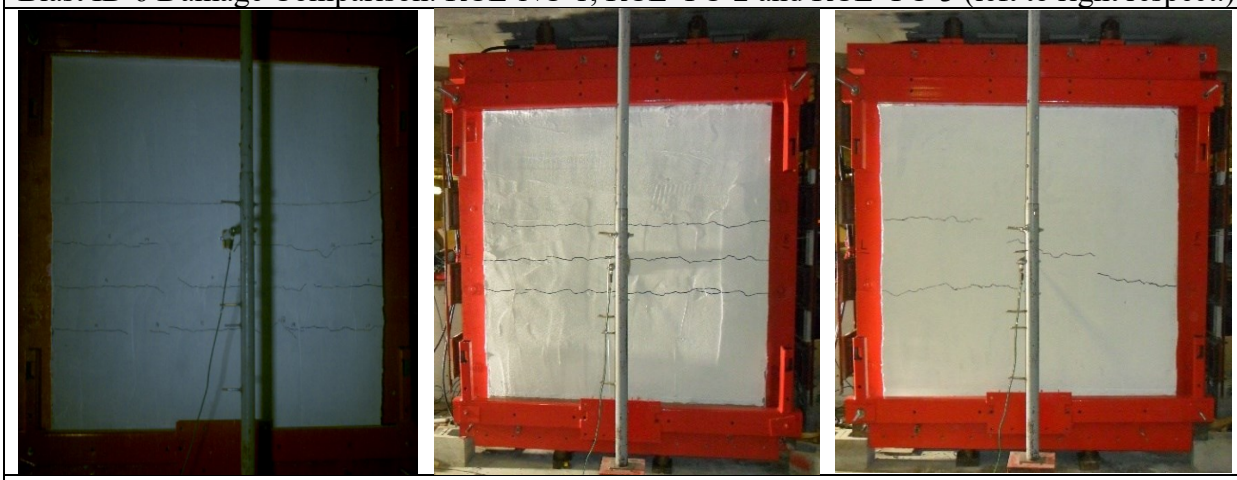

Figure 5-10. Retrofit Ratio Damage Comparison: RCL-NC-1, RCL-YC-2, RCL-YC-3

Blast ID 9 Damage Comparison: RCL-NC-1, RCL-YC-2 and RCL-YC-3 (left to right respect.)

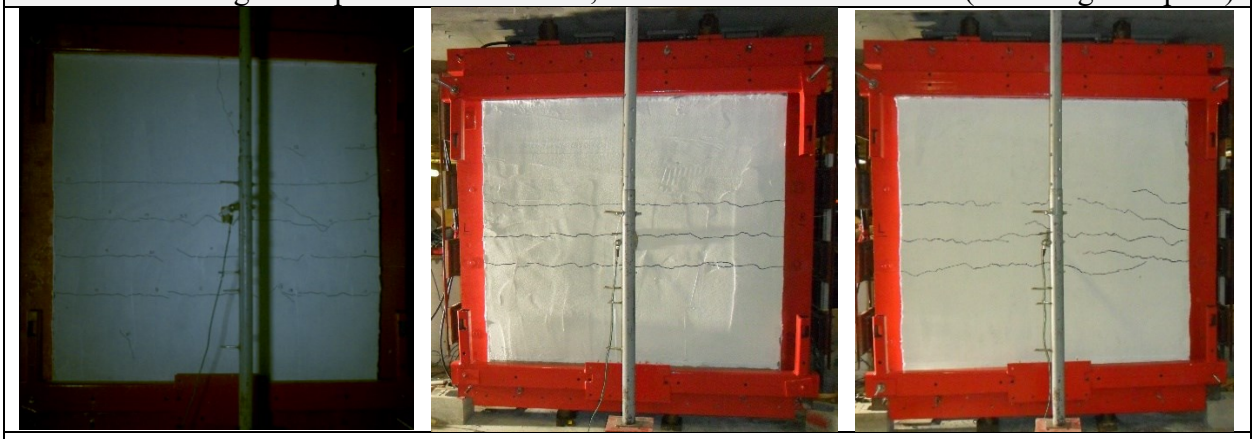

Blast ID 10 Damage Comparison:RCL-NC-1,RCL-YC-2 and RCL-YC-3 (left to right respect.)

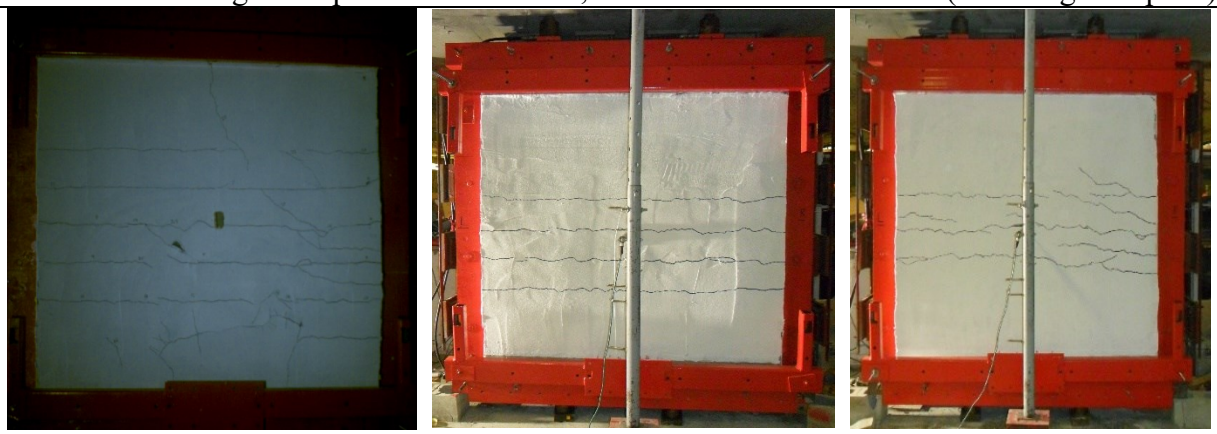

Failure Mode at Blast ID# 11, 13 and 15 for RCL-NC-1, RCL-YC-2 and RCL-YC-3 respectively.

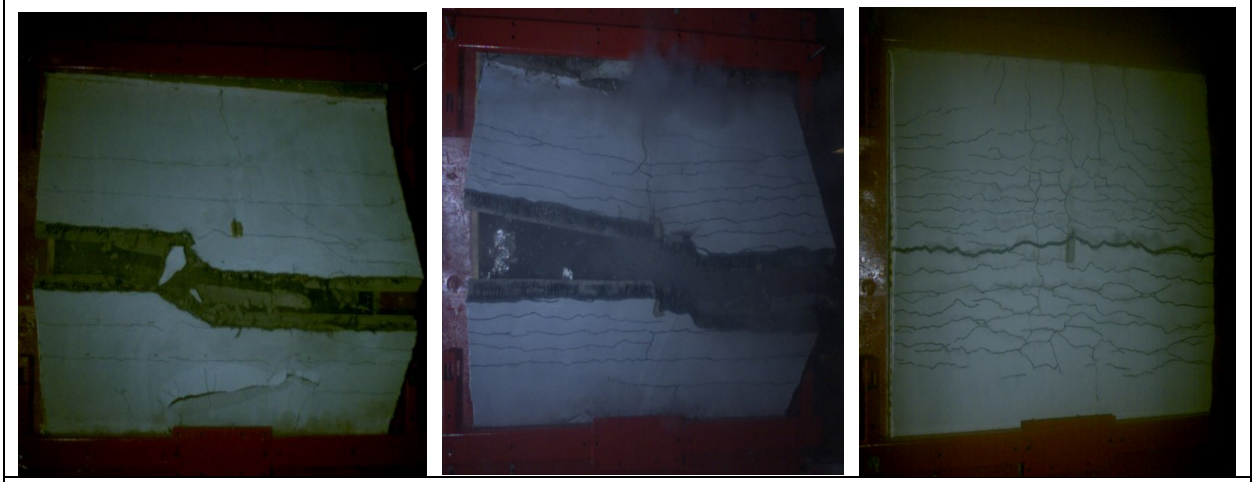

Figure 5-11. Retrofit Ratio Damage Comparison: RCL-NC-1, RCL-YC-2, RCL-YC-3 (continuation)

5.5. EFFECT OF MASONRY TYPE

5.5.1. Load-bearing-retrofitted Walls (Stone vs CMU): R-S-L vs RCL-YC-3

The effect of the FRCM retrofit in walls built with different masonry materials (stone vs CMU) can be examined by comparing the responses of walls R-S-L (tested by Jung, 2020) and RCL-YC-3, tested in this project. The R-S-L wall was built as a Stone-Load-bearing wall, with same dimensions as RCL-YC-3 (2000 x 2000 x 90 mm). In addition, the same Type S mortar was used for the joints, with an matching joint thickness of 10 mm. The walls had axial loads, of 122kN and 171kN on RCL-YC-3 and R-S-L, respectively. These axial loads represent 4 % of the wall nominal axial capacity prior to the application of the retrofit. Both walls were built in the same manner by the same mason and were retrofitted with 3 layers of FRCM composite, applied by the same professional applicators. The few differences include: the use of CMU vs Stone units, the difference in applied axial load, and the fact that RCL-YC-3 wall had concrete cast inside the CMU units to increase shear capacity, whereas the stone wall had solid units.

Figure 5-13 compares the displacements sustained by the walls during testing and presents selected displacement time history graphs and maximum/residual displacement comparisons. **Figure 5-14** presents photos of the walls at equivalent blasts and at failure.

It is observed that the two walls show similar results, with small differences in displacements and overall blast capacity. Both walls failed at the same target loading (i.e. same Blast ID). Wall R-S-L failed in a brittle manner and was demolished after six shots at Blast #15 (Pr=114.3 kPa and Ir=2002.7 kPa-ms); on the other hand, RCL-YC-3, failed after nine shots at Blast #15 (Pr=111.8 kPa, Ir=2443.4 kPa-ms), but it remained standing at the end of testing, despite the relatively larger impulse. The reflected pressure and reflected impulse for RCL-YC-3 wall at failure is 98% and 122%, when compared to R-S-L. As noted before RCL-YC-3 was not demolished at Blast #15, therefore its ultimate resistance may be larger than reported.

Examining the displacements at equivalent blasts, maximum and residual deformations were slightly smaller for the CMU retrofit wall (RCL-YC-3) when compared to the stone retrofit wall (R-S-L). For Blasts #2, #5, #9 and #11, RCL-YC-3 shows reductions of -70%, -44%, -13% and -8% in maximum displacements and -100%, -65%, -49% and -36% in residual displacements when compared against R-S-L, as shown in **Figure 5-13**.

Generally, RCL-YC-3 presented less visible damage than R-S-L, for each correspondent blast as shown in **Figure 5-14**. Nonetheless, prior to failure, the damage observed in both walls consisted of hairline/minor cracks. The stone wall, R-S-L, failed in a brittle manner and was completely demolished, launching some fragments and projectiles. The failure mechanism was a combination of debonding between the stone units and the FRCM mortar, as well as rupture of the carbon fiber mesh at the main crack which opened widely.

On the other hand, RCL-YC-3 did not fail in a brittle manner at the last shot (with same blast ID as R-S-L). Damage was limited to minor crushing of the masonry blocks on the compression side of the wall and a wide crack in the FRCM at midspan, with no rupture of the carbon fibers. Although no further blasting was applied, it is expected that a further increase in impulse would have caused rupture of the carbon grids and brittle collapse as was observed in RCL-NC-1 and RCL-YC-2. It is interesting to note that the debonding failure did not occur in the wall with CMU units, due to increased roughness of the concrete blocks. Thus, it may be important to increase the

bond capacity of the FRCM retrofit when it is applied to stone masonry substrates. **Figure 5-12** shows visible debonding signs on R-S-L wall after the 5th shot.

Figure 5-12. Visible Debonding on R-S-L, 5th shot (side), (Jung, 2020)

Retrofit Performance: RCL-YC-3 vs R-S-L

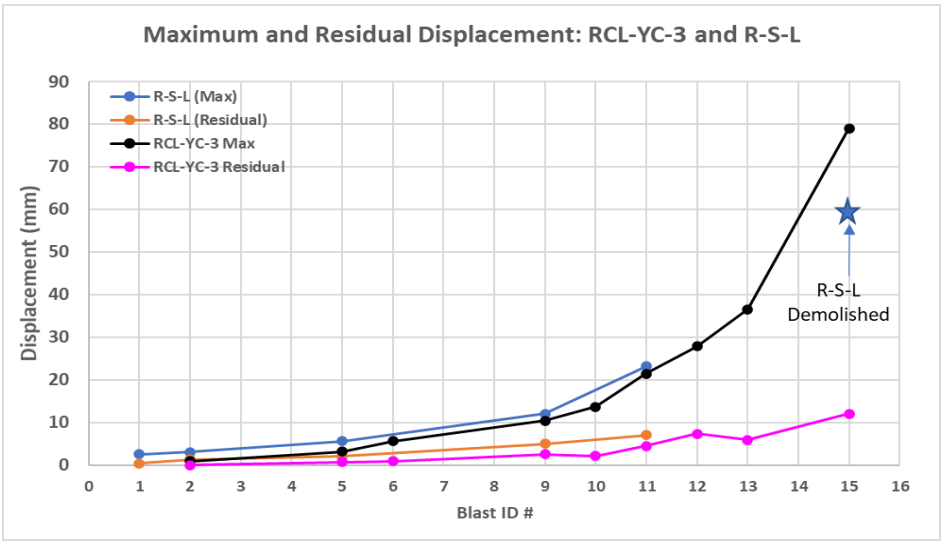

Displacement Time History Comparison: RCL-YC-3 vs R-S-L

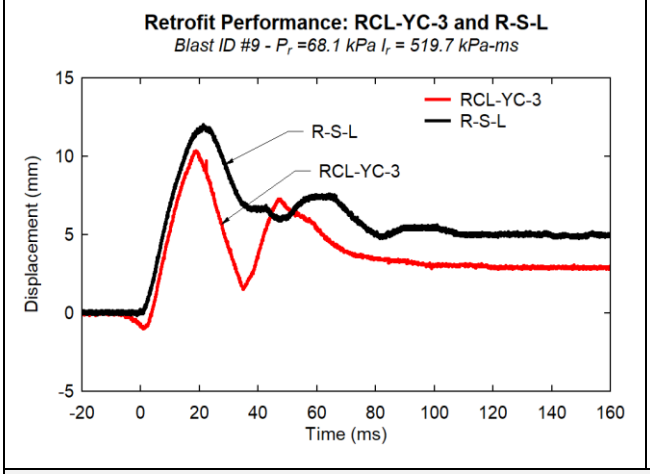

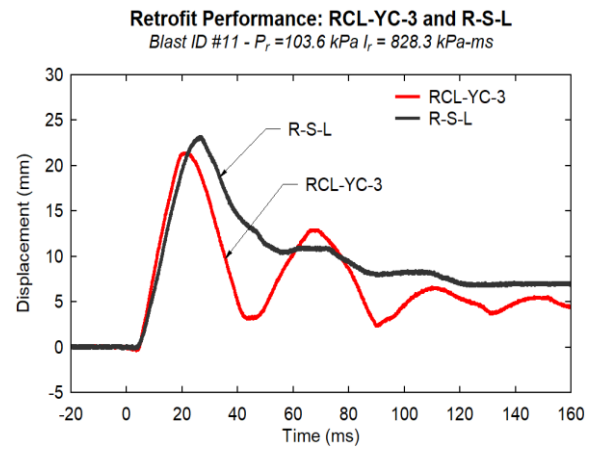

Maximum and Residual Displacements: RCL-YC-3 vs R-S-L

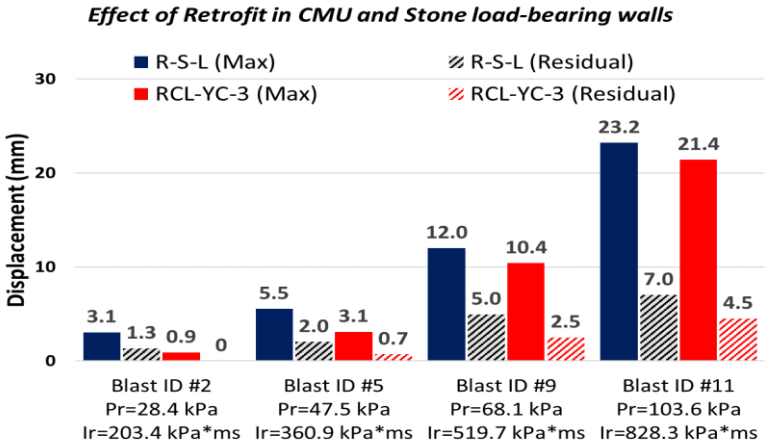

Figure 5-13. Retrofit Performance of Load-Bearing Walls (CMU vs Stone): RCL-YC-3 vs R-S-L (R-S-L data from Jung, 2020)

Blast ID 5 Damage Comparison: RCL-YC-3 vs R-S-L (Left: Jung, 2020)

Blast ID 11 Damage Comparison: RCL-YC-3 vs R-S-L (Left: Jung, 2020)

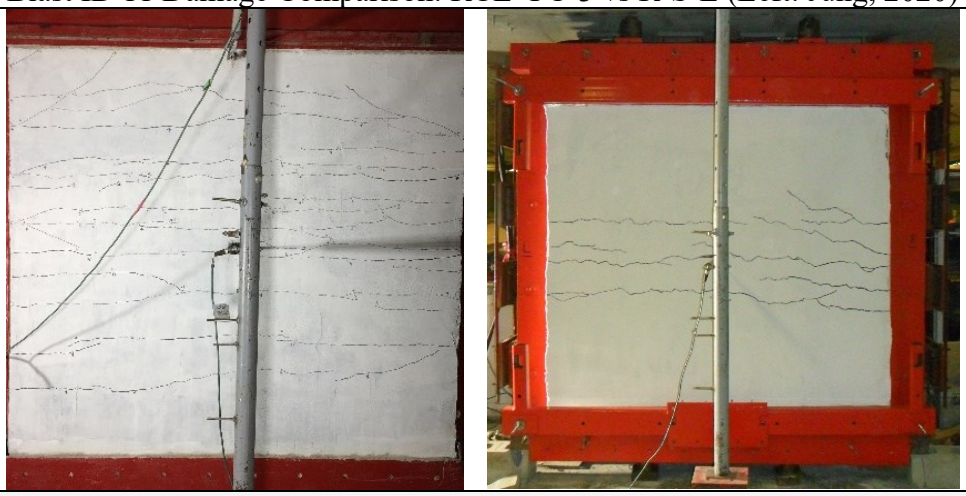

Failure Mode at Blast ID# 15: RCL-YC-3 vs R-S-L (Left: Jung, 2020)

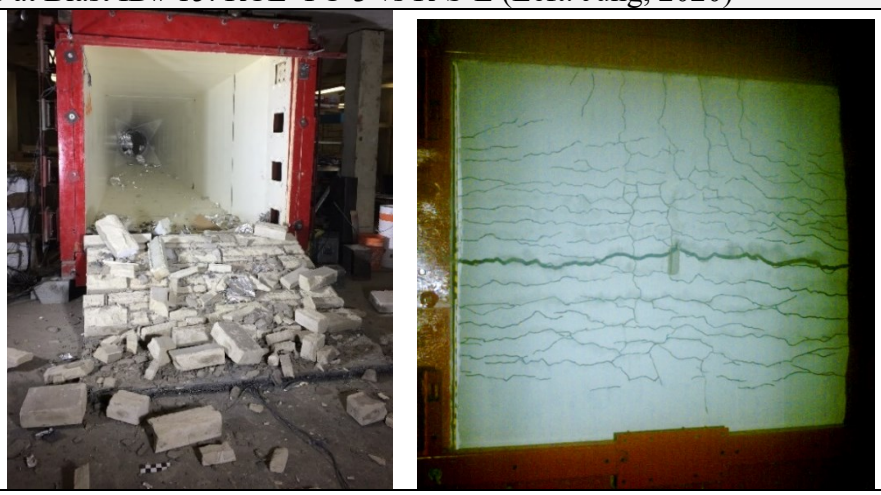

Figure 5-14. Load-Bearing Walls (CMU vs Stone), Retrofit Comparison: RCL-YC-3 vs R-S-L (R-S-L data from Jung, 2020)

5.6. EFFECT OF AXIAL LOAD

5.6.1. Load Bearing vs Infill: RCL-YC-3 vs R-C-N

The effect of axial load on CMU walls retrofitted with FRCM-composite system can be investigated by comparing the response of R-C-N (tested by Jung, 2020) and RCL-YC-3, tested in this project. Wall R-C-N was built as a Retrofitted-CMU-infill (Non-load-bearing) wall, with same planar dimensions and the same type of CMU units used in RCL-YC-3. The wall was also built with the same Type S mortar for the joints and matching joint thickness of 10 mm. Both walls were built by the same mason and retrofitted with 3 layers of FRCM composite applied by the same professional applicators. However, R-C-N was tested an infill wall (no axial load), whereas RCL-YC-3 was subjected to an axial load of 122kN. In addition, to increase shear capacity, RCL-YC-3 was infilled with SCC concrete, whereas this modification was not applied in R-C-N.

Figure 5-16 compares the displacements sustained by the walls during testing and presents selected displacement time history graphs and maximum/residual displacement comparisons. **Figure 5-17** presents photos of the walls during testing and at failure.

It can be observed that the application of the axial load enhanced the blast capacity of RCL-YC-3 as well as its shear capacity. The increase in blast capacity can be related to the presence of axial loading that adds to sectional moment capacity as well as arching action. Moreover, the axial load improves shear capacity by allowing for a better control of shear cracking. The concrete infill increased shear resistance, while also enhancing wall mass and stiffness.

Despite these differences, similar results are observed for both walls with small differences in displacements and ultimate blast capacity. The infill wall (R-C-N) ultimately failed after nine shots at Blast #14 (Pr=86.5 kPa and Ir=1838.2 kPa-ms). In comparison, RCL-YC-3 failed after nine shots, at Blast #15 which had a larger maximum pressure and impulse (Pr=111.8 kPa, Ir=2443.4 kPa-ms). Both walls, remained standing at the end of testing, with noticeable damage but without being demolished. The maximum reflected pressure and reflected impulse for RCL-YC-3 wall are 129% and 133% of the maximums recorded for wall R-C-N. It is important to note that a major shear crack occurred during the early stages of testing in wall R-C-N (see **Figure 5-15**), while shear damage was better controlled in wall RCL-YC-3.

Examining the displacements, the maximum deformations were slightly smaller for the Load-bearing wall (RCL-YC-3) when compared to the infill wall (R-C-N), but the residual displacements were slightly larger. For Blasts #2, #9, #10, #11, #12 and #13 the maximum displacements of RCL-YC-3 compared against R-C-N were reduced by -85%, -35%, -20%, -22%, -34% and -37%, respectively, and the residual displacements were bigger by 0%, +67%, +250%, +22%, +30% and +90%, respectively.

respectively (see **Figure 5-16**).

Generally, RCL-YC-3 presented less visible damage than R-C-N, for each correspondent blast, with less wide cracks. The damage observed in both walls consisted of hairline or fine cracks, which gradually developed during testing. The infill wall, R-C-N, failed with severe crushing of the CMU blocks at the compression side of the wall, and shear damage at the top of the wall. Nevertheless, the retrofit was still standing. RCL-YC-3, survived to a higher loading (Blast ID 15), with only some minor crushing in the compression side of the wall and a wide crack in the FRCM at midspan, with no breakage of the carbon fibers. It is concluded that the axial load, as well as the

concrete cast inside the CMU blocks, were effective in increasing the shear capacity and overall blast performance of wall RCL-YC-3.

Figure 5-15. R-C-N: Premature Shear cracks at 3rd shot (Jung, 2020)

Retrofit Performance: RCL-YC-3 vs R-C-N

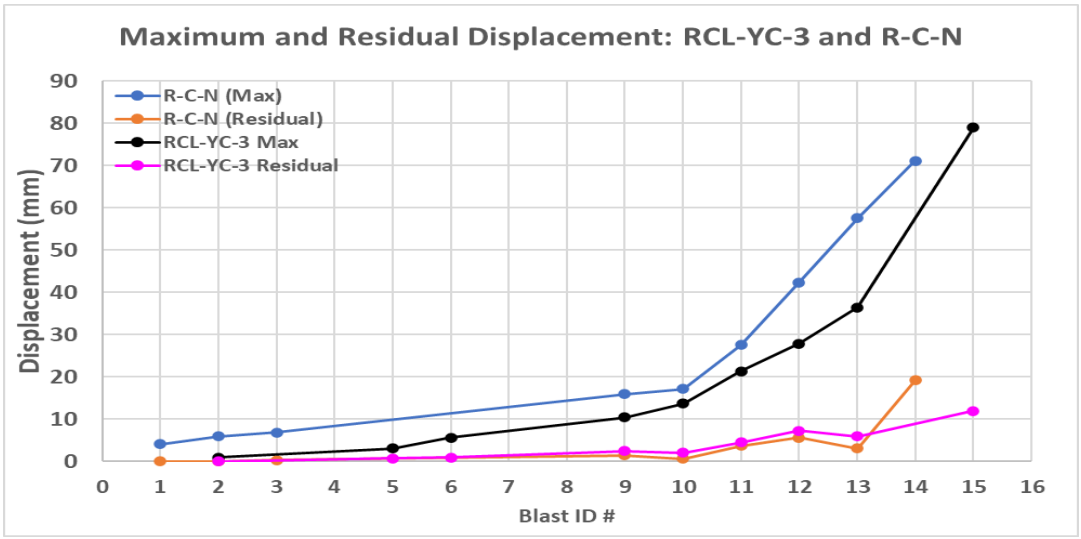

Displacement Time History Comparison: RCL-YC-3 vs R-C-N

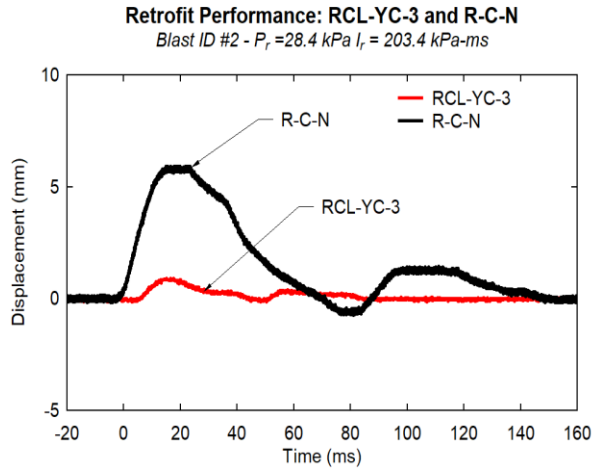

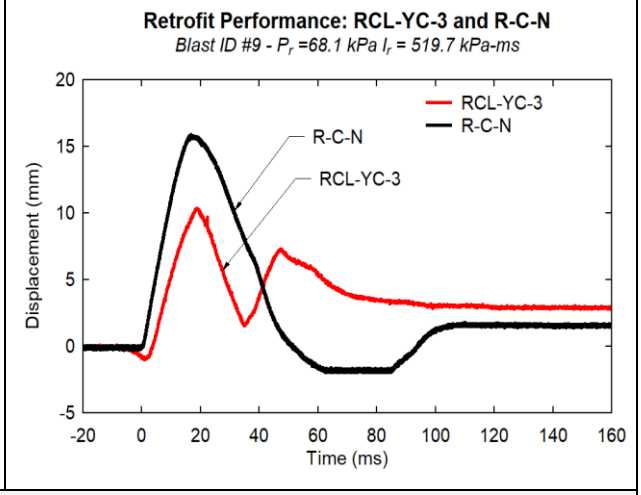

Maximum and Residual Displacements: RCL-YC-3 vs R-C-N

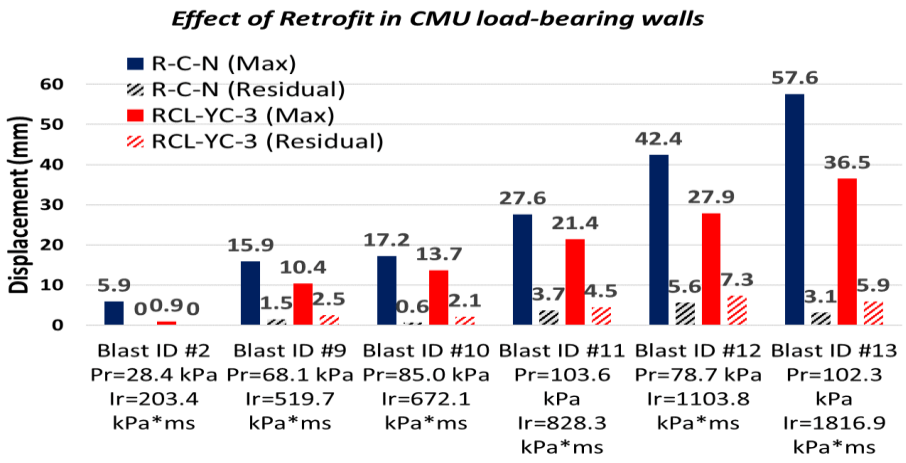

Figure 5-16. Axial Effect on CMU Walls: RCL-YC-3 vs R-C-N (R-C-N data from Jung, 2020)

Blast ID 9 Damage Comparison: RCL-YC-3 vs R-C-N (Left: Jung, 2020)

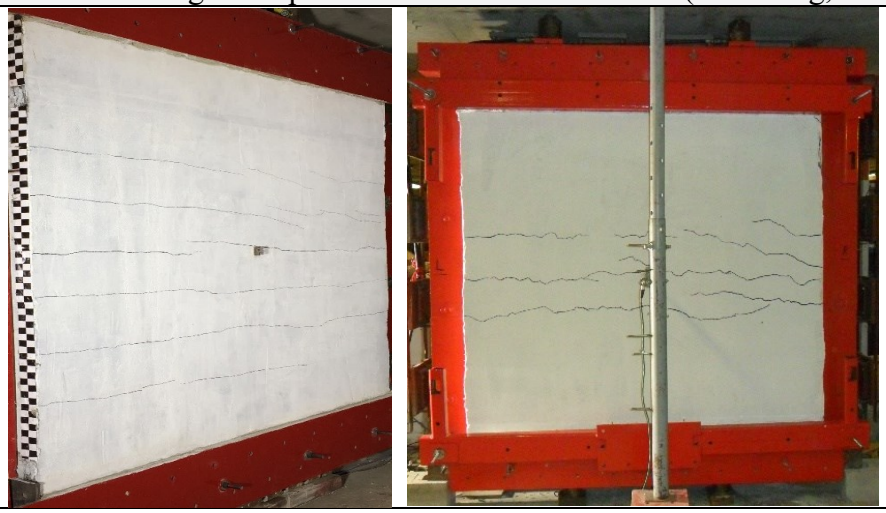

Blast ID 13 Damage Comparison: RCL-YC-3 vs R-C-N (Left: Jung, 2020)

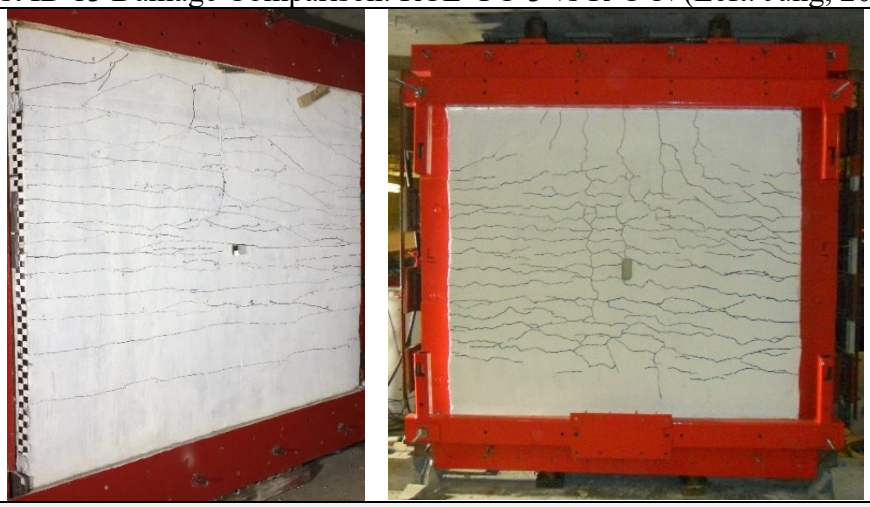

Failure Mode at Blast ID#14&15 for R-C-N & RCL-YC-3 respectively (Left: Jung,2020)

Figure 5-17. Axial Effect on CMU Walls, Performance Comparison:RCL-YC-3 vs R-C-N (R-C-N data from Jung, 2020)

CHAPTER 6. ANALSYSIS

6.1.Overview

This chapter presents the analysis of the walls tested in the research program. First the shear and flexural capacities of the walls were examined to anticipate the failure mode. Thereafter, Single Degree of Freedom (SDOF) analysis was carried out to predict the maximum mid-height displacement of each wall. For this purpose, the idealized resistance curve for each wall was obtained by calculating the wall flexural strength using sectional analysis. In addition, the experimental resistance curve for each wall was obtained from the recorded test data, as a restoring force-deformation relationship to allow for comparison of the theoretical and experimental curves. With the resistance curves established, SDOF analysis was performed to compare the analytical maximum displacements with those obtained from the tests.

6.2. Shear capacity check

The increase in FRCM layers results in increased shear demands in walls subjected to out-of-plane bending. Indeed, previous research by Jung (2019) and Babaeidarabad et al. (2013) shows that shear failure can precede flexure failure if the level of strengthening is excessive. In the current study, shear cracks were seen on wall RCL-YC-3 during testing. In order to analyze this effect, the flexural and shear capacities of the retrofitted walls are computed and compared. The out-of-plane shear capacity of the walls can be calculated according to MSJC (2011) for the case of un-grouted and grouted walls using Eq. 6.1(a) and Eq. 6.1(b), respectively. The shear capacity is also computed according to the CSA S304.1 (2004) code for comparison in Eq. 6.2:

$$\mathbf{V = Min}\left(\mathbf{3.8}A_n\sqrt{f'_m}\,;\mathbf{300}A_n;\mathbf{56}A_n+\mathbf{0.45}N_v\right) \qquad [\mathbf{MSJC\ (2011)}] \qquad [\mathbf{6\text{-}1}(\boldsymbol{a})]$$

$$\mathbf{V = Min}\left(\mathbf{3.8}A_n\sqrt{f'_m}\,;\mathbf{300}A_n;\mathbf{90}A_n+\mathbf{0.45}N_v\right) \qquad [\mathbf{MSJC\ (2011)}] \qquad [\mathbf{6\text{-}1}(\boldsymbol{b})]$$

$$\mathbf{V = 0.16}\sqrt{f'_m}\,A_e+\mathbf{0.25}P_d \le \mathbf{0.4}\sqrt{f'_m}\,A_e \qquad [\mathbf{CSA\ S304.1\ (2004)}] \qquad [\mathbf{6\text{-}2}]$$

Equation 6-1 (a-b) use the Imperial System of units and Equation 6-2 uses the International System of units, where V, A_n, f'_m, and N_v (or P_d) are the out-of-plane shear resistance, net sectional area of the wall, compressive strength of masonry, and axial load applied to the wall, respectively. A_n was 131,400 mm^2 for wall RCL-NC-1, and was 180,000 mm^2 for RCL-YC-2 and RCL-YC-3. For the case of f'_m, it was assumed to be 19.7 MPa and 12.0 MPa (average of prism tests), for walls with SCC cast inside and without SCC, respectively. The axial load, N_v (or P_d) was equal to

122 kN. Different analysis cases (with and without axial load, with and without SCC) are presented in Table 6-1 and Table 6-2.

Using these values and the MSJC equations, the actual shear strength (V_n) is 105.6 kN for wall RCL-NC-1 and 166.6 kN for walls RCL-YC-2 and RCL-YC-3. Based on the assumption in Figure 6-2, the corresponding uniform pressure, $p_{u,v}$ is computed to be 52.8 kPa for RCL-NC-1, and 83.3 kPa for both RCL-YC-2 and RCL-YC-3 (where $p_{u,v} = \frac{2V_n}{H \times L}$, with H: height of the wall, equal to 2m, and L: length of the wall, equal to 2m). In addition, the flexural capacity (M_n) of RCL-NC-1, RCL-YC-2 and RCL-YC-3 was computed following the procedures described later in this Chapter. The flexural capacity (M_n) was found to be 25.3 kN-m, 47.9 kN-m and 66.5 kN-m for walls RCL-NC-1, RCL-YC-2 and RCL-YC-3, respectively. The corresponding pressure $p_{u,f}$ was also computed and was found to be, 25.3 kPa, 47.9 kPa and 66.5 kPa for RCL-NC-1, RCL-YC-2 and RCL-YC-3, respectively (where $p_{u,f} = \frac{8M_n}{H^2}$ and H: height of the wall, equal to 2m). Table 6-1 and Table 6-2 show the results for the shear and flexural capacities, when neglecting and including the SCC and/or the axial load.

The results in Table 6-1 show that while the shear resistance of wall RCL-NC-1 is adequate, walls RCL-YC-2 and RCL-YC-3 would have failed either by shear, or by sudden crushing of the masonry, if no SCC was cast in the masonry cavities. Conversely, as shown in Table 6-2, the casting of SCC inside wall RCL-YC-2 changes its predicted failure mode from shear to flexure, where flexural failure is governed by rupture of the FRCM in tension rather than crushing of masonry in compression. Even with SCC grouting, the failure of wall RCL-YC-3, which had 3 layers of carbon fabric, is predicted to be controlled by shear rather than flexure when axial load is not considered in the analysis, although the shear-to-flexure ratio is nearly 1.0 ($\frac{p_{u,v}}{p_{u,f}} = 0.86$ when using the MSJC equations, and $\frac{p_{u,v}}{p_{u,f}} = 0.99$ when using the CSA S304 formula). When axial load is considered, the SCC in wall RCL-YC-3 allowed the wall to reach its flexural capacity, although the failure mode is predicted to be governed by crushing. Figure 6-1 shows the effects of the high shear demands on wall RCL-YC-3 after all shots were preformed (i.e. after last shot, Blast ID #15).

Table 6-1. Flexural and out-of-plane shear capacities of RCL-NC-1, RCL-YC-2 and RCL-YC-3, without considering SCC cast inside the walls.

No Axial Load Applied and No SCC Cast							
Specimen	No. of plies	Out-of-plane shear (MSJC 2011) [CSA S304.1 (2004)]		Flexural capacity			Governing capacity (MSJC 2011)
		V_n (kN)	$p_{u,v}$ (kPa)	M_n (kN-m)	$p_{u,f}$ (kPa)	Failure*	
RCL-NC-1	1	(50.7) [72.8]	(25.4) [36.4]	19.8	19.8	T	Flexural
RCL-YC-2	2			38.4	38.4	C**	Shear
RCL-YC-3	3			49.1	49.1	C	Shear
With Axial Load Applied (122KN) and No SCC Cast (Note: actual capacity for Wall RCL-NC-1)							
RCL-NC-1	1	(105.6) [103.3]	(52.8) [51.7]	25.3	25.3	T	Flexural
RCL-YC-2	2			37.9	37.9	C	Flexural
RCL-YC-3	3			48.4	48.4	C	Flexural

* T: FRCM failure (in tension side), C: crushing of the masonry

** C: Theoretical analysis shows failure is governed by crushing of the masonry in compression.

Table 6-2. Flexural and out-of-plane shear capacities of RCL-NC-1, RCL-YC-2 and RCL-YC-3, when considering SCC cast inside the walls.

No Axial Load Applied and With SCC Cast							
Specimen	No. of plies	Out-of-plane shear (MSJC 2011) [CSA S304.1 (2004)]		Flexural capacity			Governing capacity (MSJC 2011)
		V_n (kN)	$p_{u,v}$ (kPa)	M_n (kN-m)	$p_{u,f}$ (kPa)	Failure*	
RCL-NC-1	1	(111.7) [127.8]	(55.8) [63.9]	20.2	20.2	T	Flexural
RCL-YC-2	2			41.8	41.8	T	Flexural
RCL-YC-3	3			64.7	64.7	T	Shear
With Axial Load Applied (122KN) and With SCC Cast (Note: actual capacity for Walls RCL-YC2 and RCL-YC-3))							
RCL-NC-1	1	(166.6) [158.3]	(83.3) [79.2]	26.3	26.3	T	Flexural
RCL-YC-2	2			47.9	47.9	T	Flexural
RCL-YC-3	3			66.5	66.5	C**	Flexural

* T: FRCM failure (in tension side), C: crushing of the masonry

** C: Theoretical analysis shows failure is governed by crushing of the masonry in compression.

Figure 6-1. Out-of-plane shear demand on RCL-YC-3 after Blast ID #15

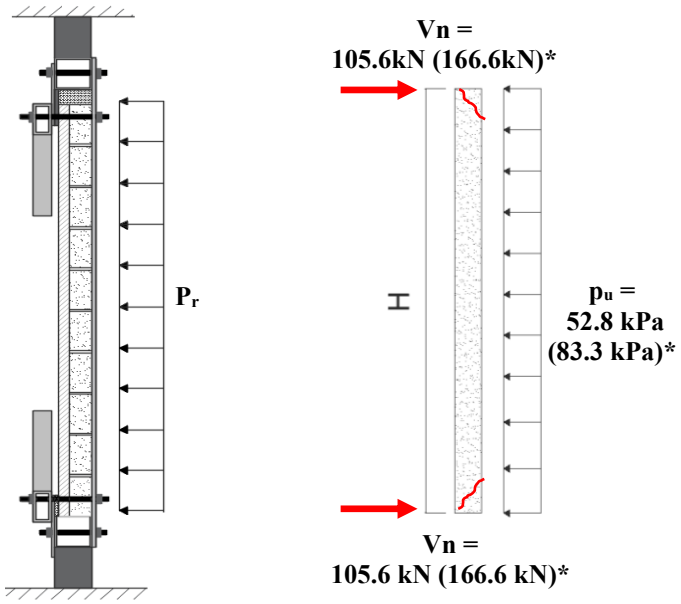

Figure 6-2. Out-of-plane shear strength capacity of RCL-NC-1, RCL-YC-2 and RCL-YC-3

* shear strength capacity of RCL-YC-2 and RCL-YC-3 is presented inside the brackets based on (MSJC 2011).

6.3.Flexural strength calculations

The flexural strengths of the retrofitted walls were computed according to ACI 549.4R (2013) and CSA S304.1 (2004). Sectional analysis was performed based on the following assumptions: i) strain compatibility between the masonry and the FRCM-composite system; ii) plane sections before bending remain plane after bending; iii) the contribution of FRCM prior to cracking is considered. The flexure capacity would be the smaller if failure by crushing of masonry is considered (i.e. when the limiting compressive strain capacity of masonry is exceeded), if FRCM fabric rupturing is observed (i.e. the tensile strain of the fabric exceeds its ultimate tensile capacity), or if FRCM debonding from the masonry substrate is seen. ACI 549.4R (2013) suggests that the minimum length of the FRCM system applied to any substrate should be more than 152 mm (6") to secure effective stress development without fabric pull-out from the FRCM system which was complied in all the specimens in this project.

ACI 549.4R (2013) limits the effective tensile strain (ε_{fe}) of a FRCM system to 0.012, that is the limiting design tensile strain (ε_{fd}) is taken as:

$$\boldsymbol{\varepsilon_{fe} = \varepsilon_{fd} \leq 0.012} \qquad [6\text{-}\mathbf{3}]$$

The effective tensile stress (f_{fe}) can be computed from Equation [6.4], where E_f is the tensile modulus of elasticity of the cracked FRCM system:

$$\boldsymbol{f_{fe} = E_f \varepsilon_{fe}} \qquad [6\text{-}\mathbf{4}]$$

The nominal flexural strength (M_n) is obtained from Equation [6.5]. M_m is the moment contribution of reinforced masonry and M_f is the moment contribution of the FRCM-composite.

$$\boldsymbol{M_n = M_m + M_f} \qquad [6\text{-}\mathbf{5}]$$

The moments M_m and M_f can be computed using sectional analysis as presented in Figure 6-3. The parabolic distribution of the masonry compressive stress is simplified using an equivalent rectangular stress block obtained using the γ and β_1 factors. ACI 549.4R (2013) recommends using 0.7 for both factors (γ and β_1) for simplicity when FRCM failure is the governing failure mode, as it is the case for all three walls tested in this study. The tension force (T) contribution from the FRCM, and the compression force (C) contribution from the masonry can be obtained with Equations [6.6] and [6.7]. For the tensile strain (ε_f) of 2 or more layers of carbon fabric, a single layer of fabric with the same cross-sectional area is assumed to be placed at the centreline of the FRCM composite (Figure 6-3). For the load-bearing walls (RCL-NC-1, RCL-YC-2 and RCL-YC-3), the axial load can be treated as an additional compressive force (C'), applied at the center of the cross section as illustrated in Equation [6.8].

$$\boldsymbol{T = (A_f L) f_f = (A_f L) E_f \varepsilon_f} \qquad [6\text{-}\mathbf{6}]$$

$$\boldsymbol{C = \gamma f'_m (\beta_1 c) L} \qquad [6\text{-}\mathbf{7}]$$

$$\mathbf{C' = f_{cs}(t_m + t_f)L = 122\ KN} \qquad [6\text{-}8]$$

where A_f, L, f'_m, c, t_m, t_f, and f_{cs} are the total area of fabrics, length of the wall, compressive strength of masonry prisms, depth of the neutral axis measured from the extreme compression fiber, thickness of the masonry wall, thickness of the FRCM retrofit, and axial compressive stress due to an axial load, respectively. Finally, the moment taken about the reinforcement on the tension side of the section is obtained with Equation [6.9].

$$\mathbf{M_n = C\left(t_m + \frac{t_f}{2} - \frac{\beta_1 c}{2}\right) - C'\left(\frac{t_m}{2}\right)} \qquad [6\text{-}9]$$

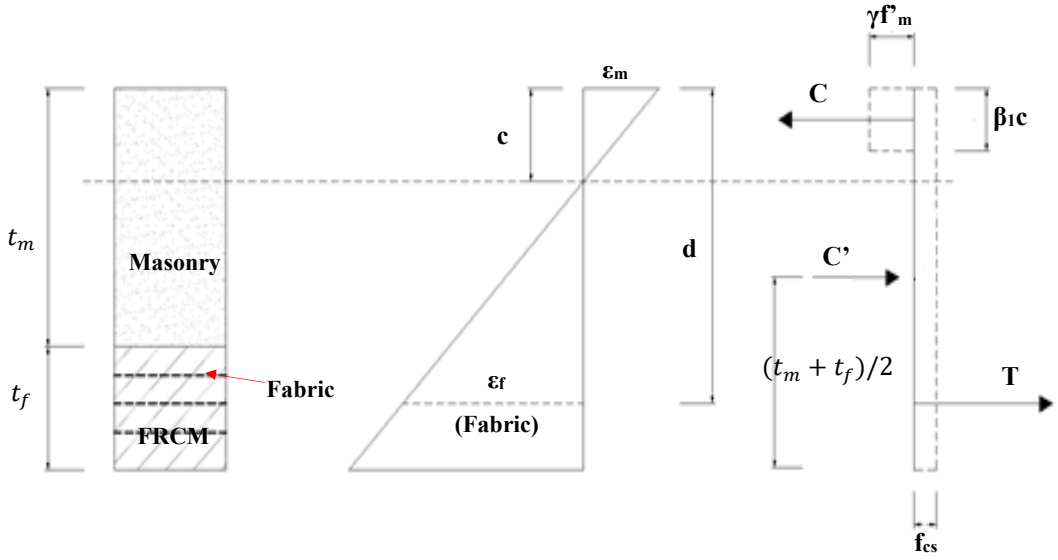

Figure 6-3. Sectional analysis of the FRCM strengthened wall

According to ACI 549.4R (2013), the arching mechanism can be neglected if the wall behaves like a simply supported wall. It can be activated if the wall has stiff supports with a height-to-thickness ratio of less than 8. Furthermore, the out-of-plane shear capacity of a masonry wall is not affected by the FRCM composite.

The cracking flexural strength (M_{cr}) can be obtained in accordance with Equation [6.10], where S and f_r stand for: sectional modulus of the uncracked wall, and modulus of rupture, respectively. For the modulus of rupture of the FRCM retrofitted masonry wall, a weighted average strength (based on relative areas) was used in the calculations, since elastic behavior was assumed in the sectional analysis (Equation [6.11]). The modulus of rupture of the masonry prisms (f_{rm}) was taken as 0.4 MPa for Type S mortar as per CSA S304.1-04 (2004), and the modulus of rupture of FRCM mortar (f_{rfm}) was taken as 4.8 MPa from the manufacturer data sheet.

$$\mathbf{M_{cr} = (f_r + f_{cs})S} \qquad [6\text{-}10]$$

$$\mathbf{f_r = \frac{f_{rm}A_n + f_{rfm}A_{fm}}{A_n + A_{fm}}} \quad [6\text{-}\mathbf{11}]$$

In the above equations, A_n is the net sectional area of masonry, and A_{fm} is the area of the FRCM composite.

According to CSA S304.1-04 (2004), the mid-height deflection of a simply supported wall can be calculated in accordance with Equation [6.12] at cracking (Δ_{cr}), and Equation [6.13] at ultimate (Δ_u), without considering the arching mechanism.

$$\mathbf{\Delta_{cr} = \frac{5M_{cr}H^2}{48E_mI_o}} \quad [6\text{-}\mathbf{12}]$$

$$\mathbf{\Delta_u = \frac{5M_{cr}h^2}{48E_mI_o} + \frac{5(M_n - M_{cr})H^2}{48E_mI_{cr}}} \quad [6\text{-}\mathbf{13}]$$

where h, E_m, I_o are the height of the wall, modulus of elasticity of the masonry wall, and uncracked moment of inertia of the wall, respectively. The modulus of elasticity of the masonry wall can be calculated with Equation [6.14] as per CSA S304.1-04 (2004).

$$\mathbf{E_m = 850f'_m \leq 20000\ MPa} \quad [6\text{-}14]$$

In the above calculations, I_{cr} is the cracked moment of inertia of the wall, and can be obtained according to Equation [6.15]; the transformed section of the retrofitted wall is used.

$$\mathbf{I_{cr} = \frac{Lc^3}{12} + Lc\left(\frac{c}{2}\right)^2 + \frac{E_f}{E_m}A_f\left(t_m + \frac{t_f}{2} - c\right)^2} \quad [6\text{-}\mathbf{15}]$$

Once the flexural strength of the wall is known, the moment can be converted to the corresponding uniformly distributed load (w) and pressure (p) in accordance with Equation [6.16] and [6.17], respectively, with the assumption of simply supported conditions.

$$\mathbf{w = \frac{8M}{H^2}} \quad [6\text{-}\mathbf{16}]$$

$$\mathbf{p = \frac{w}{L}} \quad [6\text{-}\mathbf{17}]$$

Calculation of Flexural strength of RCL-NC-1, RCL-YC-2 and RCL-YC-3

The flexural strength of the retrofitted-CMU-load-bearing wall (RCL-NC-1) was computed in accordance with the procedure described in Section 6.2. The same procedure was also used for walls RCL-YC-2 and RCL-YC-3; however, the SCC in the masonry cavities was considered in the sectional analysis. The static material properties in the walls were acquired from the material tests for the masonry, and from the manufacturer data sheet for the FRCM composite. The

properties used in the analysis of walls RCL-NC-1, RCL-YC-2 and RCL-YC-3 are presented in Table 6-3.

Table 6-3. Material Properties for RCL-NC-1, RCL-YC-2 and RCL-YC-3

SPECIMEN PROPERTIES		RCL-NC-1	RCL-YC-2 RCL-YC-3
Masonry (CMU prism)	Compressive strength (f'_m)	12.0 MPa	19.7 MPa
	Ultimate compressive strain (ε_{mu})	0.0035	0.0035
*FRCM composite	Ultimate tensile strain (ε_{fu})	0.011	0.011
	Ultimate tensile strength (f_{fu})	885 MPa	885 MPa
	Cracked tensile modulus of elasticity(E_f)	49000 MPa	49000 MPa
	Area of a fabric by unit width (A_f)	157 mm^2/m	157 mm^2/m
*FRCM mortar	Modulus of rupture (f_{rfm})	4.8 MPa	4.8 MPa
	Compressive strength (f'_{fm})	52 MPa	52 MPa

* from the data sheet provided by the manufacturer

According to the CSA S850 blast standard, material strengths under blast loads should be increased to account for the effects of high strain rates. Therefore, a Dynamic Increase Factor (DIF) of 1.2 was used for the masonry strengths in tension and compression (based on the assumption of flexural failure under far field blasts). For the FRCM composite, no DIF is available. However, in this research, a DIF of 1.2 was also assumed for the FRCM given its similarity with concrete.

The moment capacities and displacements at cracking (M_{cr}, Δ_{cr}) and ultimate (M_u, Δ_u) obtained using the dynamic material properties and the sectional analysis procedure are summarized in Table 6-4. The table also reports the corresponding uniform distributed loads (w_{cr} and w_u, where $w = \frac{8M}{H^2}$) and pressures (p_{cr} and p_u, where $p = \frac{w}{L}$).

Table 6-4. Analytical flexural strength of RCL-NC-1, RCL-YC-2 and RCL-YC-3

	at cracking				ultimate capacity			
Specimen	M_{cr} (kN-m)	Δ_{cr} (mm)	w_{cr} (kN/m)	p_{cr} (kPa)	M_u (kN-m)	Δ_u (mm)	w_u (kN/m)	p_u (kPa)
RCL-NC-1	9.7	1.4	19.3	9.7	25.3	20.5	50.6	25.3
RCL-YC-2	19.9	0.9	39.7	19.9	47.9	29.2	95.8	47.9
RCL-YC-3	26.1	0.9	52.2	26.1	66.5	25.0	132.9	66.5

6.4.Experimental restoring functions

The internal restoring force-displacement relationship of a masonry wall under blast loading can be experimentally derived if the wall behaviour is simplified using a single degree of freedom (SDOF) system. Equation [6.18] shows the generalized equation of motion of a SDOF system:

$$\mathbf{m\ddot{u}(t) + c\dot{u}(t) + ku(t) = F(t)} \qquad [6\text{-}\mathbf{18}]$$

where, m is the mass; $\ddot{u}(t)$, $\dot{u}(t)$ and $u(t)$ are the acceleration; velocity and displacement of the wall at mid-height; c = damping coefficient; k = stiffness; and F(t) = applied load as a function of time. Ignoring damping, Equation [6.19] is obtained:

$$\mathbf{K_{LM}m\ddot{u}(t) + R(t) = F(t)} \qquad [6\text{-}\mathbf{19}]$$

where, R(t) is the wall restoring force and K_{LM} is load mass factor which converts the real system into an equivalent SDOF system. This factor depends on the wall shape function (UFC 3-340-02, 2008) and can be taken as 0.78 for a wall subjected to uniformly distrusted load in one-way bending. F(t) is the forcing function which describes loading over time, which can be calculated as $P_r(t) \times A$ (reflected pressure measured in the experiments as a function of time × the loaded area of the wall).

The acceleration $\ddot{u}(t)$ can be obtained numerically by differentiating the displacement function measured by the LVDTs/camera during the tests twice. In order to smooth out the measured displacement and remove the noise, a fourth-degree polynomial was used to fit the displacement data. Since the mass (m) and acceleration ($\ddot{u}(t)$) are known quantities, and the forcing function is measured for each test, the restoring force, R(t) can then be found by rearranging Equation [6.19], i.e. $R(t) = F(t) - K_{LM}m\ddot{u}(t)$). This force was then plotted against the wall mid-height displacement to determine the wall restoring force-displacement relationships for each blast test.

Experimentally-derived restoring force function of RCL-NC-1, RCL-YC-2 and RCL-YC-3

The restoring force functions for the walls RCL-NC-1, RCL-YC-2 and RCL-YC-3 were obtained using the procedure explained above. The first step was to describe the displacement function using a polynomial equation over the first positive cycle of response. Figure 6-4 shows one example of this for each wall for Blast ID #10. The next step was to compute the velocity and acceleration of the walls by differentiating the polynomial equation obtained from the first step. Figure 6-5 shows an example of this for each wall, for the same Blast ID shot. Then, the inertia force can be computed as a function of time by multiplying the wall mass and the load mass factor with the acceleration values at each point of time. Using the applied force and calculated inertia function, the restoring force can be obtained using Equation [6.19]. Figure 6-6 shows sample results for this step for the same Blast ID shot.

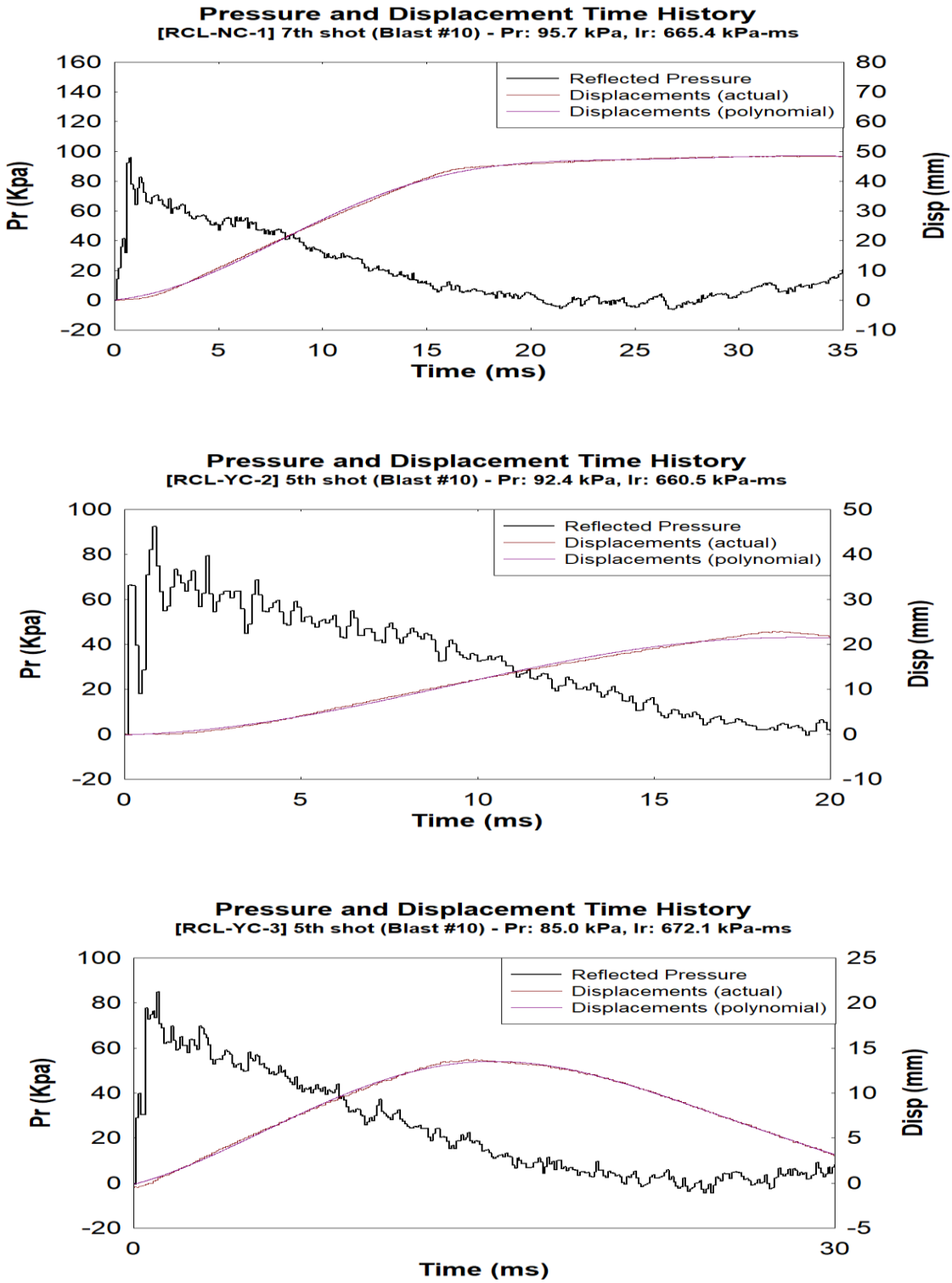

Figure 6-4. A polynomial matching to the actual displacement time history of RCL-NC-1, RCL-YC-2 and RCL-YC-3, respectively.

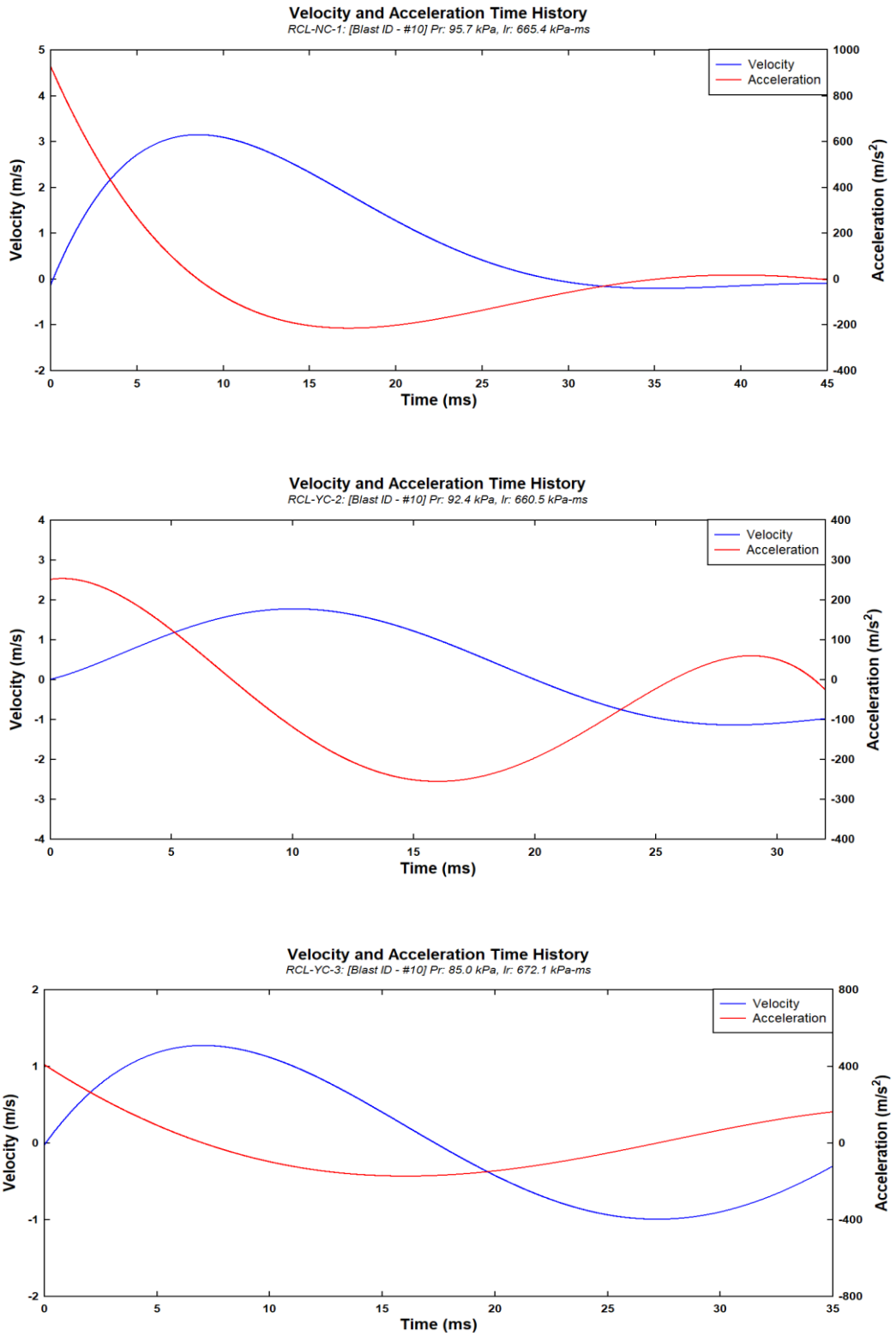

Figure 6-5. Velocity and acceleration curves of RCL-NC-1, RCL-YC-2 and RCL-YC-3, respectively.

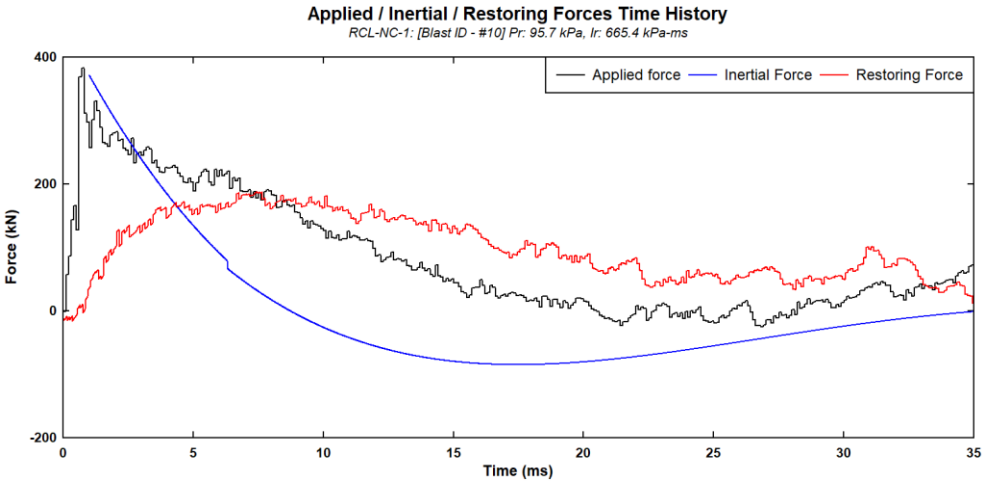

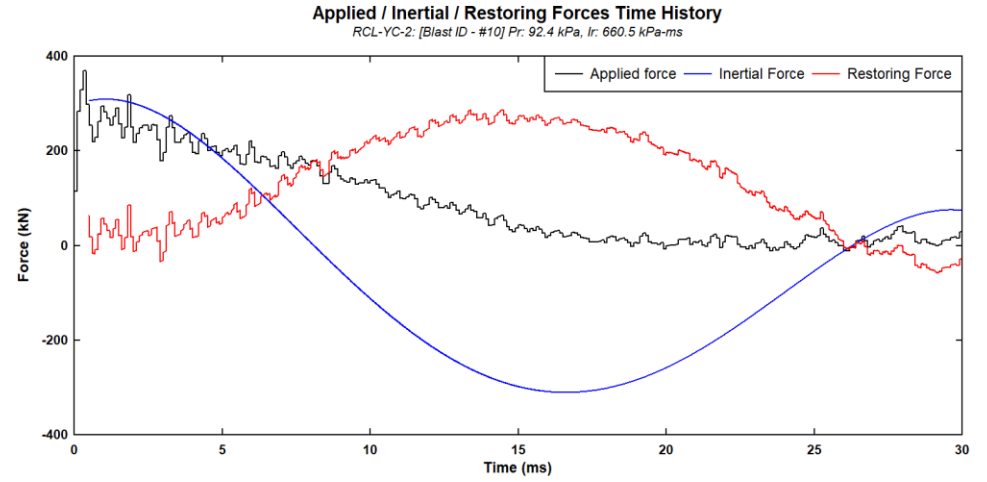

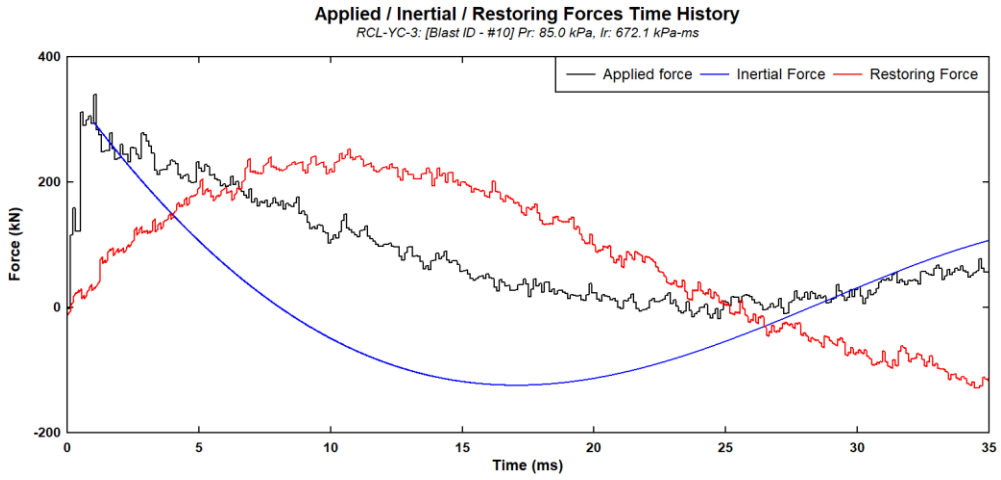

Figure 6-6. Inertial, applied, and restoring forces of RCL-NC-1, RCL-YC-2 and RCL-YC-3, respectively.

Finally, the restoring force time history can be replotted to obtain the relationship between the restoring force and the mid-height displacement at the same time points as shown in Figure 6-7. The results for all test shots of RCL-NC-1, RCL-YC-2 and RCL-YC-3 were obtained in the same manner and they are presented in Figure 6-8.

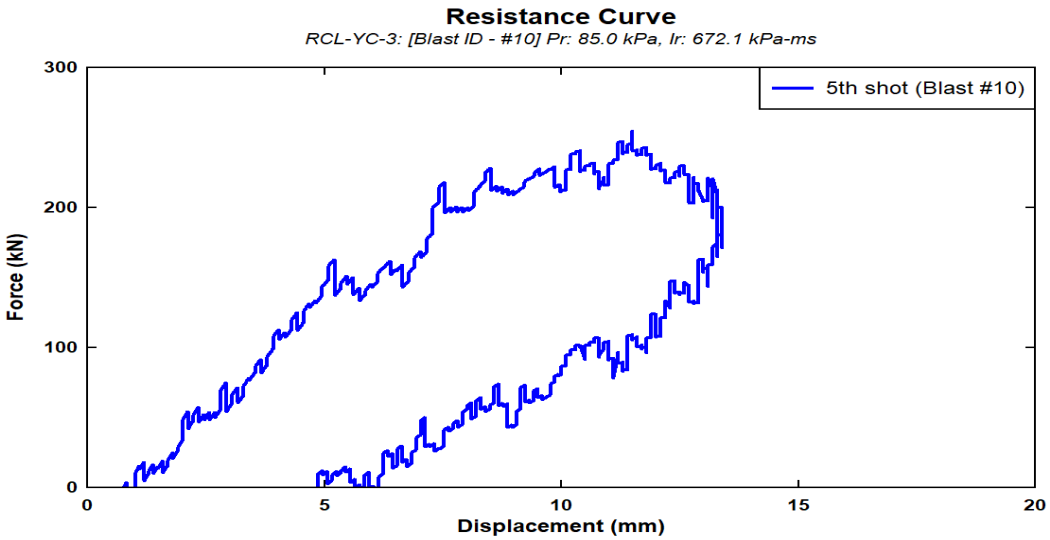

Figure 6-7. Sample restoring function for wall RCL-YC-3

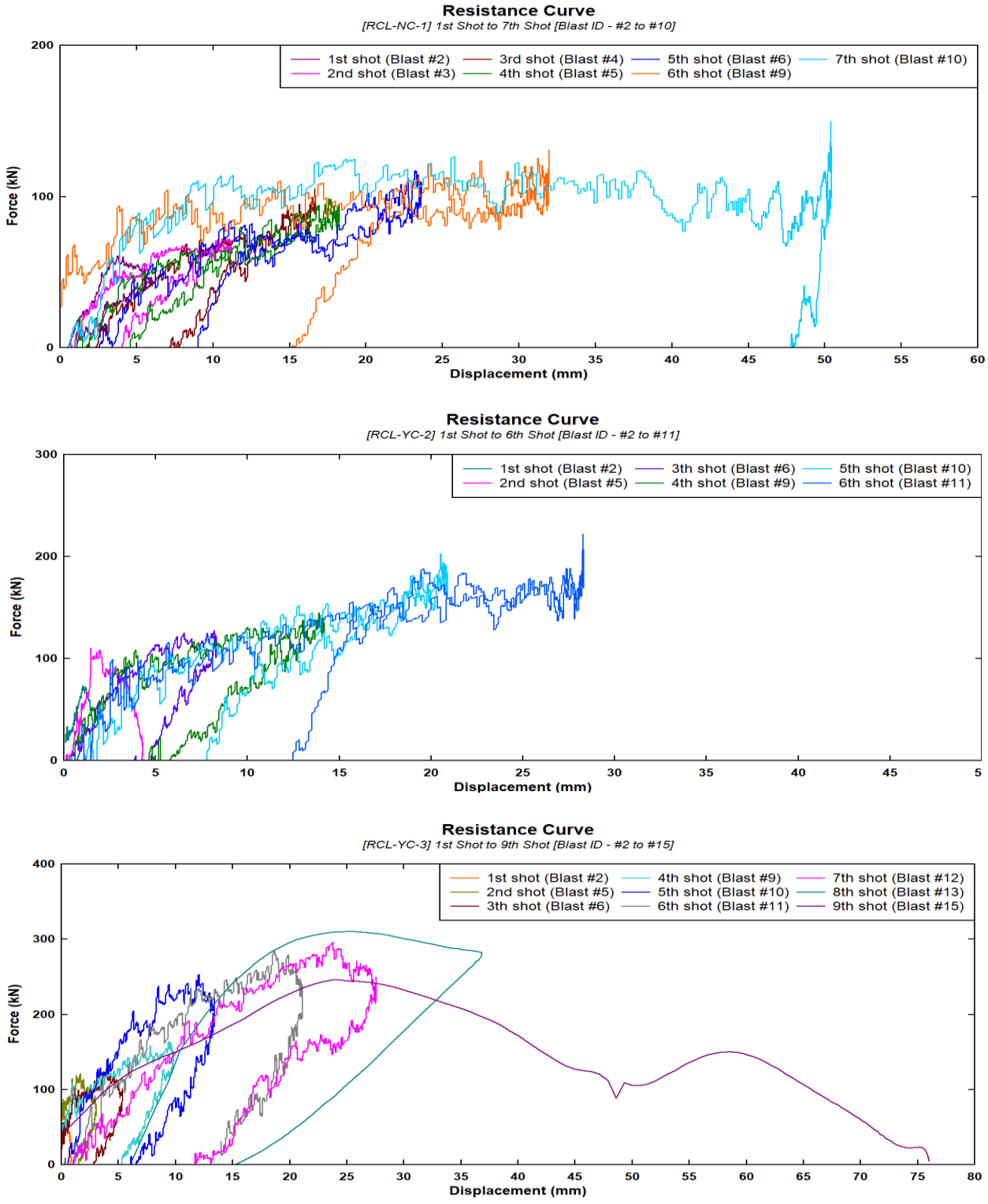

Figure 6-8. Restoring functions for RCL-NC-1, RCL-YC-2 and RCL-YC-3, respectively.

6.5.Idealized Resistance Curves

Idealized resistance curve of RCL-NC-1, RCL-YC-2 and RCL-YC-3

The idealized resistance curve of a CMU wall retrofitted with FRCM is presumed to have a tri-linear load deflection relationship with 3 linear stages of behaviour: i) elastic behaviour up to the cracking moment, ii) post-cracking response up to the ultimate resistance, and iii) strength decay region. The cracking and ultimate capacities of RCL-NC-1, RCL-YC-2 and RCL-YC-3 were computed before in Section 6.3, and the resistance force (F) can be obtained with Equation [6.19].

$$\mathbf{F = wL} \qquad [6\text{-}20]$$

where, w is the uniformly distributed load computed with Equation [6-16], and L is the length of the wall. The slope of the elastic region (first segment) can be obtained using Equation [6.21], and represents the uncracked stiffness of the wall:

$$\mathbf{k_1 = \frac{384 E_m I_o}{5H^3}} \qquad [6\text{-}21]$$

In the same manner, the slope of the post cracking region (the second segment) can be obtained using Equation [6.22]:

$$\mathbf{k_2 = \frac{384 E_m I_{cr}}{5H^3}} \qquad [6\text{-}22]$$

Finally, the slope of the strength decay region (the third segment) should be defined. In this study this portion of the idealized curve was assumed to have a plateau after the ultimate point up to the maximum displacement (dashed line in Figure 6-9). For the purpose of the dynamic analysis, the maximum displacements were taken as 50 mm, 41 mm and 40 mm for RCL-NC-1, RCL-YC-2 and RCL-YC-3, respectively. The various points which define the resistance curve are presented in Table 6-5, and the idealized resistance functions of RCL-NC-1, RCL-YC-2 and RCL-YC-3 are shown in Figure 6-9. The idealized resistance curves are compared to the experimentally-derived resistance (restoring) functions in Figure 6-10. In general, it can be observed that the analytical and experimentally-obtained curves are similar. It should be noted that experimental functions include the effects of accumulated damage, whereas this effect was ignored in the analysis. Nonetheless, it can be observed that the idealized curves match the behaviour presented in the experimental restoring functions with sufficient accuracy.

Table 6-5. Computed values for each segment of the idealized resistance curve

Specimen	1st segment			2nd segment			3rd segment*
	F_{cr} (kN)	Δ_{cr} (mm)	k_1 (kN/mm)	F_u	Δ_u	k_2	k_3
RCL-NC-1	38.6	1.4	28.3	101.1	20.5	3.3	-
RCL-YC-2	79.5	0.9	93.1	191.6	29.2	4.0	-
RCL-YC-3	104.4	0.9	121.9	265.9	25.0	6.7	-

* Assumed to be a plateau up to $\Delta = 50, 41,$ and 40 mm for walls RCL-NC-1, RCL-YC-2 and RCL-YC-3, respectively.

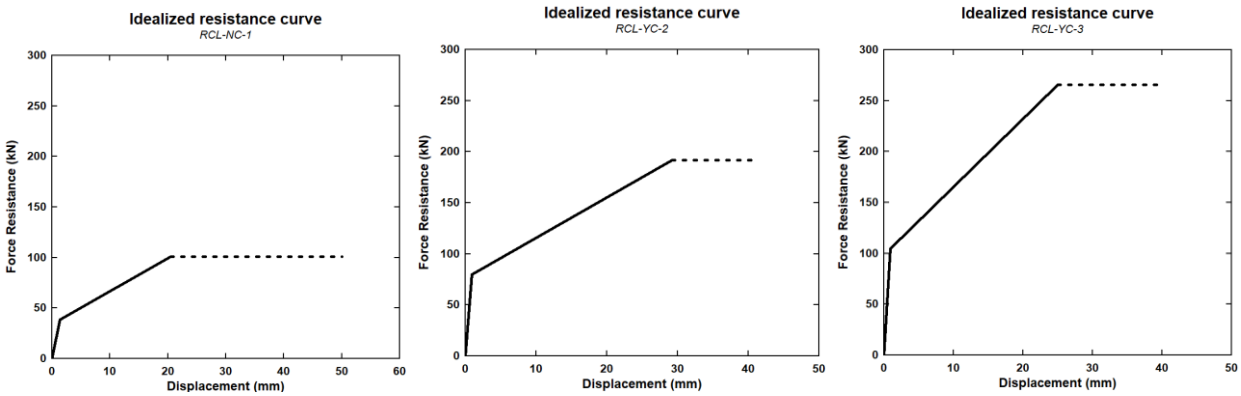

Figure 6-9. Idealized resistance curves for walls RCL-NC-1, RCL-YC-2 and RCL-YC-3.

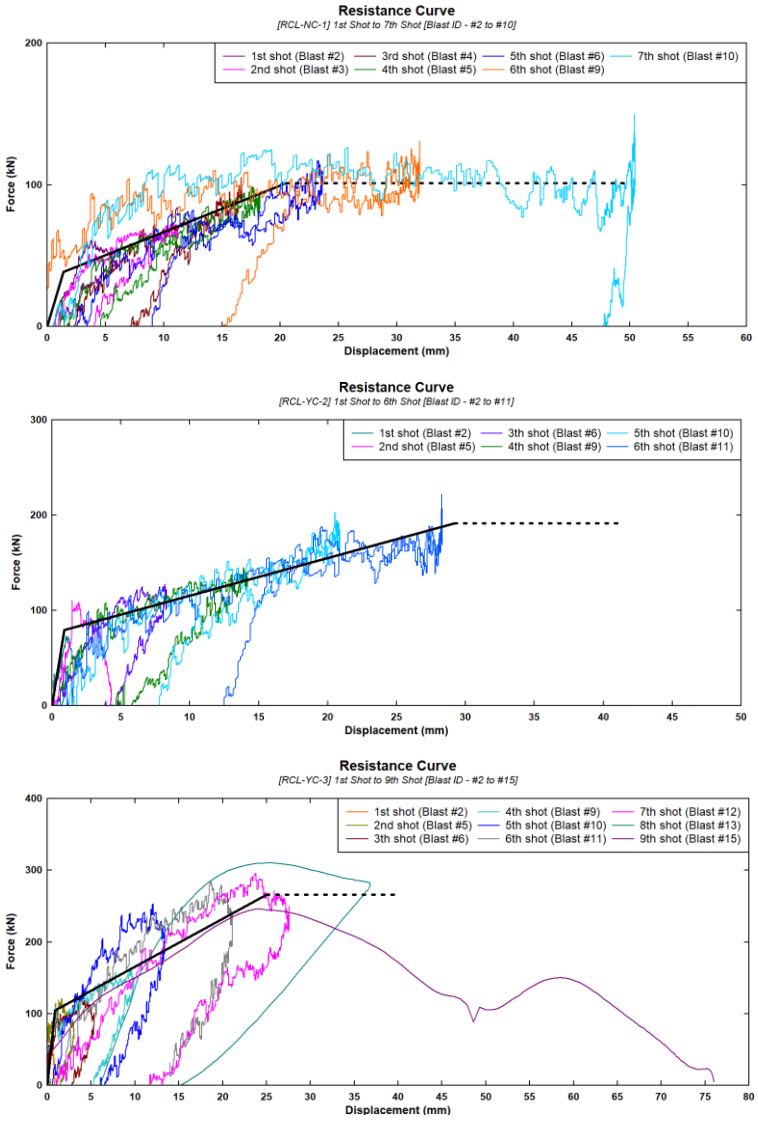

Figure 6-10. Actual vs idealized resistance curves for RCL-NC-1, RCL-YC-2 and RCL-YC-3.

6.6. SDOF Analysis

SDOF analysis was performed on the walls by solving the SDOF equation of motion shown below:

$$\mathbf{K_{LM} m\ddot{u}(t) + R_i(t) = A \cdot P_{ri}(t)} \qquad [6\text{-}23]$$

The analysis was conducted using the idealized resistance function $R_i(t)$ which was derived using the procedure presented in the previous section. In the analysis, the mass of the wall m was taken as being equal to 855 kg, 1202 kg and 1321 kg for RCL-NC-1, RCL-YC-2 and RCL-YC-3, respectively, which considers the weight of the masonry wall, the FRCM retrofit overlay and the SCC when applicable . The forcing function was defined using an idealized triangular pressure time history $P_{ri}(t)$ having the same peak reflected pressure (P_r) and impulse (I_r) observed in the experiments, but with an idealized time $t_d = 2I_r/P_r$, while the loaded area (A) was taken as being equal to the surface area of the wall (4 m^2). The load mass factor (K_{LM}) was assumed to be 0.78 for the uncracked and 0.66 for the post-cracking response regions, respectively (UFC 3-340-02).

With these inputs, the equation of motion was solved in software RCBlast (Jacques, 2014) to predict the mid-height displacements of walls RCL-NC-1, RCL-YC-2 and RCL-YC-3. This software solves the equation of motion using the average acceleration method. Figure 6-11 shows one sample of the inputs and graphical interface used in the analysis for wall RCL-NC-1 during the first shot, along with a graphical representation of the computed SDOF displacement curve.

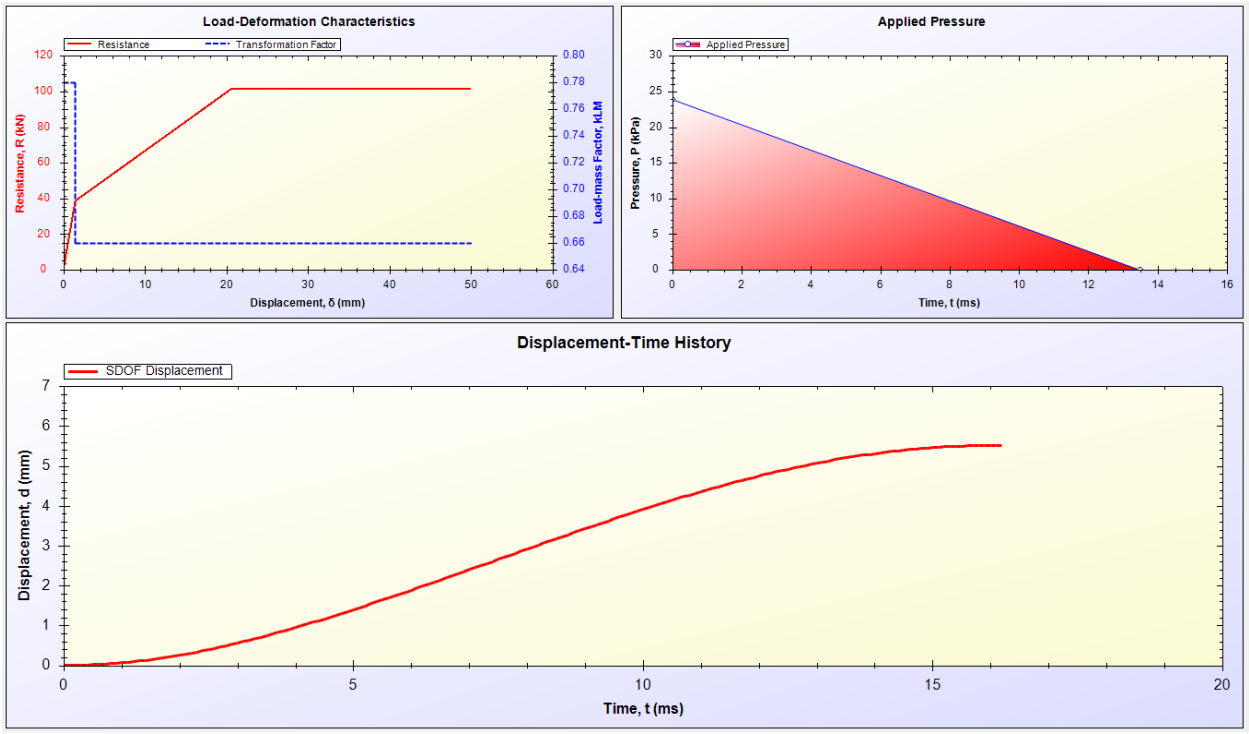

Figure 6-11. Example of the first shot of RCL-NC-1 using the software RCBlast

Table 6-6, Table 6-7 and Table 6-8 compares the results for the experimental (δ_{exp}) and analytical (δ_{anls}) maximum mid-height displacements for walls RCL-NC-1, RCL-YC-2 and RCL-YC-3, respectively, along with the prediction errors. The results are also presented graphically in Figure 6-12, Figure 6-14 and Figure 6-16. Figure 6-13, Figure 6-15 and Figure 6-17 show the displacement-time histories from the SDOF analysis and the experiments for each shot up to maximum response for walls RCL-NC-1, RCL-YC-2 and RCL-YC-3, respectively.

Results for wall RCL-NC-1

When comparing the analytical and experimental maximum displacements, the analysis produced errors which varied between 2.3% to -14.4%, for RCL-NC-1, with a mean error of -7.8%. The analytical resistance was mostly overestimated resulting in lower analytical displacement predictions when compared to the experiments. The results are reasonably accurate for both the maximum mid-height displacements and idealized resistance curve.

Table 6-6. SDOF analytical results of RCL-NC-1

Wall	Blast ID	Blast properties			Maximum mid-height displacements			
					Test	Analysis	Error (%)*	
		P_r (kPa)	I_r (kPa-ms)	t_d (ms)	δ_{exp} (mm)	δ_{anls} (mm)		$\delta_{anls}/\delta_{exp}$
RCL-NC-1	#2	23.9	160.9	13.5	6.1	5.5	-9.5	0.90
	#3	30.8	243.5	15.8	11.3	10.4	-8.4	0.92
	#4	45	297	13.2	17.4	14.9	-14.4	0.86
	#5	48.1	317.6	13.2	19.2	16.5	-14.3	0.86
	#6	53.7	383.8	14.3	24.7	21.4	-13.2	0.87
	#9	66.8	512.6	15.3	32.7	33.5	2.3	1.02
	#10	95.7	665.4	13.9	48.5	49.9	2.9	1.03
	#11	107.3	762.1	14.2	Failed	Failed	n/a	n/a
Statistical data of SDOF Analysis over experiments ($\delta_{anls}/\delta_{exp}$)					Mean Error (%)		-7.8	0.92
					Standard Deviation (%)		6.9	0.07
					Maximum Error (%)		-14.4	0.86
					Minimum Error (%)		2.3	1.02

* Error (%) = $(\delta_{anls} - \delta_{exp})/\delta_{exp} \times 100$ (%)

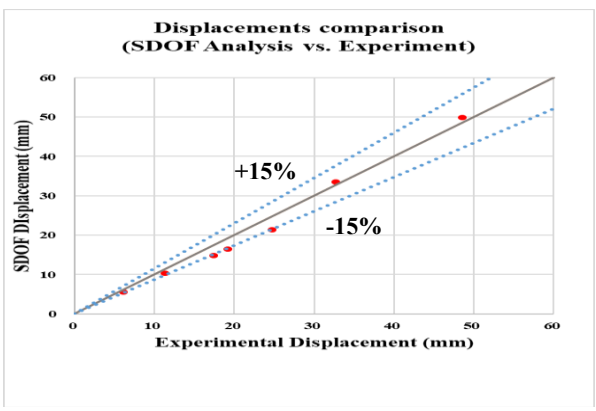

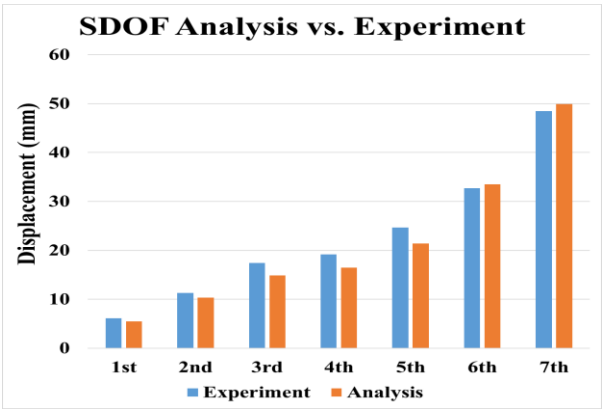

Figure 6-12. Displacement comparison of RCL-NC-1 (SDOF Analysis vs. Experiment)

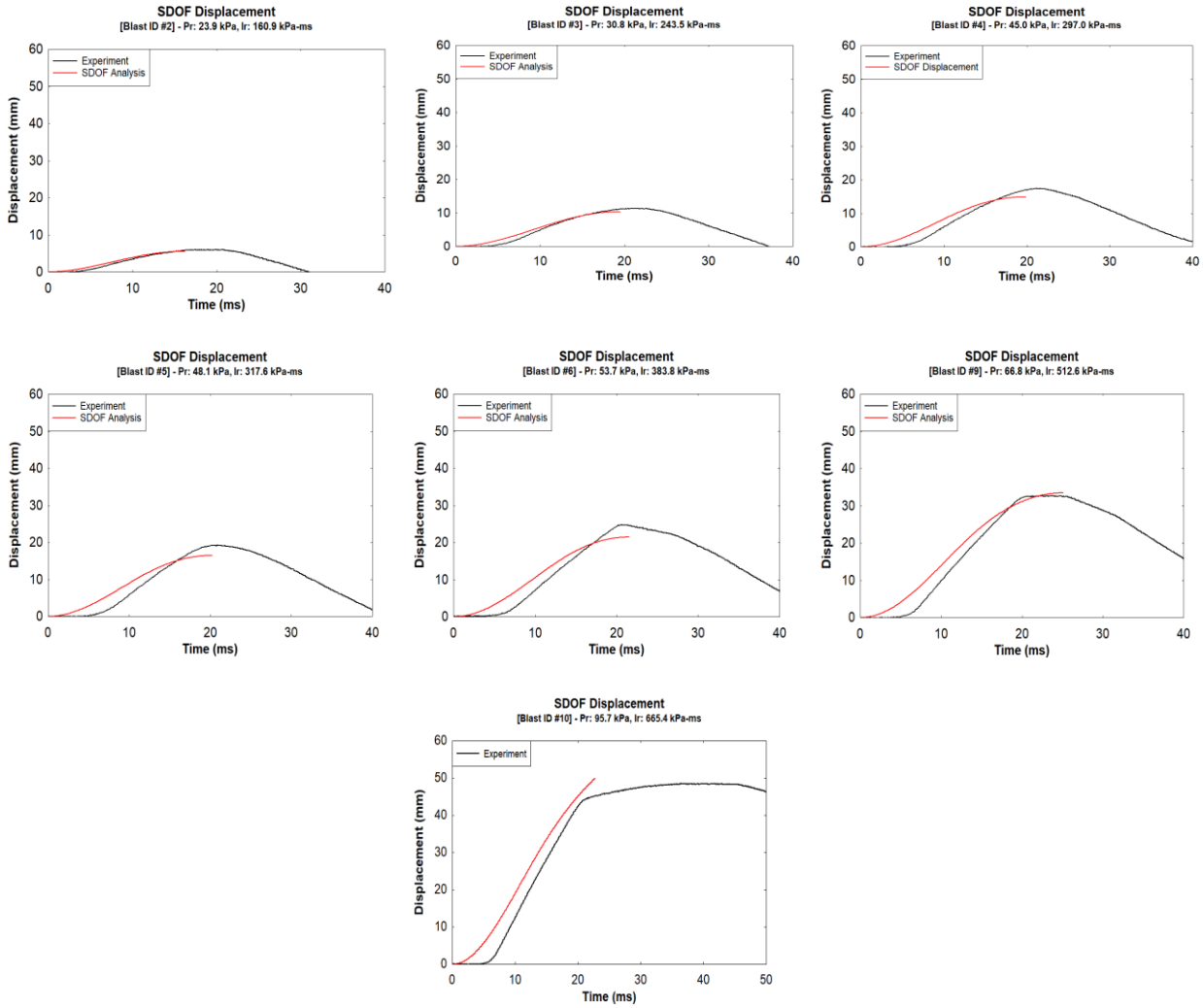

Figure 6-13. Displacement Time History of RCL-NC-1 (SDOF Analysis vs. Experiment)

Results for wall RCL-YC-2

When comparing the analytical and experimental maximum displacements, the analysis produced errors which varied between 0.6% to 23.3%, for RCL-YC-2, with a mean error of 11.0%. For RCL-YC-2, the analytical resistance was mostly underestimated resulting in higher analytical displacement predictions when compared to the experiments. The results are reasonably accurate for both the maximum mid-height displacements and idealized resistance curve.

Table 6-7. SDOF analytical results of RCL-YC-2

Wall	Blast ID	Blast properties			Maximum mid-height displacements			
					Test	Analysis	Error (%)*	
		P_r (kPa)	I_r (kPa-ms)	t_d (ms)	δ_{exp} (mm)	δ_{anls} (mm)		$\delta_{anls}/\delta_{exp}$
RCL-YC-2	#2	24.2	170.1	14.1	1.4	1.7	20.7	1.21
	#5	45.9	291.7	12.7	4.5	5.6	23.3	1.23
	#6	52.3	384.3	14.7	8.8	8.9	1.4	1.01
	#9	71	529.6	14.9	14.9	16.3	9.1	1.09
	#10	92.4	660.5	14.3	22.8	24.1	5.5	1.05
	#11	116.6	828.7	14.2	29.8	34.6	16.1	1.16
	#12	77.8	1130	29.0	40.7	41.0	0.6	1.01
	#13	89.1	1709.1	38.4	Failed	Failed	n/a	n/a
Statistical data of SDOF Analysis over experiments ($\delta_{anls}/\delta_{exp}$)					Mean Error (%)		11.0	1.11
					Standard Deviation (%)		8.5	0.09
					Maximum Error (%)		23.3	1.23
					Minimum Error (%)		0.6	1.01

* Error (%) = $(\delta_{anls} - \delta_{exp})/\delta_{exp} \times 100$ (%)

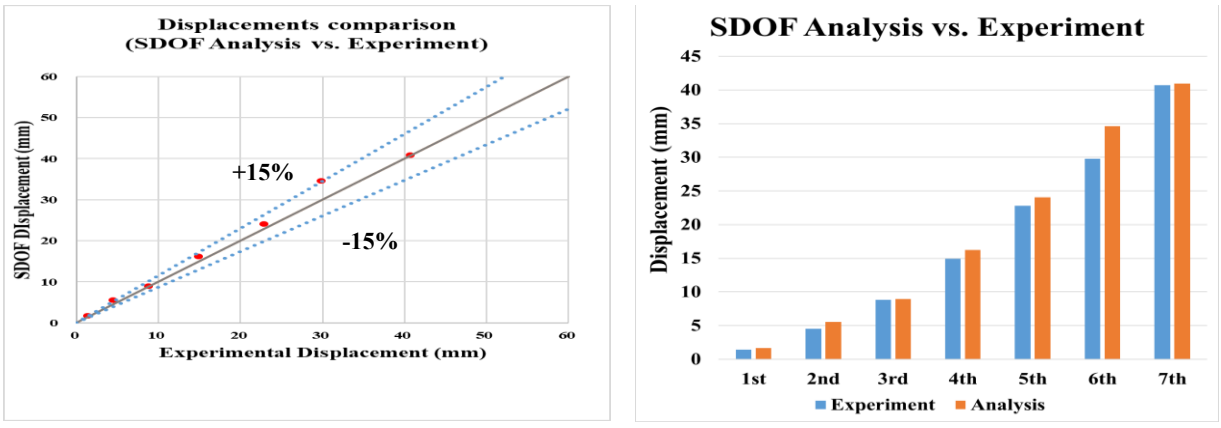

Figure 6-14. Displacement comparison of RCL-YC-2 (SDOF Analysis vs. Experiment)

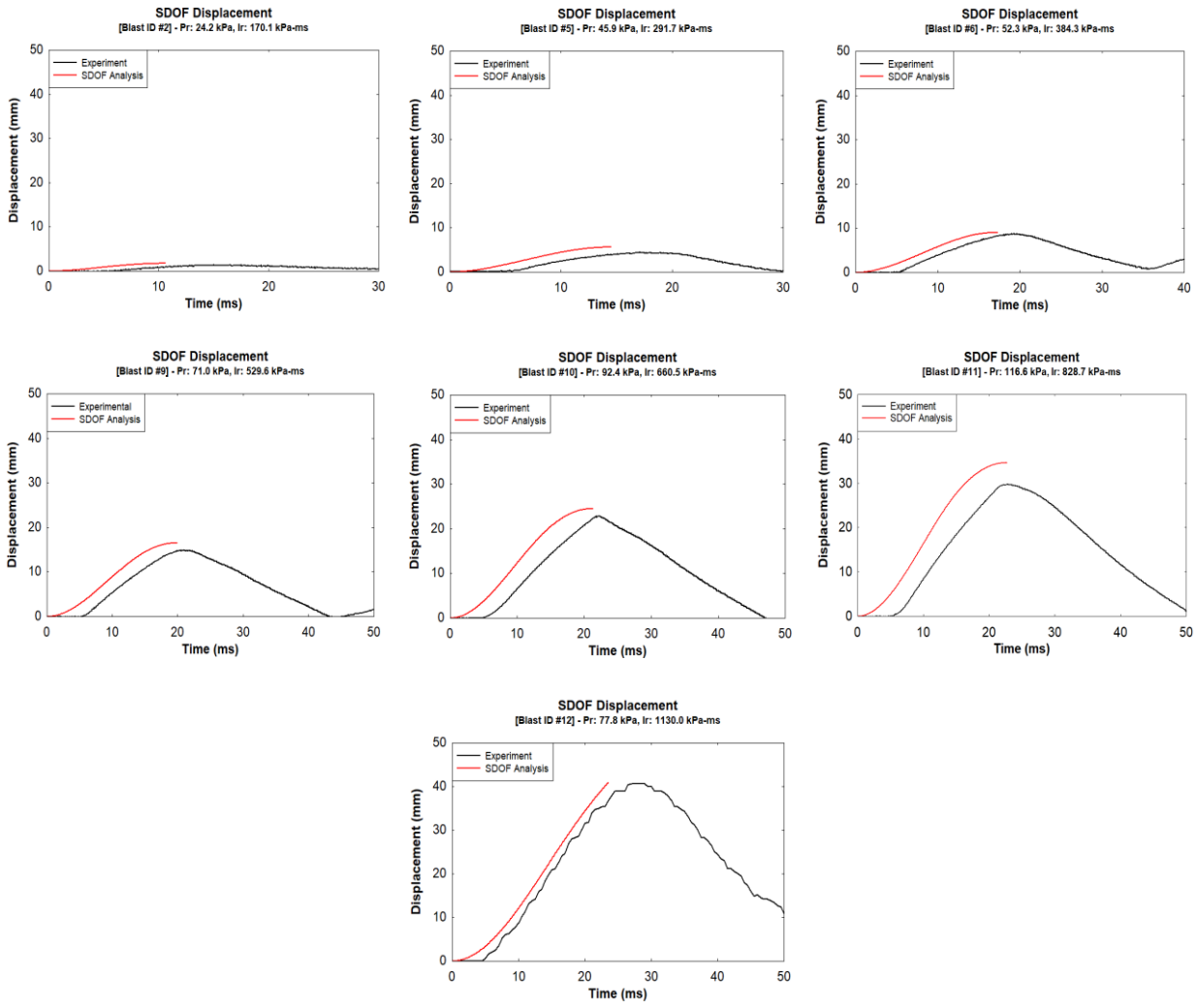

Figure 6-15. Displacement Time History of RCL-YC-2 (SDOF Analysis vs. Experiment)

Results for wall RCL-YC-3

When comparing the analytical and experimental maximum displacements, the analysis produced errors which varied between 65.4% to -3.9%, for RCL-YC-3, with a mean error of 13.9%. For RCL-YC-3, the analytical resistance was overall well estimated resulting in small errors in the analytical displacement predictions when compared to the experiments. The results are reasonably accurate for estimating the maximum mid-height displacements and idealized resistance curve.

Table 6-8. SDOF analytical results of RCL-YC-3

Wall	Blast ID	Blast properties			Maximum mid-height displacements			
					Test	Analysis	Error (%)*	
		P_r (kPa)	I_r (kPa-ms)	t_d (ms)	δ_{exp} (mm)	δ_{anls} (mm)		$\delta_{anls}/\delta_{exp}$
RCL-YC-3	#2	28.4	203.4	14.3	0.9	1.5	65.4	1.65
	#5	47.5	360.9	15.2	3.1	4.6	48.9	1.49
	#6	51.3	378.7	14.8	5.6	5.3	-5.4	0.95
	#9	68.1	519.7	15.3	10.4	10.0	-4.2	0.96
	#10	85	672.1	15.8	13.7	15.7	14.5	1.15
	#11	103.6	828.3	16.0	21.4	22.3	4.1	1.04
	#12	78.7	1103.8	28.1	27.9	25.6	-8.4	0.92
	#13	85.1	1420	33.4	36.5	35.1	-3.9	0.96
	#15	111.8	2081.4	37.2	79	Failed at 40.0	n/a	n/a
Statistical data of SDOF Analysis over experiments ($\delta_{anls}/\delta_{exp}$)					Mean Error (%)		13.9	1.14
					Standard Deviation (%)s		26.2	0.26
					Maximum Error (%)		65.4	1.65
					Minimum Error (%)		-3.9	0.96

* Error (%) = $(\delta_{anls} - \delta_{exp})/\delta_{exp} \times 100$ (%)

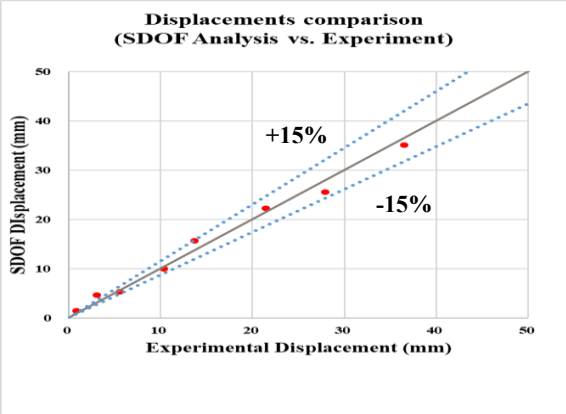

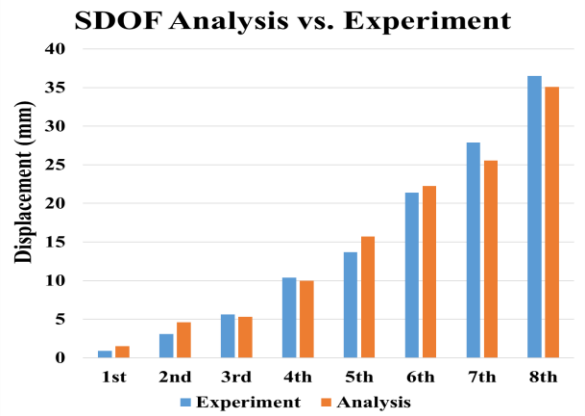

Figure 6-16. Displacement comparison of RCL-YC-3 (SDOF Analysis vs. Experiment)

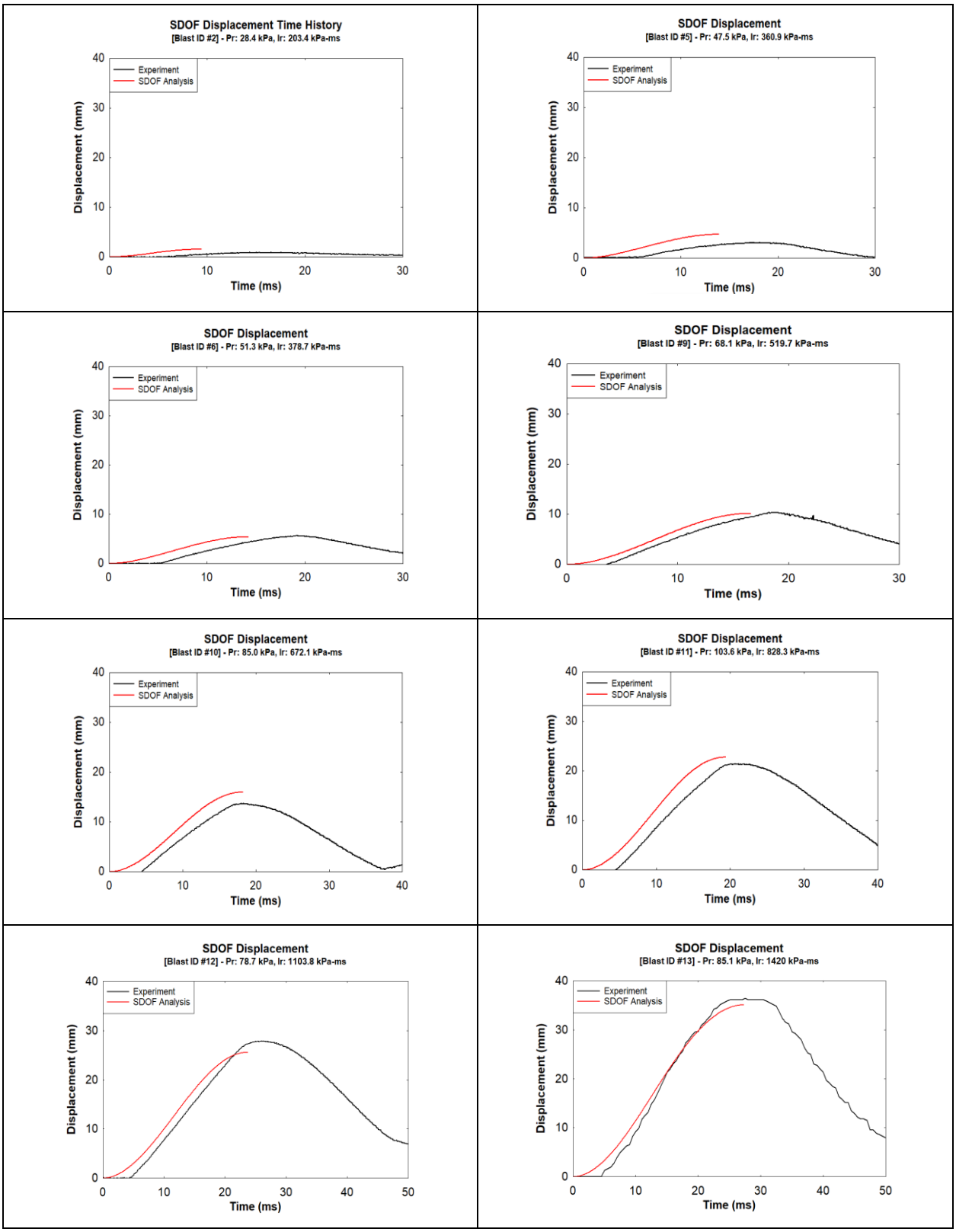

Figure 6-17. Displacement Time History of RCL-YC-3 (SDOF Analysis vs. Experiment)

CHAPTER 7. CONCLUSION

7.1.Conclusion

This project focused on an experimental research program where the main objective was to investigate the effectiveness of using Fabric-Reinforced Cementitious Matrix (FRCM) composites to improve the blast performance of unreinforced concrete masonry walls.

As part of the study, three CMU load-bearing masonry walls were retrofitted with FRCM composites and tested under blast loading using the University of Ottawa Shock tube. To increase shear capacity, two walls were grouted with SCC and one was left without grouting. The test results were firstly compared to one control (un-retrofitted) wall with identical properties tested in previous research; secondly to each other to compare the effect of the FRCM retrofit ratio; thirdly to a load-bearing stone wall (tested in previous research) to compare the effect of masonry type; and finally, to an infill CMU wall (tested in previous research), to observe the effect of axial load.

The following conclusions are drawn from this research study:

1. In general, the FRCM strengthening system proved to be an effective means of increasing the strength and energy-absorption capacity of unreinforced masonry walls subjected to blast loading, enhancing the moment resistance of the walls in the out-of-plane direction and thus the blast capacity when compared to the control (un-retrofitted) wall.
2. The retrofitted walls showed a better performance for energy dissipation under blast loading, with failure governed overall by rupture of the FRCM fibers (on the tension side of the cross section), whereas, the control wall (URM-3) failed in a brittle manner, with significant wall-debris, at relatively lower blast impulses.
3. The FRCM strengthening system also enhanced the control of displacements at equivalent blasts due to the increase in wall stiffness and mass. In all cases, the maximum displacements were lower in the retrofits when compared to the control URM-3. The retrofits reduced maximum displacements by approximately -117%, -809% and -1329% in RCL-NC-1, RCL-YC-2 and RCL-YC-3 walls, respectively.
4. The effectiveness of the FRCM strengthening system is directly related to the reinforcement ratio, where the blast performance generally improves as the number of retrofit layers is increased. On the other hand, the results show that structural elements under-reinforced for flexure, have a more efficient performance than over-reinforced elements.
5. Based on the analysis, the use of one and two layers of FRCM composite system, for RCL-NC-1 and RCL-YC-2 respectively, resulted in under-reinforced conditions in flexure, whereas the use of three plies of FRCM composite system, for RCL-YC-3, resulted in over-reinforced conditions.

6. The analysis also shows that the shear demand increases with the strengthening ratio. Considering that the FRCM strengthening system only enhances the moment resistance of the wall in the out-of-plane direction (or in-plane direction if desired), an alternative solution must be sought to increase the wall's shear capacity. In this study, the infilling of the voids in the masonry units with SCC in walls RCL-YC-2 and RCL-YC-3 increased the shear capacity as expected, and prevented overall shear failure as well as flexural failure caused by crushing of the masonry in compression. The SCC grouting also increased wall mass and stiffness.
7. The effect of masonry type was examined by comparing the results of wall RCL-YC-3 (built with CMU) with wall R-S-L (built with stone units and tested by Jung, 2020); it was observed that the two walls had similar blast performance, with small differences in displacements and blast capacity. Both walls failed at the same Blast ID, indicating that when similar conditions are presented, the effect of masonry type (CMU or stone units) is insignificant for walls strengthened with FRCM composite systems.
8. The application of the axial load enhanced the blast capacity of wall RCL-YC-3 by increasing the shear and out-of-plane flexural capacity. This increase can be due to the contribution of the axial load to the sectional moment capacity as well as arching action. Besides, the axial load improves the shear capacity by keeping together the material in a stronger way and closing small cracks.
9. Single Degree of Freedom (SDOF) analysis was performed to predict the blast behaviour of walls RCL-NC-1, RCL-YC-2 and RCL-YC-3. This was done by computing the wall flexural strength using Plane Sectional Analysis, and developing an idealized resistance curve for use in the SDOF analysis. When comparing the analytical and experimental maximum displacements, the analysis produced errors which varied from 2.3% to -14.4%, for RCL-NC-1, with a mean error of -7.8%; from 0.6% to 23.3%, for RCL-YC-2, with a mean error of 11.0% and from 65.4% to -3.9%, for RCL-YC-3, with a mean error of 13.9%. For RCL-NC-1, the analytical resistance was a bit overestimated resulting in lower analytical displacement predictions when compared to the experiments. Unlike RCL-NC-1, for RCL-YC-2 and RCL-YC-3, the analytical resistance was a bit underestimated resulting in higher analytical displacement predictions when compared to the experiments. Nonetheless, the analytical resistance functions for all three walls allowed for acceptable errors in the analytical maximum displacement predictions when compared to the experiments. The results are reasonably accurate for estimating the maximum mid-height displacements and idealized resistance curve and therefore in analysis and design.

REFERENCES

AC 434–13, Acceptance criteria for masonry and concrete strengthening using fabric-reinforced cementitious matrix (FRCM) composite systems, American Concrete Institute, Farmington Hills, MI, 2013.

ACI 549.4 R-13, Guide to design and construction of externally bonded Fabric-Reinforced Cementitious Matrix (FRCM) systems for repair and strengthening concrete and masonry structures, American Concrete Institute, Farmington Hills, MI, 2013.

ACI 549.6 R-20, Guide to Design and Construction of Externally Bonded Fabric-Reinforced Cementitious Matrix (FRCM) and Steel-Reinforced Grout (SRG) Systems for Repair and Strengthening Masonry Structures, American Concrete Institute, Farmington Hills, MI, 2020.

ASTM C39, Standard Test Method for Compressive Strength of Cylindrical Concrete Specimens, ASTM International, USA, 2018

ASTM C109, Standard Test Method for Compressive Strength of Hydraulic Cement Mortars (Using 2-in. or [50 mm] Cube Specimens), ASTM International, USA, 2020

Canadian Standard Association, CSA A179-04 Mortar and grout for unit masonry, CSA, Mississauga, ON, 2004

Canadian Standard Association, CSA A165: CSA Standard on Concrete Masonry Units, Series-04, CSA, Mississauga, ON, 2004

Canadian Standard Association, CSA S304.1-04: CSA Standard on Design of masonry structures, CSA, Mississauga, ON, 2004

Canadian Standards Association, CSA S850-12: Design and Assessment of Buildings Subjected to Blast Loads. CSA, ON, 2012

MSJC-11: Building Code Requirements and Specification for Masonry Structures and Related Commentaries

Abbas, H., Almusallam, T., Al-salloum, Y., Siddiqui, N., & Abadel, A. (2016). Omae2016-54737 TRM vs. FRP as Strengthening Material for Improving Impact, 1–8.

Al-Jaberi, Z., Myers, J. J., & ElGawady, M. A. (2018). Pseudo-static cyclic loading comparison of reinforced masonry walls strengthened with FRCM or NSM FRP. Construction and Building Materials, 167, 482–495.

Arboleda, D. (2014). Fabric Reinforced Cementitious Matrix (FRCM) Composites for Infrastructure Strengthening and Rehabilitation: Characterization Methods.

Babaeidarabad, S., Nanni, A. (2013). In-Plane Behavior of Unreinforced Masonry Walls Strengthened with Fabric-Reinforced Cementitious Matrix (FRCM). Construction and Building Materials, Elsevier, Under Review.

Babaeidarabad, S. (2013). Masonry Walls Strengthened with Fabric-Reinforced Cementitious Matrix Composite Subjected to in-Plane and Out-of-Plane Load, Doctoral dissertation, University of Miami (USA)

Babaeidarabad, S., De Caso, F., & Nanni, A. (2014). URM walls strengthened with fabric-reinforced cementitious matrix (FRCM) composite subjected to diagonal compression. Composites for Construction, 18(2): 04013045. https://doi.org/10.1061/(ASCE)CC.1943-5614.0000441

Bellini, A., Incerti, A., Bovo, M., & Mazzotti, C. (2017). Effectiveness of FRCM Reinforcement Applied to Masonry Walls Subject to Axial Force and Out- Of-Plane Loads Evaluated by Experimental and Numerical Studies. International Journal of Architectural Heritage, 12(3), 376–394. https://doi.org/10.1080/15583058.2017.1323246

Bernat-Maso, E., Escrig, C., Aranha, C., & Gil, L. (2014). Experimental assessment of Textile Reinforced Sprayed Mortar strengthening system for brickwork wallettes. Construction and Building Materials, 50, 226–236.

Bernat, E., Gil, L., Roca, P., & Escrig, C., (2013). Experimental and analytical study of TRM strengthened brickwork walls under eccentric compressive loading. Construction and Building Materials, 44, 35–47.

Ciornei, L. (2012). Performance of Polyurea Retrofitted Unreinforced Concrete Masonry Walls Under Blast Loading. Ottawa-Carleton Institute for Civil Engineering

Codispoti, R., Oliveira, D. V., Olivito, R. S., Lourenço, P. B., & Fangueiro, R. (2015). Mechanical performance of natural fiber-reinforced composites for the strengthening of masonry. Composites Part B: Engineering, 77, 74–83.

D'Ambra, C. D., Lignola, G. P., Prota, A., Sacco, E., & Fabbrocino, F. (2018). Experimental performance of FRCM retrofit on out-of-plane behaviour of clay brick walls. Composites Part B, 148, 198–206.

D'Antino, T. D., Carozzi, F.G., Colombi, P., & Poggi, C. (2018). Out-of-plane maximum resisting bending moment of masonry walls strengthened with FRCM composites. Composite Structures, 202, 881–896.

De Carvalho Bello, C. B., Cecchi, A., Meroi, E., & Oliveira, D.V. (2017). Experimental and Numerical Investigations on the Behaviour of Masonry Walls Reinforced with an Innovative Sisal FRCM System. Key Engineering Materials, 747, 190-195. https://doi.org/ 10.4028/www.scientific.net/KEM.747.190

Donnini, J., & Corinaldesi, V. (2017). Mechanical characterization of different FRCM systems for structural reinforcement. Construction and Building Materials, 145(August), 565–575.

Drysdale, R., Hamid, A., (2005). Masonry Structures: Behaviour and Design. Canadian Edition. Canada Masonry Design Centre, Mississauga, Ontario.

Escrig, C., Gil, L., & Bernat-Maso, E. (2017). Experimental comparison of reinforced concrete beams strengthened against bending with different types of cementitious-matrix composite materials. Construction and Building Materials, 137, 317–329.

Gandia, J. (2019). Blast retrofit of unreinforced masonry walls using ECC shotcrete. University of Ottawa (Canada)

Gencoglu, M. (2008). Effect of fabric types on the impact behavior of cement based composites in flexure. Materials and Structures, 42, 135–147. https://doi.org/10.1617/s11527-008-9373-y

Harajli, M., ElKhatib, H., & San-Jose, J. T. (2010). Static and Cyclic Out-of-Plane Response of Masonry Walls Strengthened Using Textile-Mortar System. Journal of Materials in Civil Engineering, 22(11), 1171–1180.

Ismail, N., & Ingham, J. M. (2016). In-plane and out-of-plane testing of unreinforced masonry walls strengthened using polymer textile reinforced mortar. Engineering Structures, 118, 167–177.

Jos, C. P. (2016). Design Procedures for the Use of Composites in Strengthening of Reinforced Concrete Structures (Vol. 19).
Jung, H. (2020). Blast retrofit of unreinforced masonry walls using Fabric Reinforced Cementitious Matrix (FRCM) composites. University of Ottawa (Canada)
Kariou, F. A., Triantafyllou, S. P., Bournas, D. A., & Koutas, L. N. (2018). Out-of-plane response of masonry walls strengthened using textile-mortar system. Construction and Building Materials, 165, 769–781.
Kolsch, H. (1998). Carbon Fiber Cement Matrix (CFCM) Overlay System for Masonry Strengthening. Journal of Composites for Construction, 2(May), 105–109.
Liu, S., Zhu, D., Ou, Y., Yao, Y., & Shi, C. (2018). Impact response of basalt textile reinforced concrete subjected to different velocities and temperatures. Construction and Building Materials, 175, 381–391.
Liu, S., Zhu, D., Ou, Y., Yao, Y., & Shi, C. (2018). Effects of Strain Rate and Temperature on the Flexural Behavior of Basalt and Glass Textile–Reinforced Concrete. Journal of Materials in Civil Engineering, 30(8): 04018172. https://doi.org/10.1061/(ASCE)MT.1943-5533.0002387.
Lloyd, A. (2010). Performance of reinforced concrete columns under shock tube induced shock wave loading (Doctoral dissertation, University of Ottawa (Canada)).
Lloyd, A., Jacques, E., Saatcioglu, M., Palermo, D., Nistor, I., & Tikka, T. (n.d.). Capabilities and Effectiveness of using a Shock Tube to Simulate Blast Loading on Structures and Structural Components.
Masonry Standards Joint Committee (MSJC). (2011). Building code requirements for masonry structures (TMS 402-11/ACI 530-11/ASCE 5-11), The Masonry Society, American Concrete Institute, and ASCE,
Ngo, T., Mendis, P., Gupta, A., & Ramsay, J. (2007). Blast Loading and Blast Effects on Structures – An Overview. EJSE Special Issue: Loading on Structures
Papanicolaou, C. G., Triantafillou, T. C., Papathanasiou, M., & Karlos, K. (2008). Textile reinforced mortar (TRM) versus FRP as strengthening material of URM walls: Out-of-plane cyclic loading. Materials and Structures/Materiaux et Constructions, 41(1), 143–157.
Pino, V., Asce, M., Nanni, A., Asce, F., Arboleda, D., Roberts-wollmann, C., … Asce, M. (2017). Repair of Damaged Prestressed Concrete Girders with FRP and FRCM Composites, 21(3), 1–14.
Saatcioglu, M., Eldabelsy, G., Majeed, M. (n.d.) Determination of the influence of masonry bond pattern on the out-of-plane resistance of historic masonry walls. Submitted to: Natural Resources Canada, Canadian Explosives Research Laboratory
Saatcioglu, M., (2019). Blast Threat Risk Analysis [Powerpoint]. Retrieved from University of Ottawa Blast Engineering Brightspace website.
Santis, S. D., Casadei, P., Canio, G. D., Felice, G. D., Malena, M., Mongelli, M., & Roselli, I. (2016). Seismic performance of masonry walls retrofitted with steel reinforced grout. Earthquake Engng Struct. Dyn. 45:229–251. https://doi.org/10.1002/eqe.2625
Silva, F. de A., Butler, M., Mechtcherine, V., Zhu, D., & Mobasher, B. (2011). Strain rate effect on the tensile behaviour of textile-reinforced concrete under static and dynamic loading. Materials Science and Engineering A, 528(3), 1727–1734.

Simpson Strong-Tie (2018). Simpson Strong-Tie® Composite Strengthening Systems CSS-UCG (Data sheet). https://www.strongtie.com/frcm_css/css-ucg_grid/p/css-ucg

UFC (United Facilities Criteria). (2008). "Structures to resist the effects of accidental explosions." UFC 3-340-02, U.S. Dept. of Defense, Washington, DC.

Valluzzi, M. R., da Porto, F., Garbin, E., & Panizza, M. (2014). Out-of-plane behaviour of infill masonry panels strengthened with composite materials. Materials and Structures 47:2131–2145. https://doi.org/ 10.1617/s11527-014-0384-6

Zhu, D., Gencoglu, M., & Mobasher, B. (2009). Low velocity flexural impact behavior of AR glass fabric reinforced cement composites. Cement and Concrete Composites, 31(6), 379–387.

APPENDIX

Reflected pressure (Pr) measured by bottom and side sensors at the end frame of the shock tube at the facilities of the University of Ottawa.

Wall ID	Shot	Blast ID	P_d (kPa)	L_d (mm)	P_r (kPa) Bottom Sensor	I_r (kPa-ms) Bottom Sensor	P_r (kPa) Side Sensor	I_r (kPa-ms) Side Sensor
RCL-NC-1	1st	#2	110.3	1829	23.9	160.9	23.0	142.4
	2nd	#3	165.5	1829	30.8	243.5	28.9	215.6
	3rd	#4	206.8	1829	41.3	297.0	45.0	299.1
	4th	#5	248.2	1829	48.1	317.6	47.9	326.5
	5th	#6	289.6	1829	53.7	383.8	46.3	373.7
	6th	#9	413.7	1829	66.8	512.6	63.8	474.5
	7th	#10	551.6	1829	95.8	665.4	79.5	634.6
	8th	#11	689.5	1829	107.3	762.1	86.6	734.2
RCL-YC-2	1st	#2	110.3	1829	24.2	170.1	23.6	137.8
	2nd	#5	248.2	1829	42.8	291.7	45.9	303.0
	3rd	#6	289.6	1829	52.3	384.3	46.9	342.5
	4th	#9	413.7	1829	71.0	529.6	62.2	480.5
	5th	#10	551.6	1829	92.4	660.5	81.6	623.0
	6th	#11	689.5	1829	116.6	828.7	88.2	767.2
	7th	#12	551.6	3353	77.8	1432.4	70.6	1073.9
	8th	#13	689.5	3353	89.1	1709.1	87.1	1635.0
RCL-YC-3	1st	#2	110.3	1829	28.4	203.4	27.2	170.3
	2nd	#5	248.2	1829	47.6	360.9	45.0	320.4
	3rd	#6	289.6	1829	45.5	378.7	51.3	395.9
	4th	#9	413.7	1829	62.7	519.7	68.1	546.5
	5th	#10	551.6	1829	85.0	672.1	78.3	634.8
	6th	#11	689.5	1829	103.6	828.3	85.4	788.0
	7th	#12	551.6	3353	78.7	1103.8	74.6	1059.7
	8th	#13	689.5	3353	102.3	1816.9	81.0	1804.3
	9th	#15	689.5	3962	111.8	2081.4	83.5	2148.0